

Preface

From April 18 through 22, 2005, Schloß Ringberg at Lake Tegernsee has provided the much enjoyed venue of a *Workshop on Interdisciplinary Aspects of Turbulence*. The origin of this workshop dates back to the summer of 2003 when Christian Beck expressed his interest and support in an interdisciplinary meeting on turbulence which one of us, Friedrich Kupka, suggested to be held and to be hosted as part of the activities of the hydrodynamics group of the MPI for Astrophysics at Garching near Munich in Germany.

The workshop was attended by 43 participants from 12 countries plus a few additional participants from the Munich area attending on a day-by-day basis. This crowd could just be handled by the seating and dining facilities at the Ringberg Castle.

As the term “turbulence” is used for an enormous variety of phenomena, at least some common grounds had to be suggested as preferred topics for contributions to the workshop. A very distinguishing feature of turbulence which was chosen for this purpose is its superior mixing capability compared to, for example, kinematic processes. A detailed quantitative prediction of how turbulent mixing occurs has turned out to be an extremely difficult problem. This has been demonstrated by work in *astrophysics, atmospheric physics, ocean physics, and engineering*.

The workshop hence brought together researchers from these four fields and from the fields of *non-linear dynamics* and *statistical mechanics* who are interested in turbulent mixing, self-organisation of large scale structures, and related properties of turbulence and the interdisciplinary aspects underlying these questions. The venue and size of the workshop were very appropriate to help vivid discussion within each individual field and also among the different fields, so as to share common problems and learn from one another.

Topics discussed during the workshop included the different approaches of modelling and simulations used in the various areas, the possibilities of testing them within individual areas through observation (and including statistical methods), the conclusions drawn on the underlying physics and mathematics – or the lack of them ! –, and most importantly, an intercomparison as well as an interchange of methods and views with researchers working in the different areas represented at the conference.

A total of 40 contributions of varying length has been presented as part of the workshop programme which also featured a number of separate discussion sessions. The following Proceedings contain a collection of extended abstracts of 30 of the contributions which were presented at the workshop. An electronic version of it is available at:

www.mpa-garching.mpg.de/mpa/publications/proceedings/proceedings-en.html

PDF files of the talks of several participants are posted on the workshop webpage:

www.mpa-garching.mpg.de/hydro/Turbulence/

References related to oral contributions not included in this volume can be found at pp. 182.

We are grateful to our co-members of the Scientific Organizing Committee of this workshop – Christian Beck (Queen Mary, Univ. of London, UK), Hans Burchard (Baltic Sea Res. Institute, Germany), Vittorio Canuto (GISS/NASA, USA), Bérengère Dubrulle (CNRS Service d’Astrophysique, CE Saclay, France), Wolfgang Hillebrandt (MPI for Astrophysics), Friedrich Kupka (chair, MPI for Astrophysics), Martin Oberlack (TU-Darmstadt, Germany), Sergej Zilitinkevich (Finnish Meteorological Institute, Helsinki, Finland) – who helped us in inviting participants who all vividly interacted with each other not only among their own but also across other disciplines as well.

The success of the workshop, of course, also depended on the financial support by the Max-Planck-Gesellschaft via the Dr. Ernst Rudolf Schloebmann foundation and, needless to say, on the enormous efficiency and friendliness of Mr. Hörmann and his crew. We would also like to express our gratitude to Fr. Maria Depner for her help in arranging accommodation of the workshop participants and in preparing these proceedings.

Garching, August 2005

Friedrich Kupka

Wolfgang Hillebrandt

List of participants	Institute
Alain Arneodo	ENS Lyon, France
Helmut Baumert	IAMARIS, Hamburg, Germany
Christian Beck	Queen Mary University, London, UK
Eberhard Bodenschatz	LASSP Cornell University, Ithaca, NY, USA & MPI f. Dynamics and Self-Organization, Göttingen, Germany
Vittorio M. Canuto	NASA GISS, New York, NY, USA
Kwing Lam Chan	HKUST, Hong Kong
Pierre-Henri Chavanis	University Paul Sabatier, Toulouse, France
François Daviaud	CEA Saclay, France
Bérengère Dubrulle	CEA Saclay, France
Jens Ewald	RWTH Aachen, Germany
Sergei Fedotov	University of Manchester, UK
Boris Galperin	University of South Florida, St. Petersburg, FL, USA
Toshiyuki Gotoh	Nagoya Institute of Technology, Japan
Martin Greiner	Siemens Munich, Germany
Vladimir Gryanik	AWI Bremerhaven, Germany
Stefan Heitmann	University of Hamburg, Germany
Christiane Helling	ESTEC, AD, Noordwijk, The Netherlands
Wolfgang Hillebrandt	MPI f. Astrophysics, Garching, Germany
Frank Jenko	IPP Garching, Germany
Alan Kerstein	Sandia Nat. Lab., Livermore, CA, USA
Spyridon Kitsionas	Astrophys. Inst. Potsdam, Germany
Friedrich Kupka	MPI f. Astrophysics, Garching, Germany
Dmitrii Mironov	DWD, Offenbach am Main, Germany
Wolf-Christian Müller	IPP Garching, Germany
Jens Niemeyer	University of Würzburg, Germany
Martin Oberlack	TU Darmstadt, Germany
Dirk Olbers	AWI Bremerhaven, Germany
Joachim Peinke	University of Oldenburg, Germany
Andrea Rapisarda	INFN Catania, Italy
Friedrich Röpke	MPI f. Astrophysics, Garching, Germany
Ian W. Roxburgh	Queen Mary University, London, UK
Wolfram Schmidt	University of Würzburg, Germany
John V. Shebalin	NASA JSC, Houston, TX, USA
Joel Sommeria	CORIOLIS Grenoble, France
Chantal Staquet	INPG Grenoble, France
Attilio Stella	INFN Padova, Italy
Semion Sukoriansky	BGU Beer-Sheva, Israel
Constantino Tsallis	Brazilian Center for Res. in Physics, Rio De Janeiro, Brasil & Santa Fe Institute, NM, USA
Lars Umlauf	Baltic Sea Research Institute Warnemünde, Germany
Sylvie Vauclair	Lab. d'Astrophysique, Obs. Midi-Pyrénées, Toulouse, France
Achim Weiss	MPI f. Astrophysics, Garching, Germany
Hua Xia	Plasma Res. Lab., The Austr. Nat. Univ., Canberra, Australia
Matteo Zampieri	ISAC-CNR Bologna, Italy
Sergej S. Zilitinkevich	FMI, University of Helsinki, Finland

Contents

Superstatistical turbulence model <i>Christian Beck</i>	6
Statistical mechanics of 2D turbulence with a prior vorticity distribution <i>P.H. Chavanis</i>	11
Measured stochastic processes for turbulence and nonlinear dynamics <i>J. Peinke, St. Barth, F. Böttcher, M. Waechter, R. Friedrich</i>	16
Multiscaling and turbulent-like behavior in self-organized criticality <i>A.L. Stella, M. De Menech</i>	21
A multifractal formalism for vector-valued random fields based on wavelet analysis: application to turbulent velocity and vorticity 3D numerical data <i>P. Kestener, A. Arneodo</i>	24
Stochastic energy-cascade process for $n+1$-dimensional small-scale turbulence <i>J. Cleve, J. Schmiegel, M. Greiner</i>	29
A one-dimensional stochastic model for turbulence simulation <i>A.R. Kerstein</i>	31
Parameter estimation for algebraic Reynolds stress models <i>Stefan Heitmann</i>	36
Turbulent mixing and entrainment in density driven gravity currents <i>S. Décamp, J. Sommeria</i>	42
Superstatistics and atmospheric turbulence <i>S. Rizzo, A. Rapisarda</i>	52
Interaction of internal gravity waves with a unidirectional shear flow <i>C. Staquet</i>	56
A Level Set Based Flamelet Model for the Prediction of Combustion in Spark Ignition Engines <i>J. Ewald, N. Peters</i>	68
Broken symmetry and coherent structure in MHD turbulence <i>J.V. Shebalin</i>	77
Energy spectrum and transfer flux in Hydrodynamic and MHD turbulence <i>T. Gotoh, K. Mori</i>	93
Turbulent transport in magnetized plasmas <i>F. Jenko</i>	99
Dynamo and Alfvén effect in MHD turbulence <i>Wolf-Christian Müller, R. Grappin</i>	102

Radiatively-driven convection in ice-covered lakes: observations, LES, and bulk modelling <i>Dmitrii V. Mironov</i>	105
Non-local features of turbulence in stably stratified geophysical boundary layers <i>Sergej S. Zilitinkevich</i>	112
A new spectral theory of turbulent flows with stable stratification <i>S. Sukoriansky, B. Galperin</i>	115
Anisotropic large-scale turbulence and zonal jets in computer simulations, in the laboratory, on giant planets and in the ocean <i>B. Galperin, S. Sukoriansky, N. Dikovskaya</i>	125
Stratified Shear turbulence at very high Reynolds numbers <i>Helmut Z. Baumert</i>	133
On the validity of the Millionshchikov quasi-normality hypothesis for convective boundary layer turbulence <i>V. M. Gryanik, J. Hartmann</i>	135
Turbulent convection in astrophysics and geophysics - a comparison <i>F. Kupka</i>	141
Situations in stars where thermohaline convection (fingers regime) is expected to take place <i>S. Vauclair</i>	149
The need for small-scale turbulence in atmospheres of substellar objects <i>Christiane Helling</i>	152
Flow Patterns and Transitions in Rotating Convection <i>K.L. Chan</i>	159
Gravoturbulent Fragmentation: Star formation and the interplay between gravity and interstellar turbulence <i>S. Kitsionas, R.S. Klessen</i>	161
Turbulent Combustion in Type Ia Supernova Models <i>F.K. Röpke, W. Hillebrandt</i>	168
Subgrid Scale Models for Astrophysical Turbulence <i>W. Schmidt, J.C. Niemeyer</i>	172
The FEARLESS Cosmic Turbulence Project <i>J.C. Niemeyer, W. Schmidt, C. Klingenberg</i>	175

Superstatistical turbulence model

Christian Beck

School of Mathematical Sciences, Queen Mary, University of London, Mile End Road, London E1 4NS, UK

Abstract

Recently there has been some progress in modeling the statistical properties of turbulent flows using simple superstatistical models. Here we briefly review the concept of superstatistics in turbulence. In particular, we discuss a superstatistical extension of the Sawford model and compare with experimental data.

Turbulence is a spatio-temporal chaotic dynamics generated by the Navier-Stokes equation

$$\dot{\vec{v}} = -(\bar{v}\nabla)\vec{v} + \nu\Delta\vec{v} + \vec{F}. \quad (1)$$

In the past 5 years there has been some experimental progress in Lagrangian turbulence measurements, i.e. tracking single tracer particles in the turbulent flow. Due to the measurements of the Bodenschatz [1, 2, 3] and Pinton groups [4, 5] we now have a better view of what the statistics of a single test particle in a turbulent flow looks like. The recent measurements have shown that the acceleration \vec{a} as well as velocity difference $\vec{u} = \vec{v}(t + \tau) - \vec{v}(t)$ on short time scales τ exhibits strongly non-Gaussian behavior. This is true for both, single components as well as the absolute value of \vec{a} and \vec{u} . Moreover, there are correlations between the various components of \vec{a} , as well as between velocity and acceleration. The corresponding joint probabilities do not factorize. Finally, the correlation functions of the absolute value $|\vec{a}|$ and $|\vec{u}|$ decay rather slowly.

How can we understand all this by simple stochastic models? There is a recent class of models that are pretty successful in explaining all these statistical properties of Lagrangian turbulence (as well as of other turbulent systems, such as Eulerian turbulence [6, 7, 8], atmospheric turbulence [9, 10, 11] and defect turbulence [12]). These are turbulence models based on superstatistics [13]. Superstatistics is a concept from nonequilibrium statistical mechanics, in short it means a ‘statistics of statistics’, one given by ordinary Boltzmann factors and another one given by fluctuations of an intensive parameter, e.g. the inverse temperature, or the energy dissipation, or a local variance. While the idea of fluctuating intensive parameters is certainly not new, it is the application to spatio-temporally chaotic systems such as turbulent flow that makes the concept interesting. The first turbulence model of this kind was introduced in [14], in the meantime the idea has been further refined and extended [15, 16, 3, 8]. The basic idea is to generate a superposition of two statistics, in short a ‘superstatistics’, by stochastic differential equations whose parameters fluctuate on a relatively large spatio-temporal scale. In Lagrangian turbulence, this large time scale can be understood by the fact that the particle is trapped in vortex tubes for quite a while [3]. Superstatistical turbulence models reproduce all the experimental data quite well. An example is shown in Fig. 1. The theoretical prediction which fits the data perfectly is given by

$$p(a) = \frac{1}{2\pi s} \int_0^\infty d\beta \beta^{-1/2} \exp\left\{-\frac{(\log(\beta/\mu))^2}{2s^2}\right\} e^{-\frac{1}{2}\beta a^2} \quad (2)$$

with $\mu = e^{\frac{1}{2}s^2}$ and only one fitting parameter, $s^2 = 3.0$. A similar formula as eq. (2) was already considered in [17], though without a dynamical interpretation in terms of a stochastic differential equation with fluctuating parameters.

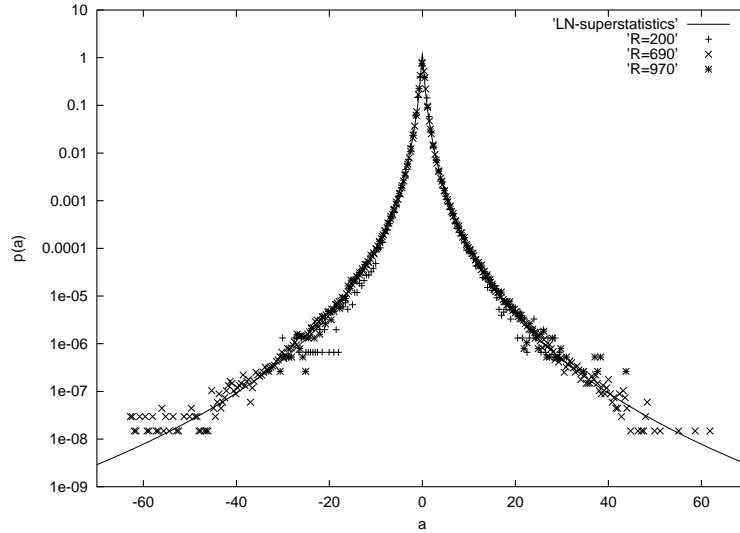


Figure 1: Probability density of an acceleration component of a tracer particle as measured by Boddenschatz et al. [1, 2]. The solid line is a theoretical prediction based on lognormal superstatistics ($s^2 = 3$) [16].

The key ingredient of superstatistical models is to start from a known model generating Gaussian behaviour, and extend it to a superstatistical version exhibiting ‘fat tails’. In general, in these types of models one has for some dynamical variable a the stationary long-term density

$$p(a) = \int_0^\infty \sqrt{\frac{\beta}{2\pi}} f(\beta) e^{-\frac{1}{2}\beta a^2} d\beta, \quad (3)$$

where $f(\beta)$ is some suitable probability density of a fluctuating parameter β . The function $f(\beta)$ fixes the type of superstatistics under consideration. In particular, it is responsible for the shape of the tails [18]. Note the mixing of two statistics, that of a and that of β .

In Lagrangian turbulence, one may first start from a Gaussian turbulence model, the Sawford model [19, 20]. This model considers the joint stochastic process $(a(t), v(t), x(t))$ of an arbitrary component of acceleration, velocity and position of a Lagrangian test particle, and assumes that they obey the stochastic differential equation

$$\begin{aligned} \dot{a} = & -(T_L^{-1} + t_\eta^{-1})a - T_L^{-1}t_\eta^{-1}v \\ & + \sqrt{2\sigma_v^2(T_L^{-1} + t_\eta^{-1})T_L^{-1}t_\eta^{-1}} L(t) \end{aligned} \quad (4)$$

$$\dot{v} = a \quad (5)$$

$$\dot{x} = v, \quad (6)$$

$L(t)$: Gaussian white noise

T_L and t_η : two time scales, with $T_L \gg t_\eta$,

$T_L = 2\sigma_v^2/(C_0\bar{\epsilon})$

$t_\eta = 2a_0\nu^{1/2}/(C_0\bar{\epsilon}^{1/2})$

$\bar{\epsilon}$: average energy dissipation

C_0, a_0 : Lagrangian structure function constants

σ_v^2 variance of the velocity distribution

$R_\lambda = \sqrt{15}\sigma_v^2/\sqrt{\nu\bar{\epsilon}}$ Taylor scale Reynolds number.

For our purposes it is sufficient to consider the limit $T_L \rightarrow \infty$, which is a good approximation for large Reynolds numbers. In that limit the Sawford model reduces to just a linear Langevin equation

$$\dot{a} = -\gamma a + \sigma L(t) \quad (7)$$

with

$$\gamma = \frac{C_0}{2a_0} \nu^{-1/2} \bar{\epsilon}^{1/2} \quad (8)$$

$$\sigma = \frac{C_0^{3/2}}{2a_0} \nu^{-1/2} \bar{\epsilon}. \quad (9)$$

Note that this is a Langevin equation for the acceleration, not for the velocity, in marked contrast to ordinary Brownian motion.

Unfortunately, the Sawford model predicts Gaussian stationary distributions for a , and is thus at variance with the recent measurements. So how can we save this model?

As said before, the idea is to generalize the Sawford model with constant parameters to a superstatistical version. To construct a superstatistical extension of Sawford model, we replace in the above equations the constant energy dissipation $\bar{\epsilon}$ by a fluctuating one. One formally defines a variance parameter [16]

$$\beta := \frac{2\gamma}{\sigma^2} = \frac{4a_0}{C_0^2} \nu^{1/2} \frac{1}{\epsilon^{3/2}}, \quad (10)$$

where ϵ fluctuates. Now, if β varies on a large spatio-temporal scale, and is distributed with the distribution $f(\beta)$, one ends up with eq. (3) describing the long-term marginal distribution of the superstatistical dynamics (7). This is basically the type of model introduced in [14], there with $f(\beta)$ chosen to be a χ^2 -distribution. Models based on χ^2 -superstatistics yield good results for atmospheric turbulence [9, 10], and ultimately lead to Tsallis statistics [21]. On the other hand, for laboratory turbulence experiments one usually obtains better agreement with experimental data if $f(\beta)$ is a lognormal distribution. In view of eq. (10) this is clearly motivated by Kolmogorov's ideas of a lognormally distributed ϵ [22].

Superstatistical models are not restricted to Lagrangian turbulence but can be also formulated for Eulerian turbulence [7, 14]. Fig. 2 shows that also here one obtains excellent agreement with experimental data: Probability densities $p(u)$ of longitudinal velocity differences u are well fitted by lognormal superstatistics on all scales. The parameter s^2 varies with the scale. In fact, not only the distribution $p(u)$ but also the distribution $f(\beta)$ can be directly measured in experiments [8], and the two can be consistently connected via the superstatistics formalism. Jung and Swinney [8] have also experimentally confirmed a simple scaling relation between β and the fluctuating energy dissipation ϵ .

It should be noted that if we know the probability densities $p(u)$ analytically, as well as the dependence of the parameter s^2 on the scale r , we can also calculate moments of velocity differences and thus determine scaling exponents ζ_m defined by

$$\langle u^m \rangle \sim r^{\zeta_m}.$$

Many different models of ζ_m can be constructed in such a way [16, 23, 24]. For further stochastic models, see e.g. [25, 26, 27].

References

- [1] A. La Porta, G.A. Voth, A.M. Crawford, J. Alexander, and E. Bodenschatz, *Nature* **409**, 1017 (2001)

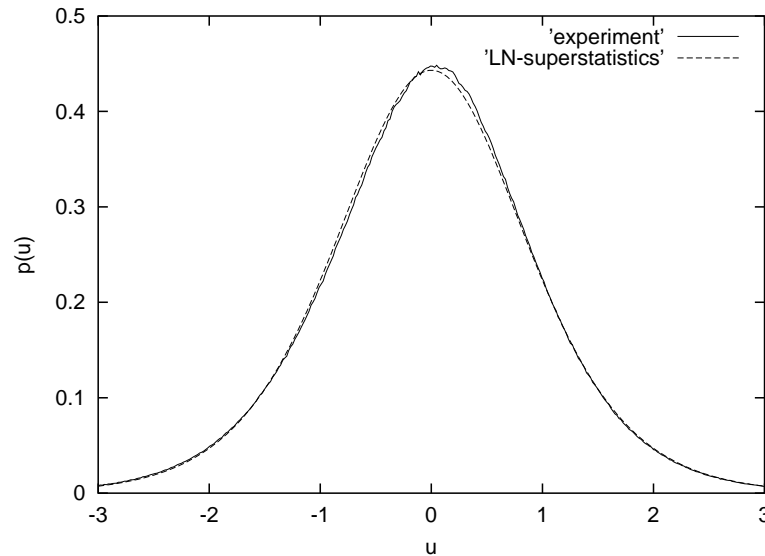


Figure 2: Experimentally measured histogram of velocity differences in a Taylor-Couette experiment [6], and comparison with a superstatistical prediction ($s^2 = 0.28$).

- [2] G.A. Voth et al., J. Fluid Mech. **469**, 121 (2002)
- [3] A.M. Reynolds, N. Mordant, A.M. Crawford and E. Bodenschatz, New Journal of Physics **7**, 58 (2005)
- [4] N. Mordant, P. Metz, O. Michel, and J.-F. Pinton, Phys. Rev. Lett. **87**, 214501 (2001)
- [5] L. Chevillard, S.G. Roux, E. Leveque, N. Mordant, J.-F. Pinton, and A. Arneodo, Phys. Rev. Lett. **91**, 214502 (2003)
- [6] C. Beck, G.S. Lewis and H.L. Swinney, Phys. Rev. **63E**, 035303(R) (2001)
- [7] C. Beck, Physica **193D**, 195 (2004)
- [8] S. Jung and H.L. Swinney, cond-mat/0502301
- [9] S. Rizzo and A. Rapisarda, in Proceedings of the 8th Experimental Chaos Conference, Florence, AIP Conf. Proc. **742**, 176 (2004) (cond-mat/0406684)
- [10] S. Rizzo and A. Rapisarda, cond-mat/0502305
- [11] F. Böttcher, St. Barth, and J. Peinke, nlin.AO/0408005
- [12] K. E. Daniels, C. Beck, and E. Bodenschatz, Physica **193D**, 208 (2004)
- [13] C. Beck and E.G.D. Cohen, Physica **322A**, 267 (2003)
- [14] C. Beck, Phys. Rev. Lett. **87**, 180601 (2001)
- [15] A. Reynolds, Phys. Rev. Lett. **91**, 084503 (2003)
- [16] C. Beck, Europhys. Lett. **64**, 151 (2003)
- [17] B. Castaing, Y. Gagne, and E.J. Hopfinger, Physica **46D**, 177 (1990)

- [18] H. Touchette and C. Beck, Phys. Rev. **71E**, 016131 (2005)
- [19] B.L. Sawford, Phys. Fluids **A3**, 1577 (1991)
- [20] S.B. Pope, Phys. Fluids **14**, 2360 (2002)
- [21] C. Tsallis, J. Stat. Phys. **52**, 479 (1988)
- [22] A.N. Kolmogorov, J. Fluid Mech. **13**, 82 (1962)
- [23] C. Beck, Physica **295A**, 195 (2001)
- [24] C. Beck, Chaos, Solitons and Fractals **13**, 499 (2002)
- [25] A.K. Aringazin and M.I. Mazhitov, cond-mat/0408018
- [26] J.-P. Laval, B. Dubrulle, and S. Nazarenko, Phys. Fluids **13**, 1995 (2001)
- [27] B. Jouault, M. Greiner, P. Lipa , Physica **136D**, 125 (2000)

Statistical mechanics of 2D turbulence with a prior vorticity distribution

P.H. Chavanis

Laboratoire de Physique Théorique
 Université Paul Sabatier
 118, route de Narbonne
 31062 Toulouse, France

Abstract

We adapt the formalism of the statistical theory of 2D turbulence in the case where the Casimir constraints are replaced by the specification of a prior vorticity distribution. A new relaxation equation is obtained for the evolution of the coarse-grained vorticity. It can be used as a thermodynamical parametrization of forced 2D turbulence (determined by the prior), or as a numerical algorithm to construct arbitrary nonlinearly dynamically stable stationary solutions of the 2D Euler equation.

Two-dimensional incompressible flows with high Reynolds numbers are described by the 2D Euler equations

$$\frac{\partial \omega}{\partial t} + \mathbf{u} \cdot \nabla \omega = 0, \quad \omega = -\Delta \psi, \quad \mathbf{u} = -\mathbf{z} \times \nabla \psi, \quad (1)$$

where ω is the vorticity and ψ the streamfunction. The 2D Euler equations are known to develop a complicated mixing process which ultimately leads to the emergence of a large-scale coherent structure, typically a jet or a vortex. Jovian atmosphere shows a wide diversity of structures: Jupiter's great red spot, white ovals, brown barges,... One question of fundamental interest is to understand and predict the structure and the stability of these equilibrium states. To that purpose, Miller [1] and Robert & Sommeria [2] have proposed a statistical mechanics of the 2D Euler equation. The idea is to replace the deterministic description of the flow $\omega(\mathbf{r}, t)$ by a probabilistic description where $\rho(\mathbf{r}, \sigma, t)$ gives the density probability of finding the vorticity level $\omega = \sigma$ in \mathbf{r} at time t . The observed (coarse-grained) vorticity field is then expressed as $\bar{\omega}(\mathbf{r}, t) = \int \rho \sigma d\sigma$. To apply the statistical theory, one must first specify the constraints attached to the 2D Euler equation. The circulation $\Gamma = \int \bar{\omega} d\mathbf{r}$ and the energy $E = \frac{1}{2} \int \bar{\omega} \psi d\mathbf{r}$ will be called *robust constraints* because they can be expressed in terms of the coarse-grained field $\bar{\omega}$ (the energy of the fluctuations can be neglected). These integrals can be calculated at any time from the coarse-grained field $\bar{\omega}(\mathbf{r}, t)$ and they are conserved by the dynamics. By contrast, the Casimir invariants $I_f = \int \bar{f}(\bar{\omega}) d\mathbf{r}$, or equivalently the fine-grained moments of the vorticity $\Gamma_{n>1}^{f.g.} = \int \bar{\omega}^n d\mathbf{r} = \int \rho \sigma^n d\sigma d\mathbf{r}$, will be called *fragile constraints* because they must be expressed in terms of the fine-grained vorticity. Indeed, the moments of the coarse-grained vorticity $\Gamma_{n>1}^{c.g.} = \int \bar{\omega}^n d\mathbf{r}$ are not conserved since $\bar{\omega}^n \neq \bar{\omega}^n$ (part of the coarse-grained moments goes into fine-grained fluctuations). Therefore, the moments $\Gamma_{n>1}^{f.g.}$ must be calculated from the fine-grained field $\omega(\mathbf{r}, t)$ or from the initial conditions, i.e. before the vorticity has mixed. Since we often do not know the initial conditions nor the fine-grained field, the Casimir invariants often appear as "hidden constraints" [3].

The statistical theory of Miller-Robert-Sommeria is based on two assumptions: (i) it is assumed that we know the initial conditions (or equivalently the value of all the Casimirs) in detail (ii) it is assumed that mixing is efficient and that the evolution is ergodic so that the system will reach

at equilibrium the most probable (most mixed) state. Within these assumptions¹, the statistical equilibrium state of the 2D Euler equation is obtained by maximizing the mixing entropy

$$S[\rho] = - \int \rho \ln \rho \, d\mathbf{r}d\sigma, \quad (2)$$

at fixed energy E and circulation Γ (robust constraints) and fixed fine-grained moments $\Gamma_{n>1}^{f.g.}$ (fragile constraints). This optimization principle is solved by introducing Lagrange multipliers, writing the first order variations as

$$\delta S - \beta \delta E - \alpha \delta \Gamma - \sum_{n>1} \alpha_n \delta \Gamma_n^{f.g.} = 0. \quad (3)$$

In the approach of Miller-Robert-Sommeria, it is assumed that the system is strictly described by the 2D Euler equation so that the conservation of all the Casimirs has to be taken into account. However, in geophysical situations, the flows are forced and dissipated at small scales (due to convection in the jovian atmosphere) so that the conservation of the Casimirs is destroyed. Ellis *et al.* [6] have proposed to treat these situations by fixing the conjugate variables $\alpha_{n>1}$ instead of the fragile moments $\Gamma_{n>1}^{f.g.}$. If we view the vorticity levels as species of particles, this is similar to fixing the chemical potentials instead of the total number of particles in each species. Therefore, the idea is to treat the fragile constraints *canonically*, whereas the robust constraints are still treated *microcanonically*. This point of view has been further developed in Chavanis [7]. The relevant thermodynamical potential is obtained from the mixing entropy (2) by using a Legendre transform with respect to the fragile constraints [7]:

$$S_\chi = S - \sum_{n>1} \alpha_n \Gamma_n^{f.g.}. \quad (4)$$

Expliciting the fine-grained moments, we obtain the *relative entropy*

$$S_\chi[\rho] = - \int \rho \ln \left[\frac{\rho}{\chi(\sigma)} \right] d\mathbf{r}d\sigma, \quad (5)$$

where we have defined the *prior vorticity distribution*

$$\chi(\sigma) \equiv \exp \left\{ - \sum_{n>1} \alpha_n \sigma^n \right\}. \quad (6)$$

We shall assume that this function is *imposed* by the small-scale forcing. Assuming ergodicity, the statistical equilibrium state is now obtained by maximizing the relative entropy S_χ at fixed energy E and circulation Γ (no other constraints). The conservation of the Casimirs has been replaced by the specification of the prior $\chi(\sigma)$. Writing $\delta S_\chi - \beta \delta E - \alpha \delta \Gamma = 0$, and accounting for the normalization condition $\int \rho d\sigma = 1$, we get the Gibbs state

$$\rho(\mathbf{r}, \sigma) = \frac{1}{Z(\mathbf{r})} \chi(\sigma) e^{-(\beta\psi + \alpha)\sigma} \quad \text{with} \quad Z = \int_{-\infty}^{+\infty} \chi(\sigma) e^{-(\beta\psi + \alpha)\sigma} d\sigma. \quad (7)$$

This is the product of a universal Boltzmann factor by a non-universal function $\chi(\sigma)$ fixed by the forcing. The coarse-grained vorticity is given by

$$\bar{\omega} = \frac{\int \chi(\sigma) \sigma e^{-(\beta\psi + \alpha)\sigma} d\sigma}{\int \chi(\sigma) e^{-(\beta\psi + \alpha)\sigma} d\sigma} = F(\beta\psi + \alpha) \quad \text{with} \quad F(\Phi) = -(\ln \hat{\chi})'(\Phi), \quad (8)$$

¹Some attempts have been proposed to go beyond the assumptions of the statistical theory. For example, Chavanis & Sommeria [4] consider a *strong mixing limit* in which only the first moments of the vorticity are relevant instead of the whole set of Casimirs. On the other hand, Chavanis & Sommeria [5] introduce the concept of *maximum entropy bubbles* (or restricted equilibrium states) in order to account for situations where the evolution of the flow is not ergodic in the whole available domain but only in a subdomain.

where $\hat{\chi}(\Phi) = \int_{-\infty}^{+\infty} \chi(\sigma) e^{-\sigma\Phi} d\sigma$. It is easy to show that $F'(\Phi) = -\omega_2(\Phi) \leq 0$, where $\omega_2 = \overline{\omega^2} - \bar{\omega}^2 \geq 0$ is the local centered variance of the vorticity, so that F is a decreasing function [8]. Therefore, the statistical theory predicts that the coarse-grained vorticity $\bar{\omega} = f(\psi)$ is a *stationary solution* of the 2D Euler equation and that the $\bar{\omega} - \psi$ relationship is a *monotonic* function which is increasing at negative temperatures $\beta < 0$ and decreasing at positive temperatures $\beta > 0$ since $\bar{\omega}'(\psi) = -\beta\omega_2$. We also note that the most probable vorticity $\langle\sigma\rangle(\mathbf{r})$ of the distribution (7) is given by [9]:

$$\langle\sigma\rangle = [(\ln \chi)']^{-1}(\beta\psi + \alpha), \quad (9)$$

provided $(\ln \chi)''(\langle\sigma\rangle) < 0$. This is also a stationary solution of the 2D Euler equation which usually differs from the average value $\bar{\omega}(\mathbf{r})$ of the distribution (7) except when $\chi(\sigma)$ is gaussian. We note that the $\bar{\omega} - \psi$ relationship predicted by the statistical theory can take a wide diversity of forms (non-Boltzmannian) depending on the prior $\chi(\sigma)$. The coarse-grained vorticity (8) can be viewed as a sort of *superstatistics* as it is expressed as a superposition of Boltzmann factors (on the fine-grained scale) weighted by a non-universal function $\chi(\sigma)$ [3]. Furthermore, the coarse-grained vorticity (8) maximizes a generalized entropy (in $\bar{\omega}$ -space) of the form [10]:

$$S[\bar{\omega}] = - \int C(\bar{\omega}) d\mathbf{r}, \quad (10)$$

at fixed circulation and energy (robust constraints). Writing $\delta S - \beta\delta E - \alpha\delta\Gamma = 0$ leading to $C'(\bar{\omega}) = -\beta\psi - \alpha$ and $\bar{\omega}'(\psi) = -\beta/C''(\bar{\omega})$, and comparing with Eq. (8), we find that C is a convex function ($C'' > 0$) determined by the prior $\chi(\sigma)$ encoding the small-scale forcing according to the relation [3]:

$$C(\bar{\omega}) = - \int^{\bar{\omega}} F^{-1}(x) dx = - \int^{\bar{\omega}} [(\ln \hat{\chi})']^{-1}(-x) dx. \quad (11)$$

The preceding relations are also valid in the approach of Miller-Robert-Sommeria except that $\chi(\sigma)$ is determined *a posteriori* from the initial conditions by relating the Lagrange multipliers $\alpha_{n>1}$ to the Casimir constraints $\Gamma_{n>1}^{f.g.}$. In this case of freely evolving flows, the generalized entropy (10) depends on the initial conditions, while in the case of forced flows considered here, it is intrinsically fixed by the prior vorticity distribution.

In that context, it is possible to propose a thermodynamical parameterization of 2D forced turbulence in the form of a relaxation equation that conserves circulation and energy (robust constraints) and that increases the generalized entropy (10) fixed by the prior $\chi(\sigma)$. This equation can be obtained from a generalized Maximum Entropy Production (MEP) principle in $\bar{\omega}$ -space [10] by writing the coarse-grained 2D Euler equation in the form $D\bar{\omega}/Dt = -\nabla \cdot \bar{\omega}\bar{\mathbf{u}} = -\nabla \cdot \mathbf{J}$ and determining the optimal current \mathbf{J} which maximizes the rate of entropy production $\dot{S} = - \int C''(\bar{\omega}) \mathbf{J} \cdot \nabla \bar{\omega} d\mathbf{r}$ at fixed energy $\dot{E} = \int \mathbf{J} \cdot \nabla \psi d\mathbf{r} = 0$, assuming that the energy of fluctuations $\mathbf{J}^2/2\bar{\omega}$ is bounded. According to this principle, we find that the coarse-grained vorticity evolves according to [10, 7]:

$$\frac{\partial \bar{\omega}}{\partial t} + \mathbf{u} \cdot \nabla \bar{\omega} = \nabla \cdot \left\{ D \left[\nabla \bar{\omega} + \frac{\beta(t)}{C''(\bar{\omega})} \nabla \psi \right] \right\}, \quad \bar{\omega} = -\Delta \psi, \quad (12)$$

$$\beta(t) = - \frac{\int D \nabla \bar{\omega} \cdot \nabla \psi d^2 \mathbf{r}}{\int D \frac{(\nabla \psi)^2}{C''(\bar{\omega})} d^2 \mathbf{r}}, \quad D \propto \omega_2^{1/2} = \frac{1}{\sqrt{C''(\bar{\omega})}}, \quad (13)$$

where $\beta(t)$ is a Lagrange multiplier enforcing the energy constraint $\dot{E} = 0$ at any time. These equations increase the entropy (H -theorem $\dot{S} \geq 0$) provided that $D > 0$, until the equilibrium state (8) is reached. The diffusion coefficient D is not determined by the MEP but it can be obtained from

a Taylor’s type argument leading to expression (13)-b [7]. This diffusion coefficient, related to the strength of the fluctuations, can “freeze” the relaxation in a sub-region of space (“bubble”) and account for *incomplete relaxation* and lack of ergodicity [11, 12]. The relaxation equation (12) belongs to the class of generalized Fokker-Planck equations introduced in Chavanis [10]. This relaxation equation conserves only the robust constraints (circulation and energy) and increases the generalized entropy (11) fixed by the prior vorticity distribution $\chi(\sigma)$. It differs from the relaxation equations proposed by Robert & Sommeria [13] for freely evolving flows which conserve all the constraints of the 2D Euler equation (including all the Casimirs) and increase the mixing entropy (2). In Eqs. (12)-(13), the specification of the prior $\chi(\sigma)$ (determined by the small-scale forcing) replaces the specification of the Casimirs (determined by the initial conditions). However, in both models, the robust constraints E and Γ are treated microcanonically (i.e. they are rigorously conserved). Furthermore, in the two-levels case $\omega \in \{\sigma_0, \sigma_1\}$, the two approaches are formally equivalent and they amount to maximizing a generalized entropy (10) similar to the Fermi-Dirac entropy at fixed circulation and energy [12]. In the viewpoint of Miller-Robert-Sommeria, this entropy describes the free merging of a system with two levels of vorticity σ_0 and σ_1 while in the other view point, it describes the evolution of a forced system where the forcing has two intense peaks described by the prior $\chi(\sigma) = \chi_0\delta(\sigma - \sigma_0) + \chi_1\delta(\sigma - \sigma_1)$ [7].

The relaxation equations (12)-(13) can also be used as a *numerical algorithm* to construct stable stationary solutions of the 2D Euler equation. Indeed, Ellis *et al.* [6] have shown that the maximization of a functional of the form (10) at fixed energy and circulation determines a stationary solution of the 2D Euler equation of the form $\omega = f(\psi)$, where f is monotonic, which is nonlinearly dynamically stable. Since the stationary solution of Eqs. (12)-(13) maximizes S at fixed E and Γ (by construction), this steady solution of the relaxation equations is also a nonlinearly dynamically stable stationary solution of the 2D Euler equations (1). Thus, by changing the convex function $C(\omega)$ in Eq. (12), we can numerically construct a wide diversity of stable solutions of the 2D Euler equations. This is a potentially interesting procedure because it is usually difficult to solve the differential equation $-\Delta\psi = f(\psi)$ directly and be sure that the solution is (nonlinearly) dynamically stable. These nonlinearly stable steady states can be an alternative to the statistical equilibrium state in case of incomplete relaxation, when the system has not mixed efficiently (non-ergodicity) so that the statistical prediction fails. In case of incomplete relaxation we cannot *predict* the equilibrium state but we can try to *reproduce* it a posteriori.

Finally, we have proposed in [10] to develop a phenomenological/effective statistical theory of 2D turbulence to deal with complex situations. The idea is that some types of entropy functional $S[\bar{\omega}]$ (in $\bar{\omega}$ -space) may be more appropriate than others to describe a given physical situation. For example, the enstrophy functional turns out to be relevant in certain oceanic situations [14] and the Fermi-Dirac type entropy in jovian flows [15, 8]. Certainly, other functionals of the same “class” would work as well for these systems. In addition, other classes of functionals $S[\bar{\omega}]$ may be relevant in other circumstances. Therefore, as a simple and practical procedure to describe a given system, we propose to pick a functional $S[\bar{\omega}]$ in the “class of equivalence” appropriate to that system and use it in the parameterization (12)-(13). We can thus describe the time evolution of the system on the coarse-grained scale. This approach is not completely predictive because we need to know in advance which type of entropy $S[\bar{\omega}]$ describes best such and such situation. In practice, it must be determined by trying and errors (e.g. by comparing with oceanic data). But once a specific entropy has been found for a physical situation, we can work with it for different initial conditions specified by the robust constraints E and Γ (the effect of the Casimirs is reported in the chosen form of entropy $S[\bar{\omega}]$). The idea is that the entropy S remains the same while E and Γ are changed. The problem is rich and non-trivial even if S has been fixed because bifurcations can occur depending on the control parameters E , Γ . This heuristic approach can be viewed as a simple attempt to account for the influence of the Casimirs while leaving the problem tractable. We use the fact that the Casimirs lead to *non-standard*

(i.e. non-Boltzmannian) $\bar{\omega} - \psi$ relationships at equilibrium which are associated with non-standard forms of entropy $S[\bar{\omega}]$ in ω -space. We propose to *fix* the S -functional depending on the situation. We do not try to *predict* its form, but rather to *adjust* it to the situation contemplated. This is based on the belief that some functionals $S[\bar{\omega}]$ are more relevant than others for a given system. Whether this is the case or not remains to be established. All the ideas presented here can be generalized to the case of quasi-geostrophic or shallow-water equations [8].

References

- [1] J. Miller, Phys. Rev. Lett. **65** (1990) 2137.
- [2] R. Robert and J. Sommeria, J. Fluid Mech. **229** (1991) 291.
- [3] P.H. Chavanis, *Coarse-grained distributions and superstatistics* [cond-mat/0409511]
- [4] P.H. Chavanis and J. Sommeria, J. Fluid Mech. **314** (1996) 267.
- [5] P.H. Chavanis and J. Sommeria, J. Fluid Mech. **356** (1998) 259.
- [6] R. Ellis, K. Haven and B. Turkington, Nonlinearity **15** (2002) 239.
- [7] P.H. Chavanis, Physica D **200** (2005) 257.
- [8] P.H. Chavanis and J. Sommeria, Phys. Rev. E **65** (2002) 026302.
- [9] N. Leprovost, B. Dubrulle and P.H. Chavanis, *Dynamics and thermodynamics of axisymmetric flows: I. Theory* [physics/0505084]
- [10] P.H. Chavanis, Phys. Rev. E **68** (2003) 036108.
- [11] R. Robert and C. Rosier, J. Stat. Phys. **86** (1997) 481.
- [12] P.H. Chavanis, J. Sommeria and R. Robert, Astrophys. J. **471** (1996) 385.
- [13] R. Robert and J. Sommeria, Phys. Rev. Lett. **69** (1992) 2776.
- [14] E. Kazantsev, J. Sommeria and J. Verron, J. Phys. Oceanogr. **28** (1998) 1017.
- [15] F. Bouchet and J. Sommeria, J. Fluid Mech. **464** (2002) 165.

Measured stochastic processes for turbulence and nonlinear dynamics

J. Peinke¹, St. Barth¹, F. Böttcher¹, M. Waechter¹, R. Friedrich²

¹ Institute of Physics, Carl von Ossietzky University,
D-26 111 Oldenburg, Germany

² Institute for Theoretical Physics, University of Münster,
Wilhelm-Klemm-Str. 9, D- 48149 Münster, Germany

Abstract

For the characterization of complex structures we present an approach which is based on the theory of stochastic Markov processes. With this analysis we achieve a characterization of the systems whose complexity may be based on nonlinear noisy dynamics or multiscale features like multifractal scaling. We show how based on the estimations of Kramers-Moyal coefficients it is possible to reconstruct from pure, parameter free data analysis the stochastic equations in form of a Fokker-Planck or a Langevin equation.

Introduction

The better understanding of complex systems is still a scientific challenge. Often the question is posed to characterize given data with respect to its complexity. In a first step one can split this task into two aspects [1].

(1) There are systems with a pronounced scale dependent complex structure like this is the case for the well known problem of turbulence. Here it is believed that it is the cascade like process of large vorticities creating smaller ones as the smaller create even smaller ones and so on, which causes the complexity. This cascade procedure leads to a scale dependent disorder or, respectively, the scale dependent complexity of a turbulent field, whose understanding is still considered as one major unsolved scientific problem.

(2) Besides these scale dependent complex structures there is the second class of systems characterized by nonlinear dynamics which may become more sophisticated by the involvement of noise. Systems whose complexity is given by nonlinear dynamics evolving in time, like chaotic systems, we call time dependent complex systems. Definitely this classification is not a rigorous one, systems of hierarchical coupled nonlinear dynamical subsystems are some how intermediate.

In this contribution we want to summarize recent works which showed ways how to characterize complex systems of both categories in a more complete way. Namely, in these works it was worked out how to reconstruct in a parameter free way to reconstruct nonlinear stochastic equations from given data. These reconstructed stochastic equations, given as a Fokker-Planck equation or a Langevin equation enables to achieve the general n-scale joint statistics of a scale dependent complex system, and accordingly the underlying nonlinear evolution equations for a time dependent complex system.

Turbulence – scale dependent complexity

As already mentioned, the profound understanding of turbulence is up to now regarded as an unsolved problem. Although the basic equations of fluid dynamics, namely the Navier Stokes equations, are known for more than 150 years, a general solution of these equations for high Reynolds numbers, i.e. for turbulence, is not known. Even with the use of powerful computers no rigorous solutions can be obtained. Thus for a long time there has been the challenge to understand at least the complexity of

an idealized turbulent situation, which is taken to be isotropic and homogeneous. This case will lead us to the well known intermittency problem of turbulence, which is nothing else than the occurrence of heavy tailed, non-Gaussian statistics. The central question is to understand the mechanism which leads to this anomalous statistics (see [2, 3, 4]).

The intermittency problem of turbulence can be reduced to the question about the statistics of the velocity differences over different distances l , measured by the so-called increments $q(l, x) = u(x + l) - u(x)$. Usually the velocity increments are taken from the velocity component in direction of the distance vector l , the so-called longitudinal velocity increments. By the use of energy considerations, a simple l -dependence of $q(l, x)$ was proposed. It can be shown that the dissipation of energy takes place on small scales, namely, scales smaller than the so-called Taylor length θ . On the other hand, the turbulence is generated by driving forces injecting energy into the flow on large scales, $l > L_0$, where L_0 is given by the correlation length. Thus the cascade process causes the transition of $q(l, x)$ to $q(l', x)$ with $l' < l$, where the same amount of energy is transferred from one scale to another as long as $L_0 > l, l' > \theta$. This range is called the inertial range, where the turbulent field develops independently from boundary conditions and dissipation effects. It has been proposed that in this range universal features of turbulence arise.

Kolmogorov proposed that the disorder of turbulence expressed by the statistics of $q(l, x)$ and its n -th order moments $\langle q(l, x)^n \rangle$ should depend only on transferred energy ϵ and the scale l : $\langle q(l, x)^n \rangle = f(\epsilon, l)$. By simple dimensional arguments it follows that

$$\langle q(l, x)^n \rangle = \langle \epsilon^{n/3} \rangle l^{n/3}. \quad (1)$$

The simplest ansatz is to take ϵ as a constant, thus the Kolmogorov scaling $n/3$ of 1941 is obtained [5]. Based on some comments of Landau, Kolmogorov and Oboukhov proposed in a refined model with a lognormal distribution for ϵ , i.e. not ϵ but $ln\epsilon$ has a Gaussian distribution, and obtained for $\langle \epsilon^{n/3} \rangle$ an additional scaling term, leading to the so-called intermittency [6] correction [7]

$$\langle q(l, x)^n \rangle = l^{\xi_n} \quad \text{with} \quad \xi_n = \frac{n}{3} - \mu \frac{n(n-3)}{18} \quad \text{and} \quad n \geq 2 \quad (2)$$

with $0.25 < \mu < 0.5$. The form of the scaling exponent ξ_n , which is related to multifractal scaling behavior, has been heavily debated during the last decades (for further details see [2]).

Here we want to point out that this nonlinear scaling exponent ξ_n , has the direct consequence that the probability densities of $p(q(l, x))$ cannot be Gaussian, but must change their form with the scale l .

The velocity increment specifies the complexity of the turbulent velocity field between two measurement points separated by the length scale l . As a next step, taking somehow the cascade idea literally, the velocity increment $q(l, x)$ is regarded as a *stochastic variable in the scale l* . Complete information about this stochastic process would be available from the knowledge of not only the one scale properties like $\langle q(l, x)^n \rangle$ or $p(q(l, x))$ but properties of all possible n -scales given by the joint probability density functions (PDF) $p(q_1, q_2, q_3, \dots, q_n)$. (Note we use here a simplified notation: $q(l_i, x) = q_i$.) Since this is practically impossible to obtain from empirical data, suitable simplifications are needed.

As a first simplification we will require the process to be Markovian. In this case the n -scale joint PDF factorize into chains of two-scale conditional PDF $p(q_{i+1}|q_i)$ describing the probability of finding the increment q_{i+1} on the scale l_{i+1} under the condition that another increment q_i on a larger scale l_i is found. It follows that now the complete stochastic information is already available from the knowledge of the two-scale conditional PDF. This simplification can be tested by evaluating

$$p(q_1|q_2, \dots, q_n) = p(q_1|q_2) \quad (3)$$

which is feasible for experimental data, at least for $n = 3$. Our second simplification requires the noise included in the process to be Gaussian distributed.

Given these two conditions, it is known [8] that the process obeys a Fokker-Planck equation

$$-\frac{\partial}{\partial l} p(q, l | q_0, l_0) = \left\{ -\frac{\partial}{\partial q} D^{(1)}(q, l) + \frac{\partial^2}{\partial q^2} D^{(2)}(q, l) \right\} p(q, l | q_0, l_0). \quad (4)$$

which describes the evolution of the conditional PDF from larger to smaller length scales (Note due to this direction of the process we have inserted the $-$ prefactor). The Fokker-Planck equation is determined by the two Kramers-Moyal-coefficients $D^{(1)}(q, l)$ and $D^{(2)}(q, l)$, where $D^{(1)}$ is commonly denoted as drift term, describing the deterministic part of the process, and $D^{(2)}$ as diffusion term, determined by the variance of a Gaussian, δ -correlated noise. Here we should note that there are different methods to verify that actually for given data the noise has these features (cf. [9, 10]). Equivalently, the Langevin equation

$$-\frac{d}{dl} q(l) = D^{(1)}(q, l) + \sqrt{D^{(2)}(q, l)} \Gamma(l) \quad (5)$$

describes the process in the scale domain, using identical coefficients $D^{(1)}$ and $D^{(2)}$, together with the Gaussian, δ -correlated noise term $\Gamma(l)$.

To derive the Kramers-Moyal coefficients $D^{(k)}(q, l)$ (and thus obtain a Fokker-Planck or Langevin equation), the limit $\Delta l \rightarrow 0$ of the conditional moments has to be performed [8, 11]:

$$D^{(k)}(q, l) = \lim_{\Delta l \rightarrow 0} M^{(k)}(q, l, \Delta l) / l, \quad (6)$$

$$M^{(k)}(q, l, \Delta l) := \frac{l}{k! \Delta l} \int_{-\infty}^{+\infty} (\tilde{q} - q)^k p(\tilde{q}, l - \Delta l | q, l) d\tilde{q}. \quad (7)$$

This procedure is described in more detail in [9, 12]. For this contribution, it is sufficient to see from Eqs. (6) and (7) that the Fokker-Planck equation can directly be obtained from experimental data by the estimation of two-scale conditional PDF.

Based on this procedure we were able to reconstruct directly from the given data the corresponding stochastic processes. Knowing these processes one can perform numerical solutions (see [9, 12, 13]).

It is easily seen that this method can also be applied to other scale dependent complex structures like rough surfaces [12, 14, 15], to financial data [13, 16] or the cosmic background radiation [17].

nonlinear dynamics – time dependent complexity

It is straight forward to extend the above mentioned method for the analysis of time series. The objection is now to reconstruct from given data $q(t)$ the dynamical equation

$$\frac{d}{dt} q(t) = D^{(1)}(q, t) + \sqrt{D^{(2)}(q, t)} \Gamma(t). \quad (8)$$

To achieve this from given data the conditional probabilities $p(q(t + \tau) | q(t))$ for fixed values $q(t)$ and their corresponding conditional moments, i.e. the Kramers-Moyal coefficients, have to be estimated [18, 19]. This method has been successfully applied to various problems in the field of complex dynamical systems like the analysis of noisy chaotic electrical circuits [19], stochastic dynamics of metal cutting [20], systems with feedback delay [21], meteorological processes like wind-driven Southern Ocean variability [22, 23] traffic flow data [24] and the dynamics of particles of different sizes in a

running avalanche [25]. A quantitative comparison of this method of time series analysis with others is reported in [26].

As a further application also data spoiled by measurement noise can be treated with this method. The basic idea here is that instead of the dynamical variable $q(t)$ a variable $y(t) = q(t) + \sigma(t)$ is analyzed, where $\sigma(t)$ represents an additive measurement noise. The conditional moments are now performed with $y(t)$. A proper stochastic calculation shows how even in this case the underlying dynamics can be reconstructed [27].

Acknowledgements

Helpful discussion with St. Lück, A. Nawroth, Ch. Renner, Th. Schneider, and M. Siefert are acknowledged.

References

- [1] J. Peinke, Ch. Renner and R. Friedrich, in Complexity from microscopic to macroscopic scales: Coherence and large deviations, eds. A. T. Skjeltrop and T. Vicsek (Kluwer Academic publishers, Dordrecht 2002) p. 151 - 169.
- [2] U. Frisch, Turbulence (Cambridge University Press, Cambridge, 1995).
- [3] K. R. Sreenivasan and R. A. Antonia, Annu. Rev. Fluid Mech. **29**, 435-472 (1997).
- [4] R. Friedrich and J. Peinke, Physica D **102**, 147 (1997).
- [5] A. N. Kolmogorov, C.R. Acad. Sci. U.R.S.S., **30**, 301 (1941).
- [6] Here it should be noted that the term "intermittency" is used frequently in physics for different phenomena, and may cause confusions. This turbulent intermittency is not equal to the intermittency of chaos. There are also different intermittency phenomena introduced for turbulence.
- [7] A.N. Kolmogorov, J. Fluid Mech. **13**, 82 (1962).
- [8] H. Risken, The Fokker-Planck equation (Springer, Berlin, 1984).
- [9] C. Renner, J. Peinke, and R. Friedrich, J. Fluid Mech. **433**, 383 (2001).
- [10] P. Marcq and A. Naert, Phys. Fluids **13**, 2590 (2001).
- [11] A. N. Kolmogorov, Math. Ann. **104**, 415 (1931).
- [12] M. Waechter, F. Riess, T. Schimmel, U. Wendt, and J. Peinke, Eur. Phys. J. B **41**, 259 (2004), preprint arxiv:physics/0404015.
- [13] Ch. Renner, J. Peinke and R. Friedrich, Physica **A 298**, 499-520 (2001).
- [14] M. Waechter, F. Riess, H. Kantz, and J. Peinke, Europhys. Lett. **64**, 579 (2003), preprint arxiv:physics/0404021.
- [15] G. R. Jafari et al., Phys. Rev. Lett. **91**, 226101 (2003).
- [16] M. Ausloos and K. Ivanova, Phys. Rev. E **68**, 046122 (2003).

- [17] F. Ghasemi, A. Bahraminasab, S. Rahvar, and M. Reza Rahimi Tabar, preprint arxiv:astro-ph/0312227 (2003).
- [18] S. Siegert, R. Friedrich, J. Peinke, Physics Letters **A 234**, 275-280 (1998)
- [19] R. Friedrich, S. Siegert, J. Peinke, St. Lück, M. Siefert, M. Lindemann, J. Raethjen, G. Deuschl, G. Pfister, Physics Letters **A 271**, 217 (2000)
- [20] J. Gradisek, I. Grabec, S. Siegert, R. Friedrich, Mechanical Systems and Signal Processing **16** (5), 831 (2002).
- [21] T. D. Frank, P. J. Beek, R. Friedrich, Phys. Lett. **A 328**, 219 (2004); T. D. Frank, R. Friedrich, P.J. Beek, Stochastics and Dynamics 9, 44 (2004).
- [22] P. Sura, S.T. Gille, Journal of Marine Research **61**, 313 (2003).
- [23] P. Sura, Journal of the Atmospheric Sciences **60**, 654 (2003).
- [24] S. Kriso, R. Friedrich, J. Peinke, P. Wagner, Physics Letters **A 299**, 287 (2002).
- [25] M. Kern , O. Buser , J. Peinke , M. Siefert , and L. Vulliet Physics Letters **A 336**, 428 (2005).
- [26] E. Racca and A. Porporato Phys. Rev.E **71**, 027101 (2005).
- [27] M. Siefert, A. Kittel, R. Friedrich, and J. Peinke. Europhys. Lett. **61**, 466 (2003).

Multiscaling and turbulent-like behavior in self-organized criticality

*A.L. Stella, M. De Menech*²

¹ Dipartimento di Fisica “Galileo Galilei” and Sezione INFN, Università di Padova, Italy

² Max-Planck-Institut für Physik komplexer Systeme, Dresden, Germany

The prototype model of self-organized criticality, the Bak–Tang–Wiesenfeld (BTW) sandpile in two dimensions [1, 2], has a remarkable history [3], rich of developments and with some surprising and contradictory aspects. In spite of being the most extensively studied model of transport in systems slowly driven out of equilibrium, this sandpile remained for long very controversial as far as the scaling properties of some avalanche quantities are concerned [4]. Recently this led many authors to focus their attention on other models [5], with more standard and transparent avalanche scalings and with presumed better applicability. On the other hand, when they proposed their sandpile, BTW had clearly in mind that this could mimic qualitatively some features of turbulence. In this phenomenon fluid flow obeys the non-linear Navier–Stokes equation and evolves under random perturbations into a stationary state with scale invariant velocity correlations [6]. In the turbulent inertial regime a continuous, non-dissipative transport of energy occurs from large to small length scales. This reminds some BTW sandpile features: sand transport is driven by random grain addition, and is controlled by non-linear local threshold mechanisms (toppling rule). Furthermore, the avalanches following each grain addition have scale invariant probability distributions for quantities like the number of topplings, the area, etc.

In spite of the original expectations, an analogy between self organized BTW critical dynamics and turbulence could not be established until very recently [9]. More generally, the possible relation between self-organized criticality and turbulence remained for long an obscure and controversial issue, and the recent literature had a tendency to emphasize differences [7], rather than analogies [8].

In Ref. [10] it was first shown that the scaling of the probability distribution of the number of topplings in the BTW avalanches can be consistently described within a multifractal framework. Suspects that this distribution could obey some form of multiscaling rather than simple scaling were expressed long before [11], but surprisingly got scarce attention in the subsequent literature. The evidence of multiscaling for the probability distribution of the number of topplings and other BTW avalanche quantities is presently based on analysis of extensive data for sandpiles of size up to 4096×4096 [12]. Calling $P(s, L)$ the probability to have an avalanche with s topplings in a sandpile of size L , such analysis shows that

$$\langle s^q \rangle = \sum P(s, L) s^q \sim L^{\sigma_q} \quad (1)$$

with a nonlinear q -dependence of σ_q indicating multiscaling. Models like the Manna stochastic sandpile [5] show instead a linear dependence, as appropriate for simple finite size scaling [10, 13].

The physical origin of the BTW multiscaling was identified [13] in the long range time correlations existing for the toppling sizes of the waves [14, 3] into which avalanches can be decomposed. These waves are distinguished by the number of times the avalanche seed site has toppled, and can be regarded as bursts within each avalanche. The scaling properties of waves, when sampled globally over a sequence of many avalanches, are well understood [14]. If measured in terms of interoccurring waves, the correlation time of wave sizes grows approximately as $L^{0.7}$ [13]. As discussed below, on temporal scales shorter than the correlation time, the statistics of waves shows novel, unexpected features [9].

These peculiar correlations, not anticipated before, are also a very important feature of the BTW model in view of possible applications. Indeed, the absence of correlations between the sizes of successive avalanches has been indicated [7] as a serious handicap of the BTW and similar models in

connection with applications to phenomena like solar flares [15]. In turbulence the (laminar) waiting times between successive bursts above a given intensity threshold are distributed as a power law [16], rather than exponentially, like in the case of BTW avalanches, which are normally uncorrelated [17]. However, this power law distribution of waiting times can be easily reproduced by considering BTW wave bursts rather than avalanches [9].

The existence of correlations for wave sizes suggests the possibility that within the correlation time the analog of an inertial turbulent scaling regime could be realized. By defining as in turbulence suitable time dependent structure functions for the wave signal, we could indeed verify the existence of an inertial multiscaling with extended self-similarity features [9]. These functions are the analog of space dependent velocity structure functions of fluid flow [6]. The similarity to turbulent scaling emerges clearly also from the definition of a turbulent “dissipation rate” associated to the wave signal [9]. One defines it as the square of the discrete time gradient of the wave size averaged over an interval of time t . As a function of t its moments show multiscalings qualitatively similar to those valid for the space averaged dissipation rate in fluid turbulence [6]. Thus, if observed at the wave time scale, BTW dynamics provides an analog of intermittent, turbulent scaling phenomena.

The scaling analysis of the wave signal “dissipation rate” proposed in Ref. [9] for the BTW model has been recently applied to time series relative to powerful X-ray flares [18] and turbulent thermal convection in fluids [19]. Besides showing that this analysis is very suitable and widely applicable tool in order to identify and characterize the intermittent character of a time series, Refs. [18, 19] reported values of the dissipation multiscaling exponents which turn out to be surprisingly close to those found for the BTW wave time series [9]. These facts suggest that the BTW model could play a prototypical role with respect to various intermittent phenomena.

The presence of long range wave correlations and of inertial-like multiscaling in the BTW sandpile rises the fundamental issue of understanding what property makes this model so peculiar in its class. In Ref. [20] it has been shown that a single BTW model with quenched random toppling rules is able to reproduce both the multiscaling of the standard, homogeneous BTW model, and the simple scaling of the stochastic Manna sandpile [5]. If the number of sand grains released at each site upon toppling is equal to the total number of grains the site receives when all neighboring sites topple, the universality class of the quenched sandpile is that corresponding to BTW multiscaling. If this balance is not precisely realized locally, but only on average across the system, the scaling falls in the Manna universality class. The symmetry associated to the precise local toppling balance determines long time correlations for the waves, which turn out to remain totally uncorrelated in its absence. The turbulent scenario identified at the level of waves for the BTW model also relies on this basic symmetry.

References

- [1] P. Bak, C. Tang and K. Wiesenfeld, Phys. Rev. Lett. **59** 381 (1987).
- [2] P. Bak, C. Tang and K. Wiesenfeld, Phys. Rev. A **38** 364 (1988).
- [3] D. Dhar, Physica A **263** 4 (1999).
- [4] M. De Menech, Phys. Rev. E **70**, 028101 (2004).
- [5] S. S. Manna, J. Phys. A **25** L363 (1991).
- [6] U. Frisch, “Turbulence”, Cambridge University Press, (1995).
- [7] G. Boffetta, V. Carbone, P. Giuliani, P. Veltri and A. Vulpiani, Phys. Rev. Lett. **83** 4662 (1999).

- [8] J. Davidsen and M. Paczuski, Phys. Rev. E **66** 050101(R) (2002); S. Hergarten and H. J. Neugebauer, Phys. Rev. Lett. **88** 238501 (2002).
- [9] M. De Menech and A. L. Stella, Physica A **309** 289 (2002).
- [10] C. Tebaldi, M. De Menech and A. L. Stella, Phys. Rev. Lett. **83** 3952 (1999).
- [11] L. P. Kadanoff, S. R. Nagel, L. Wu and S. Zhou. Phys. Rev. A **39** 6524 (1989).
- [12] M. De Menech and A. L. Stella, in preparation.
- [13] M. De Menech and A. L. Stella, Phys. Rev. E **62** R4528 (2000).
- [14] E. V. Ivashkevich, D. V. Ktitarov and V. B. Priezhev, Physica A **209** 347 (1994).
- [15] E. T. Lu and R. J. Hamilton, Astrophys. J. **380** L89 (1991).
- [16] M. Baiesi, M. Paczuski and A. L. Stella, cond-mat/0411342.
- [17] See, however, M. Baiesi and C. Maes, cond-mat/0505274.
- [18] A. Bershadskii and K. R. Sreenivasan, Eur. Phys. J. B **35** 513 (2003).
- [19] K. R. Sreenivasan, A. Bershadskii and J. J. Niemela, Physica A **340** 574 (2004).
- [20] R. Karmakar, S. S. Manna and A. L. Stella, Phys. Rev. Lett. **94**, 0880002 (2005).

A multifractal formalism for vector-valued random fields based on wavelet analysis: application to turbulent velocity and vorticity 3D numerical data

*P. Kestener*¹, *A. Arneodo*²

¹ CEA-Saclay, DSM/DAPNIA/SEDI, 91191 Gif-sur-Yvette, France

² Laboratoire de Physique, Ecole Normale Supérieure de Lyon, 46 allée d'Italie, 69364 Lyon Cédex 07, France

The multifractal formalism was introduced in the context of fully-developed turbulence data analysis and modeling to account for the experimental observation of some deviation to Kolmogorov theory (K41) of homogenous and isotropic turbulence [1]. The predictions of various multiplicative cascade models, including the weighted curdling (binomial) model proposed by Mandelbrot [2], were tested using box-counting (BC) estimates of the so-called $f(\alpha)$ singularity spectrum of the dissipation field [3]. Alternatively, the intermittent nature of the velocity fluctuations were investigated via the computation of the $D(h)$ singularity spectrum using the structure function (SF) method [4]. Unfortunately, both types of studies suffered from severe insufficiencies. On the one hand, they were mostly limited by one point probe measurements to the analysis of one (longitudinal) velocity component and to some 1D surrogate approximation of the dissipation [5]. On the other hand, both the BC and SF methodologies have intrinsic limitations and fail to fully characterize the corresponding singularity spectrum since only the strongest singularities are a priori amenable to these techniques [6].

In the early nineties, a wavelet-based statistical approach was proposed as a unified multifractal description of singular measures and multi-affine functions [6]. Applications of the so-called *wavelet transform modulus maxima* (WTMM) method have already provided insight into a wide variety of problems, e.g., fully developed turbulence, econophysics, meteorology, physiology and DNA sequences [7, 8]. Later on, the WTMM method was generalized to 2D for multifractal analysis of rough surfaces [9], with very promising results in the context of the geophysical study of the intermittent nature of satellite images of the cloud structure [10, 11] and the medical assist in the diagnosis in digitized mammograms [11, 12]. Recently the WTMM method has been further extended to 3D analysis of scalar data and applied to dissipation and enstrophy 3D numerical data issue from isotropic turbulence direct numerical simulations (DNS) [13, 14]. Thus far, the multifractal description has been mainly devoted to scalar measures and functions. In the spirit of a preliminary theoretical study of self-similar vector-valued measures by Falconer and O’Neil [15], we generalize the WTMM method to vector-valued random fields with the specific goal to achieve a comparative 3D vectorial multifractal analysis of DNS velocity and vorticity fields [14, 16].

Let us note $\mathbf{V}(\mathbf{x} = (x_1, x_2, x_3))$, a 3D vector field with square integrable scalar components $V_j(\mathbf{x})$, $j = 1, 2, 3$. Along the line of the 3D WTMM method [13, 14], let us define 3 wavelets $\psi_i(\mathbf{x}) = \partial\phi/\partial x_i(\mathbf{x})$ for $i = 1, 2, 3$ respectively, where $\phi(\mathbf{x})$ is a scalar smoothing function well localized around $|\mathbf{x}| = 0$. The wavelet transform (WT) of \mathbf{V} at point \mathbf{b} and scale a is the following tensor [14, 16]:

$$\mathbb{T}_\psi[\mathbf{V}](\mathbf{b}, a) = \begin{pmatrix} T_{\psi_1}[V_1] & T_{\psi_1}[V_2] & T_{\psi_1}[V_3] \\ T_{\psi_2}[V_1] & T_{\psi_2}[V_2] & T_{\psi_2}[V_3] \\ T_{\psi_3}[V_1] & T_{\psi_3}[V_2] & T_{\psi_3}[V_3] \end{pmatrix}, \quad (1)$$

where

$$T_{\psi_i}[V_j](\mathbf{b}, a) = a^{-3} \int d^3\mathbf{r} \psi_i(a^{-1}(\mathbf{r} - \mathbf{b}))V_j(\mathbf{r}). \quad (2)$$

In order to characterize the local Hölder regularity of \mathbf{V} , one needs to find the direction that locally corresponds to the maximum amplitude variation of \mathbf{V} . This can be obtained from the *singular value*

decomposition (SVD) [17] of the matrix $(T_{\psi_i}[V_j])$ (Eq. (1)):

$$\mathbb{T}_{\psi}[\mathbf{V}] = \mathbb{G}\Sigma\mathbb{H}^T, \quad (3)$$

where \mathbb{G} and \mathbb{H} are orthogonal matrices ($\mathbb{G}^T\mathbb{G} = \mathbb{H}^T\mathbb{H} = \mathbb{I}_d$) and $\Sigma = \text{diag}(\sigma_1, \sigma_2, \sigma_3)$ with $\sigma_i \geq 0$, for $1 \leq i \leq 3$. The columns of \mathbb{G} and \mathbb{H} are referred to as the left and right singular vectors, and the singular values of $\mathbb{T}_{\psi}[\mathbf{V}]$ are the non-negative square roots σ_i of the d eigenvalues of $\mathbb{T}_{\psi}[\mathbf{V}]^T\mathbb{T}_{\psi}[\mathbf{V}]$. Note that this decomposition is unique, up to some permutation of the σ_i 's. The direction of the largest amplitude variation of \mathbf{V} , at point \mathbf{b} and scale a , is thus given by the eigenvector $\mathbf{G}_{\rho}(\mathbf{b}, a)$ associated to the spectral radius $\rho(\mathbf{b}, a) = \max_j \sigma_j(\mathbf{b}, a)$. One is thus led to the analysis of the vector field $\mathbf{T}_{\psi, \rho}[\mathbf{V}](\mathbf{b}, a) = \rho(\mathbf{b}, a)\mathbf{G}_{\rho}(\mathbf{b}, a)$. Following the WTMM analysis of scalar fields [9, 13, 14], let us define, at a given scale a , the WTMM as the position \mathbf{b} where the modulus $\mathcal{M}_{\psi}[\mathbf{V}](\mathbf{b}, a) = |\mathbf{T}_{\psi, \rho}[\mathbf{V}](\mathbf{b}, a)| = \rho(\mathbf{b}, a)$ is locally maximum along the direction of $\mathbf{G}_{\rho}(\mathbf{b}, a)$. These WTMM lie on connected surfaces called *maxima surfaces* (see Figs 1b,c and 1e,f). In theory, at each scale a , one only needs to record the position of the local maxima of \mathcal{M}_{ψ} (WTMMM) along the maxima surfaces together with the value of $\mathcal{M}_{\psi}[\mathbf{V}]$ and the direction of \mathbf{G}_{ρ} . These WTMMM are disposed along connected curves across scales called *maxima lines* living in a $(3+1)$ space (\mathbf{x}, a) . The WT skeleton is then defined as the set of maxima lines that converge to the (x_1, x_2, x_3) hyperplane in the limit $a \rightarrow 0^+$. The local Hölder regularity of \mathbf{V} is estimated from the power-law behavior $\mathcal{M}_{\psi}[\mathbf{V}](\mathcal{L}_{\mathbf{r}_0}(a)) \sim a^{h(\mathbf{r}_0)}$ along the maxima line $\mathcal{L}_{\mathbf{r}_0}(a)$ pointing to the point \mathbf{r}_0 in the limit $a \rightarrow 0^+$, provided the Hölder exponent $h(\mathbf{r}_0)$ be smaller than the number n_{ψ} of zero moments of the analyzing wavelet ψ [18]. As for scalar fields [6, 9, 13], the tensorial WTMM method consists in defining the partition functions:

$$\mathcal{Z}(q, a) = \sum_{\mathcal{L} \in \mathcal{L}(a)} (\mathcal{M}_{\psi}[\mathbf{V}](\mathbf{r}, a))^q \sim a^{\tau(q)}, \quad (4)$$

where $q \in \mathbb{R}$ and $\mathcal{L}(a)$ is the set of maxima lines that exist at scale a in the WT skeleton. Then by Legendre transforming $\tau(q)$, one gets the singularity spectrum $D(h) = \min_q(qh - \tau(q))$, defined as the Hausdorff dimension of the set of points \mathbf{r} where $h(\mathbf{r}) = h$. Alternatively, one can compute the mean quantities:

$$\begin{aligned} h(q, a) &= \sum_{\mathcal{L} \in \mathcal{L}(a)} \ln |\mathcal{M}_{\psi}[\mathbf{V}](\mathbf{r}, a)| W_{\psi}[\mathbf{V}](q, \mathcal{L}, a), \\ D(q, a) &= \sum_{\mathcal{L} \in \mathcal{L}(a)} W_{\psi}[\mathbf{V}](q, \mathcal{L}, a) \ln(W_{\psi}[\mathbf{V}](q, \mathcal{L}, a)), \end{aligned} \quad (5)$$

where $W_{\psi}[\mathbf{V}](q, \mathcal{L}, a) = (\mathcal{M}_{\psi}[\mathbf{V}](\mathbf{r}, a))^q / \mathcal{Z}(q, a)$ is a Boltzmann weight computed from the WT skeleton. From the scaling behavior of these quantities, one can extract $h(q) = \lim_{a \rightarrow 0^+} h(q, a) / \ln a$ and $D(q) = \lim_{a \rightarrow 0^+} D(q, a) / \ln a$ and therefore the $D(h)$ spectrum.

In References [14, 16], one can find the results of some test-applications of the tensorial WTMM method to a 2D vector situation. Here we will report the results of the first application of this methodology to the velocity (\mathbf{v}) and vorticity ($\boldsymbol{\omega}$) fields generated by DNS of isotropic turbulence by Lévêque using a pseudo spectral method solver. The DNS were performed using 256^3 mesh points in a 3D periodic box. The Taylor microscale is $R_{\lambda} = 140$. In Fig. 1 are illustrated the computation of the WT modulus maxima surfaces together with the local maxima (WTMMM) of \mathcal{M}_{ψ} for one 3D snapshot of the velocity and the vorticity field. In Fig. 2 are reported the results corresponding to some averaging over 18 snapshots of $(256)^3$ DNS run [16]. As shown in Figs. 2a and 2b, both the $\mathcal{Z}(q, a)$ and $h(q, a)$ partition functions display rather nice scaling properties for $q = -4$ to 6, except at small scales ($a \lesssim 2^{1.5}\sigma_W$) where some curvature is observed in the log-log plots likely induced by dissipation effects [1, 19]. Linear regression fit of the data (Fig. 2a) in the range $2^{1.5}\sigma_W \leq a \leq 2^{3.9}\sigma_W$

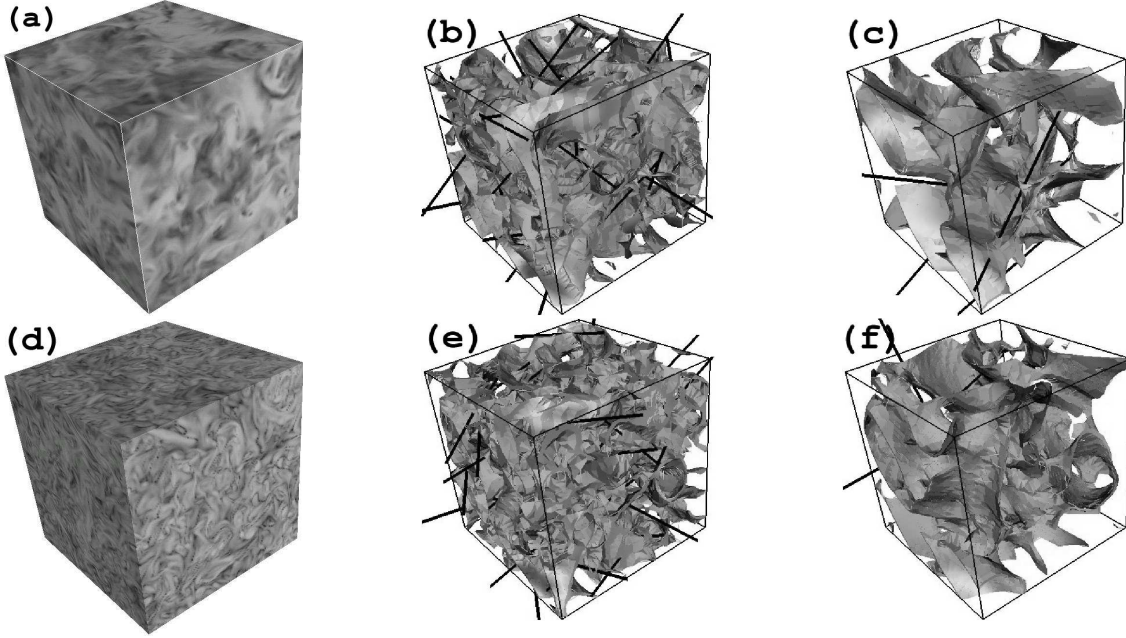


Figure 1: 3D wavelet transform analysis of the velocity and vorticity fields from (256^3) DNS by L ev eque ($R_\lambda = 140$). ψ is the third order radially symmetric analyzing wavelet (the smoothing function $\phi(\mathbf{x})$ is the isotropic mexican hat). **Velocity field:** (a) A snapshot of $\mathbf{v}(\mathbf{x})$ using a 64 gray level coding; in (b) $a = 2^2\sigma_W$ and (c) $a = 2^3\sigma_W$, are shown the TWT modulus maxima surfaces; from the local maxima (WTMM) of \mathcal{M}_ψ along these surfaces originates a black segment whose length is proportional to \mathcal{M}_ψ and direction is along $\mathbf{G}_\rho(\mathbf{x}, a)$. **Vorticity field:** (d), (e) and (f) are equivalent to (a), (b) and (c) but for the vorticity field $\boldsymbol{\omega}(\mathbf{x})$. $\sigma_W = 13$ pixels.

yields the nonlinear $\tau_v(q)$ and $\tau_\omega(q)$ spectra shown in Fig. 2c, the hallmark of multifractality. For the vorticity field, $\tau_\omega(q)$ is a decreasing function; hence $h(q)(= \partial\tau(q)/\partial q) < 0$ and the support of the $D(h)$ singularity spectrum expands over negative h values as shown in Fig. 2d. In contrast $\tau_v(q)$ is an increasing function which implies that $h(q) > 0$ as the signature that \mathbf{v} is a continuous function. Let us point out that the so-obtained $\tau_v(q)$ curve significantly departs from the linear behavior obtained for 18 $(256)^3$ realizations of vector-valued fractional Brownian motions $\mathbf{B}^{1/3}$ of index $H = 1/3$, in good agreement with the theoretical spectrum $\tau_{\mathbf{B}^{1/3}}(q) = q/3 - 3$. But even more remarkable, the results reported in Fig. 2b for $h(q, a)$ suggest, up to statistical uncertainty, the validity of the relationship $h_\omega(q) = h_v(q) - 1$. Actually, as shown in Fig. 2d, $D_\omega(h)$ and $D_v(h)$ curves are likely to coincide after translating the later by one unit on the left. This is to our knowledge the first numerical evidence that the singularity spectra of \mathbf{v} and $\boldsymbol{\omega}$ might be so intimately related: $D_v(h + 1) = D_\omega(h)$ (a result that could have been guessed intuitively by noticing that $\boldsymbol{\omega} = \nabla \wedge \mathbf{v}$ involves first order derivatives only) [16]. Finally, let us note that, for both fields, the $\tau(q)$ and $D(h)$ data are quite well fitted by log-normal parabolic spectra [19]:

$$\begin{aligned} \tau(q) &= -C_0 + C_1q - C_2q^2/2, \\ D(h) &= C_0 - (h - C_1)^2/2C_2. \end{aligned} \tag{6}$$

Both fields are found singular almost everywhere: $C_0^v = -\tau_v(q = 0) = D_v(q = 0) = 3.02 \pm 0.02$ and $C_0^\omega = 3.01 \pm 0.02$. The most frequent H older exponent $h(q = 0) = C_1$ (corresponding to the maximum of $D(h)$) takes the value $C_1^v \simeq C_1^\omega + 1 = 0.34 \pm 0.02$. Indeed, this estimate is much closer to the K41 prediction $h = 1/3$ [1] than previous experimental measurements ($h = 0.39 \pm 0.02$) based

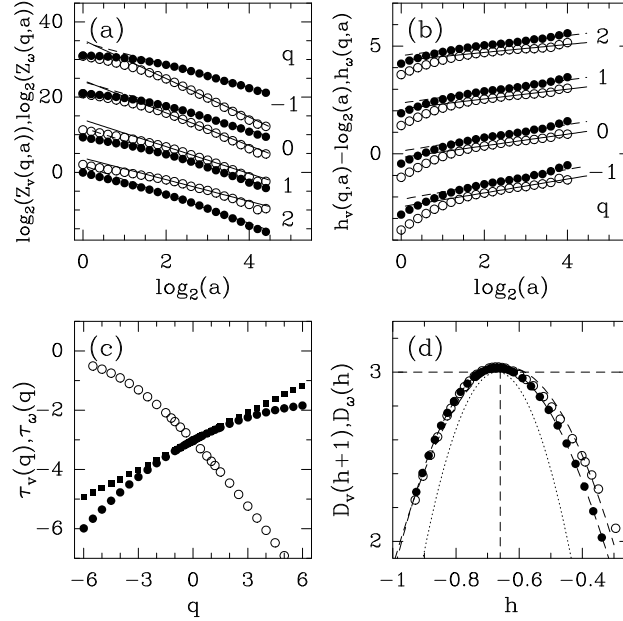


Figure 2: Multifractal analysis of Lévéque DNS velocity (\bullet) and vorticity (\circ) fields ($d = 3$, 18 snapshots) using the tensorial 3D WTMM method; the symbols (\blacksquare) correspond to a similar analysis of vector-valued fractional Brownian motions, $\mathbf{B}^{H=1/3}$. (a) $\log_2 \mathcal{Z}(q, a)$ vs $\log_2 a$; (b) $h_\omega(q, a)$ vs $\log_2 a$ and $h_v(q, a) - \log_2 a$ vs $\log_2 a$; the solid and dashed lines correspond to linear regression fits over $2^{1.5}\sigma_W \lesssim a \lesssim 2^{3.9}\sigma_W$. (c) $\tau_v(q)$, $\tau_\omega(q)$ and $\tau_{\mathbf{B}^{1/3}}(q)$ vs q ; (d) $D_v(h+1)$, $D_\omega(h)$ vs h ; the dashed lines correspond to log-normal regression fits with the parameter values $C_2^v = 0.049$ and $C_2^\omega = 0.055$; the dotted line is the experimental singularity spectrum ($C_2^{\delta v_{\parallel}} = 0.025$) for 1D longitudinal velocity increments [19].

on the analysis of longitudinal velocity fluctuations [19]. Consistent estimates are obtained for C_2 (that characterizes the width of $D(h)$): $C_2^v = 0.049 \pm 0.003$ and $C_2^\omega = 0.055 \pm 0.004$. Note that these values are much larger than the experimental estimate $C_2 = 0.025 \pm 0.003$ derived for 1D longitudinal velocity increment statistics [19]. Actually they are comparable to the value $C_2 = 0.040$ extracted from experimental transverse velocity increments [19b].

To conclude, we have generalized the WTMM method to vector-valued random fields. Preliminary applications [14, 16] to DNS turbulence data have revealed the existence of an intimate relationship between the velocity and vorticity 3D statistics that turn out to be significantly more intermittent than previously estimated from 1D longitudinal velocity increments statistics. This new methodology looks very promising to many extents. Thanks to the SVD, one can focus on fluctuations that are locally confined in 2D ($\min_i \sigma_i = 0$) or in 1D (the two smallest σ_i are zero) and then simultaneously proceed to a multifractal and structural analysis of turbulent flows. The investigation along this line of vorticity sheets and vorticity filaments in DNS is in current progress. We are very grateful to E. Lévéque for allowing us to have access to his DNS data and to the CNRS under GDR turbulence.

References

- [1] U. Frisch, *Turbulence* (Cambridge Univ. Press, Cambridge, 1995).
- [2] B. B. Mandelbrot, *J. Fluid Mech.* **62**, 331 (1974).
- [3] C. Meneveau and K. R. Sreenivasan, *J. Fluid Mech.* **224**, 429 (1991).

- [4] G. Parisi and U. Frisch, in *Turbulence and Predictability in Geophysical Fluid Dynamics and Climate Dynamics*, edited by M. Ghil *et al.* (North-Holland, Amsterdam, 1985), p. 84.
- [5] E. Aurell *et al.*, *J. Fluid Mech.* **238**, 467 (1992).
- [6] J. F. Muzy, E. Bacry, and A. Arneodo, *Phys. Rev. E* **47**, 875 (1993), *Int. J. of Bifurcation and Chaos* **4**, 245 (1994); A. Arneodo, E. Bacry, and J. F. Muzy, *Physica A* **213**, 232 (1995).
- [7] A. Arneodo *et al.*, *Ondelettes, Multifractales et Turbulences : de l'ADN aux croissances cristallines* (Diderot Editeur, Art et Sciences, Paris, 1995).
- [8] *The Science of Disasters : climate disruptions, heart attacks and market crashes*, edited by A. Bunde, J. Kropp, and H. Schellnhuber (Springer Verlag, Berlin, 2002).
- [9] A. Arneodo, N. Decoster and S. G. Roux, *Eur. Phys. J. B* **15**, 567 (2000) ; N. Decoster, S. G. Roux, and A. Arneodo, *Eur. Phys. J. B* **15**, 739 (2000).
- [10] A. Arneodo, N. Decoster, and S. G. Roux, *Phys. Rev. Lett.* **83**, 1255 (1999). S. G. Roux, A. Arneodo, and N. Decoster, *Eur. Phys. J. B* **15**, 765 (2000).
- [11] A. Arneodo *et al.*, *Advances in Imaging and Electron Physics*, **126**, 1 (2003).
- [12] P. Kestener *et al.*, *Image Anal. Stereol.* **20**, 169 (2001).
- [13] P. Kestener and A. Arneodo, *Phys. Rev. Lett.* **91**, 194501 (2003).
- [14] P. Kestener, Ph.D. thesis, University of Bordeaux I, 2003.
- [15] K. J. Falconer and T. C. O'Neil, *Proc. R. Soc. Lond. A* **452**, 1433 (1996).
- [16] P. Kestener and A. Arneodo, *Phys. Rev. Lett.* **93**, 044501 (2004); P. Kestener and A. Arneodo, *Stochastic Environmental Research and Risk* (2005), in press.
- [17] G. H. Golub and C. V. Loan, *Matrix Computations*, 2nd ed. (John Hopkins University Press, Baltimore, 1989).
- [18] Note that if $h_i(\mathbf{r}_0)$ are the Hölder exponent of the 3 scalar components $V_i(\mathbf{r}_0)$ of \mathbf{V} , then $h(\mathbf{r}_0) = \min_i h_i(\mathbf{r}_0)$.
- [19] (a) A. Arneodo, S. Manneville, and J. F. Muzy, *Eur. Phys. J. B* **1**, 129 (1998); (b) Y. Malécot *et al.*, *Eur. Phys. J. B* **16**, 549 (2000); (c) J. Delour, J. F. Muzy, and A. Arneodo, *Eur. Phys. J. B* **23**, 243 (2001).

Stochastic energy-cascade process for $n+1$ -dimensional small-scale turbulence

*J. Cleve*¹, *J. Schmiegel*², *M. Greiner*³

¹ Untere Weidenstraße 21, D-81543 München, Germany; email: jochen.cleve@web.de

² Thiele Centre for Applied Mathematics in Natural Science, Aarhus University, DK-8000 Aarhus, Denmark; email: schmiegl@imf.au.dk

³ Corporate Technology, Information&Communications, Siemens AG, D-81730 München, Germany; email: martin.greiner@siemens.com

The classical Kolmogorov picture of fully developed small-scale turbulence suggests the scaling form

$$\langle \Delta v_l^n \rangle \sim l^{\zeta_n} \sim \langle \varepsilon_l^{n/3} \rangle l^{n/3} \sim l^{n/3 - \tau_n/3} \quad (1)$$

of the structure functions within the inertial range $\eta \ll l \ll L$, confined within the dissipation and integral scales η and L . Δv_l is a velocity increment and ε_l a coarse-grained amplitude of the energy dissipation. However, the observed scaling of $\langle \Delta v_l^n \rangle$ as well as $\langle \varepsilon_l^n \rangle$ is rather poor. This raises the question: if it exists, what is the appropriate observable to detect rigorous scaling? The answer [2, 3, 4] is, two-point correlations

$$\langle \varepsilon^{n_1}(x) \varepsilon^{n_2}(x+l) \rangle \sim \left(\frac{L}{l} \right)^{\tau_{n_1 n_2}} \quad (2)$$

of the energy dissipation reveal a rigorous scaling over almost the entire inertial range $\eta < l \leq L$. This has been demonstrated for various data sets. It has also given rise to a new puzzle, that for large Reynolds numbers the intermittency exponent appears not to be universal, but to depend on the flow geometry.

From a theoretical perspective, these observational findings call for an elegant stochastic description of the energy-cascade process. Prototype models are random multiplicative cascade processes [7, 8, 13, 6]. However, due to their inherent hierarchy of scales these models are not homogeneous in space. A spatially homogeneous and causal model generalization has been presented in Ref. [12]. Its parameters are fully determined from the lowest-order two-point correlations (2). With no room for further adjustments, this model is also capable to describe the observed three-point statistics

$$\langle \varepsilon^{n_1}(x_1) \varepsilon^{n_2}(x_2) \varepsilon^{n_3}(x_3) \rangle \sim \left(\frac{L}{x_3 - x_1} \right)^{\alpha_{13}} \left(\frac{L}{x_2 - x_1} \right)^{\alpha_{12}} \left(\frac{L}{x_3 - x_2} \right)^{\alpha_{23}} \quad (3)$$

with high precision. Moreover, it also explains the scale correlations observed for breakup coefficients as an artifact of the observation [5]; see also previous work [10, 11, 1, 9] on this topic.

References

- [1] J. Cleve and M. Greiner, Phys. Lett. A **273** (2000) 104.
- [2] J. Cleve, M. Greiner and K.R. Sreenivasan, Europhys. Lett. **61** (2003) 756.
- [3] J. Cleve, M. Greiner, B.R. Pearson and K.R. Sreenivasan, Phys. Rev. E **69** (2004) 066316.
- [4] J. Cleve, T. Dziekan, J. Schmiegel, O.E. Barndorff-Nielsen, B.R. Pearson, K.R. Sreenivasan and M. Greiner, Phys. Rev. E **71** (2005) 026309.
- [5] J. Cleve, J. Schmiegel and M. Greiner, in preparation.

- [6] H. Eggers, T. Dziekan and M. Greiner, Phys. Lett. A **281** (2001) 249.
- [7] M. Greiner, H. Eggers and P. Lipa, Phys. Rev. Lett. **80** (1998) 5333.
- [8] M. Greiner, J. Schmiegell, F. Eickemeyer, P. Lipa and H. Eggers, Phys. Rev. E **58** (1998) 554.
- [9] M. Greiner and B. Jouault, Fractals **10** (2002) 321.
- [10] B. Jouault, P. Lipa and M. Greiner, Phys. Rev. E **59** (1999) 2451.
- [11] B. Jouault, M. Greiner and P. Lipa, Physica D **136** (2000) 125.
- [12] J. Schmiegell, J. Cleve, H. Eggers, B. Pearson and M. Greiner, Phys. Lett. A **320** (2004) 247.
- [13] M. Wolf, J. Schmiegell and M. Greiner, Phys. Lett. A **266** (2000) 276.

A one-dimensional stochastic model for turbulence simulation

A.R. Kerstein

Combustion Research Facility, Sandia National Laboratories, Livermore, CA 94551-0969, USA

Abstract

A stochastic model for one-dimensional (1D) simulation of 3D hydrodynamic turbulence, denoted one-dimensional turbulence (ODT), is motivated and introduced by describing the development path that led to the present formulation.

One-dimensional models of turbulent premixed combustion

The research effort described here began with an effort to develop a minimal model of turbulent premixed combustion. The initial outcome was a formulation in which the instantaneous state of a turbulent flame is idealized as a bit vector (row of integers 0 or 1) in which each pair of adjacent bits interacts in two ways.

First, each 0 is converted into a 1 at a mean rate B times the number (0, 1, or 2) of adjacent bits in state 1. This process represents laminar burning with laminar flame speed L/B , where L is the nominal spatial separation of adjacent bits. Note that there is some subtlety even at this level of description. The middle bit in a 101 configuration is deemed to burn twice as fast as in a 100 or 001 configuration because flames consume it from both sides, which is a reasonable but not uniquely plausible idealization of flame propagation. Also, this is a random process but could be plausibly formulated as a deterministic process.

Second, each pair of adjacent bits is exchanged (e.g. 01 to 10, 10 to 01, 00 and 11 unaffected) at a mean rate R , thus idealizing turbulent advection with eddy diffusivity RL^2 . (Note that bits execute simple random walks with event rate $2R$.) Like laminar burning, this process is random in time, namely a Poisson process with mean event rate R for each bit pair. Model dynamics are governed by one non-dimensional parameter, $\gamma = R/B$, which can be viewed as an idealization of the quantity u'/S that governs 3D turbulent combustion, where u' is the rms velocity fluctuation and S is the laminar flame speed. The mean number of 0-to-1 conversions per time interval $1/B$ is then the model analog of u_T/S , where u_T is the turbulent burning velocity.

For a step-function initial bit profile, this process relaxes to statistically steady propagation that captures some qualitative features of turbulent premixed combustion [1]. It has been shown that model analog of u_T is governed by the KPP velocity-selection principle in the large- γ limit [2]. To improve the physical realism of this formulation, it was extended by allowing exchanges of the positions of non-adjacent bit pairs, idealizing the effects of turbulent eddies of various sizes [3].

Linear-eddy model

Though bit-pair exchange over a range of bit separations reflects the range of eddy motions in turbulence, it does not reflect the coherence of eddy motions, meaning that a large eddy displaces a larger volume of fluid in a given direction than does a small eddy. Accordingly, an exchange process denoted block inversion was introduced, involving the reversal of the order of bits j through $j+l-1$ to represent a size- l eddy [4]. This change was necessitated by the application of the 1D approach to diffusive scalar mixing rather than flame propagation; bit-pair exchange gives far too rapid length-scale reduction in this context. This artifact occurs also for flame propagation, but is less severe in that context because

u_T is more sensitive to the distance and frequency of the largest bit displacements than to the amount of fluid transported.

Block inversion introduces scalar discontinuities at eddy endpoints. From a spectral viewpoint, this corresponds to transfer of scalar fluctuations from finite wave-number k to $k = \infty$, violating the spectral locality of length-scale reduction that is a hallmark of the inertial-range turbulent cascade [5].

To remedy this artifact, the scalar-mixing formulation, denoted the linear-eddy model (LEM), was improved by introducing a new exchange process, termed the triplet map [6]. In fact, this is not a pair exchange, but rather, a permutation of cell indices j through $j + l - 1$. Taking l to be a multiple of 3, the triplet map permutes the cell indices into the new order $j, j + 3, j + 6, \dots, j + l - 3, j + l - 2, j + l - 5, j + l - 8, \dots, j + 4, j + 1, j + 2, j + 5, j + 8, \dots, j + l - 4, j + l - 1$. This operation reduces the separation of any pair of cells by no more than a factor of three, thus satisfying the scale locality of length-scale reduction. It is the simplest of a family of permutations that preserve scale locality, and is optimal in that no other member of the family enforces as low a bound on the maximum scale-reduction factor.

LEM is parameterized by a Péclet number Pe , which is the eddy diffusivity associated with transport by the triplet-map sequence divided by the molecular diffusivity (which is the diffusive-mixing analog of the laminar flame speed in premixed combustion). On this basis, LEM has been used to study the dependencies of turbulent mixing and reaction processes on Pe and on the initial and boundary conditions imposed on one or more scalar profiles that evolve on the 1D domain [7]-[13].

One-dimensional turbulence

LEM simulates mixing induced by parametrically specified turbulent advection. To obtain a model that, instead, predicts turbulent flow evolution, profiles of one or more velocity components were introduced on the 1D domain, and the random selection of individual eddies (here parameterized by j, l , and time of eddy occurrence) was generalized [14]. In LEM, the eddy rate is a prescribed function of l , reflecting known inertial-range cascade scalings, and also depends on j if the flow is spatially inhomogeneous. In the predictive flow model, denoted one-dimensional turbulence (ODT), the sampling rate for each eddy (parameterized by j and l) is a function of the instantaneous flow state, based on turbulence production and dissipation mechanisms that are conventionally used to estimate eddy time scales [15]. A key distinction here is that conventional estimation based on mixing-length phenomenology is applied to quantities subject to some form of averaging or filtering, but in ODT, mixing-length phenomenology is applied to instantaneous property profiles that are not subject to averaging or filtering.

In ODT, the molecular process that evolves concurrently with eddy events (i.e., the analog of laminar flame propagation in premixed combustion and molecular diffusivity in LEM) is molecular viscosity, as prescribed by the viscous-dissipation term of the momentum equation. The corresponding non-dimensional parameter that governs constant-property flow evolution in ODT is a Reynolds number, Re . In ODT, as in 3D flow simulation, the nominal Reynolds number is defined in terms of domain geometry and flow initial and boundary conditions, but the turbulent Reynolds number, defined in terms of u' , the mean energy dissipation rate, and the kinematic viscosity, is an outcome of simulated flow evolution rather than an input.

Velocity profiles in ODT do not advect fluid, but they influence triplet-map advection through their role in determining eddy-sampling rates. In this sense they are auxiliary variables, but in addition, they are the flow observables. The tight two-way coupling between velocity-profile evolution and eddies (triplet maps advect velocity profiles) maintains overall consistency of velocity statistics and mapping-induced transport.

Buoyancy effects have been incorporated into ODT, and buoyant stratified flows have been studied extensively [14]-[20]. In fact, buoyancy alone (velocity profiles omitted) is a sufficient input to eddy rate determination to provide a reasonable representation of some flows of interest, motivating a simplification of ODT that is termed density-profile evolution (DPE) [14], [16]. ODT has also been used to study free-shear flow [21]-[23] and combustion [24]-[26].

1D substructure within 3D flow solvers

Both LEM and ODT have been used as subgrid models within large-eddy simulations (LES). LES with LEM-based subgrid closure has been applied to turbulent combustion [27]-[28]. ODT has been used as a near-wall momentum closure for LES of channel flow [29] and as a bulk momentum closure for LES of decaying homogeneous turbulence [30].

A concept for full multi-physics subgrid closure using ODT has been articulated [31] and has been further refined in recent unpublished work. The strategy is as follows. Three flow solutions are advanced concurrently. In each, the 3D domain (assume a Cartesian mesh of cubic control volumes) is spatially refined in one of the three coordinate directions. The intersections of this refinement (stack of thin slices) with the set of 3D control volumes defines a 2D array of ODT domains filling the 3D domain. On a fast time scale, ODT processes evolve within individual ODT domains (here assuming compressible treatment; 1D gas dynamics plus eddy events). On a slow time scale, 3D effects are introduced by fluxing flow variables laterally between adjacent ODT domains within a given array.

The lateral fluxes are based on property transfers across the corresponding interfaces during ODT evolution on 1D domains normal to those interfaces. In this manner, each array of ODT domains aligned in a given direction provides the other arrays with the information needed for closure of lateral fluxes between the ODT domains on those arrays.

This synergistic coupling of the three flow solutions (i.e., evolution on the three arrays of ODT domains) results in self-contained flow evolution based only on ODT-level variables. Because this formulation is compressible (or pseudo-compressible for low-Mach-number applications), it does not require a 3D solve of a Poisson equation to enforce continuity. Hence, filtering or averaging at the 3D-control-volume level is not needed except to generate output statistics.

This formulation involves much of the methodology developed for ODT-based 3D simulation of incompressible flow [30], but the incorporation of 1D gas dynamics into ODT will be a major extension involving considerable technical uncertainty. For example, application of a triplet map to a dilatational flow automatically introduces a form of vortical-acoustic coupling, but it remains to be determined whether this representation is physically realistic.

Full multi-physics treatment requires various extensions of the ODT model itself, such as treatment of flows with large density contrasts (demonstrated recently [23]) and multiphase phenomena (one aspect of which has been addressed [32]). Progress toward full multi-physics treatment will involve a series of further incremental steps.

Discussion

The one-dimensional stochastic simulation method described here is an outgrowth of an approach that was initially intended as an idealized conceptual model of turbulent combustion. This effort was motivated the recognition that interactions between turbulence and microscale phenomena involve qualitatively different physical behavior than turbulent flow evolution *per se*, and therefore may require modeling treatments that are fundamentally different from those developed for other purposes, e.g., for weather forecasting or airfoil design. The effort has evolved from fundamental study to development of a computational methodology that might provide useful predictive capabilities beyond what is presently available. The essential benefit of the approach in this context is the ability to provide

spatial resolution in 1D rather than 3D, with commensurate reduction of computational cost. Current efforts focus on demonstrating predictive capability of this approach that will establish it as a cost-effective alternative to existing computational models of multi-physics turbulent flow.

Acknowledgement

This research was partially supported by the U.S. Department of Energy, Office of Basic Energy Sciences, Division of Chemical Sciences, Geosciences, and Biosciences. Sandia National Laboratories is a multi-program laboratory operated by Sandia Corporation, a Lockheed Martin Company, for the United States Department of Energy under contract DE-AC04-94-AL85000.

References

- [1] A.R. Kerstein, *J. Stat. Phys.* **45** (1986) 921.
- [2] M. Bramson, P. Calderoni, A. De Masi, P.A. Ferrari, J.L. Lebowitz, and R.H. Schonmann, *J. Stat. Phys.* **45** (1986) 905.
- [3] A.R. Kerstein, *Proc. Combust. Inst.* **21** (1988) 1281.
- [4] A.R. Kerstein, *Combust. Sci. Tech.* **60** (1988) 391.
- [5] U. Frisch, *Turbulence: The Legacy of A.N. Kolmogorov* (1995) Cambridge.
- [6] A.R. Kerstein, *Combust. Sci. Tech.* **81** (1992) 75.
- [7] A.R. Kerstein, *Phys. Fluids A* **3** (1991) 1110.
- [8] A.R. Kerstein, *J. Fluid Mech.* **231** (1991) 361.
- [9] A.R. Kerstein, *J. Fluid Mech.* **240** (1992) 289.
- [10] P.A. McMurtry, T.C. Gansauge, A.R. Kerstein, and S.K. Krueger, *Phys. Fluids A* **5** (1993) 1023.
- [11] M.A. Cremer, P.A. McMurtry, and A.R. Kerstein, *Phys. Fluids* **6** (1994) 2143.
- [12] A.R. Kerstein and P.A. McMurtry, *Phys. Rev. E* **50** (1994) 2057.
- [13] A.R. Kerstein, M.A. Cremer, and P.A. McMurtry, *Phys. Fluids* **7** (1995) 1999.
- [14] A.R. Kerstein, *J. Fluid Mech.* **392** (1999) 277.
- [15] A.R. Kerstein and S. Wunsch, *Bound. Layer Meteorol.* (2005) in press.
- [16] A.R. Kerstein, *Dyn. Atmos. Oceans* **30** (1999) 25.
- [17] T.D. Dreeben and A.R. Kerstein, *Int. J. Heat Mass Transf.* **43** (2000) 3823.
- [18] S. Wunsch and A.R. Kerstein, *Phys. Fluids* **13** (2001) 702.
- [19] S. Wunsch, *Phys. Fluids* **15** (2003) 1442.
- [20] S. Wunsch and A.R. Kerstein, *J. Fluid Mech.* **528** (2005) 173.
- [21] A.R. Kerstein and T.D. Dreeben, *Phys. Fluids* **12** (2000) 418.

- [22] A.R. Kerstein, Wm.T. Ashurst, S. Wunsch, and V. Nilsen, *J. Fluid Mech.* **447** (2001) 85.
- [23] Wm.T. Ashurst and A.R. Kerstein, *Phys. Fluids* **17** (2005) 025107.
- [24] T. Echekki, A.R. Kerstein, J.-Y. Chen, and T.D. Dreeben, *Combust. Flame* **125** (2001) 1083.
- [25] J.C. Hewson and A.R. Kerstein, *Combust. Theor. Model.* **5** (2001) 669.
- [26] J.C. Hewson and A.R. Kerstein, *Combust. Sci. Tech.* **174** (2002) 35.
- [27] V.K. Chakravarthy and S. Menon, *Flow Turb. Combust.* **65** (2000) 133.
- [28] V.K. Chakravarthy and S. Menon, *Combust. Sci. Tech.* **162** (2001) 175.
- [29] R.C. Schmidt, A.R. Kerstein, S. Wunsch, and V. Nilsen, *J. Comput. Phys.* **186** (2003) 317.
- [30] R.C. Schmidt, R. McDermott, and A.R. Kerstein, Sandia National Laboratories Report SAND2005-0206 (2005).
- [31] A.R. Kerstein, *Computer Phys. Commun.* **148** (2002) 1.
- [32] J.R. Schmidt, Ph.D. thesis, Univ. of Arizona (2004).

Parameter estimation for algebraic Reynolds stress models

Stefan Heitmann

Zentrum für Modellierung und Simulation,
Fachbereich Mathematik, Univ. Hamburg, Germany

Abstract

Algebraic Reynolds stress models have been proven to be a powerful and inexpensive tool to predict turbulent stresses. In this study, the sensitivity of these models on their coefficients is investigated. Using standard mathematical optimization techniques it is studied whether predictions can be improved by tuning the model coefficients. As test problem the turbulent round jet as experimentally investigated by [4] is chosen. Improvement is found by tuning the model coefficients. However, for non-homogeneous turbulence there is a fundamental flaw in the modeling approach associated with the weak equilibrium assumption.

Introduction

Turbulence models based on the transport equations for the individual Reynolds stresses are about to replace the standard two-equation models in scientific and industrial flow computations. The effort of carrying further transport equations is usually prohibitively expensive and there is considerable interest in appropriate algebraic approximations.

Algebraic Reynolds stress models

Starting from the exact Reynolds stress transport equation, assuming infinite Reynolds number and invoking the assumption that the turbulence is close to its equilibrium state (*weak equilibrium assumption*), the Reynolds stress equations can be simplified significantly. The weak equilibrium assumption states that for the Reynolds stress anisotropy tensor $b_{ij} = \overline{u_i u_j} / (2K) - 1/3 \delta_{ij}$ convective and third-order (*turbulent diffusion*) terms balance with the time-rate-of-change terms, i.e.,

$$\frac{\partial b_{ij}}{\partial t} + U_k \frac{\partial b_{ij}}{\partial x_k} + D(b_{ij}) \approx 0, \quad (1)$$

with mean flow components U_k and turbulent diffusion $D(b_{ij})$. Now, the system of partial differential equations is reduced to the following set of nonlinear algebraic equations,

$$2b_{ij}(P - \varepsilon) = P_{ij} + \phi_{ij} - \frac{2}{3}\varepsilon\delta_{ij}, \quad (2)$$

where $P_{ij} = -(\overline{u_i u_k} \partial U_j / \partial x_k + \overline{u_j u_k} \partial U_i / \partial x_k)$ is the corresponding production term, ϕ_{ij} is the pressure-strain model while $P = 1/2 P_{kk} = -2K b_{ij} S_{ij}$ and ε are production and dissipation rate of turbulent kinetic energy, respectively. The pressure-strain model ϕ_{ij} is usually modelled in terms of the mean strain rate and rotation rate tensors, $S_{ij} = 1/2(\partial U_i / \partial x_j + \partial U_j / \partial x_i)$ and $W_{ij} = 1/2(\partial U_i / \partial x_j - \partial U_j / \partial x_i)$ as

$$\begin{aligned} \phi_{ij} = -2 \left(C_1^0 + C_1^1 \frac{P}{\varepsilon} \right) b_{ij} + C_2 S_{ij} + C_3 \left(b_{ik} S_{kj} + b_{jk} S_{ik} - \frac{2}{3} b_{mn} S_{mn} \delta_{ij} \right) \\ + C_4 (b_{ik} W_{jk} + b_{jk} W_{ik}), \end{aligned}$$

where $C_1 - C_4$ are coefficients. Inserting the pressure-strain model, the corresponding algebraic equation for the Reynolds stress anisotropy reads

$$b_{ij} = g \left(\alpha_1 S_{ij} + \alpha_2 (S_{ik} W_{kj} - W_{ik} S_{kj}) + \alpha_3 (S_{ij}^2 - \frac{1}{3} \delta_{ij} S_{kk}^2) \right). \quad (3)$$

For convenience, strain rate and rotation tensors are non-dimensionalized by the eddy turnover time scale K/ε , such that $S_{ij}^* = K/\varepsilon \cdot S_{ij}$, $W_{ij}^* = K/\varepsilon \cdot W_{ij}$ are now dimensionless quantities. The '*' will be omitted in the following. The coefficients g and α_i are related to the coefficients of the pressure-strain model by

$$g = 2 \cdot (C_1^0 + P/\varepsilon(C_1^1 + 1) - 1)^{-1}, \alpha_1 = (C_2 - 4/3)/2, \alpha_2 = (C_4 - 2)/2, \alpha_3 = (C_3 - 2)/2. \quad (4)$$

Note that due to the appearance of the production term $P = -b_{ij} S_{ij}$ in g on the right hand side of (3) this is still an *implicit* relation for the anisotropies b_{ij} . Its solution requires the solution of a cubic equation, e.g. [1]. However, in the present study the production term P is assumed to be known. For convenience, we define new coefficients β_i ($i = 1, 2, 3$) which incorporate both g and α_i , ($i = 1, 2, 3$),

$$\beta_i = g \cdot \alpha_i, (i = 1, 2, 3).$$

It might be noted that the turbulence model given by equation (3) is strictly valid only in homogeneous turbulence where mean flow gradients are constant. It is therefore expected that in non-homogeneous turbulence the coefficients are not universal. This has already been pointed out in early publications (e.g., [2], [3]).

The round jet

We choose the turbulent round jet as an example for a non-homogeneous turbulent flow. High resolution experimental data are provided by [4]. The round jet is stationary and has only one direction of homogeneity, the azimuthal direction. Therefore it is a demanding task for the turbulence model (3). In the following, we will refer to the axial and the radial direction as x_1 - and x_2 -direction, respectively. Additional features of the round jet are depicted in figure 1. Part (a) shows the radial profile of the dimensionless shear stress. It raises from zero at the axes to a constant value of about 0.14 over a large region and finally getting smaller in the outer region. This is typical for free shear flows [5]. Part (b) depicts the ratio of turbulent kinetic energy production P over dissipation ε . As the ratio is always smaller than one, the dissipation of turbulent kinetic energy must be balanced by transport processes which make the turbulence non-local. Part (c) shows the ratio of mean flow time scale and turbulence time scale. Based on the shear rate $S = (2S_{ij}S_{ij})^{1/2}$ the appropriate mean flow time scale is S^{-1} whereas the turbulence time scale is K/ε . Turbulence modelling is often based on simplified turbulence conditions in which the time scale ratio is either large or small. Whereas a large ratio allows the application of *Rapid Distortion Theory* (e.g., [6]), a small ratio allows the turbulence scales to have time to equilibrate with the slowly changing mean flow. The most basic flow of this type is decaying turbulence where S is zero. Part (c) reveals that neither of these requirements applies in the round jet where SK/ε is neither large nor small but on the order of unity.

Linear Optimization

We wish to find the set of coefficients $\underline{\beta} = (\beta_1, \beta_2, \beta_3)^T$ which, inserted in equation (3), reproduces the experimental data for the components b_{ij} of the anisotropy tensor as close as possible. Additionally,

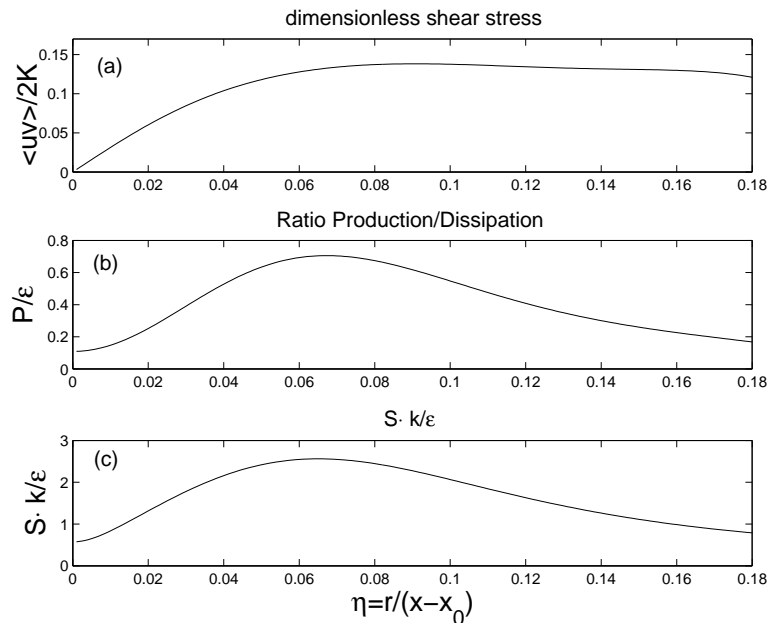


Figure 1: Features of the turbulent round jet. The dimensionless coordinate η is the ratio of radial and axial distance from the flow origin.

coefficient	C_1^0	C_1^1	C_2	C_3	C_4
Reference [7]	1.5	0	0.8	1.75	1.31
Reference [8]	1.8	0	0.8	2.00	1.11
Reference [9]	1.7	0.90	0.36	1.25	0.45

Table 1: Range of coefficients of the pressure-strain model according to several authors

the coefficients are subject to certain constraints which are dictated by physical considerations. The corresponding least-squares minimization task reads as

$$\frac{1}{2} \|\underline{M} \cdot \underline{\beta} - \underline{d}\|_2 = \min, \quad \underline{A} \cdot \underline{\beta} \leq \underline{c}, \quad (5)$$

where \underline{M} represents the coefficient matrix, \underline{d} the data vector, and $\underline{A}, \underline{c}$ describe the linear system of equations for constraints on $\underline{\beta}$. Different coefficients of the pressure-strain model $C_1 - C_4$ have been proposed by different authors [7], [8], [9] as shown in table 1. These proposals, the observed range of $0 \leq P/\varepsilon \leq 0.8$ and the application of equation (4) allow to estimate constraints on the coefficients $\beta_i, (i = 1, 2, 3)$. However, we extend the admissible range for β_2 and β_3 to positive values somewhat arbitrarily,

$$-0.4 \leq \beta_1 \leq 0, \quad -0.6 \leq \beta_2 \leq 0.8, \quad -0.3 \leq \beta_3 \leq 0.8.$$

Three approaches were tested. For reference, the values derived from the LRR-model [7] were taken. They read

$$\underline{\beta}_{LRR} = (1 + 2P/\varepsilon)^{-1} (-4/15, -1/8, -0.345)^T. \quad (6)$$

In the second one, the coefficients were assumed to be constant and the best constants are determined from the optimization procedure (5). In the third approach, the coefficients are assumed to be linear

functions of the Reynolds stress anisotropy invariants $II = -1/2b_{ij}b_{ij}$ and $III = 1/3b_{ij}b_{jk}b_{ki}$ and the normalized production-over-dissipation ratio $P/\varepsilon - 1$, i.e.,

$$\beta_i = \beta_i^{(0)} + \beta_i^{(1)} \cdot II + \beta_i^{(2)} \cdot III + \beta_i^{(3)} \cdot (P/\varepsilon - 1), (i = 1, 2, 3) \quad (7)$$

which will be referred to as the 'variable-coefficient-approach'. The invariants and the production/dissipation ratio serve to describe the flow regime and are appropriate candidates for a general scaling. The algorithm 'lsqlin' from the commercial software package MATLAB 7.0.1 [10] is used to solve the above optimization problem. It might be worth noting that from a physical point of view the shear stress term b_{12} is the most important quantity. It is therefore questionable whether it is the right strategy to determine an error in the L_2 -sense thus ignoring the dominant role of b_{12} over the other three stresses. This issue might be addressed in further studies.

Numerical results

Figure 2 displays the computed anisotropies applying the model equation (3) along with the coefficients from [7], given by equation (6). The agreement of the computed values (thin lines) with measured data (thick lines) is poor. The model fails to predict the typical free shear flow feature of the constant value of b_{12} over the range $0.06 \leq \eta \leq 0.17$. Additionally, the slope of the b_{12} -profile is overestimated near the centre axis. The centre axis values of the normal stresses are far from the observed ones but more striking is that even the qualitative behaviour of the profile is not predicted correctly. Where the observed profiles become smaller the computed ones increase and vice versa. In summary, the computed normal stresses tend to return to isotropy much faster than the experimental data indicate.

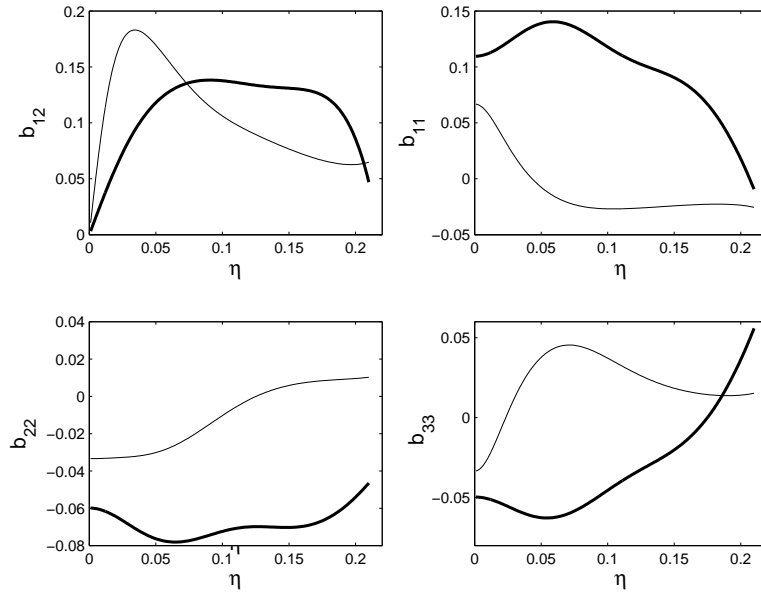


Figure 2: Reynolds stress anisotropies from experiment (thick lines) and computed with the coefficients proposed by [7], see equation (6) (thin lines).

For constant coefficients, the best agreement between model and data is achieved for the following vector of coefficients:

$$\underline{\beta} = (-0.065, 0.082, 0.027)^T.$$

coefficient	$\beta_i^{(0)}$	$\beta_i^{(1)}$	$\beta_i^{(2)}$	$\beta_i^{(3)}$	range of β_i
β_1	-0.44	-20.3	-946	-0.33	$-0.218 \leq \beta_1 \leq 0$
β_2	-0.75	-43.0	-40.8	-0.98	$0.094 \leq \beta_2 \leq 0.800$
β_3	0.00	-1.89	-121	-0.02	$0.004 \leq \beta_3 \leq 0.045$

Table 2: Computed values for the variable-coefficients approach (7)

For the variable-coefficients approach (7), the best agreement is achieved for the values listed in table 2. The corresponding computed profiles are depicted in figure 3. It is clearly seen that both approaches

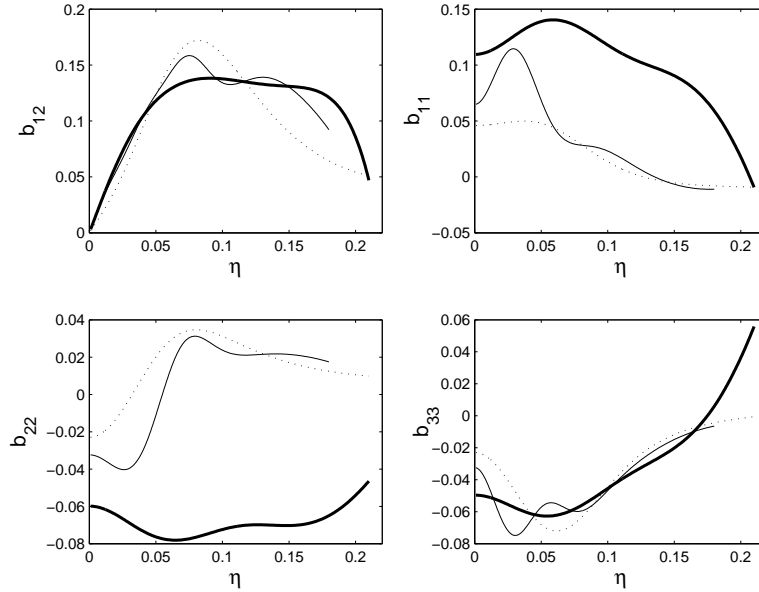


Figure 3: Reynolds stress anisotropies from experiment (thick lines) and computed with constant (dotted lines) and variable coefficients (thin solid lines).

improve the slope of the b_{12} -profile. The variable-coefficients approach is even able to predict a rather constant value for b_{12} . Unfortunately, the normal stress anisotropies have not been improved significantly compared to figure 2. The profile of b_{33} is in reasonable agreement with the experimental data. However, this is the smallest quantity. For the variable-coefficients approach it is found that close to the centre axis the normal stress profiles exhibit at least the correct qualitative behaviour. From a further analysis it is found that it is mainly the first part of (3), i.e. the downgradient part, that creates the unrealistic decrease of b_{11} and increase of b_{22} . The observed ratios $-b_{11}/S_{11}$ and $-b_{22}/S_{22}$ that might be regarded as the 'normal stress eddy viscosities' are found to change sign at $\eta \approx 0.08$ and 0.06, respectively and reach absolute values as high as 60. That means that the downgradient assumption for the normal stresses b_{11} and b_{22} leads to poor results and the other two terms of our model (3) are not able to compensate for its deficiency. It might be speculated that the local assumption inherent in the downgradient hypothesis and the model (3) underestimates the inertia of the normal stresses which evolve more slowly than the corresponding mean strain rates S_{11} and S_{22} . This interpretation is supported by the fact that the profile of b_{33} is in good agreement with data. Apparently, the underlying weak equilibrium assumption (1) is well justified for the azimuthal (the '3') component where the mean flow is zero. In contrast, the same assumption might not be

justified for the axial and radial direction, respectively. Here, the turbulence does not instantaneously adjust to local mean flow conditions. A more appropriate algebraisation procedure to replace equation (1) is currently under investigation.

Acknowledgements

We are indebted to Prof. William George for kindly providing his experimental results that were used in this work.

References

- [1] S.S. Girimaji, Phys. Fluids **9** (1997) 1067.
- [2] O. Zeman and H. Tennekes, J. Atmos. Sci. **32** 1975 1808.
- [3] O. Zeman, Ann. Rev. Fluid Mech. **13** (1981) 253.
- [4] H. J. Hussein, S. Capp, and W. K. George, J. Fluid Mech. **258** (1994) 31.
- [5] H. Tennekes and J. L. Lumley, **A first course in turbulence**. Cambridge MA:MIT Press (1972)
- [6] S. C. Crow, J. Fluid Mech. **33** (1968) 1.
- [7] B. E. Launder, G. J. Reece, and W. Rodi, J. Fluid Mech. **68** (1975) 537.
- [8] D. B. Taulbee, Phys. Fluids **4** (1992) 2555.
- [9] C. G. Speziale, S. Sarkar, and T. B. Gatski, J. Fluid Mech. **227** (1991) 245.
- [10] The MathWorks, Inc., Natick, MA, US

Turbulent mixing and entrainment in density driven gravity currents

S. Décamp, J. Sommeria

LEGI / Coriolis (UMR 5519, CNRS-UJF-INPG), 21 av. des Martyrs, 38041 Grenoble, France

Abstract

We study gravity currents flowing down a uniform slope in a homogeneous media with rotation. Those dense overflows are of particular interest in oceanography, as it is an important mechanism in renewing deep water as part of the global thermohaline convective cycle which has a strong impact on climate. The large Coriolis turntable (Grenoble) is used to study at the laboratory scale, a gravity current in similarity with the oceanic scales.

The propagation of such currents is strongly influenced by rotation, and its dynamics is turbulent and unstable, which produces the mixing with the ambient. The experiments are used to determine the stabilization depth of the main current along the coast, to measure the mixing and friction effects in a rotating system and to observe development of instabilities, also seen in the ocean. Scaling laws are derived from the initial parameters, describing the main properties of the flow in geostrophic equilibrium along the slope, such as its position, width, velocity or density. These scaling laws suppose that the buoyancy flux is conserved, which is verified by the experimental data analysis. The intensity of the turbulent stress in these overflows is also investigated, and compared to the formation of cyclonic eddies.

Introduction

Plumes are flows generated by a density contrast between a continuous source fluid and its environment, modifying the global distribution of temperature and salinity. In oceanography, these dense overflows on a continental slope are very active as they take part in the production of the North Atlantic deep waters. Cold water from Nordic seas or salty water from the Mediterranean Sea descend into the Atlantic ocean over a sill, resulting in mass exchange with high density gradient, instabilities and generation of mesoscale vortices. Observation of the dense overflow in the Denmark strait is possible from in-situ measurements of density [1]. Cooling of warm and salty waters from the Gulf stream in the Nordic seas generates the descent and spreading of the denser water masses created, which then propagate along the East Greenland coast, as shown in figure 1. This overflow is schematically reproduced in laboratory experiments described below.

The bottom friction effects and the turbulent mixing process involved in these dense currents has been studied by theoretical, numerical and experimental analysis, usually in non-rotating systems, as reviewed by Simpson [2]. The first experiments performed to study the gravity current front, on a non-rotating slope, were carried out by Ellison and Turner [3]. When the dense current flows down the continental slope, entrainment of the ambient fluid causes mixing. In the case of a two-dimensional plume on a slope (of inclination α) in a non-rotating system, Ellison and Turner [3] suggested that the entrainment is proportional to the mean velocity U in the downslope direction x , with a proportionality constant E . The mixing and turbulent entrainment theory has been further developed by Turner [4], assuming that the entrainment parameter is a function of the Richardson number $E(R_i)$. The mass continuity equation of the gravity current of height h , and the momentum conservation equation are (for a homogeneous environment at rest, and bottom friction effects negligible compared

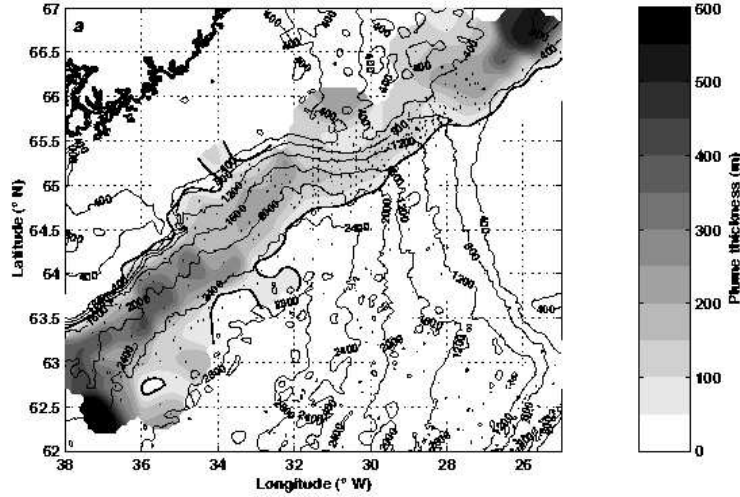


Figure 1: Thickness of the dense layer of the gravity current (for densities $\sigma_\theta > 27.81 \text{Kg.m}^{-3}$) obtained from the Poseidon / Aranda dataset (1996-98). Bathymetry contours in meters (from Smith and Sandwell) are drawn in black. The Greenland coast is visible on the upper left corner. Figure from Käse et al. [1]

to entrainment):

$$\frac{d(Uh)}{dx} = E U \quad \text{and} \quad \frac{d(U^2 h)}{dx} = g' h \sin \alpha$$

Assuming similarity of profiles, the gravity current thickness will increase linearly in distance to the source $dh/dx = E(Ri_o)$. The turbulent entrainment rate was measured experimentally [4] and can be represented to a good accuracy by

$$E = \frac{0.08 - 0.1 Ri_o}{1 + 5 Ri_o} \quad \text{where} \quad Ri_o = \frac{g' h \cos \alpha}{U^2}$$

The actual parameterization in oceanic numerical models make use of these theories, even though the Coriolis effect was missing in the experiments. These mixing model have been extended to density stratified environments by Baines [5], but the experiments show that it is not appropriate. The resulting downflow has a uniform thickness until it reaches its level of equal density. A model based on observations of the flow has been derived, describing the turbulent transfers in term of local entrainment, detrainment and drag coefficients.

But the Coriolis effect due to the earth rotation, induces significant changes on large-scale flows dynamics (Griffiths [6]). Laboratory experiments have been performed in rotating systems like Whitehead et al. [7] who observed the generation of cyclonic vortices, similar to eddies seen in the Denmark strait. Other experiments in quasi-laminar regime with no turbulent mixing confirmed this behaviour (Lane-Serff and Baines [8] or Etling et al. [9]). In fact several types of flows are observed in rotating experiments, as characterized by Cenedese et al. [10]: A laminar regime where no mixing occurs between the current and the ambient fluid; a wave regime also described by Shapiro and Zatsepin [11] where wave perturbation appear at the interface between the dense fluid and the ambient; and an unstable regime with generation of periodic cyclonic vortices in the ambient fluid, over the gravity current, modifying its propagation.

In fact, the Coriolis facility at LEGI (Grenoble) is the only turntable which allows the study of a fully turbulent gravity current strongly influenced by rotation. Thanks to its large dimension (13m in diameter), inertial regimes that characterize the ocean dynamics are approached.

The purpose of this study is to determine experimentally the main characteristics of a gravity current flowing down a slope in a rotating system. It is important to measure the effects of bottom friction influencing the current's final stabilized position along the slope, and the effects of mixing due to entrainment and detrainment with the ambient fluid, that controls the density of the gravity current and its velocity. Development of instabilities generating large cyclonic eddies propagating along the incline slope, is also observed.

Experimental setup

The experiments are performed on the large Coriolis turntable (Grenoble) with the experimental setup described in figure 2. The gravity current is created by salty water injected with a constant flux, in the ambient fluid of uniform lower density. The controlled parameters are: the initial density difference between the gravity current and the environment $g'_o = \Delta\rho/\rho_o$; the initial flow flux Q_o (generally expressed as the buoyancy flux $B_o = g'_o Q_o$); and the rotation period T of the turntable giving the Coriolis parameter $f = 4\pi/T$. Values of those experimental parameters are listed in table 3

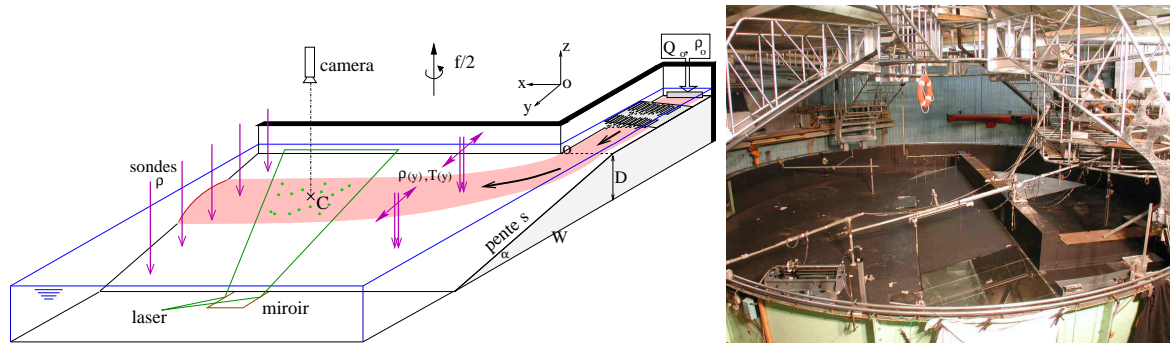


Figure 2: Schematic representation and picture of the experimental setup, with the position of the probes and laser.

The dense fluid starts flowing down the incline slope s of 2m wide, 10m long and 15° of inclination. It behaves as a gravity current in self-similarity, with intense mixing occurring at the interface with the ambient fluid, as visualized in figures 3. It is then deflected by the Coriolis force and reaches an equilibrium depth, in a state of geostrophic balance along the slope, with nearly horizontal mean velocities. However a small part of the fluid moves downward in the bottom viscous boundary layer. It is subject to a friction driven instability, as seen in figure 3a. Another instability, of baroclinic kind, is observed over the main current, generating large vortices stretching over the whole water depth, which greatly modifies the current propagation.

Velocity fields are measured by particle image velocimetry (PIV). The current is seeded with particles illuminated by a laser sheet directed along the slope at different heights from the bottom. Probes are also used to record density variations at different locations.

Similarity between laboratory and oceanic scales

The similarity between experiments and the oceanic scale is determined by keeping non-dimensional numbers constant. From the six dimensional parameters listed in table 3, one can define four independent non-dimensional parameters. These are usually defined in terms of the initial current thickness h_o , width L_o and velocity V_o . These quantities are indirectly set by the flow rate $Q_o = \frac{h_o L_o}{2} V_o$, or the related buoyancy flux $B_o = g'_o Q_o$. To connect them to the known parameters, it is assumed that the

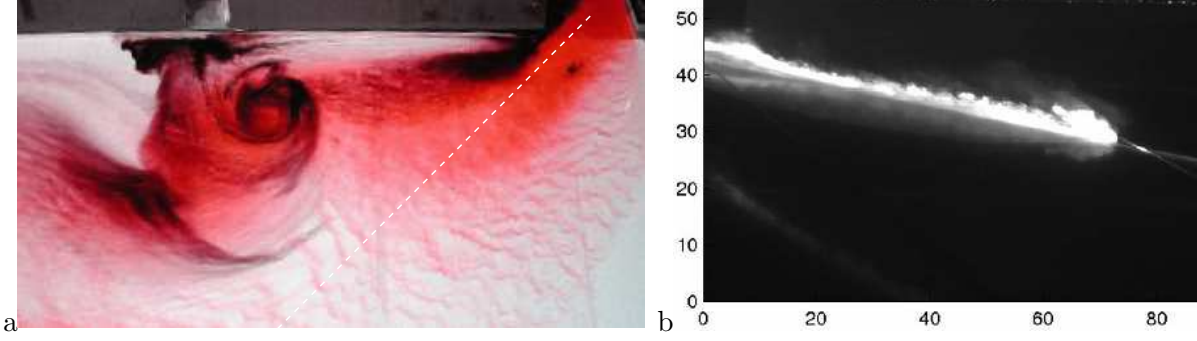


Figure 3: Visualization of the gravity current: **a.** The current (red dye) splits into a geostrophically balanced jet flowing along the slope and a thin viscous layer descending the slope. The main current is subjected to baroclinic instabilities which induce cyclonic vortices. These extend over the whole water depth, as visualized by the black dye released above the current. **b.** The vertical cut (fluorescein illuminated by a vertical laser sheet along the oblique line drawn in figure a) shows that the current thickness decreases at the beginning of the slope before growing because of turbulent mixing.

gravity current has an initial speed $V_o = c_1 \sqrt{g'_o h_o}$ (where $c_1 = 0.5$, resulting from measurements), and that the dense fluid adjusts itself in geostrophic equilibrium in the hydrostatic approximation (for large scales): $f V_o = \frac{g'_o h_o}{L_o}$.

From these relations, the thickness, width and velocity can then be expressed as:

Inlet channel

$$h_o = \frac{\sqrt{2 f B_o}}{g'_o} = \frac{4 V_o^2}{g'_o} \quad (1)$$

$$L_o = 2 \left(\frac{2 B_o}{f^3} \right)^{\frac{1}{4}} = \frac{4 V_o}{f} \quad (2)$$

$$V_o = \frac{1}{2} (2 f B_o)^{1/4} \quad (3)$$

The current width L_o is an important length scale as it should not exceed the width of the slope. This implies that

$$\frac{L_o}{W} = 2^{5/4} f^{-3/4} B_o^{1/4} W \ll 1,$$

which is one of the non-dimensional parameter of table 3, kept small and constant. The width W of the sloping bottom is considered sufficiently large so that it does not restrict the current width.

From the initial parameters (the Coriolis parameter f , the initial buoyancy flux B_o and the gravity acceleration projected onto the horizontal ($s g'_o$)), only one non-dimensional number can be derived:

$$M = s g'_o f^{-5/4} B_o^{-1/4} 2^{3/4} = \frac{s g'_o}{f V_o} = \frac{\text{topographic slope}}{\text{initial geostrophic slope}} \quad (4)$$

This important quantity is also the ratio of the topographic slope s over the natural slope of the isopycnals given by the initial geostrophic equilibrium ($h_o / L_o = f V_o / g'_o$).

The Burger number based on the initial width and velocity of the current is always constant:

$$R_o = \sqrt{g'_o h_o} / (f L_o) = 1/2$$

Finally, the Reynolds number based on the initial current height $Re = V_o h_o / \nu = \nu^{-1} (f B_o)^{3/4} g_o'^{-1} 2^{-1/4}$ is of the order of 2000 or higher in most experiments. Even though this value is much smaller than an oceanic case, it is admitted that global entrainment and turbulent mixing properties do not depend on the Reynolds number for values higher than 1000. This similarity explained in table 3 shows that a typical experiment reproduces a continental slope of 122km wide and 3km deep.

Similarity : from laboratory to oceanic scale		Reference experiment	oceanic example 1	oceanic example 2
Dimensional parameters				
Slope height	D [m]	0.5	3000	3000
Slope width	W [m]	1.94	122 000	11 600
Coriolis parameter	$f = \frac{4\pi}{T}$ [s ⁻¹]	0.314	10 ⁻⁴	10 ⁻⁴
Reduced gravity	$g_o' = g \frac{\Delta\rho}{\rho_o}$ [ms ⁻²]	0.3	0.02	1.8 10 ⁻⁴
Buoyancy source flux	$B_o = g_o' Q_o$ [m ⁴ s ⁻³]	2.4 10 ⁻⁴	1.3 10 ⁹	9.2
Viscosity	ν [m ² s ⁻¹]	10 ⁻⁶	10 ⁻⁶	10 ⁻⁶
Dimensionless parameters				
Topographic slope	$s = \frac{D}{W}$	25.8 %	2.5 %	25.8 %
Mixing number	$M = \frac{s g_o'}{f V_o}$	4.44		
Reynolds number	$Re = \frac{V_o h_o}{\nu}$	2.3 10 ⁴	2.8 10 ⁹	2.5 10 ⁷
Normalized width	$\frac{2^{5/4} f^{-3/4} B_o^{1/4}}{W}$	0.25		

Table 3: Simplified description of the similarity made to go from laboratory experiments to oceanic scales: The first column represent to typical experiment used as a reference; the second column is a typical oceanic case where dimensionless parameters are conserved, except for the topographic slope; the third column is a less realistic case for which the slope is preserved as well, the source volume flux is then very large with small density difference.

Scaling laws on the overflow

In order to analyse all the data obtained from the experiments, some scaling laws have been introduced.

The parameter M introduced in the similarity assumption can also be interpreted as a representation of the mixing. If M is small, there is no mixing and the current stays in the same state. While if M is large, the current will reach a new state of geostrophic equilibrium along the slope. The gravitational acceleration is balanced by the Coriolis effect, so that the slope of the interface of the dense current is equal to the topographic slope. The along-slope speed (known as the Nof velocity) is then:

$$U = g' s / f$$

As the flow is deviated by the Coriolis effect, the associated length scale is $L = U / f$, with a velocity also expressed as $U = c_2 \sqrt{g' h}$.

It is assumed that the initial buoyancy flux is conserved $B_o = h_o L_o V_o g_o' / 2 = h L U g'$. The dynamics of the current depends only on the initial buoyancy flux, and not on the other initial parameters. Far enough from the source, the flow seems to forget its initial mass (g_o') and momentum (Q_o) fluxes. It depends only on the buoyancy flux B_o . This is equivalent to the classical self-similarity

assumption for turbulent plumes or jets, which has been extended here to gravity currents on a sloping bottom, in presence of rotation.

A very important parameter is therefore the typical length scale L_o (equation 2) as it depends only on the buoyancy flux, and scales with the Rossby radius of deformation.

From these estimates, some simple scaling laws are derived on the ratio of flow quantities along the slope to their initial values, as a function of M :

$$\frac{g'}{g'_o} = \frac{c_2^{1/2} 2^{3/4}}{M} \propto \frac{1}{M} \quad (5)$$

$$\frac{h}{h_o} = c_2^{-3/2} 2^{-5/4} M \propto M \quad (6)$$

$$\frac{U}{V_o} = c_2^{1/2} 2^{3/4}, \quad \text{independent of } M \quad (7)$$

The characteristics of the current along the slope depend only on the initial buoyancy flux conserved (or equivalently on the length scale $L_o \propto f^{-3/4} B_o^{1/4}$) and not on the initial conditions.

Experimental analysis

It is possible to check experimentally the assumption made to derive these scaling laws from the PIV measurements in planes parallel to the sloping bottom. An example is presented on figure 6a. Density profiles also enable to determine the width or thickness of the gravity current, and to quantify the mixing process.

The first result concerns the depth reached by the flow in equilibrium along the slope. It is determined by measuring the position of the maximum mean velocity along the slope at a distance L_o from the inlet channel (see figure 6a). This distance scales with the Rossby radius of deformation ($L_o c_1 = (2 B_o f^{-3})^{1/4}$) as shown by the graph 4. The downslope excursion is found to be $(2.32 \pm 0.05) (L_o c_1)$, as obtained by Lane-Serff and Baines [8] for smaller Rossby numbers.

To summarize the experimental data, plots of the scaling laws are drawn. Figure 5a) shows the ratio of the mean velocity of jet along the slope (measured from PIV) over the initial velocity (calculated from equation 3). It is found to be independent of M as obtained from the scaling analysis.

Figure 5b) is a graph of the ratio of the reduced gravity of the current (measured by conductivity probes as the maximum density excess at 7.2m from the inlet channel) over the initial reduced gravity (known). This ratio is inversely proportional to M as expected.

Values of g'/g'_o emphasize the intense mixing occurring at the interface with the ambient fluid, mainly at the beginning of the descent of the overflow. Thereafter the geostrophically balanced jet flowing along the slope suffers very little mixing.

Those results confirm that the fluid dynamics only depends on the initial buoyancy flux. The fluid is in geostrophic equilibrium along the sloping bottom and M is the important parameter with the length scale L_o . This behaviour is also obtained from the mean along-slope velocity U profiles (made in the downslope direction), performed at the distance L_o from the channel. Those profiles, drawn in figure 6b are normalized in velocities by U/V_o and in position by y/L_o . All the curves of the experiments performed superimposed, even for runs with completely different initial parameters. This emphasizes once again that there is a kind of universal law predicting the pattern of the flow such as the along-slope velocity, the position of equilibrium or the width of the gravity current.

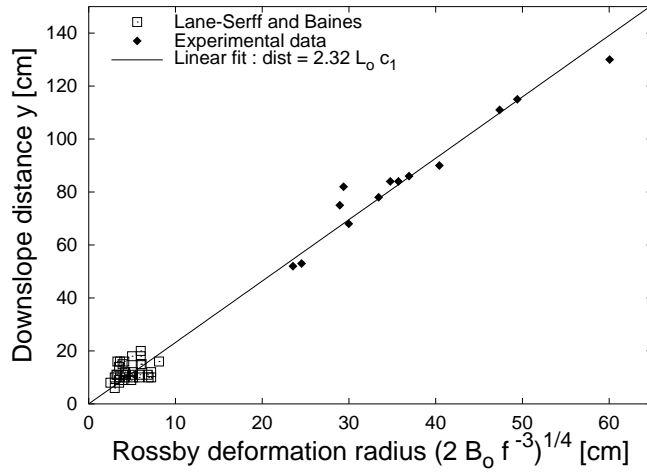


Figure 4: Downslope distance reach by the gravity current, as a function of the Rossby radius of deformation based on the initial height of the gravity current.

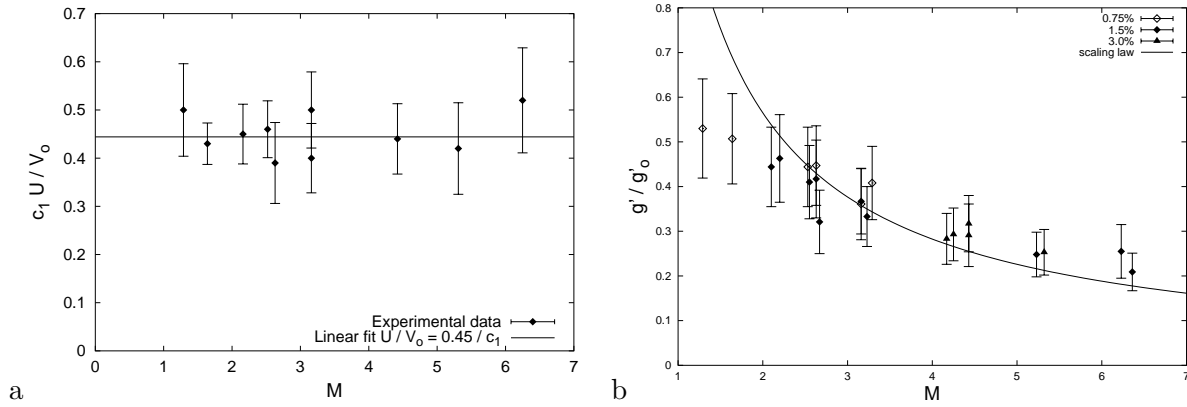


Figure 5: Measured ratio of velocities: $\frac{U}{V_0} = cst$, and measured mixing rate in the main current: $\frac{g'}{g_0} \propto \frac{1}{M}$ as a function of M

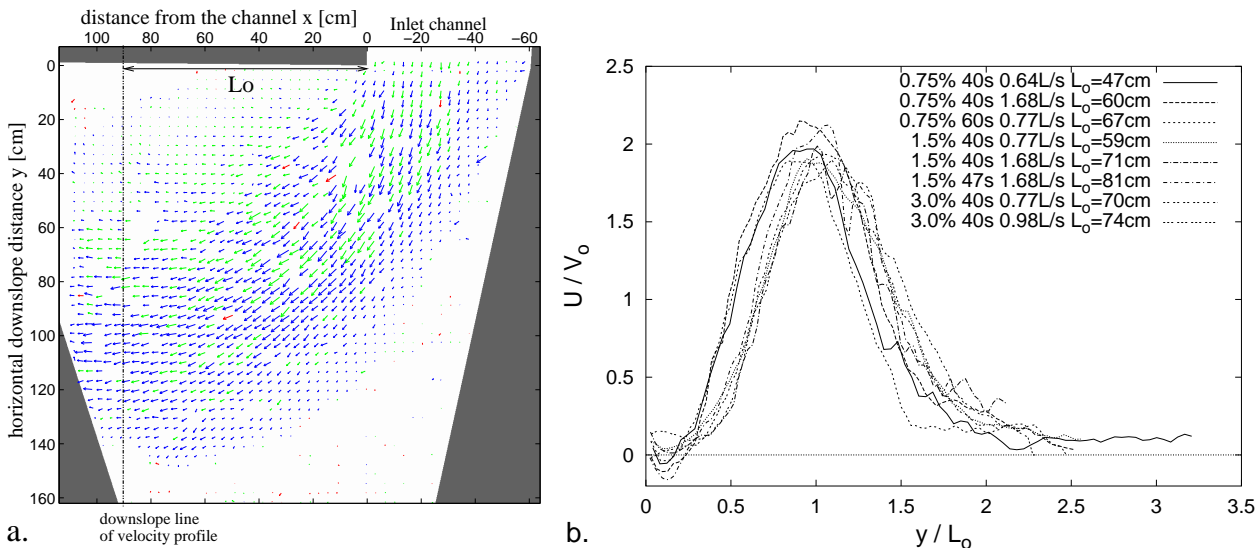


Figure 6: a. Example of velocity field obtained for the main current by PIV with a laser sheet parallel to the slope at a distance of 2cm. b. Downslope profiles of the mean along-slope velocity U made at the distance L_0 from the inlet channel

Cyclonic eddies

The frequency of the cyclonic vortices is obtained either from density records at a fixed position, or from velocity variations over the current. In both cases, the oscillations observed correspond to the passing vortices. Figure 7 shows that the ratio of the vortices period over the turntable period is constant. This is compatible with vortices created by a baroclinic instability.

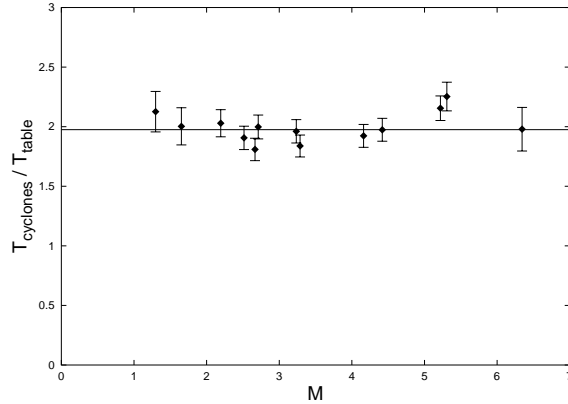


Figure 7: Ratio of the cyclones period over the turntable period. $\frac{T_{cyclones}}{T_{turntable}} \simeq 2$

Mean velocities and turbulent stress

The velocity fields, averaged in time, can be used to investigate the intensity of velocity fluctuations due to horizontal turbulence, and the Reynolds shear stress. Figure 8a) is an example of a velocity profile perpendicular to a central streamline of the current. The velocity is maximum at the center. The same graph also contains plots of the turbulent intensity of the transverse and longitudinal velocity fluctuations ($\sqrt{u'^2}$, $\sqrt{v'^2}$). These intensities strongly depend on the cyclonic vortex formation and propagation. Different kind of trajectory for the cyclones are observed, depending on the dense current thickness. When the current is thick, eddies are carried along in its wake, and they stay over it. Velocity fluctuations are therefore significant. But if the gravity current thickness is smaller, the cyclones propagation is controlled by the beta effect corresponding to the sloping bottom, and eddies leave the current to follow their own trajectory. Velocity fluctuations are weaker in that case. This shows that the thickness of the gravity current over the height of the water column over it, is an important parameter that has not been taken into account in the scaling set previously.

The second graph of figure 8 is a plot of the mean value of the product $\overline{u'v'}$, which is the turbulent shearing stress apart from a factor ρ . The curve is asymmetric about the center of the current. It is positive where the mean shear (derivative of u) is negative and vice-versa. The sign of the Reynolds shear stress correspond to the transport of momentum away from the center of the gravity current, participating to the spreading of the flow due to horizontal turbulence. The value obtained for the Reynolds stress is similar to that obtained for a self-preserving axisymmetric turbulent jet (Fukushima et al. [12])

However from these PIV measurements, only horizontal exchanges can be analysed. It is not possible to deduce the characteristics of vertical turbulence, nor of mixing due to entrainment. Precise vertical velocity profiles are needed to analyse those momentum and salinity turbulent fluxes.

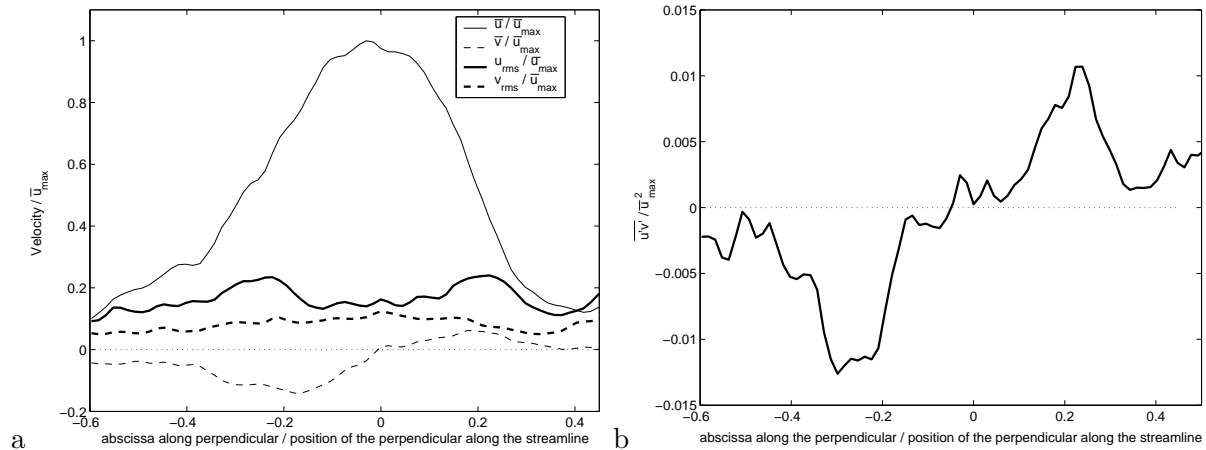


Figure 8: a. Mean velocity profiles on a perpendicular to a streamline position, with turbulent intensities of the velocity fluctuations across the gravity current. b. Corresponding turbulent shear stress.

Conclusions

The dynamics of a dense water overflow on a continental slope has been reproduced in a laboratory, including small scale turbulent mixing: effects of rotation and density stratification are reproduced in dynamical similarity, and the gravity current is fully turbulent.

The existence of a self-similar gravity current on a slope in a rotating system has been demonstrated by experimental results. The scaling laws for such flows has been obtained. The mixing of this current with the surrounding fluid has then been characterized, providing support for modeling of turbulence in such systems.

Acknowledgements

This work has been supported by DGA (grant EPSHOM CA2003/01/CMO) and by the program PATOM of INSU.

References

- [1] R.H. Käse et al., Structure and variability of the Denmark strait overflow : Model and observations. *J. Geophys. Res.* **108**, **C6** (2003) 3181.
- [2] J.E. Simpson, Gravity currents in the laboratory, atmosphere, and ocean. *Ann. Rev. Fluid Mech.* **14** (1982) 213-234.
- [3] T.H. Ellison and J.S. Turner, Turbulent entrainment in stratified flows. *J. Fluid Mech.* **6** (1959) 423-448.
- [4] J.S. Turner, Turbulent entrainment: the development of the entrainment assumption, and its application to geophysical flows. *J. Fluid Mech.* **173** (1986) 431-471.
- [5] P.G. Baines, Mixing in flows down gentle slopes into stratified environments. *J. Fluid Mech.* **443** (2001) 237-270.
- [6] R.W. Griffiths, Gravity currents in rotating systems. *Ann. Rev. Fluid Mech.* **18** (1986) 59-89.

- [7] J.A. Whitehead et al., Experimental observations of baroclinic eddies on a sloping bottom. *J. Geophys. Res.* **95** (1995) 9585-9610.
- [8] G.F. Lane-Serff and P.G. Baines, Eddy formation by overflows in stratified water. *J. Phys. Oceanogr.* **30** (2000) 327-337.
- [9] D. Etling et al., Experiments with density currents on a sloping bottom in a rotating fluid. *Dyn. Atmos. Oceans* **31** (2000) 139-164.
- [10] C Cenedese et al., A dense current flowing down a sloping bottom in a rotating fluid. *J. Phys. Oceanogr.* **34** (2004) 188-203.
- [11] G.I. Shapiro and A.E. Zatsepin, Gravity current down a steeply inclined slope in a rotating fluid. *Ann. Geophysicae* **15** (1997) 366-374.
- [12] C. Fukushima et al., Investigation of the mixing process in an axisymmetric turbulent jet using PIV and LIF. in, *Laser Techn. for Fluid Mech.* Springer, Berlin (2002) 339-356.

Superstatistics and atmospheric turbulence

*S. Rizzo*¹, *A. Rapisarda*²

¹ E.N.A.V. S.p.A., U.A.A.V. Firenze, Italy

² Dipartimento di Fisica e Astronomia, CACTUS Group Università di Catania and INFN sezione di Catania Via S. Sofia 64, I-95123 Catania, Italy

Introduction

In this very short contribution we summarize some recent results on wind velocity data recorded at Florence airport. More details can be found in the proceedings of two recent conferences [1] and in a long paper in preparation [2]. In particular we show that one can describe this example of atmospheric turbulence by means of the superstatistics approach proposed by Beck and Cohen [3]. The latter justifies the successful application of Tsallis generalized statistics in different fields [4], and more specifically in turbulence experiments [5, 6].

Discussion of the results

The wind velocity measurements, were taken at Florence airport for a time interval of six months, from October 2002 to March 2003. Data were recorded by using two anemometers, each one mounted on a 10 m high pole, located at a distance of 900 m. The sampling frequency was $3.3 \cdot 10^{-3}$ Hz. Despite this low frequency, we found many similarities with microscopic turbulence data. We investigated correlations, spectral distributions as well as probability density functions of velocity components of returns and differences. In the following we discuss only returns of the longitudinal velocity components measured by one of the two anemometers. We consider the one closest to the runway head 05 and labeled *RWY05*. Returns are defined by the following expression

$$x(t)_\tau = V_x^{RWY05}(t + \tau) - V_x^{RWY05}(t) \quad , \quad (1)$$

$V_x(t)$ being the longitudinal velocity component at time t and τ being a fixed time interval. The same analysis was done also for the transversal components and for velocity difference between the two anemometers with similar results [1, 2].

Our data show very strong correlations and power spectra with the characteristic $-5/3$ law in the high-mid portion of the entire spectrum [1]. No significant difference was found for day and night periods, when air traffic is almost absent.

The superstatistics formalism proposed recently by C. Beck and E.G.D. Cohen is a general and effective description for nonequilibrium systems [3]. One can consider the fluctuations of an intensive quantity, for example the temperature, by introducing an effective Boltzmann factor

$$B(E) = \int_0^\infty f(\beta) e^{-\beta E} d\beta \quad , \quad (2)$$

where $f(\beta)$ is the probability distribution of the fluctuating variable β . Thus one gets for the probability distribution

$$P(E) = \frac{1}{Z} B(E) \quad , \quad (3)$$

with the normalization given by $Z = \int_0^\infty B(E) dE$. One can imagine a collection of many cells, each of one with a defined intensive quantity, in which a test particle is moving. In our atmospheric turbulence

studies, the time series of the wind velocity recordings, are characterized by a fluctuating variance, so the returns (1), cannot be assumed to be a "simple" Gaussian process. They show a very high intermittent behavior stronger than that one usually found in small-scale fluid turbulence experiments.

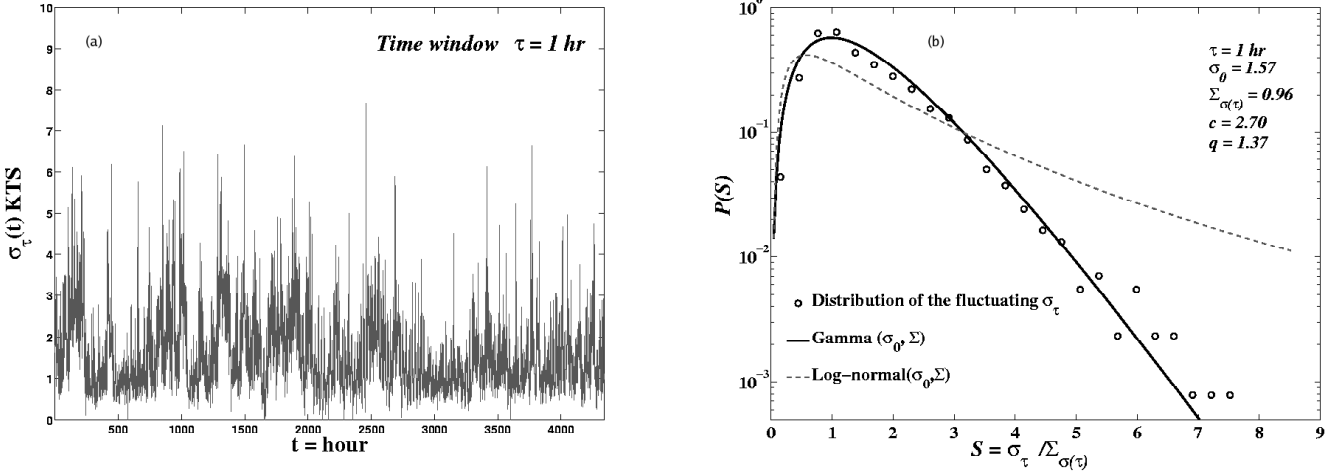


Figure 1: (a) Variance fluctuations of the longitudinal wind velocity component for the anemometer RWY05 obtained with a moving time window τ of one hour. (b) Standardized pdf of the fluctuating variance corresponding to figure (a) (open points) are compared with a Gamma distribution (full line) and with a Log-normal distribution (dashed line). The two curves share the same mean $\sigma_0 = 1.57$ and variance $\Sigma = 0.96$ extracted from experimental data.

In our analysis we considered the following quantities: (i) the wind velocity returns x defined by eq.(1), (ii) the corresponding variance of the returns x , which we indicate with σ , (iii) the fluctuations of σ , whose variance we indicate with the symbol Σ .

Using a fixed time interval τ , we extracted from the experimental data the distribution for the fluctuations of the longitudinal wind component variance. This was done in order to cut the time series in "small" pieces in which the signal is almost Gaussian and then apply superstatistics theory. This fluctuating behavior of σ is plotted in Fig.1 (a) for a time interval $\tau = 1$ hour. In Fig. 1 (b) we then plot the probability distribution of the variance σ for $\tau = 1$ hour. In this figure we plot for comparison a Gamma (full curve) and a Log-normal (dashed curve) distribution characterized by the same average and variance extracted from the experimental data. In this sense, the curves are not fits of the data. The comparison clearly shows that the Gamma distribution is able to reproduce very nicely the experimental distribution of the σ fluctuations. This is at variance with the Log-normal distribution which is usually adopted in microscopic turbulence and which in this case is not able to reproduce the experimental data. A similar behavior holds for different time intervals. Then following ref.[3] one gets for the Gamma distribution

$$f(\beta) = \frac{1}{b\Gamma(c)} \left(\frac{\beta}{b}\right)^{c-1} e^{-\beta/b} , \quad (4)$$

with

$$c = \left(\frac{\sigma(\beta)}{b}\right)^2 = \frac{1}{q-1} , \quad bc = \langle \beta \rangle = \beta_0 , \quad (5)$$

where $2c$ is the actual number of effective degrees of freedom and b is a related parameter. Inserting

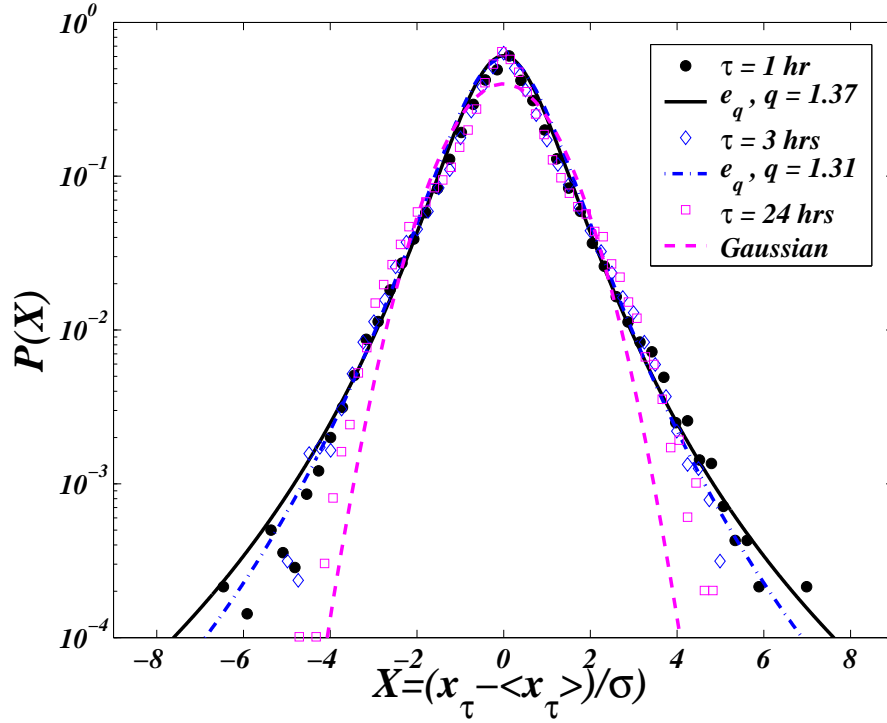


Figure 2: Comparison between standardized longitudinal velocity returns pdfs for three different time intervals ($\tau = 1, 3, 24$ hours) and the q -exponential curves with the q -value extracted from the parameter c of the Gamma distribution shown in the previous figure. A Gaussian pdf is also shown for comparison as dashed curve. See text.

this distribution into the generalized Boltzmann factor (2), one then gets the q -exponential curve [4]

$$P(x) = (1 - (1 - q)\beta_0 E(x))^{\frac{1}{1-q}} . \quad (6)$$

In our case we have $E = \frac{1}{2}x^2$ with x defined by eq.(1) [1, 2, 3]. Considering the fluctuations of the variance σ of the returns x , we get the following correspondence with the original superstatistics formalism

$$\beta = \sigma_\tau \quad , \quad \sigma(\beta) = \Sigma(\sigma_\tau) \quad , \quad \beta_0 = \langle \sigma_\tau \rangle = \sigma_0 \quad . \quad (7)$$

Therefore, for the Gamma distributions which describes the experimental variance fluctuations, we obtain the characteristic value $c = 2.70$ if $\tau = 1$ hour. If $\tau = 3$ hours we get $c = 3.22$. From these values, using eq. (5), we have the corresponding q -values $q = 1.37$ and $q = 1.31$. In Fig.2 we plot the probability density function $P(x)$ of the experimental longitudinal returns for different time intervals, i.e. 1 hour (full circles), 3 hours (open diamonds) and 24 hours (open squares). For comparison we plot a Gaussian distribution (dashed curve) and the q -exponential curves (6) characterized by the q -values extracted from the Gamma distributions for $\tau = 1$ and $\tau = 3$ respectively. The q -exponential curves reproduce very well the experimental data which, on the other hand, are very different from the Gaussian pdf. However one can notice that for a very long time interval, i.e. $\tau = 24$ hours, the data are not so far from being completely decorrelated and therefore the corresponding experimental pdf is closer to the Gaussian curve.

In a similar way one can extract theoretical curves which reproduce the pdfs of the wind velocity differences with similar entropic q -values. In that case, however, an asymmetry correction has to be considered to better reproduce the tails of the pdfs [1, 2].

Conclusions

We have studied a temporal series of wind velocity measurements recorded at Florence airport for a period of six months. The statistical analysis for the velocity components shows strong intermittent fluctuations which exhibit power-law pdfs. Applying the superstatistics formalism, it is possible to extract a Gamma distribution from the probability distributions of the variance fluctuations of wind data. The characteristic parameter c of this Gamma distribution gives the entropic index q of the Tsallis q -exponential distribution, which is then able to reproduce very well the velocity returns and differences pdfs.

Acknowledgements

We would like to thank C. Beck for several discussions.

References

- [1] S. Rizzo and A. Rapisarda, 8th Experimental Chaos Conference, 14-17 June 2004, Florence, Italy, AIP Conference proceedings Vol. 742, p.176, [cond-mat/0406684]; and Proceedings of the International workshop on "Complexity, Metastability and Nonextensivity", C. Beck, G. Benedek, A. Rapisarda and C. Tsallis Eds. World Scientific in press [cond-mat/0502305].
- [2] S. Rizzo and A. Rapisarda, (2005) to be submitted.
- [3] C. Beck and E.G.D. Cohen *Physica A* **322** (2003) 267.
- [4] C. Tsallis *J. Stat. Phys.* **52** (1988) 479. For a recent review see for example C. Tsallis, *Physica D* **193** (2004) 3 and the other papers published in the same volume.
- [5] C. Beck, G.S. Lewis and H.L. Swinney *Phys. Rev. E* **63** (2001) 035303; C.N. Baroud and H.L. Swinney *Physica D* **284** (2003) 21; L.F. Burlaga and A.F. Viñas *Geophysical Research Letters* **31** (2004) L16807.
- [6] S. Jung, H.L. Swinney [cond-mat/0502301].

Interaction of internal gravity waves with a unidirectional shear flow

C. Staquet

Laboratoire des Ecoulements Gophysiques et Industriels,
BP 53 38041 Grenoble cédex 9, France

Abstract

We investigate the interaction of a small-amplitude internal gravity wave packet with a unidirectional shear flow in a stably-stratified rotating fluid. Ray equations and three-dimensional direct numerical simulations of the Boussinesq equations are solved for this purpose. We focus on the situation where the intrinsic frequency Ω of the wave packet increases as the packet propagates into the shear flow, due to the horizontal dependence of this flow. We show that the wave packet is trapped in the neighbourhood of the $\Omega = N$ surface (where N is the local Brunt-Väisälä frequency) and always dissipates there, possibly through breaking. The wave packet is not able to induce any significant effect upon the shear flow except when the latter is inertially unstable.

Geophysical context

Internal gravity wave motions are ubiquitous in stably-stratified fluids, being created by the buoyancy force. In geophysical flows, internal gravity waves generally interact with a large scale shear flow: for instance, the shear flow is the wind in the atmosphere [6] or a current in the ocean [2]. The former case is very common: the blowing of a wind over a mountain range generates lee waves which next interact with the wind. Recent research in the Sun has revealed that the differential rotation that exists in this star creates a very strong shear at the basis of the convective zone, which must interact with the waves that are produced there [23]. How does this shear flow interact with the waves is unknown. An analogous interaction occurs when the waves encounter a temperature (or a density) front. Actually, when Coriolis effects come into play, such a front creates a vertical shear via the thermal wind balance so that the wave interact with both a density front and a shear. And when there is no large scale shear or density front, as in the deep ocean, the wave field interacts with the shear flow it induces.

Ray theory

In the following, we focus upon the interaction of internal gravity waves with a large scale horizontal shear flow \vec{U} , and, when rotation is present, with a density front as well. The medium is assumed to be infinite.

We consider a monochromatic wave of intrinsic frequency Ω and wave vector \vec{k} (or a wave packet with main intrinsic frequency and wave vector Ω and \vec{k}). The intrinsic frequency is the frequency measured in a frame of reference attached to the shear flow. In a stably-stratified medium with constant Brunt-Väisälä frequency N rotating with angular velocity $f/2$, Ω and \vec{k} are linked by the dispersion relation

$$\cos^2\theta = \frac{\Omega^2 - f^2}{N^2 - f^2}, \quad (1)$$

where θ is the angle that \vec{k} makes with the horizontal.

The simplest, and main, effect of the interaction on the internal wave is the change of the intrinsic wave frequency through the Doppler effect:

$$\omega_0 = \Omega + \vec{k} \cdot \vec{U}, \quad (2)$$

ω_0 being the frequency of the source that emits the waves. This source is supposed to be fixed in the frame of reference relative to which \vec{U} is measured. Ω changes as the wave propagates in the changing velocity field, and may approach its lower or upper bound. In this case, further propagation is no longer possible and, in the linear limit, the wave may either be trapped or reflected. Two academic situations are usually considered. Within an atmospheric context, the mean flow is a horizontal wind with a vertical shear $U(z)\vec{i}_x$; within an oceanic context, the mean flow is a horizontal current with a horizontal shear $U(y)\vec{i}_x$.

The change in Ω as the wave packet propagates into the current is most easily predicted within the WKB approximation (see [16], for a very clear presentation of this approximation). This approximation relies upon the assumption that the properties of the fluid medium that affect the wave propagation (\vec{U} and N , in the present case) vary slowly in time and space relative to the wave intrinsic frequency and wavelength respectively. Hence, the medium may be assumed to be uniform and steady over a length scale of order $|\vec{k}|^{-1}$ and over a time of order Ω^{-1} . Under this assumption, the evolution of the wave vector is known along a ray (defined as $d\vec{x}/dt = \vec{c}_g + \vec{U}$) and is driven by the gradients of the ambient velocity and buoyancy fields. In this paper, we shall consider that the fluid medium is steady (*i.e.* $\partial U/\partial t = 0$, $\partial N/\partial t = 0$). In this case, the absolute frequency is constant along a ray: $d\omega_0/dt = 0$, where $d/dt = \partial/\partial t + (\vec{c}_g + \vec{U})\cdot\nabla$ denotes the material derivative following a ray. The equations governing the refraction of the wave vector along a ray, known as the ray equations, are:

$$\frac{dk_i}{dt} = -\frac{\partial\Omega}{\partial N}\frac{\partial N}{\partial x_i} - k_j\frac{\partial U_j}{\partial x_i}, \quad (3)$$

that is, in the present case, with $\mathbf{U} = (U(y, z), 0, 0)$ and $N(y, z)$

$$\frac{dk_x}{dt} = 0 \quad (4)$$

$$\frac{dk_y}{dt} = -\frac{\partial\Omega}{\partial N}\frac{\partial N}{\partial y} - k_x\frac{\partial U}{\partial y}, \quad (5)$$

$$\frac{dk_z}{dt} = -\frac{\partial\Omega}{\partial N}\frac{\partial N}{\partial z} - k_x\frac{\partial U}{\partial z}. \quad (6)$$

As for the relative frequency, it changes along a ray according to the equation

$$\frac{d\Omega}{dt} = -c_{gi}k_x\frac{dU}{dx_i}, \quad (7)$$

where c_{gi} is the component of the group velocity along the direction x_i .

Changes of the wave amplitude are inferred from the conservation of wave action. For any slowly varying background, the action $A = E/\Omega$, where E is the wave-induced energy, satisfies the conservation equation [7]:

$$\frac{\partial A}{\partial t} + \nabla\cdot[(\vec{c}_g + \vec{U})A] = 0. \quad (8)$$

Equation (8) implies that the action contained in a small volume δV moving with the absolute group velocity is conserved, that is

$$\frac{d(A\delta V)}{dt} = 0. \quad (9)$$

The form of the WKB theory we use is the approximation of geometrical optics but, for simplicity, the terminology *WKB approximation* will be employed hereafter.

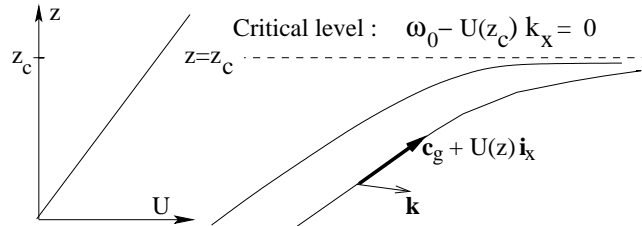


Figure 1: Sketch of a wave packet approaching a critical level $z = z_c$, within the WKB approximation. Two rays are shown in the vertical (x, z) plane, with $\vec{c}_g + U(z)\vec{i}_x$ being the absolute group velocity. The intrinsic frequency of the wave packet at the critical level, $\omega_0 - U(z_c)k_x$ (using the Doppler relation (1)) vanishes there.

Horizontal mean flow with a vertical shear $U(z)\vec{i}_x$

This situation was first investigated without rotation effect, when a wave packet propagates upwards in a vertical shear flow such that its intrinsic frequency decreases. If there exists an altitude at which Ω vanishes, the wave cannot propagate beyond this altitude, known as the critical level. Hence the critical level acts as a wave filter. This level is also defined as the altitude at which the component of the phase velocity of the wave along the wind direction equals the wind velocity (Figure 1).

The first theoretical approach to this problem was performed by Bretherton [6], who considered the Boussinesq equations in a non-rotating frame, linearized about a basic state defined by the wind and a linear stratification, under the WKB approximation. Note that this approximation implies that the Richardson number ($Ri = N^2/(dU/dz)^2$) is much larger than 1 everywhere [16]. For a wave packet approaching the critical level, Bretherton [6] showed that the vertical component of the group velocity c_{gz} decreases as η^2 , where η is the distance of the wave packet to the critical level, while k_z increases as η^{-1} . From the dispersion relation (1), $\Omega \rightarrow 0$ (since k_x and k_y are constant). Even if these results are correct as the critical level is approached, the WKB approximation diverges in the immediate vicinity of that level. The theory predicts that this level is reached in an infinite time (so that there should be no transmitted component) and that the wave-induced energy increases without bound, as η^{-1} .

Relaxing the WKB approximation, but still considering the linearized equations of motions and assuming that the Richardson number is everywhere greater than 0.25, Booker and Bretherton [5] showed that, for a monochromatic wave, momentum is actually transferred from the wave to the mean flow at the critical level, except for a weak transmitted component whose energy is the incident wave energy reduced by the factor $\exp[-2\pi(Ri_c - 1/4)^{1/2}]$, where Ri_c is the value of the Richardson number at the critical level. The transfer of momentum to the mean flow is manifested as a discontinuity in the vertical flux of wave-induced horizontal momentum $\overline{\rho u'w'}(z)$ at the critical level (where the bar denotes an average over a horizontal wavelength); this flux is otherwise constant with altitude in the absence of critical level [9]. No component is reflected in this linear limit.

For a high enough wave amplitude, the incoming wave-induced energy is higher than that absorbed by the shear flow and, consequently, the energy density increases in the neighbourhood of the trapping level. Breaking eventually occurs, thereby partly dissipating the accumulated energy (since momentum is conserved however, momentum will be locally deposited by the breaking waves). This process is well-known to occur in the atmosphere. However [15], there is a subtle effect which implies that, unless viscous effects are too strong, the linear theory always fails after some time: as the wave approaches the critical level, its intrinsic phase velocity decreases faster than the wave-induced velocity along the wind direction does because of absorption so that their ratio, which is one measure of the wave steepness, increases. Hence, breaking may occur as well.

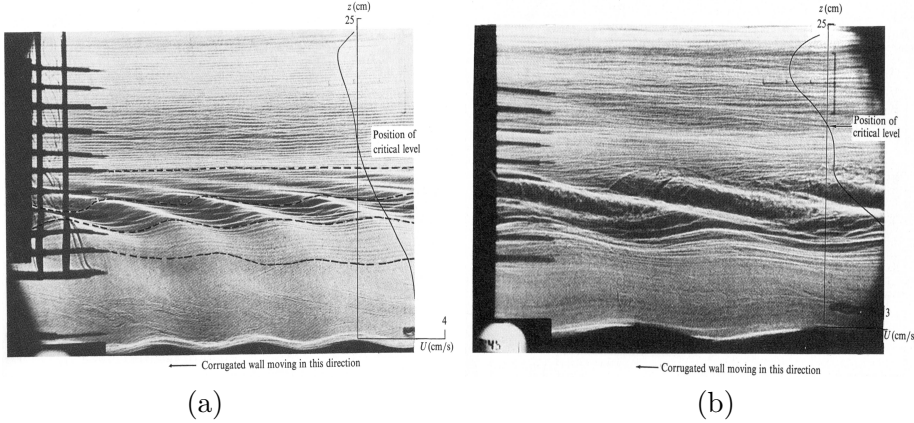


Figure 2: Laboratory experiment of an internal gravity wave interacting with a vertical shear flow. Both the shear flow and the wave field are created by a moving topography. (a) The wave amplitude is small enough for complete absorption of the wave field by the shear flow to occur; (b) for a larger wave amplitude, the wave breaks below the critical level (from [14]).

This situation was studied in detail through several experimental works (f.i. [13], [14]) and is exemplified in Figure 2a for a weak amplitude wave and in Figure 2b for a large amplitude wave. A review of the breaking processes can be found in Staquet and Sommeria [19] and in Staquet [21], [22].

The work of Booker and Bretherton [5] was extended to rotating flows by Jones [11] and by Würtele *et al.* [24]. Using a linearized approach, Jones [11] showed that, in addition to the classical critical level (characterized by $\Omega = 0$), two additional singular levels exist, corresponding to $\Omega = \pm f$. His paper contains another important result: in a rotating fluid, the vertical flux of wave-induced horizontal momentum is no longer conserved (away from the critical level). It should be replaced by the vertical flux of wave-induced angular momentum for this conservation property to hold again (away from the singular levels). Würtele *et al.* [24] further showed that the wave becomes evanescent in the neighbourhood of the critical level (since the wave can only propagate for $\Omega^2 > f^2$) so that the only effective singular levels are those where $\Omega^2 = f^2$. Würtele *et al.* [24] also investigated numerically the situation of a time developing wave, being emitted from a source at $t = 0$. In this case, the singularity develops in time as well: at early times, the propagating wave crosses the $\Omega = f$ (for instance) level and decays in the evanescent region. As time elapses and the wave reaches a steady state (*i.e.* its amplitude becomes constant), the singularity develops but non linear effects develop as well. As a result, the wave breaks in the neighbourhood of the singular level and a reflected component is emitted; the wave would be absorbed at the singular level in a linear regime. These results are thus analogous to those found by Booker and Bretherton [5] at a critical level in a non rotating fluid. Würtele *et al.* [24] also showed that the behaviour is notably different for a continuous spectrum of frequencies (such as a lee wave generated by a flow over an arbitrary topography), in which case no singular behaviour is encountered.

In the discussion above, the monochromatic wave propagates in the shear flow so that its intrinsic frequency *decreases*. When the wave propagates in a shear flow so that its intrinsic frequency *increases*, it reflects onto the horizontal plane where $\Omega = N$, in the linear limit. Jones [12] showed that overreflection occurs when the local Richardson number is smaller than 0.25 somewhere, that is, the shear flow is potentially unstable; the wave extracts energy from that flow when reflecting. When nonlinear effects come into play (due to the high initial amplitude of the wave for instance) and the background shear flow is stable, Sutherland [18] showed that a horizontally periodic wave packet

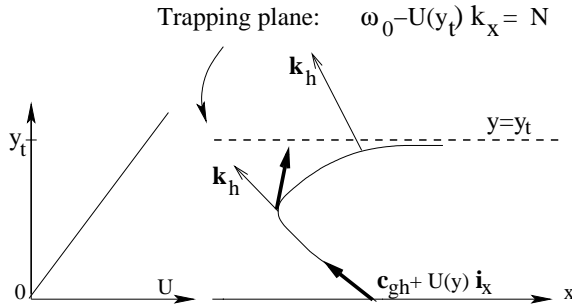


Figure 3: Sketch of a wave packet approaching a trapping plane, within the WKB approximation, and propagating against the current ($\vec{k} \cdot \vec{U} = k_x U < 0$). Two rays are shown in the horizontal (x, y) plane, with $\vec{c}_{gh} + U(y)\vec{i}_x$ being the component of the absolute group velocity in that plane. The intrinsic frequency of the wave packet, $\omega_0 - U(y_t)k_x$, from the Doppler relation, is equal to the Brünt-Väisälä frequency at the trapping plane (adapted from [20]).

permanently deposits momentum to the mean flow at altitudes close to and below the reflecting level; when the wave packet is horizontally compact, a substantial part of the finite amplitude wave packet energy may be transmitted.

Horizontal mean flow with a horizontal shear $U(y)\vec{i}_x$

Theoretical results.

The behaviour of an internal gravity wave packet in a horizontally sheared current $U(y)\vec{i}_x$ was studied thirty years ago within an oceanographic context, using the linear theory in the WKB approximation [10], [16], [4], [1], [3]. Coriolis effects are ignored in all studies except in Olbers' work. When the wave packet enters into the current and propagates against it so that its intrinsic frequency increases (Eq. (7) with $x_i = y$), it cannot propagate beyond the position y_t at which $\Omega = N$. The mean flow being barotropic, this position actually is a vertical plane if N is constant; this plane is hereafter referred to as the trapping plane (Figure 3).

Since the properties of the medium in which the wave propagates vary only with y , k_x and k_z remain unchanged (as well as ω_0 as already noted, because the medium is steady). From the linear dispersion relation (1), one easily infers that k_y goes to infinity as $\Omega \rightarrow N$. More precisely, it can be shown from WKB theory that $k_y \sim \eta^{-1/2}$ as $\eta \rightarrow 0$, where η refers again to the distance of the wave packet to the trapping plane; moreover, $c_{gy} \sim \eta^{3/2}$ and $c_{gx}, c_{gz} \rightarrow 0$ as well [20]. The latter property implies that the wave packet slows down in the neighbourhood of the trapping plane so that its energy density locally increases (in other words, the wave-induced energy accumulates in the neighbourhood of this plane). However, the WKB theory also predicts that this energy tends to infinity ($E \sim \eta^{-3/2}$) and that the trapping plane is reached in an infinite time. As in the critical level situation, the two latter results are unphysical and stem from the failure of the WKB theory in the immediate vicinity of the trapping plane. Olbers [16] actually noted that, if $E \sim \eta^{-\mu}$, the asymptotic behaviour of the wave is regular or singular depending upon whether $\mu < 1$ or $\mu \geq 1$. In the former case, the wave reaches the plane in a finite time, and this plane is for instance a reflexion plane. In the latter case, the wave reaches the plane in an infinite time; very strong gradients of the wave-induced Reynolds stress form in the close neighbourhood of the plane, which yield momentum exchange with the mean flow. Information upon the actual wave behaviour when $\mu \geq 1$ can be obtained by solving the linearized equations of motions. Ivanov and Morozov [10] thus found that the total wave-induced energy may

indeed increase, as opposed to the critical level situation studied by Booker and Bretherton [5]. In this situation, *momentum is transferred from the shear flow to the wave*, so that the potential for wave breaking exists. The three-dimensional numerical study of Staquet and Huerre [20], whereof a summary is provided below, shows that an inertia-gravity wave packet may indeed break in the neighbourhood of a trapping plane.

When the wave propagates along the current such that its intrinsic frequency decreases, k_y decreases as well. If k_y decays down to zero, Ω reaches a minimum value Ω_{min} , obtained by setting k_y to 0 in the dispersion relation. The behaviour of the wave as $\Omega \rightarrow \Omega_{min}$ may be guessed by using WKB theory. Note that the theory becomes less and less valid as the plane gets closer since the wavelength along the y -direction increases. Assuming that the theory remains valid, $k_y \sim \eta^{1/2}$, $c_{gy} \sim \eta^{1/2}$ and $E \sim \eta^{-1/2}$ as $\eta \rightarrow 0$. Here, according to Olbers [16], $\mu = 1/2$ so that the $\Omega = \Omega_{min}$ plane is a reflexion plane for the wave.

Öllers *et al.* [17] solved numerically the equation for the amplitude of a hydrostatic internal gravity wave emitted away from the shear flow and propagating toward it. The wave behaviour (transmitted, reflected, over-reflected) depends upon the stability of the shear flow. When the latter flow is inertially stable, the wave is always reflected, with a possible transmitted component. When the shear flow is inertially unstable by contrast, over-reflection is possible, with a reflection coefficient up to 3.25 (for the case considered in the paper). One may wonder whether a high enough reflexion coefficient would not lead to the instability of the reflected wave. Note the analogy between this behaviour and that found by Jones [12] for an unstable vertical shear flow.

Numerical results.

The behaviour of a wave packet in a rotating, constant- N medium propagating into a barotropic shear flow $U(y)\vec{i}_x$ has been investigated numerically by Staquet and Huerre [20]. The shear flow consists of a horizontal shear layer (with a tanh profile) while the wave packet is a plane wave whose amplitude is modulated by a gaussian function along the y -direction. The parameters of the wave (its wave vector), of the shear flow (its maximum amplitude) and of the medium (the Brunt-Väisälä and Coriolis frequencies) are chosen so that (i) the wave intrinsic frequency increases as the wave propagates in the shear flow and (ii) a trapping plane exists.

The wave behaviour is illustrated in Figure 4 for a cyclonic shear flow (that is, the vorticity of the shear flow is of the same sign as the Coriolis frequency). Constant contours of the density field are displayed at successive times in a vertical (y, z) plane. At $t = 0$ (Figure 4a), the wave packet is hardly visible due to its small steepness ($s = 0.26$). Because the horizontal shear flow does not displace the isopycnals, it is not visible either. Since N is constant, the trapping plane is a vertical plane and its intersection with the (y, z) plane is marked with a vertical line in the Figure. The wave packet exhibits two major changes as it propagates toward the shear flow: the isopycnals steepen and the wave amplitude increases. The former effect is accounted for by noting that, as k_y increases, the incompressibility condition reduces to $k_y u_y + k_z u_z \simeq 0$. Hence, the vector (k_y, k_z) is perpendicular to the phase lines in the (y, z) plane. Since $k_y \rightarrow +\infty$ while k_z remains constant, the phase lines steepen. The second effect results from the trapping of the wave. The local increase of the wave amplitude makes the wave packet break (Figure 4e) and small-scale motions are produced. The latter motions are quickly dissipated however because the primary wave packet is not forced. As well, the shear flow is hardly modified by the momentum deposit that occurs during wave breaking.

The stage of the flow that follows breaking dramatically changes when the shear flow is anticyclonic (Figure 5). Indeed, in this situation, the shear flow is subjected to an inertial instability, through which small-scale motions are most amplified. The point is that the small-scale motions resulting from wave breaking act as a perturbation to the shear flow, which triggers the instability. The medium is therefore

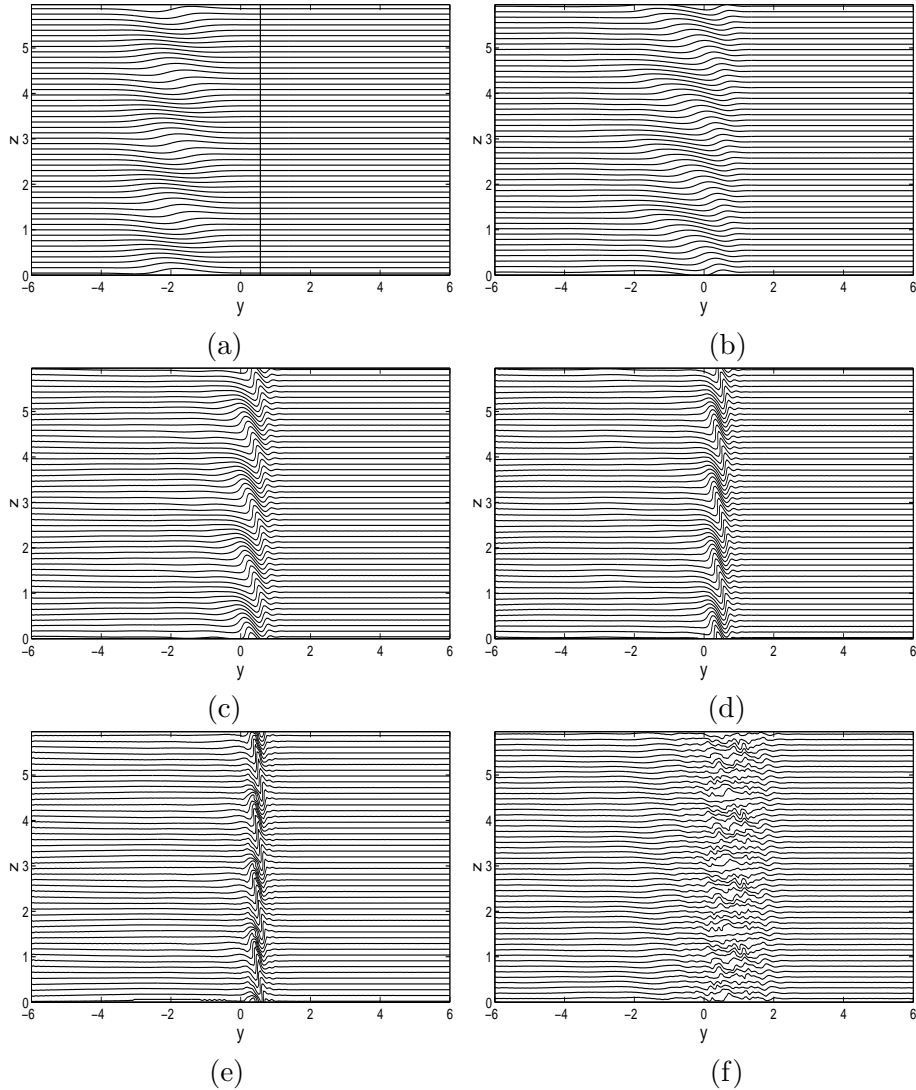


Figure 4: Interaction of a wave packet (confined along the y -direction only) with a barotropic cyclonic shear layer. Constant contours of the density field are displayed at successive times, expressed in Brunt-Väisälä periods; (a) $t = 0$, (b) $t = 1.9$, (c) $t = 3.8$, (d) $t = 4.6$, (e) $t = 5.6$, (f) $t = 11.4$. The vertical line in frame (a) marks the trapping plane.

considerably modified by the breaking of the wave in this situation, because it initiates the inertial instability of the (very energetic) shear flow. The latter instability results in momentum and mass transport: the shear of the background flow is weakened and a passive scalar is transported across the trapping plane, namely across the shear flow [20].

Horizontal mean flow with both a horizontal and a vertical shear

What does happen if a wave packet in a stably-stratified rotating medium interacts with a (thermal wind) balanced shear flow $\vec{U}(y, z)$ involving both a horizontal and a vertical shear? As discussed above, the situation is not simple. For instance, when the intrinsic frequency Ω increases and approaches N , the wave packet should be reflected by the vertical shear $\partial U/\partial z$ but trapped by the horizontal shear

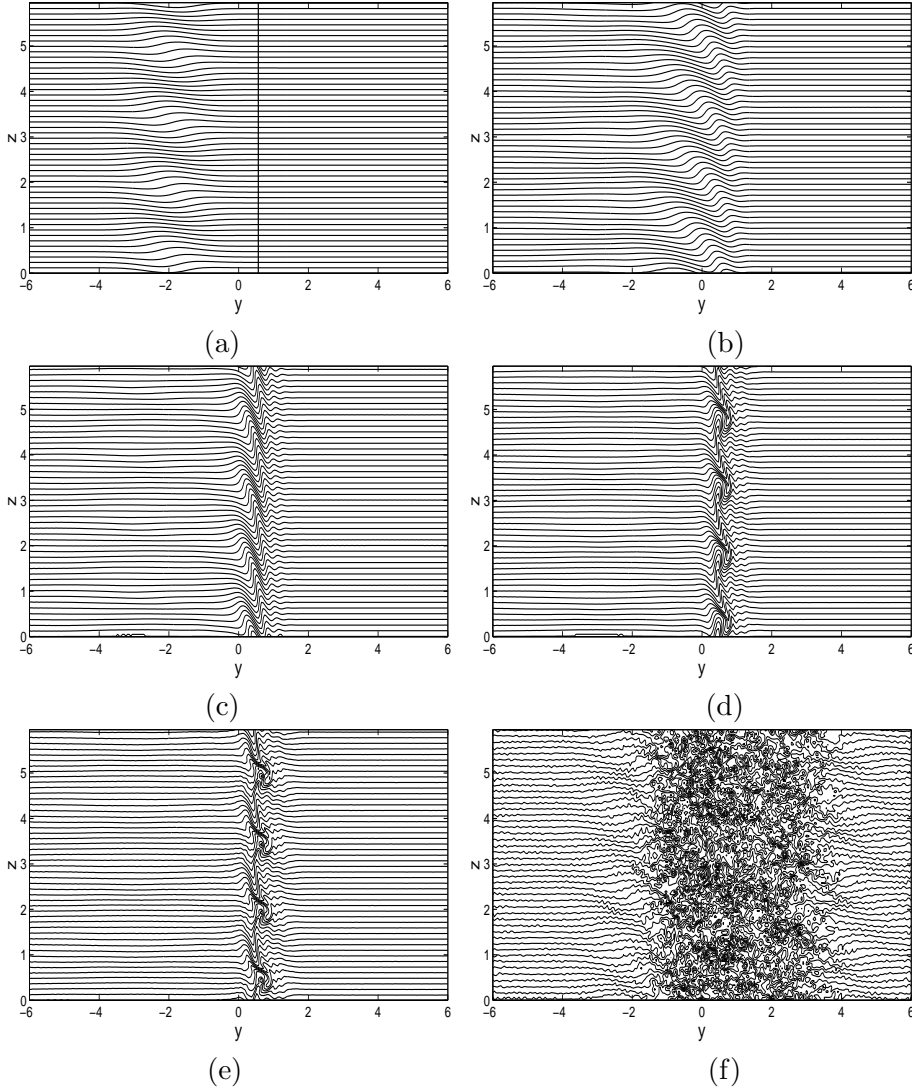


Figure 5: Interaction of a wave packet (confined along the y -direction only) with a barotropic anticyclonic shear layer. Constant contours of the density field are displayed at successive times, expressed in Brunt-Väisälä periods (a) $t = 0$, (b) $t = 1.9$, (c) $t = 3.8$, (d) $t = 4.6$, (e) $t = 4.8$, (f) $t = 9.4$. The vertical line in frame (a) marks the trapping plane (from [20]).

$\partial U / \partial y$. Also, since the shear flow satisfies the thermal wind balance, a buoyancy field $B(y, z)$ exists as well such that $f \frac{\partial U}{\partial z} = -\frac{\partial B}{\partial y}$.

We have investigated this situation in a simple context, when a wave packet confined both in the y and z directions interacts with a horizontal shear layer with a sinusoidal vertical dependency [8]. We chose the parameters such that Ω first increases because of the horizontal shear of the background flow. We explored the parameter range by solving the ray equations and performed three-dimensional direct numerical simulations (DNS) to investigate the influence of nonlinear effects on the behaviour of the wave packet.

A general behaviour is observed in the WKB theory, which is illustrated in Figure 6. The ray trajectories are displayed in frame (a) and the intrinsic frequency Ω is plotted versus time in frame

(b). In frame (a), the wave packet at initial time is represented by a set of twenty rays aligned along two perpendicular segments. The $\Omega = N$ surface, plotted with a thick dashed line, displays two important locations when the interaction with the shear flow is considered: (i) where the local radius of curvature is minimum, corresponding to a maximum value of $\partial U/\partial y$ (location 1) and where the local radius of curvature is maximum, corresponding to a minimum value of $\partial U/\partial y$ (location 2). In the former case, the $\Omega = N$ surface is nearly vertical and is a trapping surface; in the latter case, the surface is nearly horizontal and is reflecting. All rays propagate toward the $\Omega = N$ surface and reach it, either in the neighbourhood of location 1 or of location 2. In the former case (location 1), the rays are trapped at the surface and propagate along it downward, with a nearly vertical group velocity, toward location 2. Note that the group velocity has strongly decreased when location 1 is reached. All rays sooner or later reach location 2 and reflect there. The rays then propagate in the interior of the shear flow within a wave guide made by the $\Omega = N$ surface. Frame (a) also displays grey points, at which the steepness of the wave packet exceeds 1. This suggests that breaking may occur there, resulting in irreversible mass and momentum transport. Note however that WKB theory is no longer valid at the trapping plane (and at a reflecting surface) and that, most importantly as we shall see, molecular effects have been ignored in this analysis.

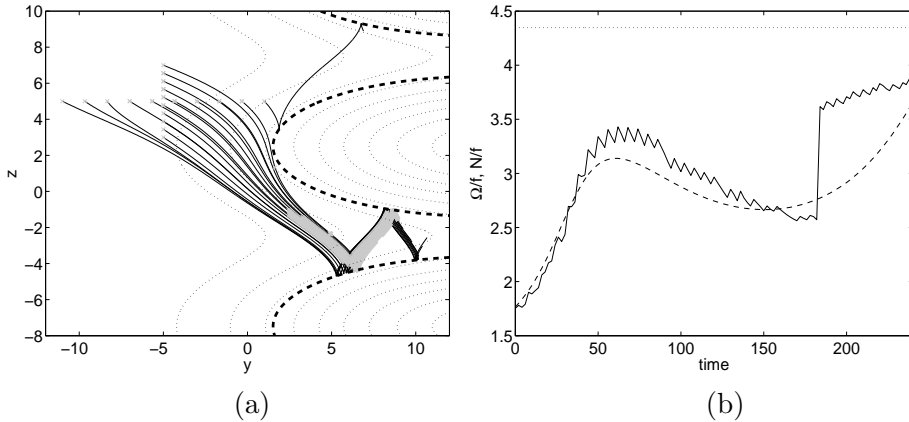


Figure 6: WKB predictions. (a) Trajectories of rays at $t = 127.3$ BVP (Brunt-Väisälä period) in a vertical (y, z) plane. The rays start from the initial wave packet location. The thick dashed line marks the intersection of the $\Omega = N$ trapping surface with the (y, z) plane and dotted lines represent contours of the shear flow velocity $U(y, z)$. Light grey circles are plotted at each time the steepness along a given ray exceeds the value of 1. (b) Temporal evolution of the intrinsic frequency Ω of the wave packet normalized by the Coriolis frequency f . Dashed line: WKB prediction for a central ray; solid line: DNS result at the packet centre; dotted line: N/f . Results are compared over the duration of the DNS ($t=240$, that is 38.2 BVP) (from [8]).

DNS results are displayed in Figure 7 through constant contours of the fluctuating buoyancy field b' about the background field B . It should be stressed that the steepness of the wave packet is twice smaller than in the barotropic case and that the varying horizontal shear ($\partial U/\partial y$) is smaller by a factor 16. Hence, the wave-shear interaction, which scales like $s^2 \partial U/\partial y$, is smaller by a factor 50. The interaction between the shear flow and the wave packet is therefore weak and one may consider that the buoyancy fluctuations displayed in Figure 7 solely belong to the wave field. The DNS behaviour is close to the WKB prediction up to the time the wave packet reaches the trapping surface at location 2 (at $t \simeq 176 \simeq 28$ BVP). This is attested in frame b) where the intrinsic frequency predicted by WKB theory and the numerical simulation are compared. Molecular effects deeply change the subsequent wave packet behaviour in the DNS, for two reasons. First, k_y increases as the packet approaches the trapping surface, implying that small scales along the y -direction are produced. These small scales

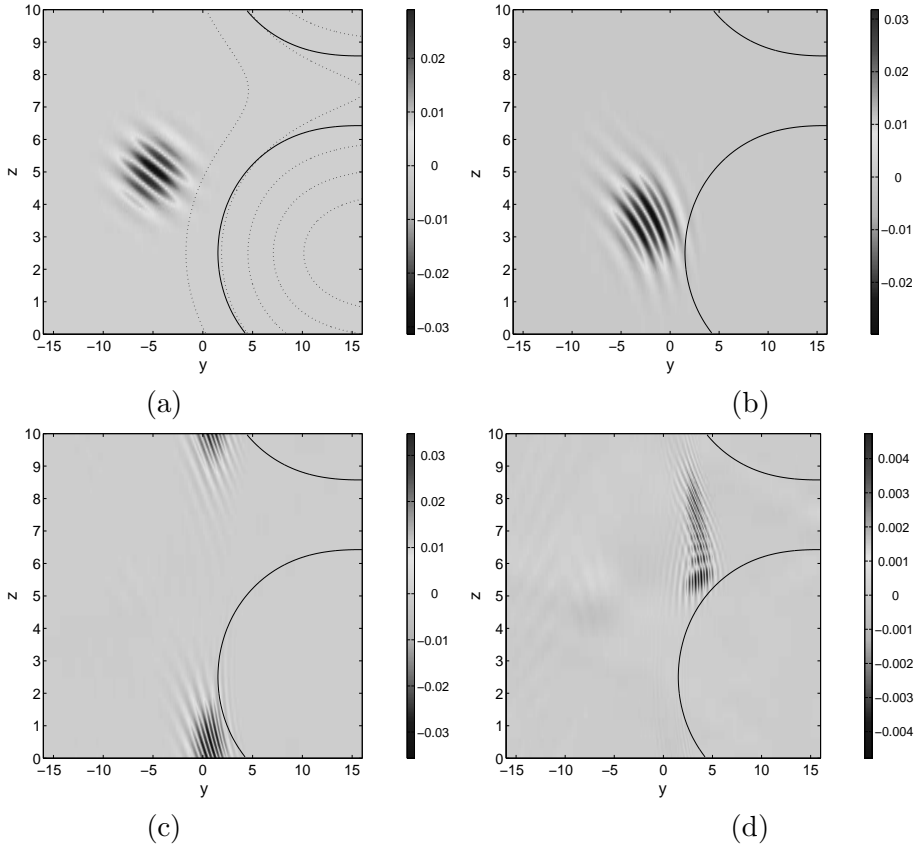


Figure 7: DNS results. Constant contours of the fluctuating buoyancy field b' are plotted in a vertical (y, z) plane at successive times (in unit of Brunt-Väisälä period): (a) $t=0$; (b) $t=8.9$, (c) $t=13.4$, (d) $t=28$. In frame (a), dotted lines represent contours of the shear flow velocity $U(y, z)$. The surface $\Omega = N$ is displayed with a solid line on all frames (from [8]).

are very sensitive to molecular effects. The second reason, connected to the first, is that the packet slows down as it approaches the trapping plane, which makes it also prone to molecular effects. As a consequence, the nearly steady, small-scale packet is dissipated locally and does not penetrate into the wave guide.

Conclusion

A single internal gravity wave packet interacting with an inertially stable shear flow is unlikely to modify its environment: in the cases we consider, the wave packet is trapped by the shear flow and dissipates locally, possibly through breaking. In geophysical flows however, waves are most often generated by a permanent source (like the interaction of the tide with the topography in the ocean) or, at least, are emitted during a long time with respect to their intrinsic period. Since the wave packet slows down as it approaches the trapping surface, a continuous emission of such packets would result in their superposition in the neighbourhood of the trapping surface, and possibly in stronger mean flow changes. We also showed that an entirely different behavior is observed when the shear flow is inertially unstable (a situation which may occur at the equator), because the breaking wave triggers the instability.

Despite the academic character of our study, a geophysical implication of our work can be proposed. Thus, because the waves are unable to cross the shear flow and are dissipated in its neighbourhood, we

expect weaker internal gravity wave activity to be found inside large-scale geophysical vortices than outside.

Acknowledgements

Computations have been performed at the french computer center IDRIS.

References

- [1] Badulin SI, Shrira VI and Tsimring LS 1985. The trapping and vertical focusing of internal waves in a pycnocline due to the horizontal inhomogeneities of density and currents. *J. Fluid Mech.* 158:199–218.
- [2] Badulin SI, Vasilenko VM and Golenko NN 1990. Transformation of internal waves in the equatorial Lomonosov current. *Atmospheric and Oceanic Physics.* 26 (2):110–117.
- [3] Badulin SI and Shrira VI 1993. On the irreversibility of internal-wave dynamics due to wave trapping by mean flow inhomogeneities. Part 1. Local analysis. *J. Fluid Mech.* 251:21–53.
- [4] Basovich AY and Tsimring LS 1984. Internal waves in a horizontally inhomogeneous flow. *J. Fluid Mech.* 142:233–249.
- [5] Booker JR and Bretherton FP 1967. The critical layer for internal gravity waves in a shear flow. *J. Fluid Mech.* 27:513–539.
- [6] Bretherton FP 1966. The propagation of groups of internal gravity waves in a shear flow. *Quart. J. Roy. Met. Soc.* 92:466–480.
- [7] Bretherton FP 1968. Propagation in slowly varying wave guides. *Proc. Roy. Soc. London* A302:555–577.
- [8] Edwards NRE and Staquet C 2005. Focusing of an inertia-gravity wave packet by a baroclinic shear flow. *Dynamics Atmos. Oceans* 40:91–113.
- [9] Eliassen A and Palm E 1961. On the transfer of energy in stationary mountain waves. *Geofys. Pub.* 22:1-23.
- [10] Ivanov YA and Morozov YG 1974. Deformation of internal gravity waves by a stream with horizontal shear. *Okeanologie* 14:457–461.
- [11] Jones WJ 1967. Propagation of internal gravity waves in fluids with shear flow and rotation. *J. Fluid Mech.* 30:439–449.
- [12] Jones WJ 1968. Reflexion and stability of waves in stably stratified fluids with shear flow: a numerical study. *J. Fluid Mech.* 34:609–624.
- [13] Koop CG 1981. A preliminary investigation of the interaction of internal gravity waves with a steady shearing motion. *J. Fluid Mech.* 113:347–386.
- [14] Koop CG and McGee B 1986. Measurements of internal gravity waves in a continuously stratified shear flow. *J. Fluid Mech.* 172:453-480.
- [15] McIntyre ME 2000. On global-scale atmospheric circulations. In *Perspectives in Fluid Dynamics*, ed GK Batchelor, HK Mofatt, MG Worster, Cambridge University Press, 557–624.

- [16] Olbers DJ 1981. The propagation of internal waves in a geostrophic current. *J. Phys. Oceanogr.* 11:1224–1233.
- [17] Öllers MC, Kamp LPJ, Lott F, Van Velthoven PFJ, Kelder HM and Sluijter FW 2003. Propagation properties of inertia-gravity waves through a barotropic shear layer and application to the Antarctic polar vortex. *Quart. J. Roy. Met. Soc.*, 129-B:2495.
- [18] Sutherland BR 2001. Finite-amplitude internal wave-packet dispersion and breaking. *J. Fluid Mech.* 429:343–380.
- [19] Staquet C and Sommeria J 2002. Mixing by breaking internal gravity waves: from instabilities to turbulence. *Annual Reviews Fluid Mech* 34:559-593.
- [20] Staquet C and Huerre G 2002. On transport across a barotropic shear flow by breaking inertia-gravity waves. *Phys. Fluids* 14(6):1993–2006.
- [21] Staquet C 2004. Gravity and inertia-gravity internal waves: breaking processes and induced mixing. *Surveys in Geophysics*, 25(3-4):281–314.
- [22] Staquet C 2005. Internal gravity waves in geophysical fluids. *CISM Lecture Notes* No 288, Springer-Verlag, to appear.
- [23] Talon S, Kumar P and Zahn JP 2002. Angular Momentum Extraction by Gravity Waves in the Sun. *Astrophys. J. Letters*, 574:L175–L178.
- [24] Wurtele MG, Datta A and Sharman RD 1996. The propagation of gravity-inertia waves and lee waves under a critical level. *J. Atmos. Sciences*, 53(11):1505.

A Level Set Based Flamelet Model for the Prediction of Combustion in Spark Ignition Engines

J. Ewald, N. Peters

Institut für Technische Mechanik, RWTH Aachen University
Templergraben 64, D-52056 Aachen, Germany

Abstract

A Flamelet Model based on the Level Set approach for turbulent premixed combustion is presented. The original model [11, 12] is enhanced in order to consistently model the evolution of the premixed flame from laminar into a fully developed turbulent flame. This is accomplished by establishing a linear relationship between the thickness of the turbulent flame brush and the turbulent burning velocity. Starting from there a model for the initial flame propagation of a spherical spark kernel immediately after ignition and for the flame propagation in 3D space is derived. In contrast to other models, the same physical modeling assumptions are employed for the phase initially after spark ignition and for the later phases of flame propagation. The model is applied to a test case in an homogeneous charge Spark Ignition (SI) engine.

Introduction

With respect to laminar premixed flames, Williams [19] postulated a kinematic equation for the advection of the laminar flame based on the scalar G . The laminar approach then was subsequently extended by Peters [10] to turbulent premixed flames. Due to the kinematic Level Set approach employed, the turbulent burning velocity s_T is model input into the kinematic equation and not a reaction rate defined per unit volume. This approach therefore overcomes problems in case that the (laminar or turbulent) flame thickness becomes small in comparison to the numerical grid used in the problem simulation and in that limit, the reaction rate would become a delta peak, which is difficult to be integrated numerically. Furthermore the interaction of the different physical phenomena of diffusion and reaction that establish the structure of the premixed flame are physically correctly represented by employing the burning velocity which is an eigenvalue of the premixed problem posed [9].

The first turbulent combustion model was then refined [11] by sub-dividing the flamelet combustion regime into the corrugated flamelets regime, in which large scale turbulence is active and the thin reaction zones regime, in which small scale turbulence dominates. In the latter regime, the smallest turbulent scales act on the laminar flamelet. This is the cause of the so-called bending effect, by which a decrease of the turbulent burning velocity is predicted for smaller Damkehler numbers.

The turbulent G -Equation concept was already successfully used for Spark Ignition (SI) Engine applications, cf. Dekena *et al.* [5] or Tan *et al.* [16, 15]. In these works, two different models, one for spark ignition and the phase immediately thereafter, and the other for the propagation of the fully turbulent developed flame at later stages of the combustion process were used. The spark ignition models in both cases predict lower turbulent burning velocities for the developing turbulent flame kernel than the turbulent burning velocity expression in [11] which assumes a fully developed flame. After a user given time period, the models are switched to the latter model equation.

In this work, a unified approach for the flame propagation during the phase immediately after ignition and one the turbulent flame is developed is presented. The key idea is to consistently relate the thickness of the turbulent flame brush to the turbulent burning velocity. Immediately after ignition

the thickness of the turbulent flame brush is zero – except for the laminar flame thickness – and laminar flame propagation is predicted.

The unified approach then is cast into two different numerical representations, one for the numerical integration in 3D space on the numerical grid of the problem. The other representation assumes the spark kernel to be spherical which allows for a grid-independent description of the developing spark, therefore overcoming to a certain extent the necessity to refine the computational grid at the position of ignition. Also, due to the geometry of the spark kernel assumed, effects of kernel curvature can easily be assessed.

Unsteady Premixed Combustion Model

The turbulent premixed combustion flamelet model by Peters [11, 12] is based on three quantities which are \tilde{G} , the mean flame front position, the variance of the flame brush $\widetilde{G''^2} = \ell_{f,t}^2$ which is related to the turbulent flame thickness $\ell_{f,t}$, and the turbulent flame surface area ratio $\tilde{\sigma}_t$.

At the mean flame front position $\tilde{G} = G_0$, the kinematic equation

$$\langle \rho \rangle \frac{\partial \tilde{G}}{\partial t} + \langle \rho \rangle \nabla \tilde{G} \cdot \tilde{\mathbf{u}} = \langle \rho \rangle D_t' \tilde{\kappa} |\nabla \tilde{G}| + \widetilde{(\rho s_T)} |\nabla \tilde{G}| \quad (1)$$

is applied while outside of this surface the distance constraint $|\nabla \tilde{G}| = 1$ is imposed. Since eqn. (1) is pertinent to the class of Level Sets, appropriate numerical solving techniques need to be employed, cf. [2, 13, 8]. The two terms on the r.h.s. are due to the modeling of the turbulent flame propagation. The last term describes the averaged turbulent mass burning rate $\widetilde{(\rho s_T)}$ and the first influences due to curvature $\tilde{\kappa} \equiv \nabla \cdot (\nabla \tilde{G} / |\nabla \tilde{G}|)$ of the mean front.

The equation for the variance is modeled in analogy to the variance equation for a passive scalar [12]

$$\langle \rho \rangle \frac{\partial \widetilde{G''^2}}{\partial t} + \langle \rho \rangle \nabla \widetilde{G''^2} \cdot \tilde{\mathbf{u}} = \nabla \cdot \left(\langle \rho \rangle D_t \nabla \widetilde{G''^2} \right) + 2 \langle \rho \rangle D_t (\nabla \tilde{G})^2 - c_s \langle \rho \rangle \widetilde{G''^2} \frac{\varepsilon}{k} \quad (2)$$

with the last two terms on the r.h.s. being the turbulent production and dissipation, respectively.

The relationship between the turbulent burning velocity s_T and the flame propagation of the laminar flamelet s_L is established by $\tilde{\sigma}_t$ as:

$$s_T = (1 + \tilde{\sigma}_t) s_L . \quad (3)$$

Here, $\tilde{\sigma}_t$ is determined by an algebraic equation to be

$$\tilde{\sigma}_t = \frac{\ell_{f,t}}{\ell_f} \left\{ - \frac{b_3^2}{4b_1} \sqrt{\frac{3c_\mu c_s}{Sc_t}} + \sqrt{\frac{b_3^4}{16b_1^2} \frac{3c_\mu c_s}{Sc_t} + \frac{c_s b_3^2}{2} \frac{\ell_f \varepsilon}{s_L k}} \right\}, \quad (4)$$

which establishes a linear relationship between the ratio of the turbulent to laminar flame thickness $\ell_{f,t}/\ell_f$ and the turbulent flame surface area ratio. The term in braces is only dependent on properties of the laminar flamelet and the turbulent time scale of the flow. The expression (4) has been chosen such that for $\ell_{f,t}$ being in equilibrium with the integral length scale of the surrounding flow, turbulent burning velocity expressions as presented in [12] again are recovered. The laminar flame thickness is defined with respect to the ratio of the thermal conductivity and the heat capacity of the flame, evaluated at the position at the inner layer of the flame:

$$\ell_f = \frac{1}{\rho_u s_L} \frac{\lambda}{c_p} \Big|_0, \quad (5)$$

Symbol	Value	definition/origin
a_4	0.37	Bray [3]
b_1	2.0	experimental data [1]
b_3	1.0	experimental data [4]
c_0	0.44	$= C_{\varepsilon_1} - 1$, [11]
c_1	4.63	DNS, [18]
c_2	1.01	$= \sqrt{\frac{3c_\mu c_s}{4\text{Sc}_t} \frac{c_1 b_3^2}{b_1}}$
c_3	4.63	$= c_1 b_3^2$
c_s	2.0	[10, 11]
Sc_t	0.7	

Table 4: Constants for the level set based turbulent premixed combustion model.

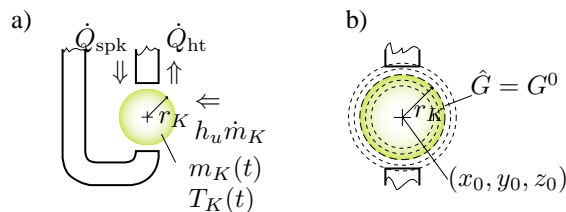


Figure 1: a) Energy balance between the spark plug electrodes and the spark kernel. b) Connection between spark kernel radius r_K and filtered \hat{G} -field.

where ρ_u indicates the unburnt gas mixture density and ‘0’ refers to the inner layer position.

The turbulent diffusivity in the curvature term of eqn. (1) in this work is expressed in analogy to a mixing length approach as

$$D'_t = \sqrt{\frac{c_\mu c_s}{2\text{Sc}_t}} \ell_{f,t} k^{1/2}, \quad (6)$$

therefore the magnitude of the modification of the turbulent burning velocity due to curvature of the mean flame front is dependent on the thickness of the turbulent flame. The constants in eqn. (6) again are chosen such that for a state of equilibrium with the turbulent flow, the standard relationship for the turbulent diffusivity of a scalar, $D_t = \nu_t/\text{Sc}_t$, is obtained.

Spark ignition modeling

For the spark ignition model, the same physical modeling assumptions are used as for turbulent premixed flame propagation in 3D space with respect to the turbulent burning velocity and the expression for the variance (2). Additionally, kernel expansion effects due to electrical spark energy and the effect of kernel curvature will be accounted for. The thermodynamical analysis is carried out similar to Tan [17]. As a first approximation of the model it is assumed that the initial spark kernel is spherical with a given initial position and radius. During the growth of this kernel to a fully turbulent flame the kernel will be assumed to be subjected to convection of the background flow.

The energy balance depicted in figure 1a reads

$$\dot{Q}_{\text{spk}} + \dot{Q}_{\text{chem}} - \dot{Q}_{\text{ht}} = \frac{dH}{dt} - h_u \dot{m}_K - V \frac{dp}{dt}, \quad (7)$$

where H represents the spark thermal and plasma enthalpy. \dot{Q}_{spk} denotes the gross electrical energy transfer from the electrodes and \dot{Q}_{ht} the heat loss to the electrodes. \dot{Q}_{chem} accounts for the heat release caused by combustion. h_u denotes the specific enthalpy of the unburnt gas mixture which is added to the spark by (laminar or turbulent) flame propagation through the mass stream \dot{m}_K .

The effect of spark energy deposited into the kernel and heat losses to the electrodes are related to each other thus forming an effectivity coefficient η_{eff} , in the following assumed to be approximately 0.3:

$$\dot{Q}_{\text{ht}} \approx (1 - \eta_{\text{eff}})\dot{Q}_{\text{spk}}. \quad (8)$$

The equation of continuity gives the following ordinary differential equation for the increase of spark kernel mass:

$$\frac{dm_K}{dt} = \dot{m}_K = 4\pi r_K^2 \rho_u s_{T,\kappa}. \quad (9)$$

Here r_K is the radius of the kernel and $s_{T,\kappa}$ an expression for the flame propagation which takes into account the turbulent burning velocity and the effect of laminar and turbulent kernel curvature as done in equation (1). The radius can be readily obtained by

$$r_K = \sqrt[3]{\frac{3m_K}{4\pi\rho_b}}; \quad (10)$$

however, the density of the gas in the spark ρ_b needs to be known which is – depending on ignition conditions – lower than the density of adiabatically burned gas due to plasma effects of the electrical energy which cause an increased kernel temperature. In order to approximate this temperature T_K eqn. (7) needs to be further modified.

The derivative of the kernel enthalpy gives

$$\frac{dH}{dt} = \dot{m}_K h_K + \dot{h}_K m_K \quad (11)$$

and the heat release due to premixed combustion can be expressed as

$$\dot{Q}_{\text{spk}} = \dot{m}_K (h_{\text{ad}} - h_u). \quad (12)$$

The burning velocity $s_{T,\kappa}$ – modified by curvature effects – can be deduced from (1), in which the curvature of the spherical kernel amounts to $\kappa = 2/r_K$.

$$s_{T,\kappa} = s_T - \frac{2}{r_K} D'_t \quad (13)$$

An equation describing the thickness of the flame brush can be deduced from (2) by assuming uniform turbulent profiles:

$$\frac{d\widetilde{G}_{\text{spk}}''^2}{dt} = 2\hat{D}_{t,\text{spk}} - c_s \frac{\varepsilon}{\hat{k}_{\text{spk}}} \widetilde{G}_{\text{spk}}''^2 \quad (14)$$

For engine combustion $\widetilde{G}_{\text{spk}}''^2 = \widehat{G}_{\text{spk}}''^2 = 0$ as initial condition. The spark only sees only those turbulent eddies which are smaller equal diameter of the eddy itself. When the flame kernel reaches a specified size $r_{K,\text{end}}$, the model is switched to the 3D equations.

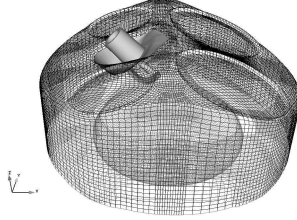


Figure 2: Unstructured computational grid of the closed engine geometry highlighting the modeled spark plug. This mesh comprises 302,000 grid cells.

Bore	86 mm
Stroke	86 mm
Displacement	0.5 L
Compression Ratio	10.3
Engine speed	2000 rpm
MAP	95 kPa
Intake mixture:	propane/air w. $\phi = 0.6$
Spark Timing	40BTDC
Spark Energy	60 J/s
Initial Spark Radius	$r_{K,0} = 1$ mm

Table 5: Operating parameters of the engine

Results

Basis of the model computation is a optical test engine operated in homogeneous charge mode fueled with a lean propane/air mixture [6]. The operating parameters are listed in table 5. The numerical computations were carried out by the code AC-FluX by Advanced Combustion GmbH, a Finite Volume based CFD simulation tool that operates on unstructured meshes and is able to perform adaptive local grid refinement during calculation.

The simulation was carried out employing two meshes, one with the intake ports modeled. After intake valve closure, the calculation was interrupted at 90 degrees Crank Angle before Top Dead Center ($^{\circ}$ CA BTDC) and the solution at this time step was mapped onto a new grid featuring a closed geometry which is shown in figure 2.

For the laminar flamelet calculation, laminar burning velocity correlations according to Mller *et al.* [7] were employed with a correction of the burnt gas temperature in order to account for the effects of rest gas in the previous cycle, which was assumed here otherwise as inert. For the flame diffusivity λ/c_p , the correlation for hydrocarbons due to [14] was used as basis.

In figure 3, a comparison of measured and calculated cylinder pressure is depicted. In figure 4 both the evolution of the mean flame front surface and the global mass burning rate are plotted. It can be seen, even although both quantities cannot be directly compared to each other quantitatively, the increase in mass burning is preceded by the increase in surface of the mean flame front. This can be explained by the fact that initially, flame propagation is close to laminar and it takes approximately 5° CA after ignition to develop turbulent flame propagation. The area of the mean flame front surface $\tilde{G} = G_0$ increases until about -3° CA while the heat release increases until approx. 2° CA after Top Dead Center (ATDC). This can be explained by most parts of the flame coming into contact with the wall region. After that, another increase of mean flame front surface can be observed, which does not

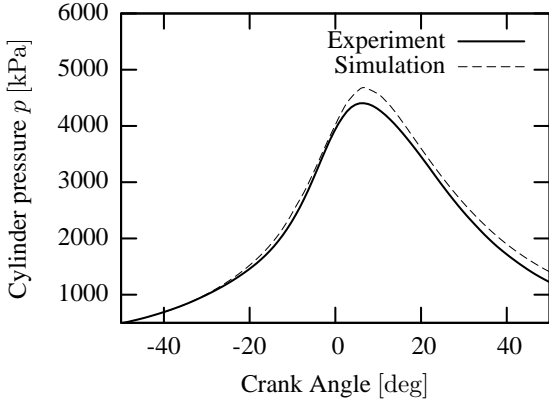


Figure 3: Comparison of cylinder pressures

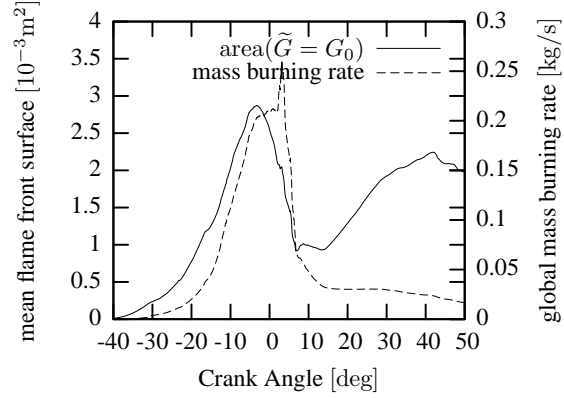


Figure 4: Plot of the mean flame front surface (measured on the left ordinate) and the global mass burning rate (measured on the right ordinate) during the combustion phase.

contribute to a repeated increase in flame surface because the flame propagates in the squish region. Shortly after Top Dead Center (TDC), a sharp peak in mass burning rate is observed. 3D image analysis of the simulation shows that at TDC (see figure 8b) in the in-cylinder region opposing the spark plug a substantial area of the mean flame front surface is visible that is rapidly reduced by flame propagation when the flame burns out in this region and continues to propagate into the squish region further. This observation is also supported by the slope of the $\text{area}(\tilde{G} = G_0)$ plot in figure 4, which shows at the same time a steep decrease.

These observations are also supported by the results displayed in fig. 5. The quantity \dot{m}'' is equal to the mass burning rate (ρs_T), averaged on the total mean flame surface area. Also the turbulent flame surface area ratio $\tilde{\sigma}_t$ is averaged over the total mean flame surface area. It can be seen that the profile of $\tilde{\sigma}_t$ predicts the evolution of the laminar flame kernel into a moderately turbulent flame to take place within 5°CA . As a comparison, the turbulent time scale k/ε at the spark plug immediately prior to ignition spans for this engine speed 13°CA . Immediately after Top Dead Center, both maximum values of averaged $\tilde{\sigma}_t$ and mass burning rates are reached which coincide with the location of maximum heat release.

The main mechanism that drives the development of the turbulent flame can be explained by the comparison of the turbulent flame brush thickness $\ell_{f,t}$ with the turbulent length scale. In order to facilitate the comparison, a turbulent length scale is defined for this purpose assuming production=dissipation and neglecting the temporal and spatial derivatives in eqn. (2). The result is the ‘‘algebraic flame brush thickness’’

$$\ell_{f,t,\text{alg}} \equiv \sqrt{\frac{2c_\mu}{c_s S c_t} \frac{k^{3/2}}{\varepsilon}}. \quad (15)$$

Both the turbulent length scale and the flame brush thickness are again averaged over the mean flame front surface area and therefore describe the turbulent scale that the flame sees. Both quantities are increasing in time, while the turbulent flame brush thickness due to the initial condition starts at zero and remains smaller than the turbulent length until immediately after TDC. This is explained by the spatial distribution of the turbulent scales, which are small in vicinity to the wall and also in the region of the spark plug and increase towards the inner region of the combustion chamber. The flame therefore is ignited in regions where small turbulent eddies prevail and then later on expands

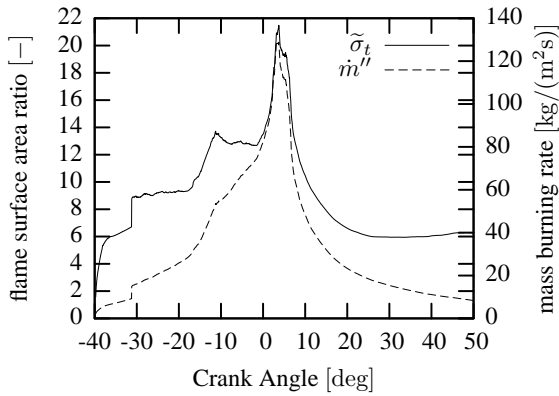


Figure 5: Qualitative comparison of turbulent flame surface area ratio $\tilde{\sigma}_t$ area weight averaged on the $\tilde{G} = G_0$ surface (left ordinate) and the area weight averaged flame surface area mass burning rate \tilde{m}'' (right ordinate).

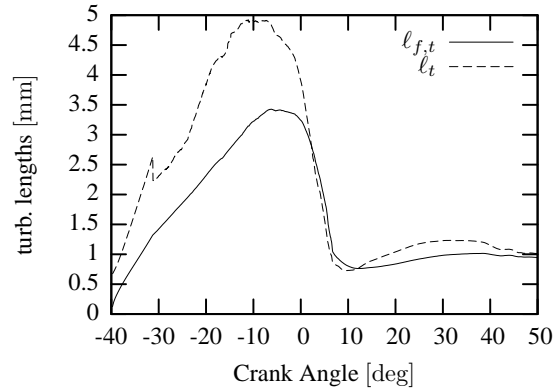


Figure 6: Comparison of turbulent flame brush thickness $l_{f,t}$ and turbulent length scale $l_{f,t,alg}$ averaged on the mean flame front surface.

into regions with larger turbulent eddies. The turbulent flame brush thickness requires time to follow that increase in turbulent length.

The combustion regime in which the engine operates in that mode is depicted in figure 7. The ratios v'/s_L and $l_{f,t,alg}/l_f$ are logarithmically averaged over the mean flame front surface. The average of these quantities indicate that the combustion predominantly takes place in the corrugated flamelets regime [11]. Until TDC the dimensionless turbulence intensity v'/s_L remains approximately constant. After this point, this quantity decreases again since the flame burns out close to the wall and propagates in the squish region.

Acknowledgements

The authors gratefully acknowledge the contribution of the engine data by Andreas Lippert, Todd Fansler, and Michael Drake and the computational mesh by Mark Huebler, all from the Powertrain Systems Research Lab, General Motors R&D in Warren, MI.

References

- [1] R. G. Abdel-Gayed and D. Bradley. A two-eddy theory of premixed turbulent flame propagation. *Phil. Trans. of the Royal Soc. of London A*, 301(1457):1–25, 1981.
- [2] D. Adalsteinsson and J. A. Sethian. The fast construction of extension velocities in level set methods. *Journal of Computational Physics*, 148:2–22, 1999.
- [3] K. N. C. Bray. Studies of the turbulent burning velocity. *Proc. Roy. Soc. Lond., A* 431:315–335, 1990.
- [4] G. Damköhler. Der Einfluss der Turbulenz auf die Flammgeschwindigkeit in Gasgemischen. *Zeitschr. f. Elektrochemie*, 46(11):601–626, 1940.
- [5] M. Dekena and N. Peters. Combustion modeling with the G -Equation. *Oil & Gas Sci. Tech. – Rev. IFP*, 54(2):265–270, 1999.

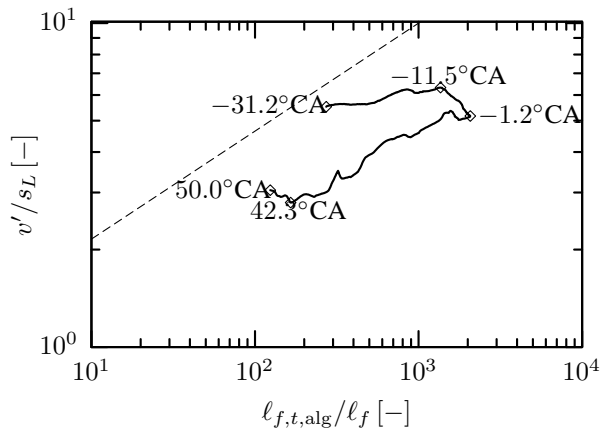


Figure 7: Combustion regime diagram. The dashed line indicates the boundary between the corrugated flamelets which is on the lower right section of the plot and the thin reaction zones regime at the upper left.

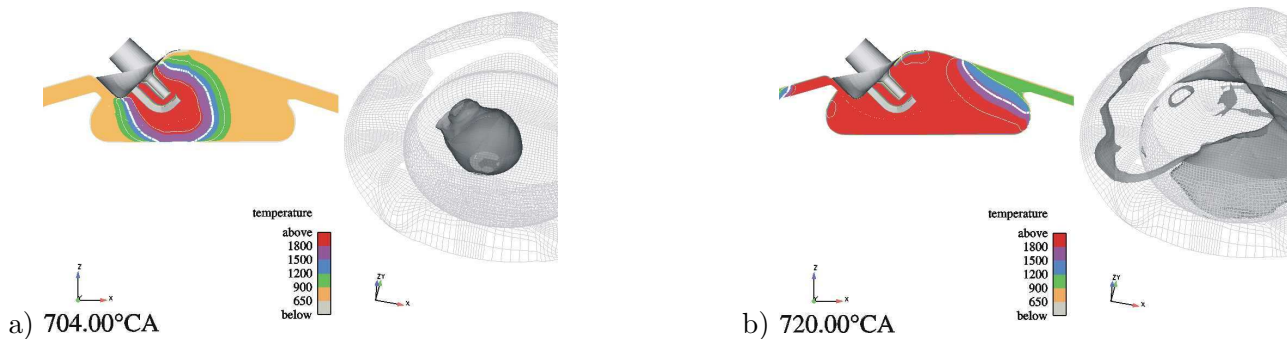


Figure 8: Two plots of the combustion progress in the engine each at two different crank angle degrees. On the left plots a vertical cut through the center of the chamber, showing the spark plug geometry is displayed along with the color coded mean temperature. By solid white lines both the mean flame front $\tilde{G} = G_0$ (thick line) and the boundary of the flame brush region (thin lines) is displayed).

- [6] A. M. Lippert, T. D. Fansler, and M. C. Drake. High-speed imaging and CFD modeling of sprays and combustion in a spray-guided spark ignition direct injection engine. In *6th Int. Symp. on Internal Combustion Diagnostics*, Baden-Baden, Germany, June 15–16 2004.
- [7] U. C. Müller, M. Bollig, and N. Peters. Approximations for burning velocities and markstein numbers for lean hydrocarbon and methanol flames. *Combust. Flame*, 108:349–356, 1997.
- [8] S. Osher and R. Fedkiw. *Level Set Methods and Dynamic Implicit Surfaces*. Springer, 2003.
- [9] N. Peters. *Fifteen Lectures on Laminar and Turbulent Combustion*. Ercoftac Summer School, September 14-28 1992. Institut für Technische Mechanik, RWTH Aachen, 1992.
- [10] N. Peters. A spectral closure for premixed turbulent combustion in the flamelet regime. *J. Fluid Mech.*, 242:611–629, 1992.
- [11] N. Peters. The turbulent burning velocity for large scale and small scale turbulence. *J. Fluid Mech.*, 384:107–132, 1999.
- [12] N. Peters. *Turbulent Combustion*. Cambridge University Press, 2000.
- [13] J. A. Sethian. Fast marching methods. *SIAM Review*, 41(2):199–235, 1999.
- [14] M. D. Smooke and V. Giovangigli. Formulation of the premixed and nonpremixed test problems. In M. D. Smooke, editor, *Reduced Kinetic Mechanisms and Asymptotic Approximations for Methane-Air Flames*, volume 384 of *Lecture Notes in Physics*, pages 1–28. Springer-Verlag, 1990.
- [15] Z. Tan, S. C. Kong, and R. D. Reitz. Modeling premixed and direct injection SI engine combustion using the G -equation model. *SAE Technical Paper Series*, no. 2003-01-1843, 2003.
- [16] Z. Tan and R. Reitz. Modeling ignition and combustion in spark-ignition engines using a level set method. *SAE Technical Paper Series*, no. 2003-01-0722, 2003.
- [17] Z. Tan and R. D. Reitz. Development of G -Equation combustion model for direct injection SI engine simulations. In *13th Int. Multidim. Engine Modeling User's Group Meeting*, Detroit, MI, March 2 2003.
- [18] H. Wenzel. *Direkte numerische Simulation der Ausbreitung einer Flammenfront in einem homogenen Turbulenzfeld*. Dissertation, RWTH Aachen University, 2000.
- [19] F. A. Williams. Turbulent combustion. In J. Buckmaster, editor, *The Mathematics of Combustion*, pages 97–131. SIAM, Philadelphia, 1985.

Broken symmetry and coherent structure in MHD turbulence

J.V. Shebalin

NASA Johnson Space Center, Houston, Texas 77058 USA

Abstract

The statistical theory of ideal magnetohydrodynamic (MHD) turbulence is extended to cases with and without rotation, and with and without a mean magnetic field. One notable result is the discovery of a new ideal invariant, the ‘parallel helicity,’ which arises when rotation and mean magnetic field vectors are aligned. Numerical results from several long-time simulations of five general cases on a 32^3 grid are presented. The basic equations and statistical theory are symmetric under the parity or charge reversal transformations. However, the presence of invariant cross, magnetic or parallel helicity dynamically breaks this symmetry, because these helicities are pseudoscalars under parity or charge reversal (or both). The basic theoretical result is that ideal MHD turbulence is, in general, non-ergodic due to the decomposability of the constant energy surface in phase space. This non-ergodicity can be manifested in the appearance of coherent structure as long as magnetic or parallel helicity is invariant. The fact that MHD turbulence inherently contains coherent structure in certain general cases may have important implications for dynamo theory.

Introduction

In this paper we study ideal (*i.e.*, non-dissipative), homogeneous, three-dimensional (3-D), incompressible, magnetohydrodynamic (MHD) turbulence in a rotating frame of reference with and without a mean magnetic field. Ideal MHD turbulence without rotation and without a mean magnetic field has energy, cross helicity and magnetic helicity as invariant integrals, but rotation removes cross helicity and a mean magnetic field removes magnetic helicity from the set of invariant integrals. However, there is a new invariant integral which arises when the angular velocity of rotation and the mean magnetic field are both non-zero and collinear. This new invariant will be called the *parallel helicity* and it is a linear combination of the cross and magnetic helicities.

Absolute equilibrium ensemble theory for these various cases of ideal MHD turbulence (with and without rotation, and with and without a mean magnetic field) is presented here. The theory is generally non-ergodic, due to the presence of invariant helicities, and this non-ergodicity can be manifested in the appearance of coherent structure, although this is not necessary. Here, the five general cases of ideal, magnetized, rotating MHD turbulence are examined, both analytically and by numerical simulation. Although real (*i.e.*, dissipative) turbulence is not considered here, recent numerical simulations have demonstrated that real 2-D MHD turbulence appears to have behavior similar to that seen in the ideal limit [Shebalin 2005]

The results presented here may have relevance to a number of physical systems. Rotating, magnetized MHD turbulence seems to arise within and around the earth, the sun, distant stars, and other astrophysical plasmas, as well as in magnetically confined laboratory plasmas. In the present work, we assume that the source of the mean magnetic field is fixed with respect to rotation, *e.g.*, a global solar magnetic field that permeates relatively small, local regions within the solar convection zone. While large-scale processes in the sun have been investigated elsewhere [Brun 2004, Fan 2004], the physical arenas we wish to study are small regions, within an extensive magneto-fluid, where turbulence can be considered homogeneous and incompressible, and where an externally imposed, constant magnetic field can be considered to be co-rotating with the small volume of interest.

To reiterate, the homogeneous MHD turbulence considered in this paper is *ideal*. Dissipation is, of course, critical in realistic rotating, magnetized MHD turbulence, and various aspects of such flows have been studied by many authors (see, for example, [Canuto 1986]). However, an investigation of dissipative 3-D MHD turbulence with particular regard to symmetry and ergodicity is beyond the scope of this work, and will, for the present, be deferred. Nevertheless, the results presented in this paper may still be relevant to real turbulence, since the most important effects to be demonstrated manifest themselves most strongly at the smallest dynamical wave numbers of the flow, *i.e.*, the largest eddies, where dissipation has the weakest effect.

Basic Equations

The non-dimensional form of the MHD equations in a rotating frame of reference with constant angular velocity $\boldsymbol{\Omega}_o$ and a mean (*i.e.*, uniform and constant) magnetic induction \mathbf{B}_o are

$$\frac{\partial \boldsymbol{\omega}}{\partial t} = \nabla \wedge [\mathbf{u} \wedge (\boldsymbol{\omega} + 2\boldsymbol{\Omega}_o) + \mathbf{j} \wedge (\mathbf{b} + \mathbf{B}_o)] + \nu \nabla^2 \boldsymbol{\omega}, \quad (1)$$

$$\frac{\partial \mathbf{b}}{\partial t} = \nabla \wedge [\mathbf{u} \wedge (\mathbf{b} + \mathbf{B}_o)] + \eta \nabla^2 \mathbf{b}. \quad (2)$$

(See, for example, [Lesieur 1997] and [Biskamp 2003]. Also, in the above and following sets of equations, ‘ \wedge ’ denotes the vector cross product.)

In addition to equations (1) and (2), we also have

$$\begin{aligned} \nabla \cdot \mathbf{u} &= 0, & \boldsymbol{\omega} &= \nabla \wedge \mathbf{u}, \\ \nabla \cdot \mathbf{b} &= 0, & \mathbf{j} &= \nabla \wedge \mathbf{b}. \end{aligned} \quad (3)$$

In equations (1), (2) and (3), \mathbf{u} , $\boldsymbol{\omega}$, \mathbf{b} and \mathbf{j} are the turbulent velocity, vorticity, magnetic induction and electric current density, respectively, of the magneto-fluid. (The equations of rotating Navier-Stokes fluid turbulence arise if $\mathbf{b} = \mathbf{B}_o = 0$.)

If we set $\nu = 0$ in (1) and $\eta = 0$ in (2), we obtain the equations of ‘ideal’ MHD turbulence. While any real flows have $\nu \neq 0$ and $\eta \neq 0$, a study of ideal turbulence produces some interesting theoretical results that may help in understanding aspects of real turbulence, particularly at larger scales of the flow where dissipation is minimal. In the next two sections we will examine some theoretical considerations, and following these, the numerical solution of eqs. (1) and (2).

Ideal MHD Turbulence

At this point, it is useful to ‘uncurl’ eq. (1), to produce the velocity equation for MHD turbulence:

$$\frac{\partial \mathbf{u}}{\partial t} = -\nabla p' + \mathbf{u} \wedge (\boldsymbol{\omega} + 2\boldsymbol{\Omega}_o) + \mathbf{j} \wedge (\mathbf{b} + \mathbf{B}_o) + \nu \nabla^2 \mathbf{u}. \quad (4)$$

Here, the ‘total pressure’ is $p' = p + \frac{1}{2} u^2 - \frac{1}{2} (\mathbf{r} \wedge \boldsymbol{\Omega}_o)^2$, where p is the thermodynamic pressure and the last term in p' is the centrifugal potential. The pressure can, as usual, be determined by taking the divergence of both sides of eq. (4) and solving the resulting Poisson’s equation. In doing so, there is an ambiguity related to the choice of origin for \mathbf{r} , but this does not effect the dynamics of the homogeneous, incompressible magneto-fluid.

Let us define the vector potential \mathbf{a} by $\mathbf{b} = \nabla \wedge \mathbf{a}$ and $\nabla \cdot \mathbf{a} = 0$. We can then uncurl eq. (2) to produce an equation for \mathbf{a} :

$$\frac{\partial \mathbf{a}}{\partial t} = -\nabla \Phi + \mathbf{u} \wedge (\mathbf{b} + \mathbf{B}_o) + \eta \nabla^2 \mathbf{a}. \quad (5)$$

In eq. (5), Φ is the electric potential.

Next, define the volume average of a quantity $\phi(\mathbf{r})$ in a periodic box of side length 2π as

$$[\phi] \equiv (2\pi)^{-3} \int \phi(\mathbf{r}) d^3x. \quad (6)$$

Since all functions are periodic, we can use equations (1) through (6), along with integration by parts to derive the following relations:

$$\frac{dE}{dt} = -2(\nu\Omega + \eta J), \quad (7)$$

$$\frac{dH_C}{dt} = \mathbf{\Omega}_o \cdot [\mathbf{b} \wedge \mathbf{u}] - \frac{1}{2}(\nu + \eta) [\mathbf{j} \cdot \boldsymbol{\omega}], \quad (8)$$

$$\frac{dH_M}{dt} = \mathbf{B}_o \cdot [\mathbf{b} \wedge \mathbf{u}] - \eta [\mathbf{j} \cdot \mathbf{b}]. \quad (9)$$

Above, we have the (volume-averaged) energy E , enstrophy Ω , mean-squared current J , cross helicity H_K and magnetic helicity H_M :

$$E = \frac{1}{2} [u^2 + b^2], \quad \Omega = \frac{1}{2} [|\boldsymbol{\omega}|^2], \quad J = \frac{1}{2} [|\mathbf{j}|^2], \quad (10)$$

$$H_C = \frac{1}{2} [\mathbf{u} \cdot \mathbf{b}], \quad H_M = \frac{1}{2} [\mathbf{a} \cdot \mathbf{b}]. \quad (11)$$

At this point we note that if $\mathbf{\Omega}_o = \sigma \mathbf{B}_o$, *i.e.*, if $\mathbf{\Omega}_o$ and \mathbf{B}_o are non-zero and parallel, then eq. (8) can be added to $-\sigma$ times eq. (9) to yield

$$\frac{dH_P}{dt} = -\frac{1}{2}(\nu + \eta) [\mathbf{j} \cdot \boldsymbol{\omega}] - \eta [\mathbf{j} \cdot \mathbf{b}], \quad H_P \equiv H_C - \sigma H_M. \quad (12)$$

The quantity H_P will be called the ‘parallel helicity.’

When $\nu = \eta = 0$, equations (7), (8), (9) and (12) lead us immediately to the invariant integrals for MHD turbulence for various values of \mathbf{B}_o and $\mathbf{\Omega}_o$. First, if $\mathbf{B}_o = \mathbf{\Omega}_o = 0$, then E , H_C and H_M are all constant. Second, if $\mathbf{B}_o \neq 0$ but $\mathbf{\Omega}_o = 0$, then E and H_C are constant, but not H_M . Third, if $\mathbf{B}_o = 0$ but $\mathbf{\Omega}_o \neq 0$, then E and H_M are constant, but not H_C . Fourth, if $\mathbf{B}_o \neq 0$ and $\mathbf{\Omega}_o \neq 0$, with $\mathbf{B}_o \wedge \mathbf{\Omega}_o \neq 0$, then only E is constant. Fifth, if $\mathbf{B}_o \neq 0$ and $\mathbf{\Omega}_o \neq 0$, with $\mathbf{\Omega}_o = \sigma \mathbf{B}_o$, then E and H_P are the only constants of the motion. The parallel helicity H_P is a new invariant for 3-D MHD turbulence, one that occurs only when \mathbf{B}_o and $\mathbf{\Omega}_o$ are non-zero and collinear.

These various cases are placed in Table 6 for easier reference. Note that Case II can be thought of as a particular example of Case V, one for which $\sigma = 0$, while Case III can be thought of as another example of Case V, one for which $\sigma \rightarrow \infty$. Thus, we see that as a mean field is applied or an overall rotation is imposed or both, the number of invariants drop from three to two to one.

Absolute Equilibrium Ensembles

As is well known, the existence of integral invariants allows ideal MHD turbulence to be described by Gibbsian statistical mechanics. The theory was initiated by [Lee 1952], partially developed by [Kraichnan 1973, 1975], [Frisch 1975] and [Fyfe 1976], and then extended by [Shebalin 1982, 1983, 1989, 1996, 2002] and [Stribling 1990]. The physical fields \mathbf{u} and \mathbf{b} are represented by truncated

Case	Mean Field	Rotation	Invariants
I	$\mathbf{B}_o = 0$	$\boldsymbol{\Omega}_o = 0$	E, H_C, H_M
II	$\mathbf{B}_o \neq 0$	$\boldsymbol{\Omega}_o = 0$	E, H_C
III	$\mathbf{B}_o = 0$	$\boldsymbol{\Omega}_o \neq 0$	E, H_M
IV	$\mathbf{B}_o \neq 0$	$\boldsymbol{\Omega}_o \wedge \mathbf{B}_o \neq 0$	E
V	$\mathbf{B}_o \neq 0$	$\boldsymbol{\Omega}_o = \sigma \mathbf{B}_o$	E, H_P

Table 6: Invariants for ideal MHD turbulence ($H_P \equiv H_C - \sigma H_M$).

Fourier series, whose coefficients are the ‘interacting particles’ of the canonical ‘absolute equilibrium ensemble’:

$$\mathbf{u}(\mathbf{x}) = \sum_{0 < |\mathbf{k}| \leq K} \tilde{\mathbf{u}}(\mathbf{k}) e^{i\mathbf{k} \cdot \mathbf{x}}, \quad (13)$$

$$\mathbf{b}(\mathbf{x}) = \sum_{0 < |\mathbf{k}| \leq K} \tilde{\mathbf{b}}(\mathbf{k}) e^{i\mathbf{k} \cdot \mathbf{x}}. \quad (14)$$

The wave vectors \mathbf{k} in k-space have integer components between $-N/2$ and $+N/2$, while the corresponding discrete set of position vectors \mathbf{x} in x-space have components that are integer multiples of $2\pi/N$, where N is the number of grid points in each dimension. The ‘isotropic truncation’ radius is K , which is chosen to ensure that retained coefficients fit within a sphere in k-space; the exact value of K is dictated by algorithmic requirements [Patterson 1971]. Since \mathbf{u} and \mathbf{b} are both real, their coefficients satisfy a ‘reality condition’, *e.g.*, $\tilde{\mathbf{u}}(\mathbf{k}) = \tilde{\mathbf{u}}^*(-\mathbf{k})$, where ‘*’ denotes complex conjugation. Thus, only half of the \mathbf{k} in the sums (13) and (14) are independent. Let the total number of \mathbf{k} in these sums be \mathcal{N} , so that the number of independent \mathbf{k} is

$$\mathcal{N}' = \frac{1}{2} \sum_{0 < |\mathbf{k}| \leq K} 1 = \frac{1}{2} \mathcal{N}. \quad (15)$$

The number \mathcal{N}' will appear again in later formulas.

The probability distribution function D of the absolute equilibrium ensemble, for Case I in Table 6, has the form

$$D \sim \exp(-\alpha E - \beta H_C - \gamma H_M). \quad (16)$$

The function D is normalized by requiring that its integral over the whole phase space defined by the independent Fourier coefficients be unity. In regard to the other cases in Table 6, eq. (16) applies as follows: Case II, set $\gamma = 0$; Case III, set $\beta = 0$; Case IV, set $\beta = \gamma = 0$; and in Case V, set $\gamma = -\sigma\beta$, so that eq. (16) becomes

$$D \sim \exp(-\alpha E - \beta H_P). \quad (17)$$

Thus, to determine various ensemble predictions for Cases II through V in Table 6, we merely take previously determined results for Case I ([Frisch 1975], [Shebalin 1989, 1994, 2002], [Stribling 1990]) and substitute for β and γ as indicated above.

Using (16), ensemble predictions for moments of the $\tilde{\mathbf{u}}(\mathbf{k})$ and $\tilde{\mathbf{b}}(\mathbf{k})$ can now be made for the different cases in Table 6. Denoting the ensemble prediction of a quantity $Q(\mathbf{k})$ by $\langle Q(\mathbf{k}) \rangle$, the predicted first-order moments are $\langle \tilde{\mathbf{u}}(\mathbf{k}) \rangle = \langle \tilde{\mathbf{b}}(\mathbf{k}) \rangle = 0$ for all cases. The ensemble predictions for second-order moments are given in Table 7 for the five cases listed in Table 6.

Case	$\langle \tilde{\mathbf{u}}(\mathbf{k}) ^2 \rangle$	$\langle \tilde{\mathbf{b}}(\mathbf{k}) ^2 \rangle$
I	$\frac{3\alpha(\delta^2 - \gamma^2/k^2)}{\delta^4 - \alpha^2\gamma^2/k^2}$	$\frac{3\alpha\delta^2}{\delta^4 - \alpha^2\gamma^2/k^2}$
II	$3\alpha/\delta^2$	$3\alpha/\delta^2$
III	$3/\alpha$	$\frac{3\alpha}{\alpha^2 - \gamma^2/k^2}$
IV	$3/\alpha$	$3/\alpha$
V	$\frac{3\alpha(\delta^2 - \sigma^2\beta^2/k^2)}{\delta^4 - \sigma^2\alpha^2\beta^2/k^2}$	$\frac{3\alpha\delta^2}{\delta^4 - \sigma^2\alpha^2\beta^2/k^2}$

Table 7: Second-order moments ($\delta^2 = \alpha^2 - \beta^2/4$).

In Table 7, the modal expectation values are for $|\tilde{\mathbf{u}}(\mathbf{k})|^2 = |\tilde{\mathbf{u}}_R(\mathbf{k})|^2 + |\tilde{\mathbf{u}}_I(\mathbf{k})|^2$ and $|\tilde{\mathbf{b}}(\mathbf{k})|^2 = |\tilde{\mathbf{b}}_R(\mathbf{k})|^2 + |\tilde{\mathbf{b}}_I(\mathbf{k})|^2$, and the real and imaginary parts of these have equal share (*i.e.*, one half of the expected values in Table 7). Also, the expectation values of the modal helicities are

$$\langle \tilde{\mathbf{u}}_S(\mathbf{k}) \cdot \tilde{\mathbf{b}}_S(\mathbf{k}) \rangle = -\frac{\beta}{2\alpha} \langle |\tilde{\mathbf{b}}_S(\mathbf{k})|^2 \rangle, \quad S = R, I \quad (18)$$

$$\langle \tilde{\mathbf{a}}_S(\mathbf{k}) \cdot \tilde{\mathbf{b}}_S(\mathbf{k}) \rangle = \alpha \langle |\tilde{\mathbf{u}}_S(\mathbf{k})|^2 - |\tilde{\mathbf{b}}_S(\mathbf{k})|^2 \rangle.$$

The second-order moments in Table 7 are functions of the inverse temperatures α , β and γ , which must be determined. Previous work ([Shebalin 1989, 1994, 2002]) has shown that α , β and γ can be expressed in terms of one variable parameter, which can be chosen to be the expectation value of the magnetic energy $\mathcal{E}_M = \langle E_M \rangle$, where $E_M = \frac{1}{2} [|\mathbf{b}|^2]$. Using $\mathcal{E} = \langle E \rangle$, $\mathcal{H}_C = \langle H_C \rangle$ and $\mathcal{H}_M = \langle H_M \rangle$, we have for Case I,

$$\alpha = \frac{3\mathcal{N}'\mathcal{E}_M}{\mathcal{E}_M(\mathcal{E} - \mathcal{E}_M) - \mathcal{H}_C^2}, \quad (19)$$

$$\beta = -2\alpha \frac{\mathcal{H}_C}{\mathcal{E}_M}, \quad (20)$$

$$\gamma = \alpha \frac{\mathcal{E} - 2\mathcal{E}_M}{\mathcal{H}_M}. \quad (21)$$

Note that while \mathcal{E} , \mathcal{H}_C and \mathcal{H}_M are constant to within canonical fluctuations, \mathcal{E}_M can vary appreciably.

The inverse temperatures α , β and γ can be determined by minimizing an entropy functional with respect to variation of a free parameter [Khinchin 1949], [Shebalin 1982, 1996] (here, the parameter is \mathcal{E}_M). This gives us *a priori* values for α , β and γ , which can then be placed in the expressions in Table 7 to predict the shape of the ideal spectra for Case I. (One could also use the time-averaged value of E_M to give approximate, but still fairly accurate, *a posteriori* estimates of α , β and γ .)

Recall that the basic equations (1) and (2) are invariant under the discrete classical symmetry transformations P (parity, or coordinate inversion: $\mathbf{x} \rightarrow -\mathbf{x}$), C (charge reversal: $e \rightarrow -e$), and

(if $\nu = \eta = 0$) T (time reversal: $t \rightarrow -t$). However, helicities are not invariant under P and C [Shebalin 1998]. In eqs. (19) – (21), \mathcal{H}_C and \mathcal{H}_M are pseudoscalars under P and C , while the energies \mathcal{E} and \mathcal{E}_M are scalars. (Under time-reversal, \mathcal{H}_C and \mathcal{H}_M are scalars.) Therefore, it is clear from eqs. (20) and (21) that β is a pseudoscalar under P and C , and γ is a pseudoscalar under P , so that $\beta\mathcal{H}_C$ and $\gamma\mathcal{H}_M$ are scalars under P or C . Furthermore, eq. (19) indicates that α is a scalar under P or C .

Thus, both the governing equations (1) and (2), and the probability density functions (16) and (17) are invariant under P , C and T . The importance of this is the following. The phase space Γ of the absolute equilibrium ensemble of ideal MHD turbulence is defined by the independent components of the Fourier modes $\tilde{\mathbf{u}}(\mathbf{k})$ and $\tilde{\mathbf{b}}(\mathbf{k})$ for $0 < k \leq K$; let the dimension of this phase space be denoted by N_Γ . In this phase space, the quadratic form E defines a hypersurface, and $|H_C|$ and $|H_M|$ define two hypersurfaces each, all of dimension $N_\Gamma - 1$. (We use $|H_C|$ and $|H_M|$ since both signs of H_C and H_M are included in the statistical theory, by symmetry.)

The hypersurface defined by E is the *surface of constant energy* Γ_E [Khinchin 1949]. The hypersurface Γ_E will generally be broken into disjoint regions, in all cases except Case IV of Table 6, because either H_C or H_M (or both) or H_P are additional invariants. In each case in Table 6, it is the intersection of Γ_E with all the hypersurfaces associated with both signs of the invariant helicities that is the subset of the phase space Γ on which the phase point can reside. In Case I, there are four disjoint components, in Cases II, III and V, there two disjoint components, and in Case IV, there is only one component [Shebalin 1998].

As an example, let us consider Case I of Table 6, for which there are three invariant integrals. The surface of constant energy Γ_E has dimension $N_\Gamma - 1$, and this intersects with the surfaces of constant $\pm H_C$ and $\pm H_M$ to confine the phase point to subsets of Γ of dimension $N_\Gamma - 3$. Let $S_C = \text{sgn } H_C$ and $S_M = \text{sgn } H_M$, where $S_C, S_M \in \{+, -\}$. Also let $\Gamma_E(S_C, S_M)$ denote the component of Γ_E on which H_C and H_M have signs S_C and S_M , respectively. Since S_C and S_M are set functions which separate one component from another, the components $\Gamma_E(S_C, S_M)$ with different values of S_C and S_M are disjoint (rather, *effectively* disjoint since we have a canonical ensemble).

Thus, the ensemble phase space contains a surface of constant energy Γ_E that has subsets $\Gamma_E(S_C, S_M)$ on which essentially all ensemble phase points reside. The union of all these subsets is the subset of Γ containing, with non-vanishing probability, all of the phase points that make up the theoretical ensemble. Call this union the ‘reduced’ surface of constant energy Γ'_E :

$$\Gamma'_E = \Gamma_E(+, +) \cup \Gamma_E(+, -) \cup \Gamma_E(-, +) \cup \Gamma_E(-, -). \quad (22)$$

It is clear that under P and C , $\Gamma'_E \rightarrow \Gamma'_E$ because Γ'_E has the topological structure given in (22), *i.e.*, a structure that ensures symmetry under P and C (and, of course, T).

Inverse Temperatures

Equations (19), (20) and (21), are used to determine the inverse temperatures α , β and γ , respectively, for Case I. These equations can be used for Cases II-V by making the substitutions discussed following the probability distribution function (16). Also, for Cases II and IV, the substitution $\gamma = 0$ is equivalent to the assignment $\mathcal{E}_M = \frac{1}{2}\mathcal{E}$ in eq. (21). Making the various replacements leads to the results in Table 8 (for more detail, see [Shebalin 2002]).

The inverse temperatures α and β for Case V are determined as follows. First, if $\gamma = -\sigma\beta$, then eqs. (19), (20) and (21) can be used to show that α and β satisfy two algebraic equations:

$$\alpha\mathcal{E} + \beta\mathcal{H}_P = 6\mathcal{N}', \quad (23)$$

$$\alpha\mathcal{E} - \beta\mathcal{H}_P + \left(\beta + \frac{4/a^2}{\beta}\right)\mathcal{H}_C = 0. \quad (24)$$

In fact, eqs. (19), (20) and (21) were originally found by setting up three similar algebraic equations [Shebalin 1989]. Let us now define p , which is constant to within canonical fluctuations, and c , which is a variable parameter:

$$p = \frac{\mathcal{H}_P}{\mathcal{E}} \quad \text{and} \quad c = \frac{\mathcal{H}_C}{\mathcal{E}}. \quad (25)$$

Equations (23) and (24) can be solved to yield

$$\alpha(c) = \frac{3\mathcal{N}'}{\mathcal{E}} \frac{3p - 2c \pm p[1 + 16c(p - c)]^{\frac{1}{2}}}{2p - c(1 + 4p^2)}, \quad (26)$$

$$\beta(c) = \frac{3\mathcal{N}'}{\mathcal{E}} \frac{1 - 8cp \mp p[1 + 16c(p - c)]^{\frac{1}{2}}}{2p - c(1 + 4p^2)}. \quad (27)$$

Here, the sign \pm is chosen so that $\alpha > 0$ and so that the second order moments in Table 7 are positive.

Case	α	β	γ
I	$\frac{3\mathcal{N}'\mathcal{E}_M}{\mathcal{E}_M(\mathcal{E} - \mathcal{E}_M) - \mathcal{H}_C^2}$	$-2\alpha\mathcal{H}_C/\mathcal{E}_M$	$\alpha(\mathcal{E} - 2\mathcal{E}_M)/\mathcal{H}_M$
II	$\frac{6\mathcal{N}'\mathcal{E}}{\mathcal{E}^2 - 4\mathcal{H}_C^2}$	$-4\alpha\mathcal{H}_C/\mathcal{E}$	0
III	$\frac{3\mathcal{N}'}{\mathcal{E} - \mathcal{E}_M}$	0	$\alpha(\mathcal{E} - 2\mathcal{E}_M)/\mathcal{H}_M$
IV	$6\mathcal{N}'/\mathcal{E}$	0	0
V	eq. (26)	eq. (27)	$-\sigma\beta$

Table 8: Inverse temperatures for Cases I–V.

Numerical Simulation

The MHD equations (1) and (2) were solved by a Fourier spectral transform method [Canuto 1988, Boyd 2001] on an N^3 grid, where $N = 32$. The non-linear terms in eqs. (1) and (2) were de-aliased by the Orszag-Patterson technique of shifted-grids [Patterson 1971]. The de-aliasing technique sets the maximum wave vector magnitude in eqs. (13) and (14) to $K = \sqrt{2}N/3$, corresponding to $K^2 = 227$. The equations were integrated forward in time by a ‘partially corrected’ third-order method [Gadzag 1976]. The time step size for all runs was $\Delta t = 10^{-3}$. The initial conditions are such that the kinetic and magnetic Fourier modes have random phases and satisfy

$$|\mathbf{u}(\mathbf{k})| = |\mathbf{b}(\mathbf{k})| \sim k \exp(-k^2/k_p^2) \quad \text{at } t = 0. \quad (28)$$

The kinetic and magnetic energy spectra, defined as the modal energies integrated over solid angle in \mathbf{k} -space, are $E_K(k)$ and $E_M(k)$, respectively. Using (28), these energy spectra can be seen to have

the form

$$E_K(k) \approx E_M(k) \sim k^4 \exp(-2k^2/k_p^2) \text{ at } t = 0. \quad (29)$$

For all runs reported here, the initial peak wave number is $k_p = 4$.

Run	Case	\mathbf{B}_o	$\mathbf{\Omega}_o$
A0	I	(0, 0, 0)	(0, 0, 0)
A1	II	(0, 0, 1)	(0, 0, 0)
A2	III	(0, 0, 0)	(1, 0, 0)
A3	IV	(0, 0, 1)	(1, 0, 0)
A4	V	(0, 0, 1)	(0, 0, 1)
A5	V	(0, 0, $\frac{1}{2}$)	(0, 0, 1)
A6	V	(0, 0, 1)	(0, 0, $\frac{1}{2}$)

Table 9: Ideal MHD Simulations ($\nu = \eta = 0$).

Seven runs are presented here. These all had the same initial conditions ($E = 1.0000$, $H_C = 0.3567$ and $H_M = 0.1398$ at $t = 0$). The values of \mathbf{B}_o and $\mathbf{\Omega}_o$ associated with these runs are given in Table 9. In all of the runs in Table 9 the energy E is conserved to within 0.2%, although the kinetic and magnetic energies can fluctuate significantly – (20% initially and about 3% when the ideal MHD turbulence is in equilibrium).

For brevity, a minimum number of figures will be shown here. Rather, we will include such figures for a future publication [Shebalin 2005a]. Suffice it to say that the runs in Table 9 behaved as expected, *i.e.*, H_C was conserved in Runs A0 and A1, while H_M was conserved in Runs A0 and A2. Also, H_P , a canonical invariant in Run A4, behaved as predicted, while H_C and H_M were no longer invariant. The behavior of H_P for Runs A5 and A6 was also a canonical invariant, as it was for Run A4. The values of H_P for A6, A4 and A5 were 0.2868 ($\sigma = 0.5$), 0.2169 ($\sigma = 1.0$) and 0.0771 ($\sigma = 2.0$), respectively. These were not linear in σ , though a determination of the exact functional dependence is beyond the scope of the present work.

As an example of the efficacy of the statistical theory, we use eqs. (26) and (27) to predict the average energy spectrum for Run A4, and this is shown in Figure 1. The numerical average is taken over the last quarter of the run ($t = 1500$ to 2000). Using the formulas (26) and (27) with s and c as defined in eq. (25), and \mathcal{E} , \mathcal{H}_C and \mathcal{H}_M determined by averaging from $t = 0$ to 2000, we get $\alpha = 1.593067$, $\beta = -1.290033 = -\gamma$. However, the low- k values of $E_{av}(k)$ are very sensitive to the value of β ; adjusting this value to $\beta = -1.303590$ gives the fit in Figure 1. The goodness-of-fit in Figure 1 is typical of what is seen when the statistical theory is applied to any of the ideal cases in Table 9. Also, equilibrium spectra show no anisotropy because, in these ideal cases, there is no dissipation. (The difference between isotropic ideal spectra and anisotropic real spectra in the presence of a mean magnetic field was first explained in [Shebalin 1982, 1983].)

However, absolute equilibrium ensemble theory, as originally formulated ([Kraichnan 1973, 1975], [Frisch 1975], [Fyfe 1976]) predicts that all Fourier modes will have zero mean, and this is not necessarily so in any given ideal MHD simulation. In Figure 2, the evolution of the Fourier modes for $\mathbf{k} = (1, 0, 0)$ in Run A0 is presented. The non-zero components of all of the independent Fourier modes $\tilde{\mathbf{u}}(\mathbf{k})$ and $\mathbf{b}(\mathbf{k})$ define a phase space of large dimension (here, the dimension is about 10^5). Figure 2 is essentially a projection of the phase trajectory into a plane; if the ensemble predictions were correct, then the projected phase trajectory would be a random walk centered on the origin. That it is not is evident in Figure 2, where the initial point of the trajectory is close to the origin, but after a transition

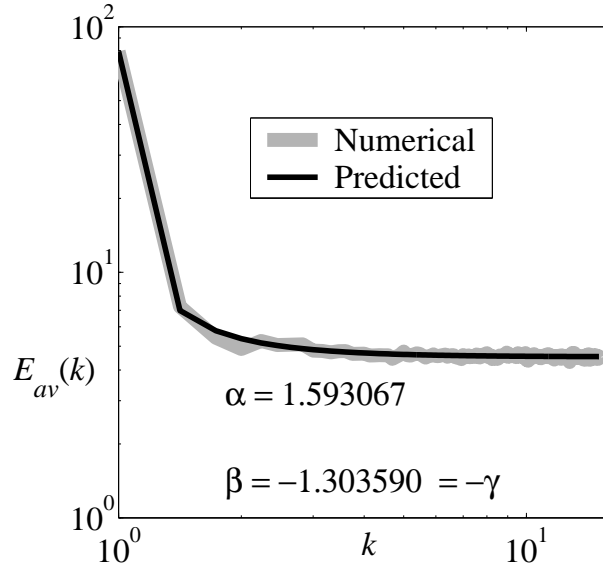


Figure 1: Predicted and numerically averaged ($t = 1500$ to 2000) spectra for Run A4 in Table 9.

lasting from $t = 0$ to about $t = 30$, the phase point appears to arrive at an attractor in phase space. This behavior can also be seen when modes with other values of $k = |\mathbf{k}| = 1$ are examined. However, when $k > 1$, the mean of the Fourier modes appears to be zero. Thus, non-ergodicity is manifested in the modes with the lowest value of k , as simulated time averages do not match predictions of the statistical theory.

In addition to examining the detailed behavior of individual modes, we can also examine time-averaged behavior of all modes by defining the ‘coherent energies’ E^c , E_K^c and E_M^c :

$$E^c = E_K^c + E_M^c, \quad E_K^c \equiv \frac{1}{2} \sum_{\mathbf{k}} |\langle \tilde{\mathbf{u}}(\mathbf{k}) \rangle_T|^2, \quad E_M^c \equiv \frac{1}{2} \sum_{\mathbf{k}} |\langle \tilde{\mathbf{u}}(\mathbf{k}) \rangle_T|^2. \quad (30)$$

The Fourier coefficients in the sum are time-averaged, *e.g.*:

$$\langle \tilde{\mathbf{b}}(\mathbf{k}) \rangle_T \equiv \frac{1}{T} \int_0^T \tilde{\mathbf{b}}(\mathbf{k}, t) dt. \quad (31)$$

If the dynamical system were ergodic, E^c would tend to zero with time; if not, the non-zero mean Fourier modes effectively define a *coherent structure* in ideal MHD turbulence. The appearance of coherent structures has been noted before in long-time 2-D simulations [Shebalin 1989, 2005] and in some preliminary 3-D runs [Shebalin 1994]; here we see them for long-time 3-D runs. The explanation for these coherent structures then, as now, lies in the disjoint nature of phase space [Shebalin 1998].

In Figure 3, the coherent energy for Runs A0–A4 are presented. It is clear that whenever magnetic helicity remains an invariant (Runs A0 and A2), that the coherent energy E^c is relatively large. Furthermore, when coherent energy is evident, it is primarily magnetic, as in Runs A0 and A2, for which $E_M^c \approx 0.12$ at $t = 2000$; the difference between E^c for Runs A0 and A2 in Figure 3 is due to $E_K^c \sim 0.06$ for Run A0 and $E_K^c \sim 0$ for Run A2. (Remember that total energy is $E = 1$). We also see in Figure 3 that E^c for Run A4 settles into a small, but non-zero value; this is due to the presence of H_M in the invariant H_P , as will be discussed presently. (Although these are ideal runs, similar behaviour has been seen in long-time dissipative 2-D MHD runs, where $\nu \neq 0$ and $\eta \neq 0$ [Shebalin 2005].)

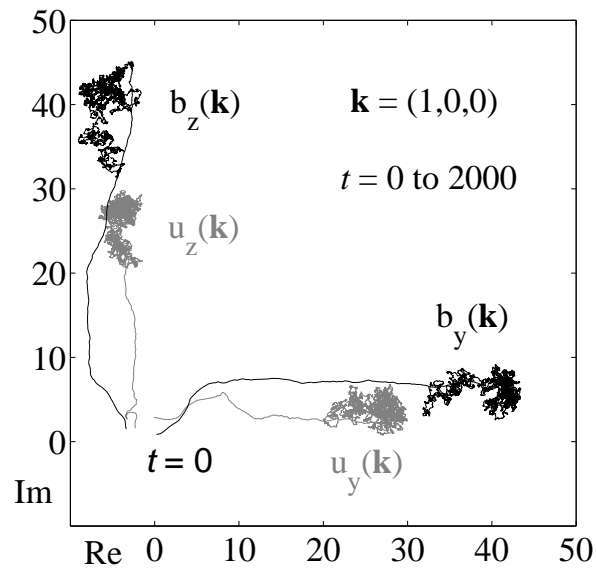


Figure 2: Projection of the phase trajectory for Case I in Table 6 (Run A0 in Table 9).

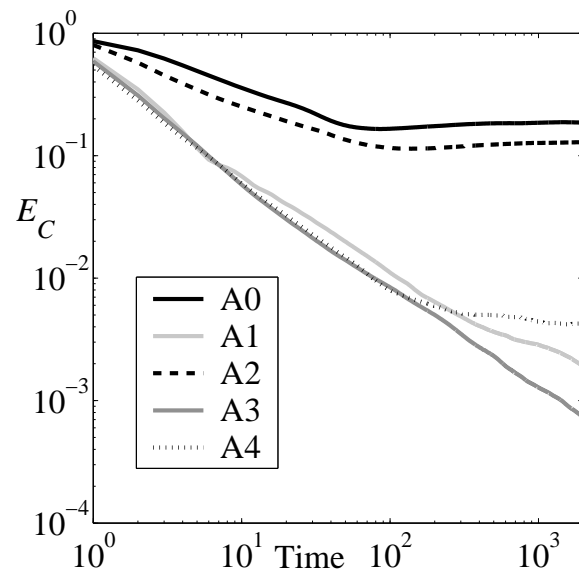


Figure 3: Coherent energy for Runs A0 – A4 in Table 9.

One interesting point to note is that although the theoretically predicted and numerically observed ideal MHD spectra are quite close, as in Figure 1, the ensemble prediction is that all of the power in the spectrum for a given value of k is due to zero-mean Fourier modes, while numerical simulations shows us that, in the case of $k = 1$, much of the energy seems locked up in the non-zero-mean part of the mode, as Figure 2 clearly shows. This was seen before in ideal 2-D MHD turbulence [Shebalin 1982, 1989, 1994, 2005], and it appears again here in ideal 3-D MHD turbulence.

Another interesting point is that Runs A1 and A3 in Figure 3 have coherent energies that do not level off but appear to fall exponentially towards zero. This indicates that magnetic helicity is critical to the appearance of coherent structure in ideal MHD turbulence, since it is either an invariant or part of an invariant (H_P) in those runs that do have non-zero coherent energy. In Runs A1 and A3, the presence of non-zero \mathbf{B}_o eliminates H_M as an ideal invariant, due to the first term on the right side of equation (9). In Run A3, \mathbf{B}_o and $\mathbf{\Omega}_o$ are non-zero and not parallel, so that only E is an ideal invariant; in this case we expect the phase surface Γ_E of the absolute equilibrium ensemble to have only one component, so that all Fourier modes do, in fact, have zero mean. However, In Run A1, H_C is still an ideal invariant, along with E , yet there appears to be no coherent energy. In this latter case, the surface of constant energy Γ_E must still have two disjoint components. The reason for the appearance of zero-means in Run A1 is as follows.

When $\mathbf{B}_o \neq 0$ but $\mathbf{\Omega}_o = 0$, as in Run A1 (Case II of Table 6), we have two invariants, E and H_C , and these can be transformed into two equivalent invariants E^+ and E^- ,

$$E^\pm = E \pm 2H_C = \frac{1}{2} [|\mathbf{u} \pm \mathbf{b}|^2] = \frac{1}{2} [|\mathbf{z}^\pm|^2]. \quad (32)$$

The quantities E^+ and E^- are the energies associated with the Elsässer variables [Elsässer 1956]

$$\mathbf{z}^+ = \mathbf{u} + \mathbf{b}, \quad \mathbf{z}^- = \mathbf{u} - \mathbf{b}. \quad (33)$$

Thus, we have two separate sets of variables, each having its own unique invariant. The phase space Γ of the Fourier modes $\tilde{\mathbf{u}}(\mathbf{k})$ and $\tilde{\mathbf{b}}(\mathbf{k})$ is a ‘direct sum space’ [Halmos 1958],

$$\Gamma = \Gamma^+ \oplus \Gamma^-. \quad (34)$$

Here, Γ^+ is the phase space of the $\tilde{\mathbf{z}}^+(\mathbf{k})$ and Γ^- is the phase space of the $\tilde{\mathbf{z}}^-(\mathbf{k})$.

Using the Elsässer variables (33), the energy and cross helicity can be written as

$$E = \frac{1}{4} [|\mathbf{z}^+|^2 + |\mathbf{z}^-|^2], \quad H_C = \frac{1}{8} [|\mathbf{z}^+|^2 - |\mathbf{z}^-|^2]. \quad (35)$$

Thus, in Case II of Table 6, invariant energy and cross helicity are equivalent to the two invariant energies E^+ and E^- .

The set of Elsässer Fourier modes $\tilde{\mathbf{z}}^+(\mathbf{k})$ are constrained to move on a hypersphere $\Gamma_{E^+}^+$ in their phase space Γ^+ , and the variables $\tilde{\mathbf{z}}^-(\mathbf{k})$ are constrained to move on a hypersphere $\Gamma_{E^-}^-$ in their phase space Γ^- . If H_M is not an invariant, then there is no constraint on where the $\tilde{\mathbf{z}}^+(\mathbf{k})$ can move on the hypersphere $\Gamma_{E^+}^+$, and where the $\tilde{\mathbf{z}}^-(\mathbf{k})$ can move on the hypersphere $\Gamma_{E^-}^-$, in which case the surface of constant energy for, say, $H_C > 0$ is $\Gamma_{E^+}^+ \times \Gamma_{E^-}^-$, *i.e.*, a *product space* [Hocking 1988] between $\Gamma_{E^+}^+$ and $\Gamma_{E^-}^-$.

Suppose that $E^+ = \mathcal{E}_1$ and $E^- = \mathcal{E}_2$, with $\mathcal{E}_1 > \mathcal{E}_2$. The product space in this case is $\Gamma_{\mathcal{E}_1}^+ \times \Gamma_{\mathcal{E}_2}^-$. Under P or C , we have $H_C \rightarrow -H_C$, which implies $\tilde{\mathbf{z}}^+(\mathbf{k}) \rightleftharpoons \tilde{\mathbf{z}}^-(\mathbf{k})$, so that, now, $E^+ = \mathcal{E}_2$ and $E^- = \mathcal{E}_1$. Thus, Under P or C , a second component product space $\Gamma_{\mathcal{E}_2}^+ \times \Gamma_{\mathcal{E}_1}^-$ appears. Therefore, the

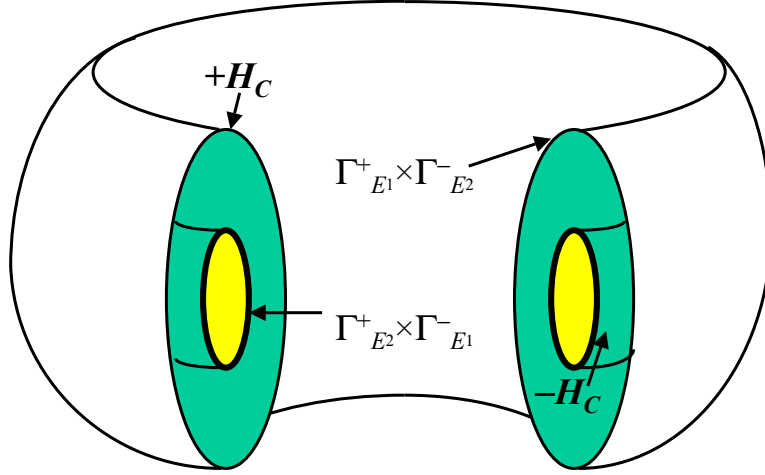


Figure 4: Phase space structure for Case II of Table 6.

reduced constant energy surface for Case II of Table 6 is

$$\begin{aligned} \left[\Gamma_{\mathcal{E}_1}^+ \times \Gamma_{\mathcal{E}_2}^- \right] \cup \left[\Gamma_{\mathcal{E}_2}^+ \times \Gamma_{\mathcal{E}_1}^- \right] &= \Gamma'_E \\ \left[\Gamma_{\mathcal{E}_1}^+ \times \Gamma_{\mathcal{E}_2}^- \right] \cap \left[\Gamma_{\mathcal{E}_2}^+ \times \Gamma_{\mathcal{E}_1}^- \right] &= \emptyset. \end{aligned} \quad (36)$$

Since Γ'_E has two disjoint components, as shown in (36), the system is non-ergodic. [The surface of constant energy Γ_E is broken into two components of smaller dimension (Γ'_E , the union of nested ‘hyper-tori’), rather than four components as in (22), because H_M is not invariant here.]

To visualize this disjoint structure, consider Figure 4, which pertains to Case II of Table 6, represented by Run A1 in Table 9. The ensemble average is over both components (gray and black), while a time average is taken only over the gray or the black component. Here, the subspaces $\Gamma_{\mathcal{E}_{1,2}}^+$ and $\Gamma_{\mathcal{E}_{2,1}}^-$ in the union of direct product spaces are hyperspheres and thus symmetric about their respective origins, so that the Elsässer variables have zero mean values for Case II of Table 6.

In terms of the Elsässer variables (33), the magnetic helicity can be written as

$$H_M = \frac{1}{4} \sum_{\mathbf{k}} \mathbf{k} \cdot [\mathbf{z}_R^+(\mathbf{k}) - \mathbf{z}_R^-(\mathbf{k})] \wedge [\mathbf{z}_I^+(\mathbf{k}) - \mathbf{z}_I^-(\mathbf{k})]. \quad (37)$$

In Cases I and III of Table 6, the presence of a constant H_M introduces a constraint which serves to decompose the nested hypertori $\Gamma_{\mathcal{E}_1}^+ \times \Gamma_{\mathcal{E}_2}^-$ and $\Gamma_{\mathcal{E}_2}^+ \times \Gamma_{\mathcal{E}_1}^-$ into two components each, for a total of four components of the reduced surface of constant energy Γ'_E , as shown in (22). In this case we have coherent structure, in addition to non-ergodicity as evinced in the behavior of the coherent energies for Runs A0 and A2 in Figure 3. Also, in Case V, where $H_P = H_C - \sigma H_M$ is an ideal invariant, both H_C and H_M affect the topology of the available phase space, as seen in the behavior of the coherent energy for Run A4 in Figure 3.

Broken Ergodicity

Here, a summary of the preceding results is given, along with a more detailed discussion of ‘broken ergodicity’. It has been noted in Section 4 that the governing equations (1) and (2), and the probability

density functions (16) and (17) are invariant under P , C and T , while H_C , H_M and H_P are not. The reason is that the probability densities (16) and (17) are invariant because the inverse temperatures β and γ are pseudoscalars, so that the products βH_C , γH_M and βH_P are scalars. Thus, when the integration over all of phase space required to determine an ensemble expectation value is done analytically, it includes regions with both signs of the helicities H_C , H_M and H_P , which automatically leads to $\langle \tilde{\mathbf{u}}(\mathbf{k}) \rangle = \langle \tilde{\mathbf{b}}(\mathbf{k}) \rangle = 0$.

Note that the expectation values of the pseudoscalars (under P or C) \mathcal{H}_C and \mathcal{H}_M (for Case I) can be written in terms of the scalar (under P or C) partition function $Z = \int Dd\Gamma$ as

$$\mathcal{H}_C = -\frac{\partial \ln Z}{\partial \beta}, \quad \mathcal{H}_M = -\frac{\partial \ln Z}{\partial \gamma}. \quad (38)$$

Since β and γ are themselves pseudoscalars, the relations (38) are invariant under P or C (or T). Therefore, one may state that the theory predicts the signs of the scalars $\beta \mathcal{H}_C$ and $\gamma \mathcal{H}_M$, rather than the signs of \mathcal{H}_C or \mathcal{H}_M alone. Alternatively, one may say that the absolute values $|\mathcal{H}_C|$ and $|\mathcal{H}_M|$ are predicted and that ensemble expectation values are taken over those parts of the energy surface where $H_C = \pm \mathcal{H}_C$ and $H_M = \pm \mathcal{H}_M$.

However, when a numerical simulation is run, a given invariant helicity H_C or H_M will be either positive or negative and will remain so during the dynamical evolution. Therefore, the symmetry of absolute equilibrium ensemble theory is dynamically broken, and ensemble predictions are not necessarily the same as time averages. That they are not the same is clear from the evidence presented in Section 5, especially in the comparison of the time averages $\langle \tilde{\mathbf{u}}(\mathbf{k}) \rangle_T$ and $\langle \tilde{\mathbf{b}}(\mathbf{k}) \rangle_T$, which are generally nonzero for $k = 1$, with the ensemble averages for $k = 1$, which are zero. Some cases of ideal MHD turbulence, as described by absolute equilibrium ensemble theory, are clearly not ergodic since ensemble expectation values (analytical integrations) and time averages (numerical integrations) are not equal. This situation is often called *broken ergodicity* [Palmer 1982].

Even if we did not happen to observe the inequality of time and ensemble averages the non-ergodicity found in MHD turbulence is essentially tied to the decomposability or indecomposability of the surface of constant energy Γ_E in phase space. This is the content of the Khinchin-Birkhoff theorem [Khinchin 1949, pp 55–57]: ‘the metric indecomposability of the surfaces of constant energy is a necessary and sufficient condition for a positive answer to the ergodic problem . . .’. The essential point is that if metric decomposability occurs (*i.e.*, a surface of constant energy has disjoint components), then the system is non-ergodic, and conversely, if the surface of constant energy cannot be broken into disjoint components, then the system is ergodic.

We note again that the occurrence of nonzero mean values of first-order time-averaged moments such as $\langle \tilde{\mathbf{u}}(\mathbf{k}) \rangle_T$ and $\langle \tilde{\mathbf{b}}(\mathbf{k}) \rangle_T$ (*i.e.*, coherent structure) is sufficient for non-ergodicity, but not necessary. In the discussion of the Elsässer variables (33), it was seen in eqs. (36) and in Fig. 4 that the surface of constant energy consisted of the union of two disjoint subspaces, indicating non-ergodicity. However, the coherent energy for Run A1 in Figure 3 is clearly falling to zero, indicating a lack of coherent structure. Thus, non-ergodicity is due to the presence of at least one invariant helicity (whose sign serves as the set function that differentiates between unconnected components).

Conclusion

The results presented here are not exhaustive, and further studies are necessary to understand the detailed effects that varying the parameter σ , the initial values of H_C and H_M , the magnitudes and directions of \mathbf{B}_0 and $\mathbf{\Omega}_0$ as well as the Rossby number, $Ro \equiv \sqrt{\Omega}/2\Omega_0$, where the enstrophy Ω is

defined in eq. (10). However, several novel features have been presented here. These include the discovery of a new integral invariant, the parallel helicity H_P .

A major topic requiring further investigation is a precise characterization of how the presence of invariant integrals affects the topology of the available phase space. A step in this direction is the realization that use of the Elsässer variables allows the invariant components of the surface of constant energy Γ_E to be represented as a union of the disjoint, direct product subspaces $\Gamma_{\mathcal{E}_1}^+ \times \Gamma_{\mathcal{E}_2}^-$ and $\Gamma_{\mathcal{E}_2}^+ \times \Gamma_{\mathcal{E}_1}^-$ called the reduced surface Γ'_E ; see eq. (36). If E and H_C are constant, but not H_M , then motion over the hyperspheres $\Gamma_{\mathcal{E}_{1,2}}^+$ and $\Gamma_{\mathcal{E}_{2,1}}^-$ produces a zero-mean time average, as evidenced here numerically by examining the time evolution of the coherent energy. The manifest symmetry of the $\Gamma_{\mathcal{E}_{1,2}}^+$ and $\Gamma_{\mathcal{E}_{2,1}}^-$ about their respective origins, in fact, requires that mean values of the various Fourier components be zero. However, when H_M or H_P are constant, the surface of constant energy is broken into additional disjoint components (in the case of constant H_P , the dependence on σ is a topic requiring further inquiry).

The results given here pertain to *ideal* 3-D MHD turbulence, and an important question is how the broken ergodicity observed in this non-dissipative flow might also appear in realistic, *i.e.*, dissipative, 3-D MHD turbulence. Results from 2-D simulations or real turbulence [Shebalin 2005] indicate that broken ergodicity is still present, so perhaps similar effects will be seen in real 3-D flows. A numerical investigation into this would benefit from a large computational grid, in order to make the maximum wave number in the Fourier space as large as possible. Going to a large grid, of course, greatly increases numerical run times, so that a numerical investigation in which several important parameters are systematically varied may require a long-term research commitment; thus, smaller grids may still prove useful. Further studies should also show the connection between broken ergodicity, selective decay and inverse cascades more clearly. In addition, analytical theories of MHD turbulence do not currently offer any explanations of the behavior reported in this paper, and perhaps this will be seen as an inducement for an extension of these theories.

Finally, an essential physical feature uncovered here (and in previous work) is, in specific cases, the presence of coherent structure in MHD turbulence. We have observed numerically that, in a number of cases, coherent structures seem to arise spontaneously in MHD turbulence. This hints at the possibility that magnetic dynamo activity may be more an inherent feature of MHD turbulence and less an induced phenomenon due to rotation and convection. It may turn out that rotation and convection (for example, in the earth's outer core or in the sun's convective zone) are needed as sources of turbulence, and may also affect the level of coherent energy attained, but that it is the turbulence itself that contains all that is required for dynamo action: broken ergodicity.

Acknowledgements

I wish to thank Dr. Friedrich Kupka of the Max-Planck-Institute for Astrophysics for organizing a splendid 'Workshop on Interdisciplinary Aspects of Turbulence' at the Ringberg Castle in Bavaria, 18-22 April 2005, where the talk related to this paper was presented.

References

- [Biskamp 2003] D. Biskamp, "Magnetohydrodynamic Turbulence," Cambridge U. P., UK, 2003, Chap. 2.
- [Boyd 2001] J. P. Boyd, "Chebyshev and Fourier Spectral Methods," 2nd Ed., Dover, Mineola, NY, 2001.
- [Brun 2004] A. S. Brun, M. S. Miesch and J. Toomre, *Global-scale turbulent convection and magnetic dynamo action in the solar envelope*, Ap. J., **614** (2004) 1073–1098.

- [Canuto 1988] C. Canuto, M. Y. Hussaini, A. Quateroni, and T. A. Zang, “Spectral Methods in Fluid Dynamics,” Springer-Verlag, New York, 1988.
- [Canuto 1986] V. M. Canuto, and G. J. Hartke, *Convective turbulence with rotation and magnetic fields*, *Astron. Astrophys.*, **168** (1986) 89–104.
- [Elsässer 1956] W. M. Elsässer, *Hydromagnetic Dynamo Theory*, *Rev. Mod. Phys.*, **28** (1956) 135–163.
- [Fan 2004] Y. Fan, *Magnetic fields in the solar convection zone*, *Living Rev. Solar Phys.*, **1** (2004) 1–63.
- [Frisch 1975] U. Frisch, A. Pouquet, J. Leorat, and A. Mazure, *Possibility of an inverse cascade of magnetic helicity in magnetohydrodynamic turbulence*, *J. Fluid Mech.*, **68** (1975) 769–778.
- [Fyfe 1976] D. Fyfe and D. Montgomery, *High beta turbulence in two-dimensional magneto-hydrodynamics*, *J. Plasma Phys.*, **16** (1976) 181–191.
- [Gadzag 1976] J. Gadzag, *Time-differencing schemes and transform methods*, *J. Comp. Phys.*, **20** (1976) 196–207.
- [Halmos 1958] P. R. Halmos, “Finite-Dimensional Vector Spaces,” Van Nostrand, Princeton, 1958, pp 28–32.
- [Hocking 1988] J. G. Hocking and G. S. Young, “Topology,” Dover, New York, 1988, pp 21–23.
- [Khinchin 1949] A. I. Khinchin, “Mathematical Foundations of Statistical Mechanics,” Dover, New York, 1949, 137-145.
- [Kraichnan 1973] R. H. Kraichnan, *Helical turbulence and absolute equilibrium*, *J. Fluid Mech.*, **59** (1973) 745–752.
- [Kraichnan 1975] R. H. Kraichnan, *Statistical dynamics of two-dimensional flows*, *J. Fluid Mech.*, **67** (1975) 155–175.
- [Kraichnan 1988] R. H. Kraichnan and R. Panda, *Depression of nonlinearity in decaying isotropic turbulence*, *Phys. Fluids*, **31** (1988) 2395–2397.
- [Lee 1952] T. D. Lee, *On some statistical properties of hydrodynamical and magneto-hydrodynamical fields*, *Q. Appl. Math.*, **10** (1952) 69–74.
- [Lesieur 1997] M. Lesieur, “Turbulence in Fluids,” 3rd Ed., Kluwer, Dordrecht, 1997, Chap. II.
- [Palmer 1982] R. G. Palmer, *Broken ergodicity*, *Adv. Phys.*, **31** (1982) 669–735.
- [Patterson 1971] G. S. Patterson and S. A. Orszag, *Spectral calculation of isotropic turbulence: Efficient removal of aliasing interaction*, *Phys. Fluids*, **14** (1971) 2538–2541.
- [Shebalin 1982] J. V. Shebalin, *Anisotropy in MHD turbulence due to a mean magnetic field*, Ph.D. Dissertation, College of William and Mary, 1982.
- [Shebalin 1983] J. V. Shebalin, W. H. Matthaeus, and D. Montgomery, *Anisotropy in MHD turbulence due to a mean magnetic field*, *J. Plasma Phys.*, **29** (1983) 525–47.
- [Shebalin 1989] J. V. Shebalin, *Broken ergodicity and coherent structure in homogeneous turbulence*, *Physica D*, **37** (1989) 173–191.
- [Shebalin 1994] J. V. Shebalin, *Broken symmetry in ideal magnetohydrodynamic turbulence*, *Phys. Plasmas*, **1** (1994) 541–547.
- [Shebalin 1996] J. V. Shebalin, *Absolute equilibrium entropy*, *J. Plasma Phys.* **56** (1996) 419–427.

- [Shebalin 1998] J. V. Shebalin, *Phase space structure in ideal homogeneous turbulence*, Phys. Lett. A, **250** (1998) 319–322.
- [Shebalin 2002] J. V. Shebalin, *The statistical mechanics of ideal homogeneous turbulence*, NASA TP-2002-210783, Johnson Space Center, Houston, TX, 2002.
- [Shebalin 2005] J. V. Shebalin, *Theory and simulation of real and ideal magnetohydrodynamic turbulence*, Discrete & Continuous Dynamical Systems B, **5** (2005) 153–175.
- [Shebalin 2005a] J. V. Shebalin, *Ideal MHD Turbulence with Rotation and Mean Magnetic Field*, J. Plasma Phys., submitted (2005).
- [Stribling 1990] T. Stribling and W. H. Matthaeus, *Statistical properties of ideal three-dimensional magnetohydrodynamics*, Phys. Fluids B, **2** (1990) 1979–1988.

Energy spectrum and transfer flux in Hydrodynamic and MHD turbulence

T. Gotoh, K. Mori

Graduate School of Engineering, Engineering Physics,
Nagoya Institute of Technology, Nagoya, 466-8555, Japan

Abstract

Transfer flux of the kinetic energy, passive scalar variance and of the total energy in MHD turbulence is studied. It is found by direct numerical simulation and spectral theory of turbulence that the transfer in the mean flux is local in scale, and that the energy transfer in 4-dimensions is more efficient than that in 3d. Fluctuations of the transfer flux around its mean value become positive and negative and are very intermittent as the scale decreases.

Introduction

In turbulence at large Reynolds numbers, energy is pumped in at the rate ϵ_{in} per unit mass and unit time at macroscopic scale L , transferred at the rate Π to smaller scales by nonlinear interaction through the inertial range, and then it is dissipated into heat at the rate ϵ_{out} at scale η due to molecular viscosity [1, 2]. When turbulence is in a steady state, the averages of the above three rates are equal: $\bar{\epsilon}_{in} = \Pi = \bar{\epsilon}_{out}$. Also for a passive scalar convected by turbulence and for the MHD turbulence the same dynamics can be expected, in which the transferred quantities are the variance of the scalar fluctuations and the sum of the kinetic and magnetic energy, respectively. The transfer flux $\Pi^{(\sigma)}$ due to the nonlinear interaction, where σ is NS (Navier Stokes), θ (scalar), or M (MHD), is the most fundamental quantity in the turbulence dynamics. The transfer occurs in stepwise (local cascade process) or in a radiative way (nonlocal process) in scale space. We have examined the statistical nature of $\Pi^{(\sigma)}$ by using direct numerical simulation (DNS) of the isotropic NS, scalar, and MHD turbulence from the view points of (1) degree of locality of the mean transfer flux in wavenumber space, (2) its dependency on the Reynolds number, (3) effects of spatial dimensions, (4) fluctuations of the flux around its mean value.

Mean transfer flux

We assume that the turbulent fields are statistically homogeneous, isotropic, and in a steady state. Spectra of the kinetic energy, magnetic energy, and the scalar variance are defined as

$$\frac{\langle \mathbf{u}^2 \rangle}{2} = \int_0^\infty E(k, t) dk, \quad \frac{\langle \mathbf{b}^2 \rangle}{2} = \int_0^\infty E_b(k, t) dk, \quad \frac{\langle \theta^2 \rangle}{2} = \int_0^\infty E_\theta(k, t) dk, \quad (1)$$

respectively, where $\langle \rangle$ denotes ensemble average. The equations for the spectra are

$$\left(\frac{\partial}{\partial t} + 2\nu k^2 \right) E(k, t) = T_{NS}(k, t), \quad (2)$$

$$\left(\frac{\partial}{\partial t} + (\nu + \mu)k^2 \right) E_M(k, t) + (\nu - \eta)k^2 E_R(k, t) = T_M(k, t), \quad (3)$$

$$\left(\frac{\partial}{\partial t} + 2\kappa k^2 \right) E_\theta(k, t) = T_\theta(k, t). \quad (4)$$

where $E_M(k) = E(k) + E_b(k)$ and $E_R(k) = E(k) - E_b(k)$. We consider the only case of $\nu = \eta = \kappa$ in which the contributions from the molecular action to the transfer flux are the same. Functions T_{NS} , T_M , and T_θ denote the energy, scalar, and MHD energy transfer functions, respectively and arise from the nonlinear and/or convective terms in the fundamental equations. The mean transfer flux $\Pi^{(\sigma)}$ is defined as [1, 2, 3, 4]

$$\Pi^{(\sigma)}(k, t) = \int_k^\infty T_\sigma(k', t) dk'. \quad (5)$$

Physical meaning of the transfer flux is the total amount of the energy, scalar variance, or the MHD energy transferred from all the Fourier components below k to those higher than k by triad interactions. On the other hand, the transfer functions T_σ 's are those quantities transferred to the wavenumber k , and generally of the form of

$$T_\sigma(k) = \iint_\Delta S_\sigma(k, p, q) dpdq, \quad (6)$$

$$S_\sigma(k, p, q) = 2\text{Real}(\mathbf{M}_\sigma : \langle \mathbf{w}_\sigma(\mathbf{p}) \mathbf{w}_\sigma(\mathbf{q}) \mathbf{w}_\sigma(-\mathbf{k}) \rangle), \quad (7)$$

where $\mathbf{M}_\sigma(\mathbf{k})$ is a geometric factor arising from the nonlinear or convective terms, and $\mathbf{w}_\sigma(\mathbf{k})$ denotes the Fourier amplitude of the velocity, magnetic vectors or passive scalar. In the triad interaction $\mathbf{k} = \mathbf{p} + \mathbf{q}$, we define the scale disparity parameter α as the ratio of the longest to the shortest wavenumber: [3, 4]

$$\alpha = \frac{\text{Max}(k, p, q)}{\text{Min}(k, p, q)}. \quad (8)$$

When α is close to unity, it means that fluid motions of similar size interact, while when α is very large, motions at very large and very small scales interact. Thus, α measures the degree of locality or nonlocality of the interactions among different scales. The mean transfer flux of Eq. (5) is written as follows,

$$\frac{\Pi^{(\sigma)}(k)}{\bar{\epsilon}^{(\sigma)}} = \int_1^\infty W^{(\sigma)}(\alpha, k) \frac{d\alpha}{\alpha}, \quad (9)$$

$$W^{(\sigma)}(\alpha, k) = \frac{1}{\bar{\epsilon}^{(\sigma)}} \int_k^\infty dk' \int_0^\infty dp' \int_0^\infty dq' S_\sigma(k', p', q', \alpha), \quad (10)$$

where $\bar{\epsilon}^{(\sigma)}$ denotes the mean dissipation rate for the kinetic and magnetic energy, or the passive scalar variance. $W^{(\sigma)}(\alpha, k)$ represents the fractional contributions to the total mean transfer flux from the interactions in the range $[\alpha, \alpha + d\alpha]$ at wavenumber k [3, 4, 5, 6, 7, 8, 9, 10, 11].

Figures 1 and 2 show the energy spectra in steady state in which curves are compensated by multiplying $k^{5/3}$ [13, 14]. It is clearly seen that the spectra of the kinetic and passive scalar have small but finite width of flat portion at $R_\lambda = 427$, indicating that they obey the $k^{-5/3}$ spectrum, but it is difficult to definitely decide whether or not $E_M(k) \propto k^{-5/3}$ at $R_\lambda = 160$ [14, 20, 21]. For these spectra, we have computed $W^{(\sigma)}$, which are shown in Figs. 3 and 4 [15]. The $W^{(\sigma)}$ curves attain the maxima at about $\alpha = 2$ and slowly decay for large α , which indicates that the transfer of the energy and scalar variance is local in scale. The smooth curves for $W^{(NS)}$ and $W^{(\theta)}$ show the theoretical prediction by the spectral theory of turbulence (Lagrangian Renormalized Approximation, LRA) [15, 23]) which agrees well with the DNS curves. $W^{(M)}$ is very similar to $W^{(NS)}$ in spite of the difference in the Reynolds numbers. Since in the MHD turbulence the kinetic energy dominates the total energy spectrum in the low wavenumber range as seen in Fig.2, the effects of the magnetic field on the transfer flux are expected to be small, which in turn implies that the locality of $\Pi^{(NS)}$ is insensitive to the Reynolds numbers.

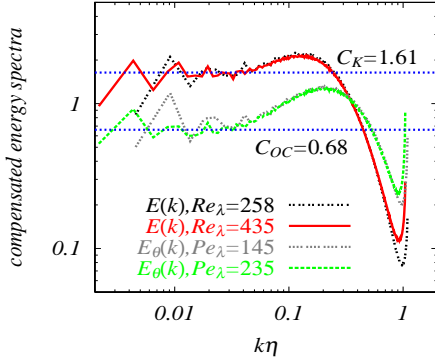


Fig.1 Compensated energy spectrum $k^{5/3}\bar{\epsilon}^{-2/3}E(k)$ and the scalar spectrum $k^{5/3}\bar{\epsilon}^{1/3}\bar{\chi}^{-1}E_\theta(k)$ at $R_\lambda = 427$. The Kolmogorov and Obukhov-Corrsin constants are $K = 1.61 \pm 0.09$ and $C_{OC} = 0.68 \pm 0.04$, respectively.

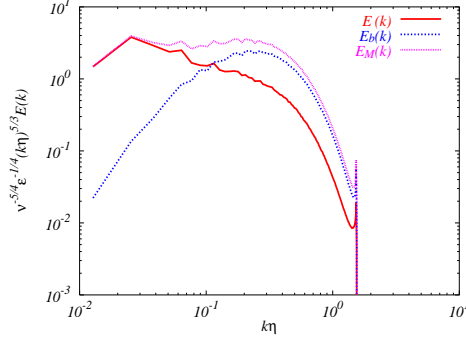


Fig.2 Compensated energy spectra $k^{5/3}\bar{\epsilon}^{-2/3}E(k)$, $k^{5/3}\bar{\epsilon}_b^{-2/3}E_b(k)$, and $k^{5/3}\bar{\epsilon}_{total}^{-2/3}E_M(k)$ at $R_\lambda = 160$.

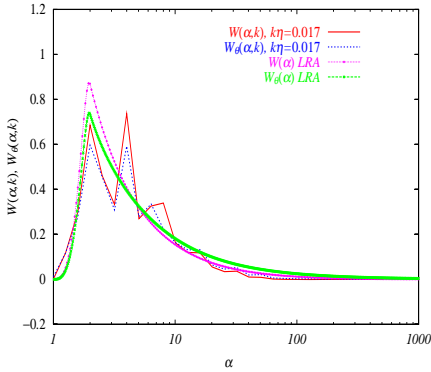


Fig.3 Comparison of $W^{(NS)}(\alpha)$ and $W^{(\theta)}(\alpha)$ at $R_\lambda = 427$. Smooth curves are the results of the spectral theory of turbulence (LRA).

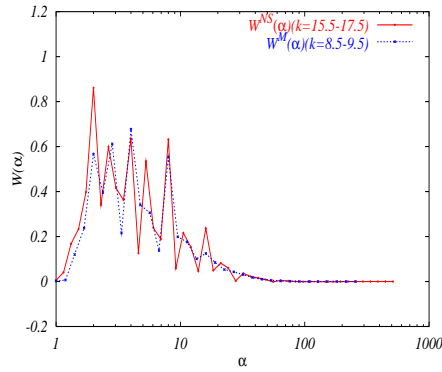


Fig.4 Comparison of $W^{(NS)}(\alpha)$ ($R_\lambda = 427$) and $W^{(M)}(\alpha)$ ($R_\lambda = 160$).

Dimension effects

In order to see effects of the spatial dimension on the transfer of the kinetic energy in scale space, we have examined the decaying NS turbulence in 4-dimensions and compared with the 3-dimensional turbulence [16]. The initially Gaussian random velocity field with a support compact spectrum was integrated in time. The total kinetic energy and the average energy dissipation are defined by $E_d(t) = d(U_0^2/2) = \langle \mathbf{u}^2(\mathbf{x}, t) \rangle / 2$ and $dE_d(t)/dt = -\bar{\epsilon}_d$, respectively, where $d = 3$ or 4 , so that the energy in one direction is the same for both dimensions.

Variation of $\bar{\epsilon}_d(t)/\bar{\epsilon}_d(0)$ is shown in Fig.5. The dissipation rates attain the maxima at about $k_0 U_0 t \sim 1$ in both dimensions. Initially the ratio $\bar{\epsilon}_4(0)/\bar{\epsilon}_3(0)$ is about $4/3$, but later $\bar{\epsilon}_4(t)/\bar{\epsilon}_4(0)$ becomes larger than $\bar{\epsilon}_3(t)/\bar{\epsilon}_3(0)$. This fact indicates that the energy transfer in 4d is more efficient than in 3d. Correspondingly to this, we observed that the normalized energy flux function $\Pi_d(k, t)/\bar{\epsilon}_d(t)$ was larger in 4d than in 3d (figures not shown). The decay of the normalized turbulent energy is shown in Fig.6; the curves are well fitted by $(t - t_0)^{-n}$ with $n = 1.35$ in 3d and $n = 1.60$ in 4d, where $t_0 \approx 0$ [17, 18]. The larger exponent in 4d is due to the larger energy transfer rate.

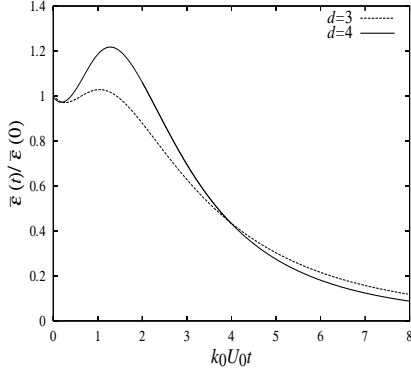


Fig.5 The variation of the energy dissipation rate in 4d and 3d.

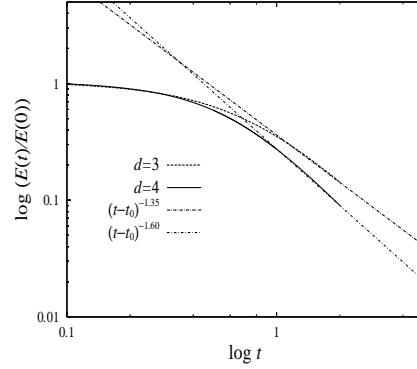


Fig.6 The decay of turbulent energy in 4d and 3d. Lines are the best fit ones.

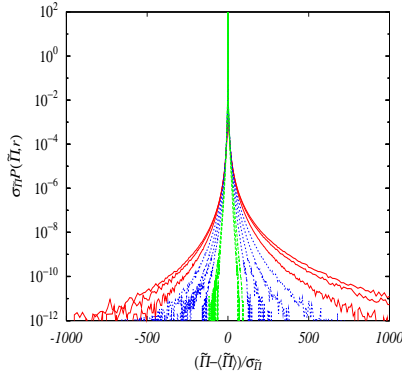


Fig.7 $P(\tilde{\Pi}, r)$. $r_n = 2^{n-1} \Delta x$, $n = 1, \dots, 10$, $\Delta x = 2\pi/N$, $R_\lambda = 427$. Curves are from the inner to outer as n decreases.

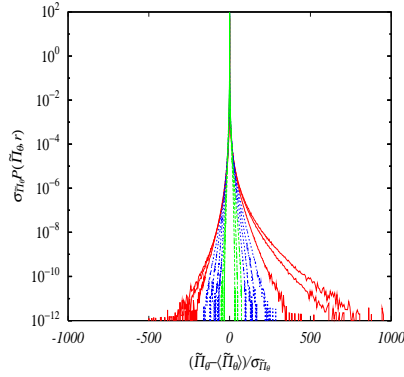


Fig.8 $P(\tilde{\Pi}_\theta, r)$. $r_n = 2^{n-1} \Delta x$, $n = 1, \dots, 10$, $\Delta x = 2\pi/N$, $R_\lambda = 427$. Curves are from the inner to outer as n decreases.

Fluctuations of the transfer flux

It is very interesting and important to know how much the flux fluctuates around its mean. The probability density function (PDF) of the transfer flux is suitable for this purpose, but we need expression for the transfer flux in the physical space. We use surrogate expression for the flux in the physical space defined in terms of the structure functions by

$$\tilde{\Pi}(\mathbf{x}, \mathbf{r}) = -\frac{(\delta u_L(\mathbf{x}, \mathbf{r}))^3}{r}, \quad \tilde{\Pi}_\theta(\mathbf{x}, \mathbf{r}) = -\frac{\delta u_L(\mathbf{x}, \mathbf{r})(\delta\theta(\mathbf{x}, \mathbf{r}))^2}{r}, \quad (11)$$

which are motivated by the 4/5 and 4/3 laws [19, 22]. The means of the two members of Eq.(11) are equal to $\Pi^{(NS)}(r) = \langle \tilde{\Pi}(\mathbf{x}, \mathbf{r}) \rangle = \bar{\epsilon}^{NS}$, and $\Pi^{(\theta)}(r) = \langle \tilde{\Pi}_\theta(\mathbf{x}, \mathbf{r}) \rangle = \bar{\epsilon}^\theta$ for the separation distance r in the inertial range, respectively.

Figures 7 and 8 show PDF's of $\tilde{\Pi}$ and $\tilde{\Pi}_\theta$ for $R_\lambda = 427$ and $Sc = 1$. Both PDF's have cusps at small amplitudes, and tails that become longer for large amplitudes as r decreases. $\tilde{\Pi}$ and $\tilde{\Pi}_\theta$ take positive or negative values, meaning that the energy and the scalar variance are transferred in both directions, from small to large scales and from large to small scales. The PDF of $\tilde{\Pi}_\theta$ is more positively skewed than that of $\tilde{\Pi}$, which means that large negative amplitudes of the scalar transfer flux occur less frequently than large positive amplitudes. This is due to the fact that there is no pressure term

in the equation of the passive scalar, so that the scalar variance undergoes straining more persistently and efficiently by the velocity field [15].

Summary

We have examined the nature of the transfer flux in the NS, MHD, and passive scalar turbulence. The mean transfers are local in scale, which means that those quantities are transferred in stepwise by the interaction among similar size of scales of motion. This is consistent with the conventional understanding. It was also suggested that the locality in the transfer flux was insensitive to the Reynolds numbers. The fluctuations of the flux around the mean value are very intermittent, and both strong positive and negative fluctuations can occur, but they cancel mostly, and yield only small mean value of the flux as net effects. When the spatial dimension was increased from 3 to 4, it was found that the transfer of the kinetic energy was enhanced when compared to the case in 3d. This is due to the fact that the role of the pressure in 4d becomes less important and strong velocity gradients occur more frequently than in 3d.

Acknowledgements

T.G thanks Dr. Kupka and Max Planck Institute for their hospitality during workshop. The Daiko foundation is acknowledged for his partial financial support. The Nagoya University Computation Center and the Computer Center of the National Fusion Science of Japan are acknowledged for providing the computational resources.

References

- [1] U. Frisch, *Turbulence: The Legacy of A. N. Kolmogorov*, Cambridge University Press. (1995).
- [2] T. Gotoh, *An introduction to the turbulence theory* (in Japanese), Asakura Shoten (1998).
- [3] R. H. Kraichnan, Phys. Fluids **9** 1728 (1966).
- [4] R. H. Kraichnan, J. Fluid Mech. **47** (1971).
- [5] J. A. Doramadzki and R. S. Rogallo, Phys. Fluids **A2** 413 (1990).
- [6] Y. Zhou, Phys. Fluids **A5** 1092 (1993).
- [7] Y. Zhou, Phys. Fluids **A5** 2511 (1993).
- [8] P. K. Yeung, Phys. Fluids **6** 2245 (1994).
- [9] P. K. Yeung, J. G. Brasseur, and Q. Wang, J. Fluid Mech. **283** 43 (1994).
- [10] J. A. Brasseur and C. H. Wei, Phys. Fluids **6** 642 (1994).
- [11] Y. Zhou, P. K. Yeung, and J. G. Brasseur, Phys. Rev. E **53** 1261 (1996).
- [12] T. Gotoh, D. Fukayama & T. Nakano, Phys. Fluids, **14** (2002) 1065-1081.
- [13] T. Watanabe and T. Gotoh, New J. Phys. <http://www.iop.org/EJ/abstract/1367-2630/6/1/E03/> (2004).
- [14] K. Mori, *Direct Numerical Simulation of MHD turbulence* NIT Master Thesis (in Japanese) (2005).
- [15] T. Gotoh and T. Watanabe, Submitted to J. of Turbulence, (2005).
- [16] E. Suzuki, T. Nakano, N. Takahashi, and T. Gotoh, Submitted to Phys. of Fluids. (2005).
- [17] M. Oberlack, PAMM Proc. Appl. Math. Mech. **1** (2002) 294.
- [18] P. A. Davidson, *Turbulence*, Oxford (2004).
- [19] A. N. Kolmogorov, Dokl. Akad. Nauk SSSR **30**, 9 (1941). Dokl. Akad. Nauk SSSR, **32**, 16-18 (1941).
- [20] D. Lohse and A. Müller-Groeling, Phys. Rev. Lett. **74** 1747 (1995),

- [21] D. Lohse and A. Müller-Groeling, Phys. Rev. E, **54** 395 (1996).
- [22] A. M. Yaglom, Dokl. Akad. Nauk SSSR **69**, (1949) 743.
- [23] Y. Kaneda, J. Fluid Mech. **107** 131 (1981).

Turbulent transport in magnetized plasmas

F. Jenko

MPI für Plasmaphysik, Boltzmannstr. 2, D-85748 Garching, Germany

Abstract

This is a brief introduction to the area of plasma turbulence from a theoretical perspective. Hopefully, it stimulates some cross-disciplinary exchanges and collaborations.

Introduction

As is widely known, turbulent flows play a central role in magnetic confinement fusion (MCF) research. Turbulence, known for its high transport rates, causes the magnetic device to 'leak'. While in the absence of turbulence, it would be possible to create a burning (i.e., self-sustaining) plasma in a table-top device, real MCF experiments tend to have linear extensions of the order of 5-10 m. While this 'brute-force' solution (building bigger and thus more expensive experiments) to the turbulence problem works, there is a significant amount of work being done to characterize, understand, and control plasma turbulence. Encouraging results in this respect were obtained in the mid 1990s, when it became possible to create so-called 'internal transport barriers' in which the turbulent diffusivities are suppressed by up to an order of magnitude over radially extended regions. This discovery showed that turbulence control is indeed possible. The present contribution is meant as a brief introduction to the area of plasma turbulence from a theoretical perspective.

Plasma turbulence versus fluid turbulence

The classic example of a turbulent system is that of a neutral fluid at high Reynolds number. Its theoretical description is based on the Navier-Stokes equation, and many of its basic features can be described in the framework of Kolmogorov's scaling theory. Since many readers will be familiar with this kind of turbulent dynamics, it might be useful to introduce plasma turbulence by stressing the similarities and differences with respect to fluid turbulence.

First, turbulence in magnetized plasmas is quasi-two-dimensional. The strong background magnetic field leads to a strong anisotropy in the plasma particles' motion. While they are able to move more or less freely (up to magnetic mirror effects) along the magnetic field lines, the cross-field motion is restricted to slow drifts of the gyrocenters. This is reflected in the fact that the correlation lengths of the turbulent fluctuations are, respectively, of the order of 10 m and 1 cm. One may thus consider the turbulent dynamics to occur in planes perpendicular to the background magnetic field which are then coupled by the parallel motion. Interestingly, the simplest theoretical description of plasma turbulence, which is based on the two-dimensional model by Hasegawa and Mima [1], is isomorphic to the Charney equation in geophysics. This fact leads to close links between those two areas of research. Moreover, the Hasegawa-Mima-Charney equation is similar to the two-dimensional Navier-Stokes equation. This allows for many useful comparisons between these two systems.

Second, plasma turbulence is not universal. While in fluid turbulence, one is usually interested in the small spatial scales characterizing the inertial range which exhibit universal behavior, plasma turbulence is subject to a variety of drive and saturation mechanisms on different spatio-temporal scales. This means that often, an inertial range (in the strict sense of the word) does not exist. It is common to name the type of turbulence for a given set of plasma parameters after its dominant drive

mechanism, i.e., after a certain microinstability caused by radial gradients in the background density, electron temperature and/or ion temperature. Under typical circumstances, the turbulent transport in a plasma is dominated by the 'drive range' scales, and simulations of the large-eddy type may be performed, keeping the inertial range rather small and neglecting backscatter effects which tend to complicate respective investigations in fluid systems.

Third, plasma turbulence may be studied within a number of frameworks, ranging from simple fluid models to fully kinetic ones, and from simple 2D geometries to complicated 3D ones. So while there is little doubt that *ab initio* simulations are to be based on the so-called gyrokinetic equation (here, the fast gyrophase dependence has been removed analytically) in full toroidal geometry, it turns out to be useful to also study reduced systems. The latter allow for the identification of basic physical processes in systems that are easier to understand. On the other hand, the more complicated models are necessary to avoid artefacts from over-simplifications, and they also allow for direct comparisons with experimental results. Thus such a multi-level approach is very helpful.

Some special aspects of plasma turbulence: Structure formation, multi-scale dynamics, and particle statistics

One of the most fascinating aspects of plasma turbulence research is the tendency of the turbulent system to form spatial and spatio-temporal structures. As has been discovered a few years ago, the dominant eddies are sometimes strongly elongated in the radial (background gradient) direction.[2] These structures were named 'streamers', and their importance lies in the fact that the associated turbulent transport can exceed basic mixing-length type estimates by more than one order of magnitude. On the other hand, plasma turbulence is also often characterized by strong shear flows whose potential (stream function) depends solely on the radial coordinate.[3] These 'zonal flows' are also observed in a large number of other physical systems, ranging from laboratory shallow water experiments to atmospheric jets to zonal flows on the solar system's giant planets to accretion disks. Some examples are presented in other contributions to this book of proceedings. Since streamers and zonal flows are associated with flows in different perpendicular directions, one might expect that the plasma shows a tendency to create states which are dominated by either one or the other. Simulations confirm this intuition, and experiments looking for turbulent structures are also underway. The understanding of structure formation has seen some progress in recent years, but a lot of physics remains to be unravelled.

Another challenge in plasma turbulence research has to do with the fact that it tends to be driven simultaneously by several microinstabilities on different spatio-temporal scales. Only very recently have multi-scale simulations become feasible. The first of their kind are shown in Ref. [4]. This work allows for the conclusion that, in general, the superposition principle is violated. Some underlying mechanisms are discussed in that paper. More work is underway. In particular, the idea of catastrophe-like transitions between different flow states has been put forward by Itoh and co-workers (see Refs. [23,25] in Ref. [4]). It will be a prime goal in our future work to verify or else falsify this scenario, especially since it might be closely linked to the physics of transport barriers in which the turbulent diffusivities are suppressed by up to an order of magnitude over radially extended regions.

A third area of active research centers around the statistics of passive particles in turbulent plasmas. Although the transported plasma particles are usually not passive, this simplification still allows for valuable insights into the turbulent dynamics. E.g., Vlad and co-workers have shown in a series of papers since 1998 (see Ref. [5] and references therein) that their newly developed 'decorrelation trajectory method' is able to capture the trapping of particles in turbulent eddies, an effect which is lost if the commonly used Corrsin approximation is used. Recently, we were able to confirm their results by means of direct numerical simulations.[6] In the presence of finite Larmor radius effects,

the transport coefficients can even increase with respect to the zero Larmor radius limit, in contrast to naive expectations. Moreover, it was shown that particles embedded in a turbulent plasma may exhibit 'strange' (i.e., non-Gaussian) kinetics which can be described as a continuous time random walk (CTRW).[7] Such an approach may be of help in the attempt to understand nonlocal transport phenomena in MCF plasmas which cannot be captured by a conventional (Fickian) diffusion Ansatz.

Final remarks

In this short note, we tried to give the reader at least a flavor of some of the pressing open problems in plasma turbulence research. What makes this field particularly interesting is that it combines fundamental issues like structure formation or the statistics of particles in turbulent fields with the quest for a novel source of energy. We believe that an intensified dialogue between people working in plasma physics and those working in neighboring areas like fluid dynamics, geophysics, or astrophysics, would be beneficial to both sides. Maybe this paper is useful in that respect.

Acknowledgements

I would like to thank my co-workers T. Dannert and T. Hauff for valuable discussions, and the Helmholtz-Gesellschaft for financial support in the framework of the Helmholtz-University Young Investigators Group "Theory and ab initio simulation of plasma turbulence."

References

- [1] A. Hasegawa and K. Mima, Phys. Rev. Lett. **39** (1977) 205; Phys. Fluids **21** (1978) 87.
- [2] F. Jenko, W. Dorland, M. Kotschenreuther M, and B.N. Rogers, Phys. Plasmas **7** (2000) 1904.
- [3] P.H. Diamond, S.I. Itoh, K. Itoh, and T.S. Hahm, Plasma Phys. Control. Fusion **47** (2005) R35.
- [4] F. Jenko, Journal of Plasma and Fusion Research SERIES **6** (2004) 11.
- [5] M. Vlad *et al.*, Plasma Phys. Control. Fusion **46** (2004) 1051.
- [6] T. Hauff and F. Jenko, to be published.
- [7] D. del-Castillo-Negrete, B.A. Carreras, and V.E. Lynch, Phys. Rev. Lett. **94** (2005) 065003.

Dynamo and Alfvén effect in MHD turbulence

Wolf-Christian Müller¹, R. Grappin²

¹ Max-Planck-Institut für Plasmaphysik, 85748 Garching, Germany

² Observatoire Paris-Meudon, 92195 Meudon, France

This extended abstract reports a spectral relation between residual and total energy, $E_k^R = |E_k^M - E_k^K|$ and $E_k = E_k^K + E_k^M$ respectively, as well as the influence of an imposed mean magnetic field on the spectra. The proposed physical picture, which is confirmed by accompanying direct numerical simulations, embraces two-dimensional MHD turbulence, globally isotropic three-dimensional systems as well as turbulence permeated by a strong mean magnetic field. The results have direct implications on the current understanding of the energy cascade in MHD turbulence.

In the following reference is made to two high-resolution pseudospectral direct numerical simulations of incompressible MHD turbulence which we regard as paradigms for isotropic (I) and anisotropic (II) MHD turbulence. The dimensionless MHD equations

$$\partial_t \boldsymbol{\omega} = \nabla \times [\mathbf{v} \times \boldsymbol{\omega} - \mathbf{b} \times (\nabla \times \mathbf{b})] + \mu \Delta \boldsymbol{\omega} \quad (1)$$

$$\partial_t \mathbf{b} = \nabla \times (\mathbf{v} \times \mathbf{b}) + \eta \Delta \mathbf{b} \quad (2)$$

$$\nabla \cdot \mathbf{v} = \nabla \cdot \mathbf{b} = 0. \quad (3)$$

are solved in a 2π -periodic cube with spherical mode truncation to reduce numerical aliasing errors [1]. The equations include the flow vorticity, $\boldsymbol{\omega} = \nabla \times \mathbf{v}$, the magnetic field expressed in Alfvén speed units, \mathbf{b} , as well as dimensionless viscosity, μ , and resistivity, η .

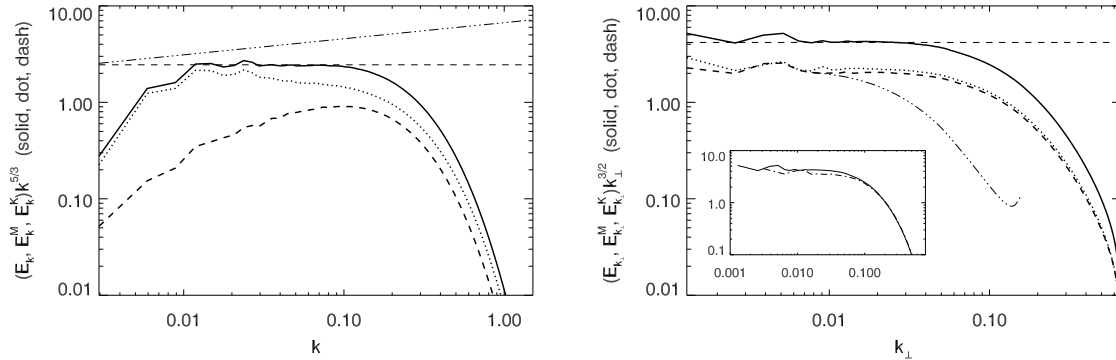


Figure 1: Total (solid), kinetic (dashed), and magnetic (dotted) energy in a 1024^3 simulation of decaying isotropic MHD turbulence (left) and in a $1024^2 \times 256$ simulation of anisotropic turbulence permeated by a strong mean magnetic field, $b_0 = 5$ (right, spectra are based on field perpendicular fluctuations). The dash-dotted line in the graph on the left illustrates a $k^{-3/2}$ power-law while the dashed horizontal lines indicate $k^{-5/3}$ -behavior (left) and $k^{-3/2}$ -scaling (right). The dash-dotted curve on the right shows the high- k part of the field-parallel total energy spectrum. The inset displays the difference in the perpendicular total energy spectrum when switching resolution from 512^2 (dash-dotted) to 1024^2 (solid).

Simulation I evolves globally isotropic freely decaying turbulence represented by 1024^3 Fourier modes. Total kinetic and magnetic energy are initially equal with $E^K = E^M = 0.5$. The dissipation

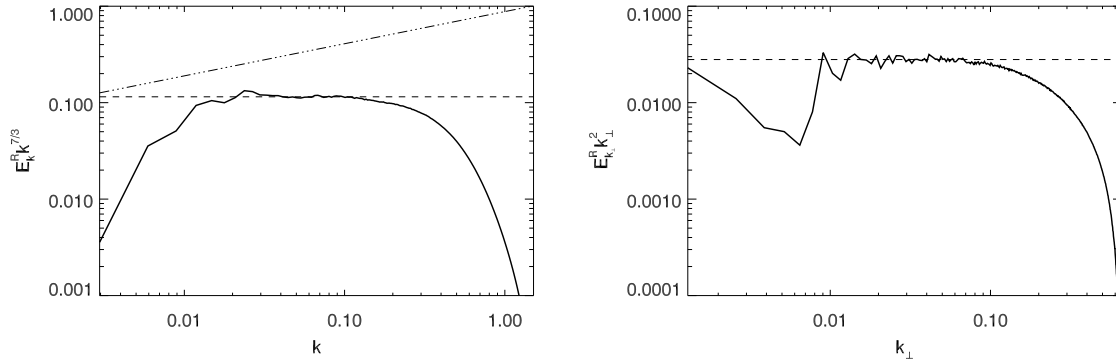


Figure 2: Compensated and space-angle-integrated residual energy spectrum, $E_k^R = |E_k^M - E_k^K|$, for the same systems as in Fig. 1 (isotropic:left, mean magnetic field: right). The dash-dotted line depicts scaling expected for a total energy spectrum following Iroshnikov-Kraichnan scaling.

parameters are set to $\mu = \eta = 1 \times 10^{-4}$. Case II is a $1024^2 \times 256$ forced turbulence simulation with an imposed constant mean magnetic field of strength $b_0 = 5$ in units of the large-scale rms magnetic field $\simeq 1$ with $\mu = \eta = 9 \times 10^{-5}$.

Fourier-space-angle integrated spectra of total, magnetic, and kinetic energy for case I are shown in Fig. 1 (left). To neutralize secular changes as a consequence of turbulence decay, amplitude normalization assuming a Kolmogorov total energy spectrum, $E_k \rightarrow E_k/(\varepsilon\mu^5)$, $\varepsilon = -\partial_t E$, with wavenumbers given in inverse multiples of the associated dissipation length, $\ell_D \sim (\mu^3/\varepsilon)^{1/4}$. Clearly, Kolmogorov scaling applies for the total energy in the well-developed inertial range, $0.01 \lesssim k \lesssim 0.1$.

In case II, pictured in Fig. 1 (right), strong anisotropy is generated due to turbulence depletion along the mean magnetic field, \mathbf{b}_0 . This is visible when comparing the normalized and time-averaged field-perpendicular one-dimensional spectrum, $E_{k_\perp} = \iint dk_1 dk_2 E(k_\perp, k_1, k_2)$ (solid line) with the field-parallel spectrum, defined correspondingly and adumbrated by the dash-dotted line in Fig. 1 (right).

While there is no discernible inertial range in the parallel spectrum, its perpendicular counterpart exhibits an interval with Iroshnikov-Kraichnan scaling, $E_{k_\perp} \sim k_\perp^{-3/2}$ [2, 3]. This is in contradiction with the anisotropic cascade phenomenology of Goldreich and Sridhar for strong turbulence predicting $E_{k_\perp} \sim k_\perp^{-5/3}$ [4].

The observation that field-parallel fluctuations are restricted to large scales while the perpendicular spectrum extends more than half a decade further suggests that the strong \mathbf{b}_0 constrains turbulence to quasi-two-dimensional field-perpendicular planes as is well known and has been shown for this particular system [5].

Another intriguing feature of system II is that $E_k^K \simeq E_k^M$ with only slight dominance of E^M (cf. Fig. 1, right) in contrast to the growing excess of spectral magnetic energy with increasing spatial scale for case I. Both states presumably represent equilibria between two competing nonlinear processes: field-line deformation by turbulent motions on the spectrally local time scale $\tau_{NL} \sim \ell/v_\ell \sim (k^3 E_k^K)^{-1/2}$ leading to magnetic field amplification (turbulent small-scale dynamo) and energy equipartition by shear Alfvén waves with the characteristic time $\tau_A \sim \ell/b_0 \sim (kb_0)^{-1}$ (Alfvén effect).

By using the spectral EDQNM equation for the residual energy in spectrally local and non-local approximations [6] and by assuming that the residual energy is a result of a dynamic equilibrium between turbulent dynamo and Alfvén effect, one obtains for stationary conditions and in the inertial

range,

$$E_k^{\text{R}} \sim kE_k^2 \sim \left(\frac{\tau_{\text{A}}}{\tau_{\text{NL}}} \right)^2 E_k. \quad (4)$$

with $\tau_{\text{A}} \sim (kb_0)^{-1}$, where b_0 is the mean magnetic field carried by the largest eddies, $b_0 \sim (E^{\text{M}})^{1/2}$, and by re-defining $\tau_{\text{NL}} \sim \ell/(v_\ell^2 + b_\ell^2)^{1/2} \sim (k^3 E_k)^{-1/2}$. The modification of τ_{NL} is motivated by the fact that turbulent magnetic fields are generally not force-free so that magnetic pressure and tension contribute to eddy deformation as well.

Apart from giving a prediction which allows to verify the proposed model of nonlinear interplay between kinetic and magnetic energy, relation (4) also has some practical utility. It is a straightforward consequence of (4) that the difference between possible spectral scaling exponents, which is typically small and hard to measure reliably, is enlarged by a factor of two in E_k^{R} . Even with the limited Reynolds numbers in today's simulations such a magnified difference is clearly observable (e.g. dash-dotted lines in Figs. 1 and 2).

In summary, based on the structure of the EDQNM closure equations for incompressible MHD a model of the nonlinear spectral interplay between kinetic and magnetic energy is formulated. The quasi-equilibrium of turbulent small-scale dynamo and Alfvén effect leads to a relation linking total and residual energy spectra, in particular $E_k^{\text{R}} \sim k^{-7/3}$ for $E_k \sim k^{-5/3}$ and $E_k^{\text{R}} \sim k^{-2}$ for $E_k \sim k^{-3/2}$. Both predictions are confirmed by high-resolution direct numerical simulations of isotropic turbulence exhibiting Kolmogorov scaling and forced anisotropic turbulence displaying Iroshnikov-Kraichnan scaling perpendicular to the mean field direction. The findings limit the possible validity of the Goldreich-Sridhar phenomenology to MHD turbulence with weak mean magnetic fields and emphasize the important role of the Iroshnikov-Kraichnan picture for a large class of turbulent MHD systems.

References

- [1] A. Vincent and M. Meneguzzi, *Journal of Fluid Mechanics* **225**, 1 (1991).
- [2] P. S. Iroshnikov, *Soviet Astronomy* **7**, 566 (1964), [*Astron. Zh.*, 40:742, 1963].
- [3] R. H. Kraichnan, *Physics of Fluids* **8**, 1385 (1965).
- [4] P. Goldreich and S. Sridhar, *Astrophysical Journal* **485**, 680 (1997).
- [5] W.-C. Müller, D. Biskamp, and R. Grappin, *Physical Review E* **67**, 066302 (2003).
- [6] R. Grappin, A. Pouquet, and J. Léorat, *Astronomy and Astrophysics* **126**, 51 (1983).

Radiatively-driven convection in ice-covered lakes: observations, LES, and bulk modelling

*Dmitrii V. Mironov*²

German Weather Service, Offenbach am Main, Germany

Introduction

Convection driven by radiation heating is discussed. Such regime of convection is encountered in ice-covered fresh-water lakes in late spring, when the snow cover overlying the ice disappears and the solar radiation penetrates the ice. The solar heating is vertically inhomogeneous, the upper layers gain more heat than the lower layers. As the water temperature is below the temperature of maximum density, volumetric radiation heating raises the water density leading to gravitational instability that drives convective motions. The structure of the evolving temperature profile shows evidence of penetrative convection.

Following the pioneering study by Birge [2] and the first systematic study of radiatively-driven convection in an ice-covered fresh-water lake by Farmer [5], a number of observational and modelling studies have been performed that extended our knowledge of radiatively-driven convection in ice-covered lakes (summaries are given in [5] and [18]). In this note, a brief summary of some recent findings is presented. A bulk mixed-layer scaling suitable for radiatively-driven convection, the flow structures present in the convective boundary layer (CBL), some turbulence statistics, and a bulk model of radiatively-driven CBL are briefly discussed. The reader is referred to [1], [5], [6], [7], [9], [10], [13], [14], [16], [17] and [18] for a more detailed account.

Data

Measurements of temperature fluctuations beneath the ice were taken in Lake Vendyurskoe during the period 19–24 April 1999, using a temperature microstructure profiler [6]. The dissipation rate ϵ of turbulence kinetic energy (TKE) was determined by fitting the Batchelor-type model temperature spectrum to the measured temperature spectra (see [6] for details of the procedure). The data presented in Fig. 2(a) are the result of averaging over eleven profiles.

Large-eddy simulation (LES) data reported in [14], [13] and [18] are used. Convection is simulated in a rectangular domain, doubly periodic in the horizontal x and y directions. Cases T1, T2 and T4 are the low resolution runs with $64 \times 64 \times 64$ grid points. Case L1 has higher resolution with $144 \times 144 \times 100$ grid points in the x , y and z directions, respectively. Cases T1 and L1 mimic the CBL observed in Lake Vendyurskoe, Karelia, north-western Russia, 21–23 April 1995 ([9], [10]). Case T2 mimics the CBL observed in Lake Peters, Alaska, 16 May – 19 June 1959 [1]. A two-band approximation of the decay law for the kinematic flux of solar radiation (i.e. the radiation heat flux divided by density and specific heat of water), $I(t, z) = I_s(t)[a_1 \exp(-\gamma_1 z) + a_2 \exp(-\gamma_2 z)]$, is used in cases T1 and L1, and a one-band approximation ($a_1 = 1$ and $a_2 = 0$) in case T2. Estimates of the solar radiation flux I_s at the lower surface of the ice, of the fractions a_1 and a_2 of the total radiation flux for different wavelength bands, and of the attenuation coefficients γ_1 and γ_2 are taken from measurements. Case T4 is similar to case T1, but a one-band approximation of the decay law is used, and the surface radiation flux is

²Corresponding address: Deutscher Wetterdienst, Abteilung Meteorologische Analyse und Modellierung, AP2003, Kaiserleistr. 29/35, D-63067 Offenbach am Main, Germany. Phone: +49-69-8062 2705, fax: +49-69-8062 3721, email: dmitrii.mironov@dwd.de

set to an artificially large value. Further details of the simulations performed are given in [14], [13] and [18].

The turbulence statistics are derived by averaging over horizontal planes and over a number of recorded time steps. The sampling period covers several large-eddy turnover times, following the model spin-up period. The turbulence quantities are normalised by the convective scales [18] of length, $h - \delta$, velocity, $w_R = [-(h - \delta)B_R]^{1/3}$, and temperature, $\theta_R = I(\delta)/w_R$, prior to time averaging. Here, $B_R = \beta[\theta(\delta)]I(\delta) + \beta[\theta(h)]I(h) - 2(h - \delta)^{-1} \int_{\delta}^h I dz$ is the buoyancy flux scale, and $\beta = \beta(\theta)$ is the buoyancy parameter that depends on temperature θ . These scales are pertinent to convection driven by radiation heating which is not confined to the boundary but is distributed over the water column. The depth h to the CBL bottom is defined from the ice-water interface to the level in the entrainment zone where the vertical buoyancy flux is a minimum. The depth δ of the stably stratified surface layer that separates a convectively mixed layer from the lower surface of the ice is defined from the ice-water interface to the level of the first zero-crossing of the vertical buoyancy flux. Results from simulations of radiatively-driven convection are compared with the results from simulation of boundary-layer convection driven by the surface buoyancy flux. The LES data from the case R0 reported in [12] are used, where the now classical Deardorff ([3], [4]) convective scales, h , $w_* = (\beta Q_s h)^{1/3}$ and $\theta_* = Q_s/w_*$, Q_s being the surface temperature flux, are used to make turbulent quantities dimensionless.

The flow structure

Figure 1 illustrates the flow structure in simulation L1 of radiatively-driven convection and in simulation R0 of convection driven by the surface buoyancy flux. The $x - y$ plane vertical-velocity and temperature snapshots are taken halfway through the CBL. Elongated patterns of descending motions and of positive temperature anomalies are readily identified in case L1. These patterns form a quasi-regular mesh. The picture is rather different from that in simulation R0 of the CBL driven by the surface buoyancy flux. More isolated structures often referred to as convective plumes are readily identified in the central part of the surface-flux-driven CBL (see e.g. [11], [19] and [15] for discussions).

Mixed-layer scaling

Figure 2(a) shows the TKE dissipation rate from measurements and from LES. Numerical and empirical data agree closely with each other. The dissipation rate profiles made dimensionless with the length scale $h - \delta$ and the velocity scale w_R show a clear tendency to group together, whereas the dimensional values of ϵ (not shown) differ by more than an order of magnitude between the simulations. Figure 2(b) shows the dimensionless TKE obtained from LES. Although the dimensional TKE values (not shown) differ significantly between the four cases, dimensionless TKE profiles group together nicely. This lends considerable support to the mixed-layer scaling based on $h - \delta$ and w_R ([5], [18]).

Skewness

Figure 3 shows the vertical velocity skewness $S_w = \langle w'^3 \rangle / \langle w'^2 \rangle^{3/2}$ and the temperature skewness $S_\theta = \langle \theta'^3 \rangle / \langle \theta'^2 \rangle^{3/2}$. Primes denote turbulent fluctuations. The LES approximations to the ensemble means are denoted by angle brackets. In both simulations L1 and R0, the vertical velocity field and the temperature field are positively skewed, indicating that the downdraughts and positive temperature anomalies are more localised than updraughts and negative temperature anomalies. Both S_w and S_θ are larger in simulation R0 than in simulation L1, the difference in S_θ being larger in the mid-CBL than the difference in S_w . As the skewness is indicative of the importance of non-local effects in turbulence, Figure 3 suggests that turbulence in the radiatively-driven CBL is less non-local than in the CBL driven by the surface buoyancy flux. This result is corroborated by the analysis of the

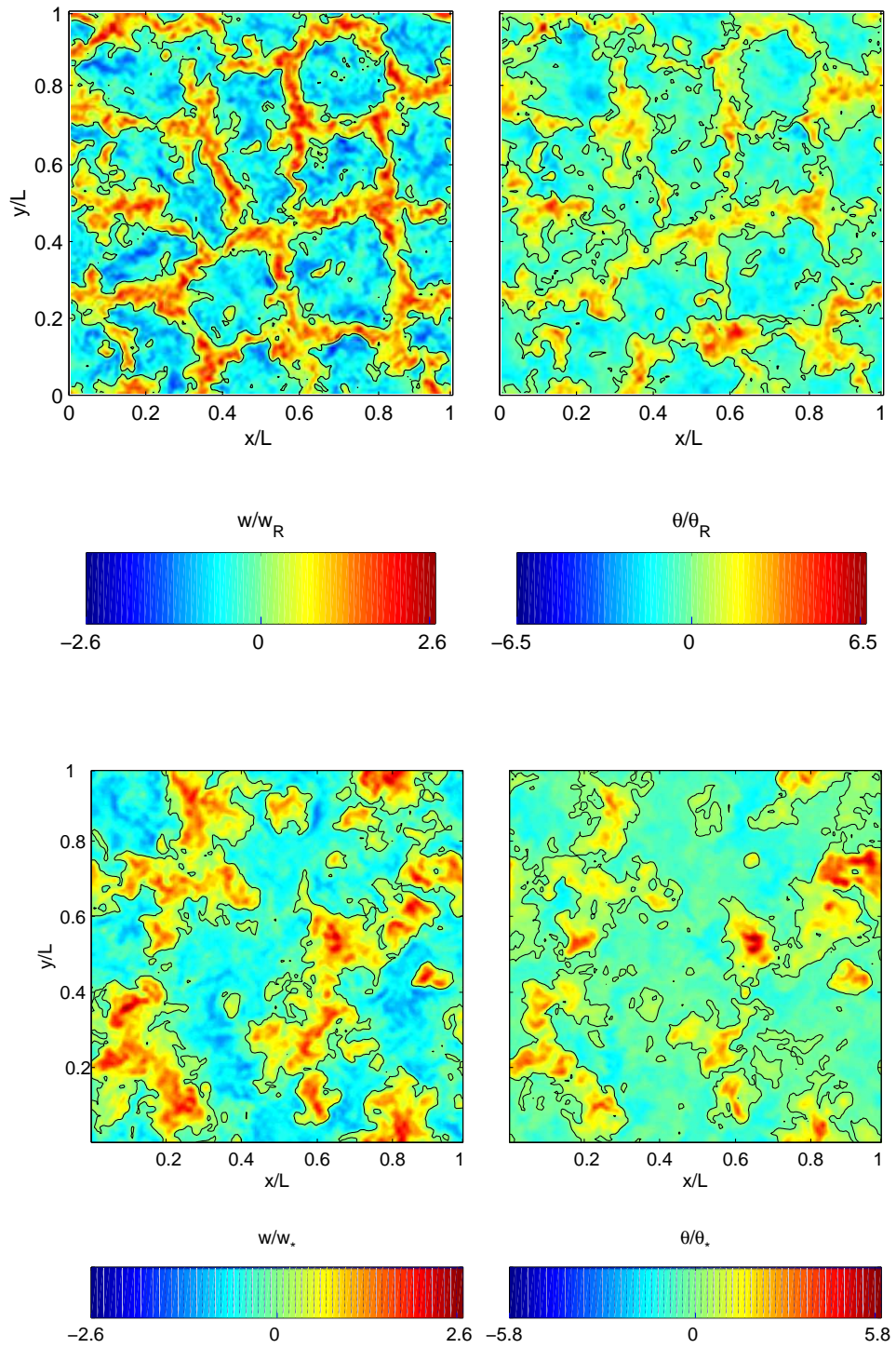


Figure 1: Horizontal cross-sections of the dimensionless vertical-velocity fluctuations, w/w_R and w/w_* , and of the dimensionless temperature fluctuations, θ/θ_R and θ/θ_* , about their horizontal means for simulation L1 – upper panels, and for simulation R0 – lower panels. L is the numerical domain size in the x and y horizontal directions. Red (blue) colours correspond to high (low) values of $w/w_R, w/w_*, \theta/\theta_R$ and θ/θ_* as shown with the colour scale bars. Lines are zero contours.

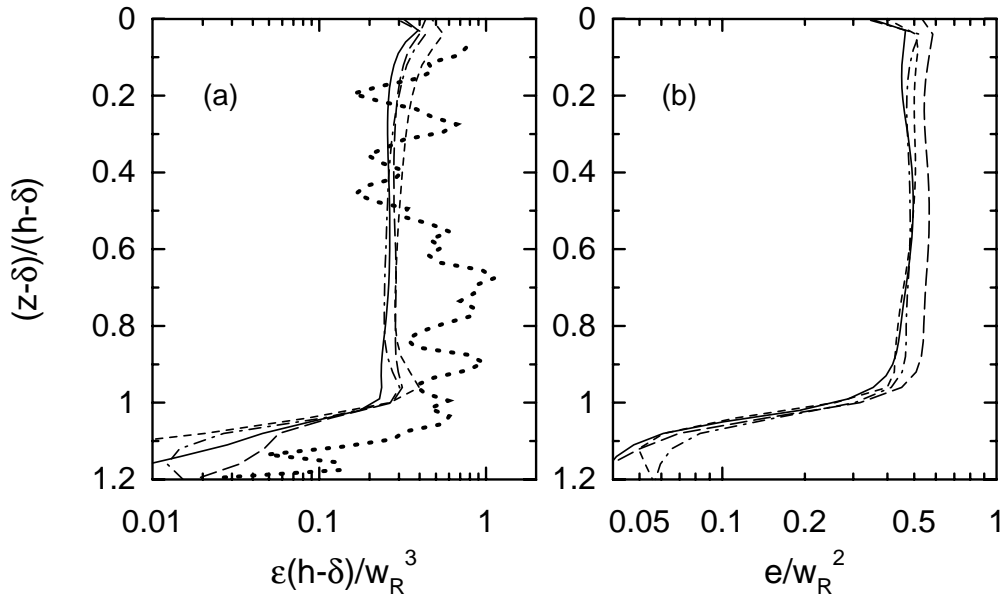


Figure 2: (a) dimensionless TKE dissipation rate $\epsilon(h-\delta)/w_R^3$ and (b) dimensionless turbulence kinetic energy e/w_R^2 versus dimensionless depth $(z-\delta)/(h-\delta)$. Heavy dotted curve shows measurements in Lake Vendyurskoe [6]. Thin curves show LES data ([14], [13], [18]) for simulation L1 – solid curves, T1 – dot-dashed curves, T2 – short-dashed curves, and T4 – long-dashed curves.

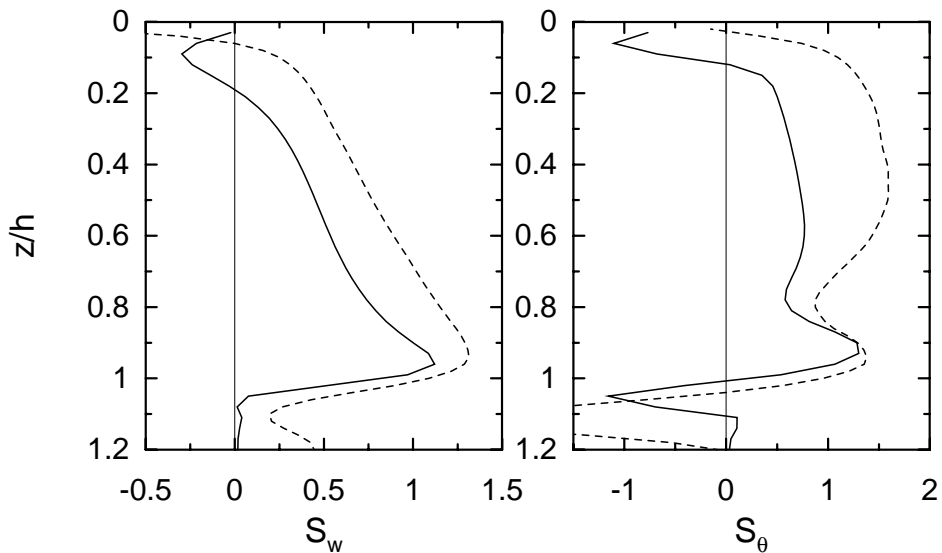


Figure 3: Vertical profiles of the vertical-velocity skewness S_w and of the temperature skewness S_θ for simulations L1 of radiatively-driven convection – solid curves, and R0 of convection driven by the surface buoyancy flux – dashed curves.

budget of the temperature variance ([14], [13]). The relative importance of the third-order turbulent transport term in the temperature variance budget (not shown) is reduced in case L1 as compared to R0.

Mixed-layer model

A bulk mixed-layer model is developed and applied to simulate the CBL deepening ([16], [17], [18]). The model is based on a four-layer self-similar representation of the evolving temperature profile, where a stably stratified surface layer, a convectively mixed layer, an interfacial entrainment layer, and a stably stratified quiescent layer are distinguished. A stationary solution to the heat transfer equation is used to describe the structure of the stably stratified layer just beneath the ice [1]. The structure of the entrainment layer is approximated by the zero-order temperature jump [8]. The evolution equation for the mixed-layer depth, the so-called entrainment equation, is derived, using the TKE budget equation integrated over the mixed layer and the mixed-layer scaling. The model is favourably tested against data from observations in a number of temperate and polar lakes [18]. Figure 4 illustrates the model performance.

An extension of the mixed-layer model for the case of salt water is proposed and tested against observations ([7], [18]). Although the salinity is very low in most temperate and polar lakes, its dynamical effect can be significant when the water temperature is close to the temperature of maximum density.

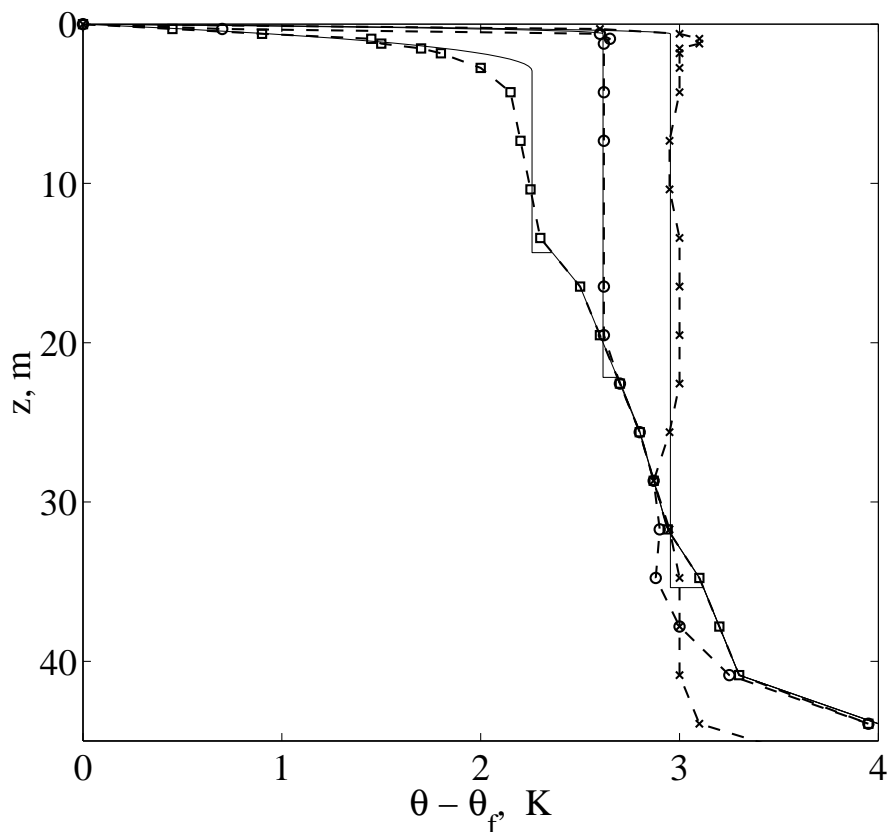


Figure 4: Successive temperature profiles in Lake Peters, Alaska, 16 May – 19 June 1959. θ_f is the fresh-water freezing point. Solid curves are computed with the mixed-layer model. Symbols show measured profiles [1]. A one-band approximation of the exponential decay law for solar radiation flux is used with $\gamma = 0.3 \text{ m}^{-1}$. The surface radiation flux I_s increases linearly from $4 \cdot 10^{-7} \text{ K} \cdot \text{m} \cdot \text{s}^{-1}$ to $8 \cdot 10^{-6} \text{ K} \cdot \text{m} \cdot \text{s}^{-1}$ over the period of simulation.

Concluding remarks

Apart from being a prominent example of naturally occurring convective flows, a deep insight into the structure and transport properties of radiatively-driven convection in ice-covered lakes is important in many respects. An understanding of convection under the ice during spring is required for accurate interpretation and prediction of chemical and biological processes in lakes. For example, convective motions help suspend non-motile phytoplankton species in the surface layer, enhancing their growth. Radiatively-driven convection in ice-covered lakes provides an excellent test case for turbulence models. It is a rare example of geophysical convective flows where there is no mean shear. Data sets generated through measurements in ice-covered lakes and through LES can be used to test and further develop turbulence models of convective flows.

Acknowledgements

This work was partially supported by the EU Commissions through the Projects INTAS-97-0734 and CARTUM (EC Contract Mas3-CT98-0172).

References

- [1] Barnes, D. F., and J. E. Hobbie, 1960: Rate of melting at the bottom of floating ice. *Geological Survey Research – Short Papers in the Geological Sciences*, B392-B394.
- [2] Birge, E. A., 1910: The apparent sinking of ice in lakes. *Science*, **32**, 81–82.
- [3] Deardorff, J. W., 1970: Preliminary results from numerical integrations of the unstable planetary boundary layer. *J. Atmos. Sci.*, **27**, 1209–1211.
- [4] Deardorff, J. W., 1970: Convective velocity and temperature scales for the unstable planetary boundary layer and for Rayleigh convection. *J. Atmos. Sci.*, **27**, 1211–1213.
- [5] Farmer, D. M., 1975: Penetrative convection in the absence of mean shear. *Quart. J. Roy. Meteor. Soc.*, **101**, 869–891.
- [6] Jonas, T., A. Y. Terzhevik, D. V. Mironov, and A. Wüest, 2003: Investigation of radiatively-driven convection in an ice covered lake using temperature microstructure technique. *J. Geophys. Res.*, **108**, 14-1–14-18. doi:10.1029/2002JC001316
- [7] Kirillin, G., D. Mironov, and A. Terzhevik, 2001: Radiatively-driven convection in ice-covered lakes: the effect of salt concentration. *Proc. of the 6th Workshop on Physical Processes in Natural Waters*, X. Casamitjana, Ed., University of Girona, Girona, Spain, 199–203.
- [8] Lilly, D. K., 1968: Models of cloud-topped mixed layers under a strong inversion, *Quart. J. Roy. Meteor. Soc.*, **94**, 292–309.
- [9] Malm, J., A. Terzhevik, L. Bengtsson, P. Boyarinov, A. Glinsky, N. Palshin, and M. Petrov, 1997: Temperature and salt content regimes in three shallow ice-covered lakes. 1. Temperature, salt content, and density structure. *Nordic Hydrology*, **28**, 99–128.
- [10] Malm, J., A. Terzhevik, L. Bengtsson, P. Boyarinov, A. Glinsky, N. Palshin, and M. Petrov, 1997: Temperature and salt content regimes in three shallow ice-covered lakes. 2. Heat and mass fluxes. *Nordic Hydrology*, **28**, 129–152. *Nordic Hydrology*, **28**, 129–152.

- [11] Mason, P. J., 1989: Large-eddy simulation of the convective atmospheric boundary layer. *J. Atmos. Sci.*, **46**, 1492–1516.
- [12] Mironov, D. V., 2001: Pressure-potential-temperature covariance in convection with rotation. *Quart. J. Roy. Meteor. Soc.*, **127**, 89–110.
- [13] Mironov, D. V., 2001: Penetrative convection driven by the radiation heating: a study of spring convection in ice-covered lakes. *Proc. of the 2001 International Symposium on Environmental Hydraulics*, Arizona State University, Tempe, Arizona, USA.
- [14] Mironov, D. V., S. D. Danilov, and D. J. Olbers, 2001: Large-eddy simulation of radiatively-driven convection in ice-covered lakes. *Proc. of the 6th Workshop on Physical Processes in Natural Waters*, X. Casamitjana, Ed., University of Girona, Girona, Spain, 71–75.
- [15] Mironov, D. V., V. M. Gryanik, C.-H. Moeng, D. J. Olbers, and T. H. Warncke, 2000: Vertical turbulence structure and second-moment budgets in convection with rotation: a large-eddy simulation study. *Quart. J. Roy. Meteor. Soc.*, **126**, 477–515.
- [16] Mironov, D. V., and A. Yu. Terzhevik, 1998: Spring convection in an ice-covered lake: observations, scaling and a simple mixed-layer model. *Proc. 3rd Workshop on Physical Processes in Natural Waters*, B. Boehrer and M. Schimmele, Eds., UFZ-Umweltforschungszentrum Leipzig-Halle GmbH, Sektion Gewässerforschung Magdeburg, Magdeburg, Germany, 79–83.
- [17] Mironov, D. V., and A. Yu. Terzhevik, 2000: Spring convection in ice-covered fresh-water lakes. *Izv. RAS. Fizika Atmosfery i Okeana*, **36**, 681–688. (in Russian; English translation: *Izvestiya, Atmospheric and Oceanic Physics*, p. 627–634)
- [18] Mironov, D., A. Terzhevik, G. Kirillin, T. Jonas, J. Malm, and D. Farmer, 2002: Radiatively driven convection in ice-covered lakes: Observations, scaling, and a mixed layer model. *J. Geophys. Res.*, **107**, 7-1–7-16. doi:10.1029/2001JC000892
- [19] Schmidt, H., and U. Schumann, 1989: Coherent structure of the convective boundary layer derived from large-eddy simulation. *J. Fluid Mech.*, **200**, 511–562.
- [20] Zilitinkevich, S. S., 1991: *Turbulent Penetrative Convection*. Avebury Technical, Aldershot, 179 pp.

Non-local features of turbulence in stably stratified geophysical boundary layers

Sergej S. Zilitinkevich^{1,2}

¹ Division of Atmospheric Sciences, University of Helsinki, Finland
(postal address: FMI, Vuorikatu 15 A, P.O. Box 503, 00101 Helsinki, Finland;
e-mail: Sergej.Zilitinkevichfmi.fi)

² Nansen Environmental and Remote Sensing Centre / Bjerknes Centre for Climate Research, Bergen, Norway

Summary

Turbulent boundary layers control the exchange processes between the atmosphere and the ocean/ice/land. The key practical problem is to determine the momentum, energy and matter fluxes in a wide range of boundary-layer regimes from stable and neutral to convective. This paper focuses on recently recognised non-local mechanisms typical of stable stratification, first of all, on the effect of the free-flow stability on vertical transports in turbulent boundary layers. This work is motivated by necessity to improve boundary-layer parameterisations in modern, very high resolution environmental models, particularly, in coupled atmosphere-hydrosphere-biosphere models. Theoretical results are compared with data from large-eddy simulation (LES) and data from field or lab experiments.

It is common knowledge that basic features of the stable boundary layer (SBL) exhibit a noticeable dependence on the free-flow static stability and baroclinicity. However, the concern of the traditional boundary-layer meteorology was almost without exception the barotropic nocturnal SBL, which develops at mid latitudes on the background of a neutral or slightly stable residual layer. The latter separates the SBL from the free atmosphere. It is not surprising that the nature of turbulence in the nocturnal SBLs is basically local, and their integral features do not depend on the properties of the free flow. The near-surface and the inner portions of these layers are well described by the Monin-Obukhov and the Nieuwstadt similarity theories, respectively. The nocturnal SBLs are sufficiently accurately modelled using traditional, comparatively simple local closure schemes.

An alternative type of the SBL frequently observed in Polar and coastal regions is the long-lived SBL that is the layer in which the stable stratification is maintained day and night. Then no residual layer is observed, so that the SBL is placed immediately below the stably stratified free flow. Under these conditions, the turbulent transports of momentum and scalars even in the surface layer - far away from the SBL outer boundary - depend on the free-flow Brunt-Väisälä frequency, N . Furthermore, integral measures of the long-lived SBLs (their depths and the resistance law functions) depend on N and also on the baroclinic shear, S . One of essential mechanisms responsible for non-local features of the long-lived SBLs is the damping effect of N on vertical extension of coherent eddies in the upper part of the SBL. The above reasoning obviously calls for revision of the traditional theory. The papers quoted in References and reflected in this presentation include the following developments:

- *Generalised scaling for the surface layer turbulence accounting for the distant effect of the free-flow stability.* In the nocturnal SBL, this scaling is consistent with the classical Monin-Obukhov theory.
- *SBL depth formulation accounting for the free-flow stability, baroclinicity and non-steady processes.* It covers a wide range of regimes overlooked in earlier works and shows quite narrow limits of applicability of the widely used bulk Richardson number approach. For the truly neutral

planetary boundary layer it yields the Rossby-Montgomery depth-scale and for the nocturnal SBL, the Zilitinkevich depth-scale.

- *Generalised SBL bulk resistance and heat/mass transfer laws accounting for the effects of the free-flow stability and baroclinicity on the A, B, C and D-stability functions.* The inclusion of the dependences on N and S results in essential collapse of LES data on these functions. Thus the resistance and heat/mass transfer laws are rehabilitated as a practical tool the SBL parameterisation. This approach has no alternative in very shallow SBLs, where traditional surface-layer flux-profile relationships become inapplicable.

The above theoretical results are verified against LES and atmospheric data. The new theory answers a number of questions, which looked puzzling until present, in particular, how well-developed turbulence is maintained in the stable surface layer at much larger Richardson numbers than the classical theory permits. It affords development of principally improved SBL parameterisations for use in applied environmental models.

The physical nature of the stably stratified turbulent layers in the ocean is principally the same as in the long-lived atmospheric SBL. In both cases large eddies in the boundary layer are strongly affected by the static stability in the adjacent free flow (the thermocline in the ocean or lakes), which causes considerable reduction of the vertical extension of the vertical turbulent length scales. Thus the above developments could be reformulated in oceanographic term and after appropriate modification (in particular including the Langmuir circulations) and validation employed in ocean modelling.

References

- [1] S. Zilitinkevich and D.V. Mironov, A multi-limit formulation for the equilibrium depth of a stably stratified boundary layer. *Boundary-Layer Meteorol.*, **81**, 325-351 (1996).
- [2] S. Zilitinkevich, P.-E. Johansson, D.V. Mironov and A. Baklanov, A similarity-theory model for wind profile and resistance law in stably stratified planetary boundary layers. *Journal of Wind Engineering and Industrial Aerodynamics*, **74-76**, 209-218 (1998).
- [3] S. Zilitinkevich and P. Calanca, An extended similarity-theory for the stably stratified atmospheric surface layer. *Quart. J. Roy. Met. Soc.*, **126**, 1913-1923 (2000).
- [4] V. Perov, and S. Zilitinkevich, Application of an extended similarity theory for the stably stratified atmospheric surface layer to the HIRLAM. *HIRLAM Newsletter*, **35**, 137-142 (2000).
- [5] V. Perov, S. Zilitinkevich and K.-I Ivarsson, Implementation of new parameterisation of the surface turbulent fluxes for stable stratification in the 3-D HIRLAM. *HIRLAM Newsletter*, **37**, 60-66 (2001).
- [6] S. Zilitinkevich, A. Baklanov, J. Rost, A.-S. Smedman, V. Lykosov and P. Calanca, Diagnostic and prognostic equations for the depth of the stably stratified Ekman boundary layer. *Quart. J. Roy. Met. Soc.*, **128**, 25-46 (2002).
- [7] S. Zilitinkevich, Third-order transport due to internal waves and non-local turbulence in the stably stratified surface layer. *Quart. J. Roy. Met. Soc.*, **128**, 913-925 (2002).
- [8] T. Soomere and S.S. Zilitinkevich, Supplement to "Third-order transport due to internal waves and non-local turbulence in the stably stratified surface layer". *Quart. J. Roy. Met. Soc.*, **128**, 1029-1031 (2002).

- [9] S.S. Zilitinkevich, V.L. Perov and J.C. King, Near-surface turbulent fluxes in stable stratification: calculation techniques for use in general circulation models. *Quart. J. Roy. Met. Soc.*, **128**, 1571-1587 (2002).
- [10] S.S. Zilitinkevich and A. Baklanov, Calculation of the height of stable boundary layers in practical applications. *Boundary-Layer Meteorol.*, **105**, 389-409 (2002).
- [11] S.S. Zilitinkevich and I.N. Esau, On integral measures of the neutral, barotropic planetary boundary layers. *Boundary-Layer Meteorol.*, **104**, 371-379 (2002).
- [12] S.S. Zilitinkevich and I.N. Esau, The effect of baroclinicity on the depth of neutral and stable planetary boundary layers. *Quart. J. Roy. Met. Soc.*, **129**, 3339-3356 (2003).
- [13] S.S. Zilitinkevich and I.N. Esau, Resistance and heat transfer laws for stable and neutral planetary boundary layers: Old theory, advanced and re-evaluated. *Quart. J. Roy. Met. Soc.*, in press (2005).

A new spectral theory of turbulent flows with stable stratification

*S. Sukoriansky*¹, *B. Galperin*²

¹Department of Mechanical Engineering, Ben-Gurion University of the Negev, Beer-Sheva 84105, Israel

²College of Marine Science, University of South Florida, St. Petersburg, FL 33701, USA

Introduction

Turbulence is one of the principal unsolved problems in physics. Difficulties in the theory of turbulence stem from strong nonlinearity of the equations of motion. Various instabilities at large Reynolds number Re lead to excitation of secondary flows, such as vortices and waves, developing on different spatial and temporary scales. Nonlinear interactions between motions on various scales generate highly irregular, “stochastic” flow field. Solutions exist only for simplest flows that are locally isotropic and depend on a single nondimensional parameter Re .

In the context of geophysical, planetary and astrophysical turbulence, turbulent flows are further complicated by such factors as spatial anisotropy and waves. On relatively small scales, gravity force causes density stratification and emergence of internal gravity waves. On larger scales, Coriolis force, caused by the planetary rotation, leads to flow quasi-two-dimensionalization and emergence of inertial waves. On yet larger, planetary scales, the variation of the Coriolis force with latitude, or the so-called β -effect, leads to the emergence of Rossby waves and flow zonalization. Models of turbulence used to simulate all these flows must be capable of accounting for different effects on different scales. Reynolds averaging does not differentiate between scales lumping them all together. On the other hand, a spectral approach does account for scale-specific phenomena. This presentation is concerned with the development of a spectral model for turbulent flows with stable density stratification.

Basics of the new spectral theory of turbulent flows with stable stratification

The theory is developed for a fully three-dimensional turbulent flow field with imposed vertical, stabilizing temperature gradient. The flow is governed by the momentum, temperature and continuity equations in the Boussinesq approximation,

$$\frac{\partial \mathbf{u}}{\partial t} + (\mathbf{u}\nabla)\mathbf{u} - \alpha g T \hat{e}_3 = \nu_0 \nabla^2 \mathbf{u} - \frac{1}{\rho} \nabla P + \mathbf{f}^0, \quad (1)$$

$$\frac{\partial T}{\partial t} + (\mathbf{u}\nabla)T + \frac{d\Theta}{dz} u_3 = \kappa_0 \nabla^2 T, \quad (2)$$

$$\nabla \mathbf{u} = 0, \quad (3)$$

where, P is the pressure, ρ is the constant reference density, ν_0 and κ_0 are the molecular viscosity and diffusivity, respectively, α is the thermal expansion coefficient, g is the acceleration due to gravity directed downwards, and T is the fluctuation of mean temperature Θ . The external solenoidal force \mathbf{f}^0 mimics the effect of large-scale instabilities and maintains turbulence in a statistically steady state. Note that the temperature equation (2) does not involve a separate forcing implying that the temperature fluctuations are excited by the velocity fluctuations.

The central problem in solving Eqs. (1-3) is dealing with the nonlinearity. Another, but less severe problem is caused by the coupling of equations (1) and (2). It would be natural to think of a perturbative solution based upon the expansion in powers of Re . However, with large Re , this expansion would be strongly divergent.

The spectral approach appears to be the most appropriate to deal with both problems. The general idea of this approach: since Re is small for smallest scales of motion, one can derive a perturbative solution for these small scales. Then, using this solution, one can perform averaging over infinitesimal band of small scale modes. This averaging yields corrections to “effective” or “eddy” viscosity and diffusivity. Then, one repeats this procedure for the next band of smallest scales, etc. In this process of successive small scale modes elimination the eddy viscosity and eddy diffusivity increase while effective Re based upon eddy viscosity remains $O(1)$.

Fourier-transformed velocity and temperature equations

Using continuity equation (3), eliminate pressure from the momentum equation. Then, write the momentum equation in a self-contained form using formal solution to the temperature equation:

$$u_\beta(\hat{k}) = G_{\alpha\beta}(\hat{k})f_\alpha^0(\hat{k}) - \frac{i}{2}G_{\alpha\beta}(\hat{k})P_{\alpha\mu\nu}(\mathbf{k}) \int u_\mu(\hat{q})u_\nu(\hat{k} - \hat{q}) \frac{d\hat{q}}{(2\pi)^4}, \quad (4)$$

$$T(\hat{k}) = G_T(\hat{k})f_T(\hat{k}) - iG_T(\hat{k})k_\alpha \int u_\alpha(\hat{q})T(\hat{k} - \hat{q}) \frac{d\hat{q}}{(2\pi)^4}, \quad (5)$$

where $\hat{k} = (\omega, \mathbf{k})$ is a four-dimensional vector in Fourier space. The velocity Green function, $G_{\alpha\beta}(\hat{k})$, has a non-diagonal tensorial structure that reflects the anisotropy introduced by stable stratification,

$$G_{\alpha\beta}(\omega, \mathbf{k}) = G(\omega, \mathbf{k}) [\delta_{\alpha\beta} + A(\omega, \mathbf{k})P_{\alpha 3}(\mathbf{k})\delta_{\beta 3}]. \quad (6)$$

The auxiliary Green function, $G(\omega, \mathbf{k})$, is given by

$$G(\omega, \mathbf{k}) = (-i\omega + \nu_h k^2 + \nu_z k_3^2)^{-1}, \quad (7)$$

and the temperature Green function is

$$G_T(\omega, \mathbf{k}) = (-i\omega + \kappa_h k^2 + \kappa_z k_3^2)^{-1}, \quad (8)$$

where ν_h , ν_z , κ_h and κ_z are horizontal and vertical eddy viscosities and eddy diffusivities, and $P_{\alpha\beta}(\mathbf{k})$ is the projection operator. The function $A(\omega, \mathbf{k})$ in Eq. (6) is given by

$$A(\omega, \mathbf{k}) = -\frac{N^2}{(-i\omega + \nu_h k^2 + \nu_z k_3^2)(-i\omega + \kappa_h k^2 + \kappa_z k_3^2) + N^2 \sin^2 \phi}, \quad (9)$$

where $N \equiv (\alpha g \frac{d\Theta}{dz})^{1/2}$ is the buoyancy, or Brunt-Väsälä frequency, and ϕ is the angle between \mathbf{k} and the vertical. Note that the complex poles in (9) are due to the presence of N in the denominator of A . These poles reflect the appearance of internal waves in turbulent flow field. Finally, the forcing in Eq. (5) is

$$f_T(\hat{k}) = -\frac{d\Theta}{dz}u_3(\hat{k}), \quad (10)$$

expressing the fact that the temperature fluctuations are governed by the velocity fluctuations.

Quasi-Normal Scale Elimination Model (QNSE)

We seek the solutions in the form of the Langevin equations:

$$u_\alpha(\omega, \mathbf{k}) = G_{\alpha\beta}(\omega, \mathbf{k})f_\beta(\omega, \mathbf{k}), \quad (11)$$

$$T(\omega, \mathbf{k}) = -\frac{d\Theta}{dz}G_T(\omega, \mathbf{k})u_3(\omega, \mathbf{k}). \quad (12)$$

Here, $f_\beta(\omega, \mathbf{k})$ is a stochastic force which represents the stirring of a given velocity mode by all other modes. It is postulated to be Gaussian, solenoidal, zero-mean, white noise in time and homogeneous in space. Thus,

$$\langle f_\alpha(\omega, \mathbf{k})f_\beta(\omega', \mathbf{k}') \rangle \sim \epsilon k^{-3}P_{\alpha\beta}(\mathbf{k})\delta(\omega + \omega')\delta(\mathbf{k} + \mathbf{k}'). \quad (13)$$

The Green functions $G_{\alpha\beta}(\omega, \mathbf{k})$ and $G_T(\omega, \mathbf{k})$ include effective viscosities and diffusivities and describe the damping of a mode \mathbf{k} by nonlinear interactions with all other modes. The method based upon Eqs. (11) and (12) is a *mapping* of the Fourier-transformed velocity and temperature fields onto quasi-Gaussian fields whose modes are governed by the Langevin equations. The parameters of the mapping, i.e., eddy viscosities and eddy diffusivities, are calculated using systematic process of successive averaging over small shells of velocity and temperature modes that eliminates them from the equations of motion. To ensure correct energy balance, the amplitude of the modal forcing is related to the dissipation rate ϵ and the buoyancy destruction, i.e., balance is enforced between energy gain due to the eddy forcing and energy loss due to the eddy damping. The energy budget is systematically adjusted for every mode.

Corrections to effective viscosities and diffusivities

The mathematical procedure of the small-scale modes elimination algorithm is mathematically involved and cannot be described here; the details are given in [1]. Analytical expressions for corrections for the inverse velocity and temperature Green functions after one step in the small-scale elimination procedure are:

$$\Delta G_{\alpha\beta}^{-1}(\omega, k, k_3) = P_{\alpha\mu\theta}(\mathbf{k}) \int^> P_{\nu\sigma\beta}(\mathbf{k} - \mathbf{q})G_{\theta\nu}(\omega - \Omega, |\mathbf{k} - \mathbf{q}|, k_3 - q_3)U_{\mu\sigma}(\Omega, q, q_3) \frac{d\mathbf{q} d\Omega}{(2\pi)^4}, \quad (14)$$

$$\Delta G_T^{-1}(\omega, k, k_3) = k_\alpha k_\beta \int^> U_{\alpha\beta}(\Omega, q, q_3)G_T(\omega - \Omega, q, q_3) \frac{d\mathbf{q} d\Omega}{(2\pi)^4}, \quad (15)$$

where the velocity correlation tensor is

$$U_{\mu\sigma}(\hat{q}) = 2Dq^{-3}G_{\alpha\mu}(\hat{q})G_{\beta\sigma}^*(\hat{q})P_{\alpha\beta}(\mathbf{q}) \quad (16)$$

and $\int^>$ means that the integration is performed over the shell of the smallest scales that are being eliminated. These corrections, in turn, yield corrections to effective viscosities and diffusivities. Due to anisotropy, corrections to viscosities and diffusivities are different in the vertical and horizontal directions. Terms proportional to k_3^2 and k_h^2 contribute to corrections in the vertical and horizontal directions, respectively. Finally, a coupled system of four differential equations is obtained to calculate all corrections. This system can be solved analytically for weak and numerically for arbitrary stratification to obtain scale-dependent, horizontal and vertical eddy viscosities and diffusivities.

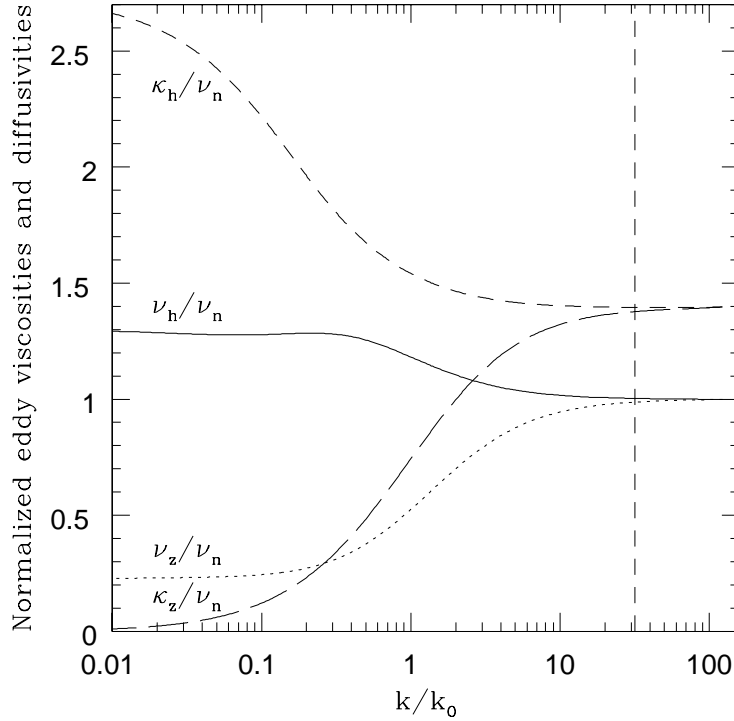


Figure 1: Horizontal and vertical eddy viscosities and diffusivities normalized with the corresponding value of the eddy viscosity in the neutral case, ν_n , as functions of k/k_O , $k_O = (N^3/e)^{1/2}$ is the Ozmidov wave number. Dashed vertical line indicates the maximum wave number threshold of internal wave generation in the presence of turbulence, Eq. (20).

QNSE model results

Figure 1 demonstrates different behavior of horizontal and vertical eddy viscosities and eddy diffusivities with increasing stable stratification. While vertical viscosity and diffusivity are suppressed compared to their values in neutral stratification, their horizontal counterparts are enhanced. Also, while under the action of strong stable stratification the vertical eddy diffusivity becomes very small, the vertical eddy viscosity retains a finite value compared to its corresponding neutral value.

Modification of the internal wave dispersion relation by turbulence

An approach based upon the Langevin equations provides a convenient framework for characterization of nonlinear waves. Indeed, write the Langevin equation (11) as

$$G_{\alpha\beta}^{-1}(\omega, \mathbf{k})u_{\beta}(\omega, \mathbf{k}) = f_{\alpha}(\omega, \mathbf{k}). \quad (17)$$

This equation describes linear, forced, stochastic oscillator whose eigenfrequencies are given by the secular equation

$$\det \left[G_{\alpha\beta}^{-1}(\omega, \mathbf{k}) \right] = 0 \quad (18)$$

which yields the dispersion relation for internal waves in the presence of turbulence:

$$\omega = \omega_0 \left\{ 1 - \left(\frac{k}{k_O} \right)^{4/3} \left[\frac{\left(\frac{\kappa_z}{\nu_n} - \frac{\nu_z}{\nu_n} \right) \cos^2 \theta + \left(\frac{\kappa_h}{\nu_n} - \frac{\nu_h}{\nu_n} \right) \sin^2 \theta}{4 \sin \theta} \right]^2 \right\}^{1/2}. \quad (19)$$

In the limit of strong stratification, classical dispersion relation for linear waves, $\omega = N \sin \theta$, is recovered. At small scales, turbulence dominates. Criterion for waves generation is:

$$k_t(\theta) = k_O \left| \frac{4 \sin \theta}{\left(\frac{\kappa_z}{\nu_n} - \frac{\nu_z}{\nu_n} \right) \cos^2 \theta + \left(\frac{\kappa_h}{\nu_n} - \frac{\nu_h}{\nu_n} \right) \sin^2 \theta} \right|^{3/2} \simeq 32 k_O |\sin \theta|^{3/2}. \quad (20)$$

RANS modeling

Invoking the energy balance equation, the turbulent exchange coefficients can be recast in terms of the gradient Richardson number, $Ri = N^2/S^2$, or Froude number, $Fr = \epsilon/NK$, where S is the mean shear and K is the turbulence kinetic energy, see Fig. 2.

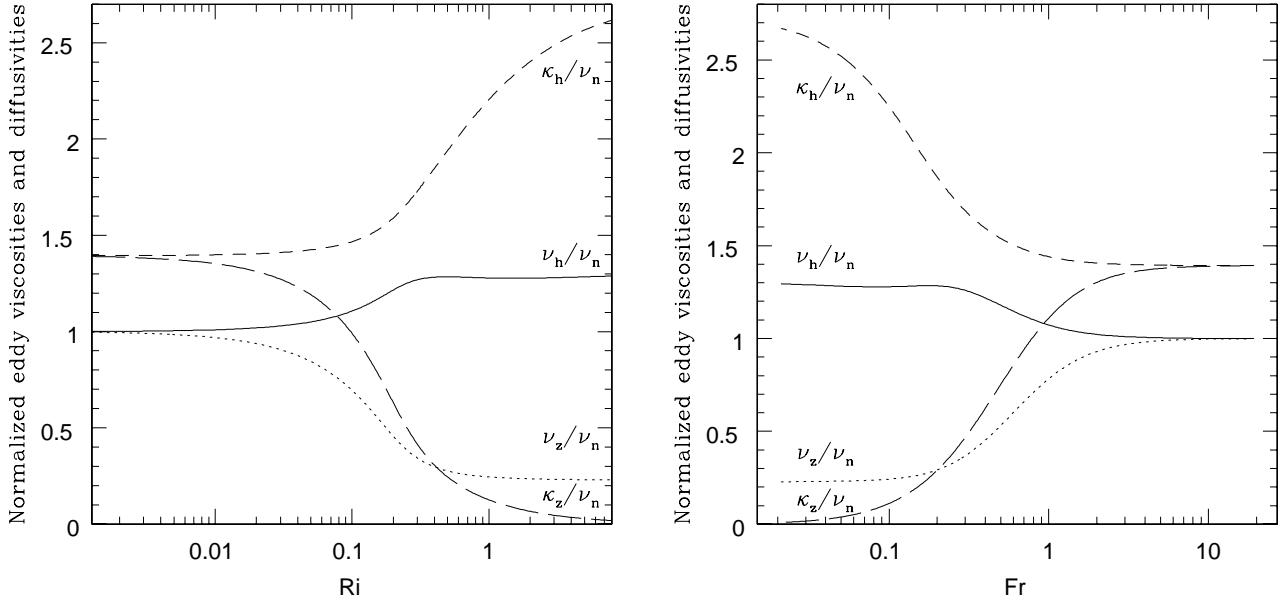


Figure 2: Horizontal and vertical turbulent exchange coefficients normalized with ν_n as functions of Ri and Fr .

Following conclusions can be inferred from Fig. 2:

- For $Ri > 0.1$, both vertical viscosity and diffusivity decrease, with the diffusivity decreasing faster than the viscosity (supposedly, due to the mixing from internal gravity waves);
- While, with increasing stratification, the vertical eddy diffusivity becomes small, the vertical eddy viscosity remains equal to about 25% of its neutral value. This behavior indicates that internal waves are more effective in mixing the momentum than the scalar;
- Horizontal mixing increases with Ri ; the model accounts for flow anisotropy;
- The crossover from neutral to stratified flow regime is replicated as a sharp drop in the vertical eddy

viscosities and eddy diffusivities compared to their neutral values;

- These results suggest that the critical Ri does not exist - turbulence survives even under very strong stable stratification.

Comparison with experimental data

Vertical turbulent Prandtl number is important characteristic of momentum and temperature mixing under the action of stable stratification. We have compared QNSE model predictions with laboratory data from [2] and observations from [3]; see Figs. 3 and 4. In both cases the agreement was very good even for large values of Ri .

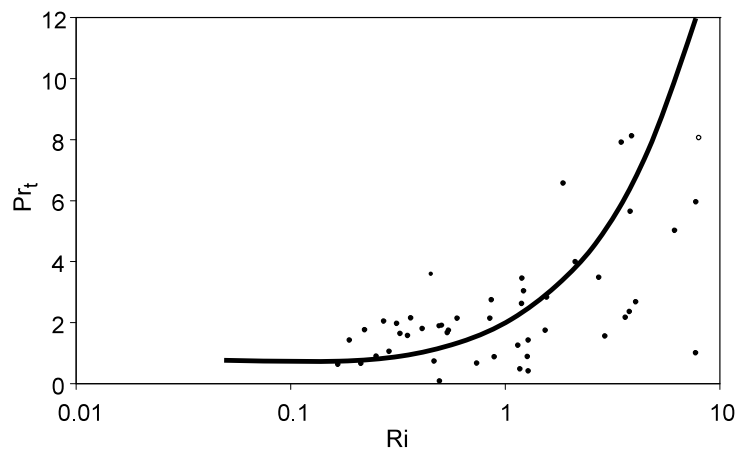


Figure 3: Vertical turbulent Prandtl number as a function of Ri . Data points are laboratory measurements from [2]; solid line represents QNSE models results.

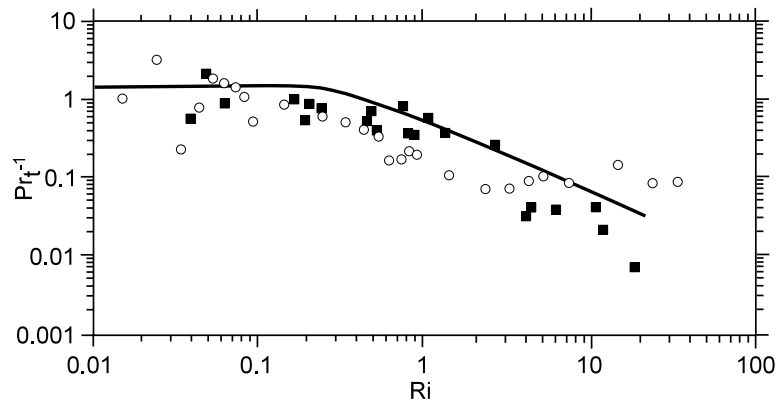


Figure 4: Inverse Prandtl number, $Pr_t^{-1} = \kappa_z/\nu_z$, as a function of Ri . Experimental data points are from [3].

Turbulence spectra

Due to the flow anisotropy, traditional 3D energy spectrum provides only limited information. Various 1D spectra were computed analytically for weak stratification:

$$E_1(k_3) = \frac{8}{(2\pi)^4} \int U_{11}(\omega, \mathbf{k}) d\omega dk_1 dk_2 = 0.626 \epsilon^{2/3} k_3^{-5/3} + 0.214 N^2 k_3^{-3}. \quad (21)$$

The QNSE model reproduces the k_3^{-3} spectrum; the transition from the Kolmogorov $-5/3$ to stable stratification dominated -3 spectrum takes place on large scales. The coefficients in Eq. (21) are in very good agreement with experimental data and LES [4].

For other 1D spectra one obtains:

$$E_3(k_1) = \frac{8}{(2\pi)^4} \int U_{33}(\omega, \mathbf{k}) d\omega dk_2 dk_3 = 0.626 \epsilon^{2/3} k_3^{-5/3} - 0.704 N^2 k_3^{-3}, \quad (22)$$

$$E_3(k_3) = \frac{8}{(2\pi)^4} \int U_{33}(\omega, \mathbf{k}) d\omega dk_1 dk_2 = 0.47 \epsilon^{2/3} k_3^{-5/3} - 0.143 N^2 k_3^{-3}. \quad (23)$$

The anisotropization of the flow field manifests itself as energy increase in the horizontal velocity components at the expense of their vertical counterpart.

Comparison with experimental data: Composite spectrum of the vertical shear in the upper ocean

Composite spectrum of the vertical shear in the upper ocean was compiled in [5]; it has never been derived theoretically. We have succeeded to derive it analytically from the QNSE model in the limit of weak stable stratification, $k/k_0 \geq 1$; see Fig. 5. Note that although Eq. (21) has been derived in the asymptotics $k/k_0 \geq 1$, we have extended this solution beyond this range for illustration of the -3 slope.

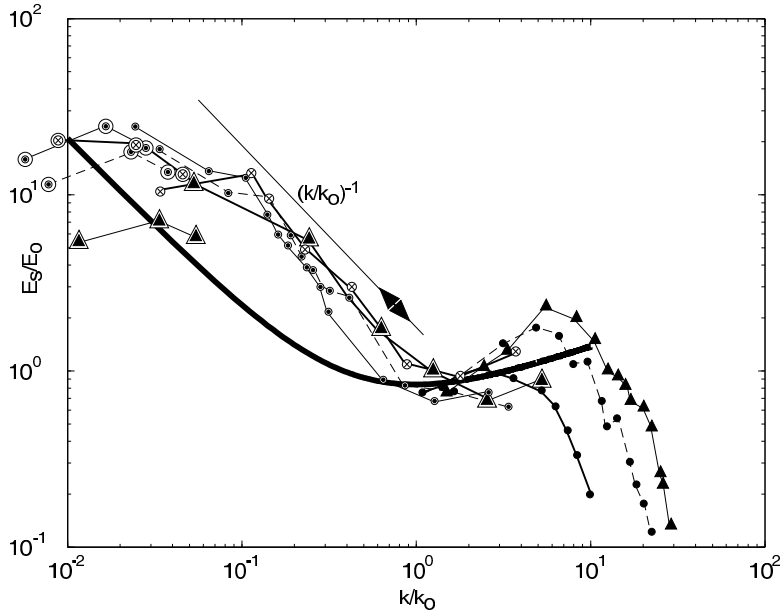


Figure 5: Composite spectrum of the vertical shear in the upper ocean: data is from [5], the solid line is Eq. (21).

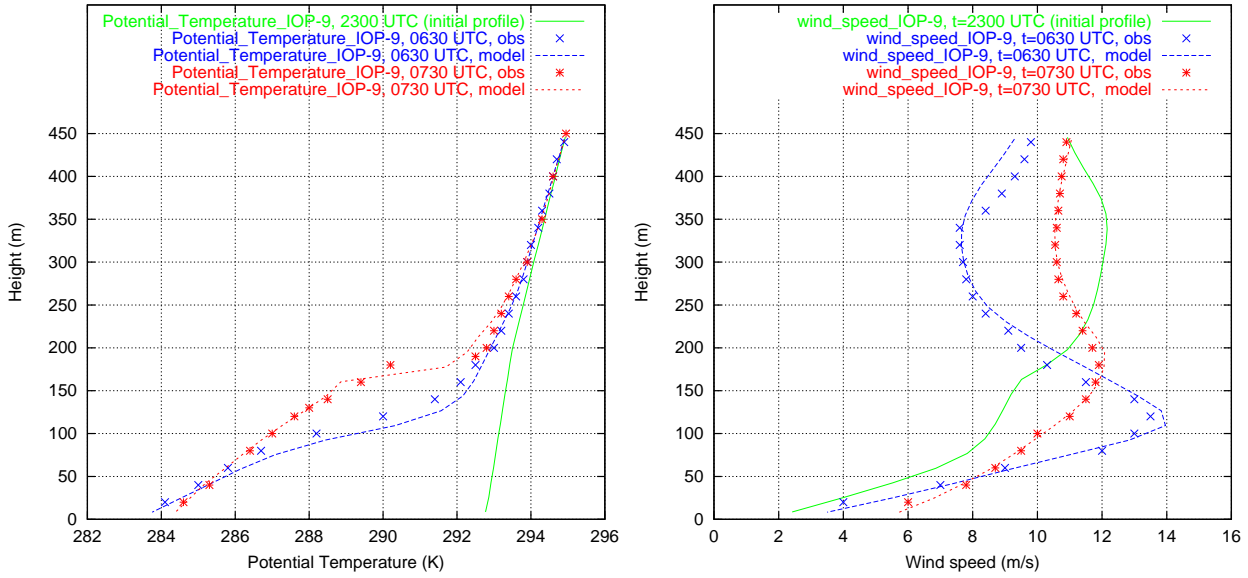


Figure 6: Evolution of the potential temperature (left panel) and wind (right panel) profiles in CASES99 as simulated by the new $K - \epsilon$ model.

A new $K - \epsilon$ model

Based upon the QNSE theory, we have developed a new $K - \epsilon$ model. The effect of stratification was incorporated in the ϵ -equation similarly to the effect of rotation in the Detering & Etling (1985) model [6]. The new model has been implemented in the 1D version of the weather forecast model HIRLAM and tested against observational data collected in several campaigns. Details of the new model and extensive comparisons with data are given in [7]. Here we show only several examples of these comparisons in order to demonstrate good agreement between the data and new model predictions.

Conclusions

- The QNSE is a quasi-normal spectral model; its derivation is maximally proximate to first principles;
- The QNSE model explicitly resolves horizontal-vertical anisotropy induced by stable stratification;
- The model accounts for the combined effect of turbulence and waves;
- Anisotropic turbulent viscosities and diffusivities are in good agreement with experimental data;
- Anisotropic spectra are calculated; it is demonstrated that the energy of the horizontal flow components increases at the expense of vertical component;
- Transition from the Kolmogorov to the $N^2 k_3^{-3}$ spectra for the 1D, $E_1(k_3)$ spectrum is derived analytically for the first time;
- Model yields modification of the classical dispersion relation for internal waves that accounts for turbulence;
- Model provides subgrid-scale closures for both LES and RANS;
- Theory has been implemented in $K - \epsilon$ model of stratified ABL;
- This $K - \epsilon$ model applies to engineering flows and ABL with/without effects of rotation and stratification using invariant set of constants;
- Good agreement with CASES99, BASE and SHEBA data sets has been found for cases of moderate and strong stable stratification.

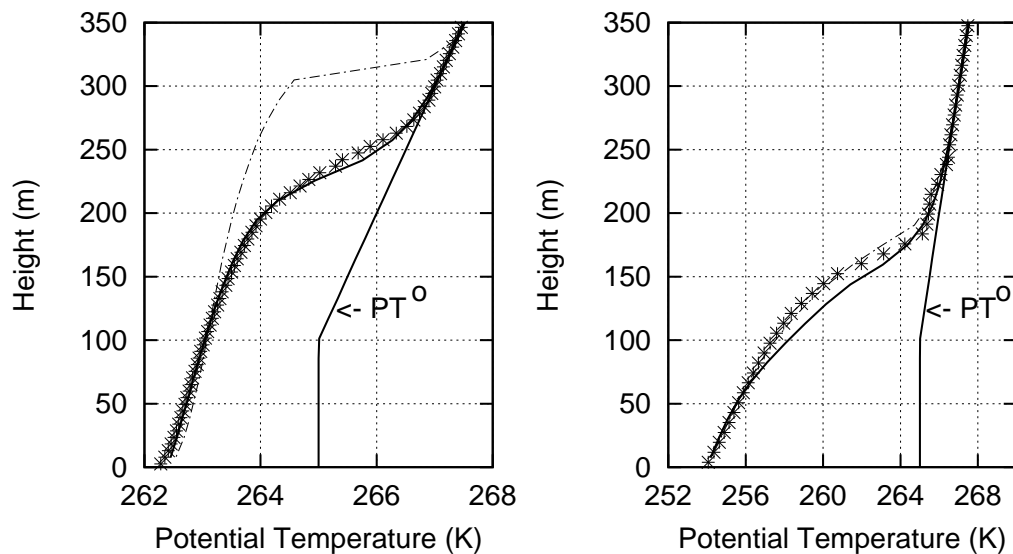


Figure 7: Vertical profiles of mean potential temperature (PT) for the cases of moderate (left panel) and strong (right panel) stable stratification simulated with the new (solid line) and standard (dashed-dotted line) $K - \epsilon$ models. The LES results by Kosovic and Curry (2000) [8] are shown by asterisks. The initial PT profiles (marked as PT^0) are shown by straight solid lines.

Acknowledgments

This research has been partially supported by the US Army Research Office and Israel Science Foundation.

References

- [1] S. Sukoriansky, B. Galperin and I. Staroselsky, *Phys. Fluids* (2005), in review.
- [2] P. Huq and E. Stewart, *J. Phys. Oceanogr.* (2005) in preparation.
- [3] P. Monti, H.J.S. Fernando, M. Princevac, W.C. Chan, T.A. Kowalewski, and E. R. Pardyjak, *J. Atmos. Sci.*, **59** (2002) 2513.
- [4] G. Carnevale, M. Briscolini and P. Orlandi, *J. Fluid Mech.* **427** (2001) 205.
- [5] A. Gargett, P. Hendricks, T. Sanford, T. Osborn and A. Williams III, *J. Phys. Oceanogr.*, **11** (1981) 1258.
- [6] H. Detering and D. Etling, *Bound.-Layer Meteor.*, **33** (1985) 113.
- [7] S. Sukoriansky, B. Galperin and V. Perov, *Bound.-Layer Meteor.* (2005) in press.
- [8] B. Kosovic and J.A. Curry, *J. Atmos. Sci.*, **57** (2000) 1052.

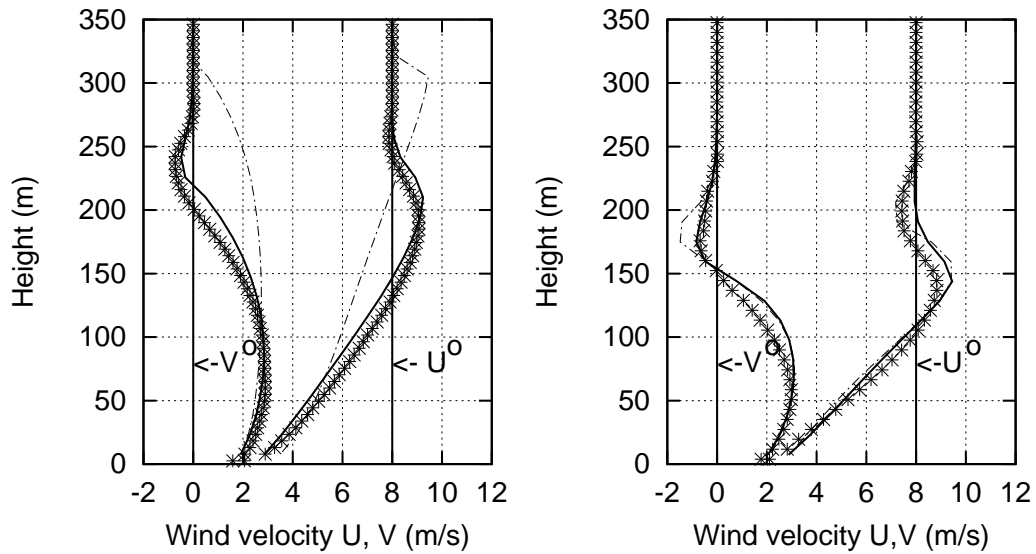


Figure 8: Vertical profiles of mean horizontal wind components, U and V , simulated with the new and standard $K - \epsilon$ models. The initial profiles are marked as U^0 and V^0 , respectively. The order of the panels and the description of the lines and asterisks are the same as in Fig. 7.

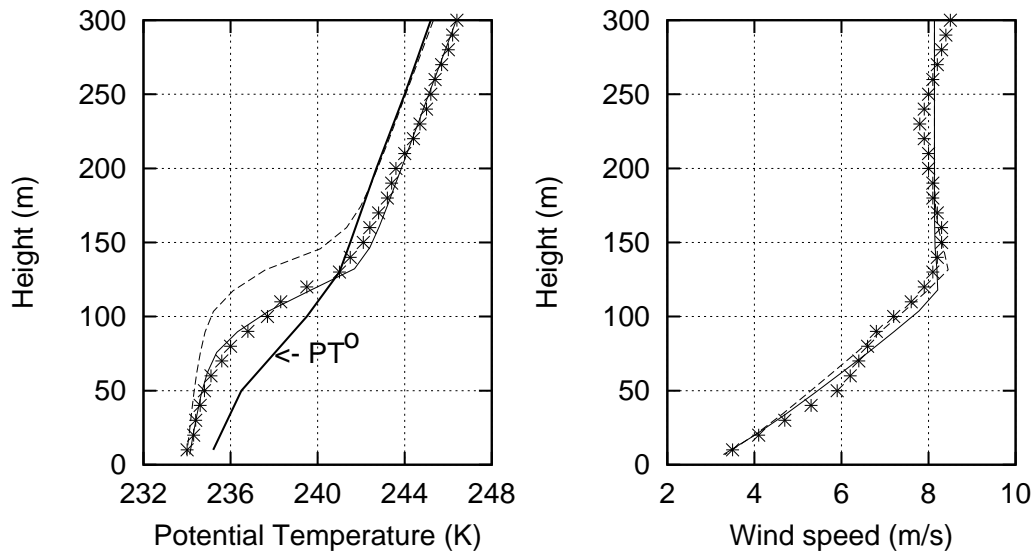


Figure 9: Vertical profiles of potential temperature (left panel) and wind speed (right panel) in SHEBA experiment. The observational data is represented by asterisks, the simulations with the new $K - \epsilon$ model are shown by thin solid lines. The short dashed lines refer to the case in which the vertical advection is not accounted for.

Anisotropic large-scale turbulence and zonal jets in computer simulations, in the laboratory, on giant planets and in the ocean

B. Galperin¹, S. Sukoriansky², N. Dikovskaya²

¹College of Marine Science, University of South Florida, St. Petersburg, FL 33701, USA

²Department of Mechanical Engineering, Ben-Gurion University of the Negev, Beer-Sheva 84105, Israel

Introduction

Planetary rotation, stable density stratification, geometrical constraints etc. lead to quasi-two-dimensionalization of the atmospheric and oceanic circulation on large scales. On even larger scales, the circulations are affected by the latitudinal variation of the Coriolis parameter (β -effect). The β -effect breaks the horizontal isotropy of the flow field and facilitates its self-organization in the zonal (east-west) direction giving rise to quasi-one-dimensional structures - zonal jets. The basic physics of anisotropic turbulence with the β -effect can be captured by a two-dimensional (2D) vorticity equation solved on a plane tangential to the spherical planetary surface (the so called β -plane approximation) or on the entire surface of a rotating sphere. Anisotropic properties of this vorticity equation and their manifestation in computer simulations, terrestrial and planetary environment are the subject of this presentation.

Computer simulations

In 2D setting with small-scale forcing and without large-scale drag, vorticity equation does not have a steady-state solution because due to inverse cascade, energy propagates to ever smaller wave number modes. A steady state can be attained in flows where large-scale drag is introduced. Important questions then arise about the physical nature of this steady-state and its sensitivity to the choice of the drag, i.e., about the universality of the steady state. Due to the importance of these issues, simulations with and without the drag will be discussed separately.

Unsteady simulations

There exist numerous studies of the 2D vorticity equation on β -plane; Chekhlov et al. [1] have provided detailed analysis of anisotropic energy transfer and anisotropic spectrum. They considered forced, non-steady-state vorticity equation,

$$\frac{\partial \zeta}{\partial t} + \frac{\partial (\nabla^{-2} \zeta, \zeta)}{\partial (x, y)} + \beta \frac{\partial}{\partial x} (\nabla^{-2} \zeta) = \nu_o \nabla^2 \zeta + \xi, \quad (1)$$

where ζ is the fluid vorticity, ν_o is the molecular viscosity, and ξ is the forcing; x and y are directed eastward and northward, respectively; the constant β is the background vorticity gradient describing the latitudinal variation of the normal component of the Coriolis parameter, $f = f_0 + \beta y$; the forcing ξ was concentrated around some high wave number k_ξ , was supplying energy to the system with the rate ϵ , and was assumed random, zero-mean, Gaussian and white noise in time. By equating the isotropic turbulence turnover time and the period of the Rossby wave, one can find a transitional wave number separating regions of turbulence and Rossby wave domination,

$$k_t(\phi) = k_\beta \cos^{3/5} \phi, \quad k_\beta = (\beta^3 / \epsilon)^{1/5}, \quad \phi = \arctan(k_y / k_x). \quad (2)$$

The contour (2) in Fourier space has been coined “the dumb-bell shape” by Vallis and Maltrud [2] or “lazy 8” by Holloway [3]. While the β -effect and ensuing flow anisotropy are relatively weak for the

modes $k > k_\beta$, the modes inside the dumbbell are strongly anisotropic and Rossby wave dominated. Furthermore, we have established by direct calculation that there exists strong anisotropic energy flux to zonal modes from all other modes which rapidly increases for smaller modes [1]. As a result, the energy spectrum becomes strongly anisotropic. For zonal ($\phi \rightarrow \pm\pi/2$) and non-zonal, or residual ($\phi \neq \pm\pi/2$) components, the following spectral distributions were established:

$$E_Z(k) = C_Z \beta^2 k^{-5}, \quad \phi = \pm\pi/2; \quad C_Z \text{ 0.3 to 0.5}, \quad (3)$$

$$E_R(k) = C_K \epsilon^{2/3} k^{-5/3}, \quad \phi \neq \pm\pi/2; \quad C_K \text{ 4 to 6}. \quad (4)$$

A similar anisotropic spectral distribution was later found on the surface of a rotating sphere [4, 5]. In this case, β should be replaced by Ω/R , where Ω and R are the angular velocity and the radius of the sphere, respectively. The zonal and residual spectra can then be written as

$$E_Z(n) = C_Z (\Omega/R)^2 n^{-5}, \quad C_Z \simeq 0.5, \quad m = 0 \quad (5)$$

$$E_R(n) = C_K \epsilon^{2/3} n^{-5/3}, \quad C_K \text{ 4 to 6}, \quad m \neq 0., \quad (6)$$

where n and m are the zonal and meridional wave numbers, respectively, for spherical harmonics (precise definitions of $E_Z(n)$ and $E_R(n)$ are given in [5]). The transitional wave number k_β , defined in Eq. (2), should be replaced by $n_\beta = [(\Omega/R)^3/\epsilon]^{1/5}$ in spherical geometry.

Steady-state simulations and the nature of universality

When large-scale drag is present, the balance between small-scale energy injection and large-scale energy withdrawal makes a steady-state solution possible. To understand the physical nature of this solution, the following important questions need to be addressed:

- What is the parameter range that admits the steady-state regime?
- How sensitive is the steady state to the large-scale friction?
- How sensitive is the steady state to the forcing?
- Is the steady state stochastic?

In our previous investigation [5, 6] it was found that the functional representation of the large-scale friction should be close to the linear (Rayleigh) drag; higher-order inverse Laplacian formulation (the so-called hypofriction) is expected to distort the inverse energy cascade and lead to a non-universal behavior. In addition, the steep zonal spectrum results in very slow evolution of the flow field; if τ is characteristic time scale of the large-scale drag, then the establishment of a steady-state has duration of about 10τ while to assemble sufficient statistics for spectral analysis, one needs to extend integration to about 100τ [7]. Keeping these requirements in mind, we have investigated the nature of the steady-state in a series of long-term simulations using the 2D vorticity equation on the surface of a rotating sphere. It was found that the parametric range which admits the flow regime with the spectrum (5)-(6) is restricted by the following criteria:

- (a) forcing acts on scales largely unaffected by β -effect;
- (b) n_β/n_{fr} should be at least half a decade, to ensure sufficient inertial range (n_{fr} is the wave number characterizing the large-scale drag);
- (c) $n_{fr} \geq 4$ – large-scale drag is relatively small yet large enough to prevent accumulation of energy in the largest available planetary modes;
- (d) small-scale dissipation is large enough to suppress the enstrophy subrange.

Parameter range delineated by these criteria is shown as triangle on Fig. 1. All simulations with parameters complying with these limitations are shown as dots concentrated within the triangle; they point to the existence of the universal anisotropic flow regime. On the other hand, most of the triangles and stars pertain to simulations whose parameters are outside of the aforementioned triangle; they reveal lack of universal behavior [8, 9].

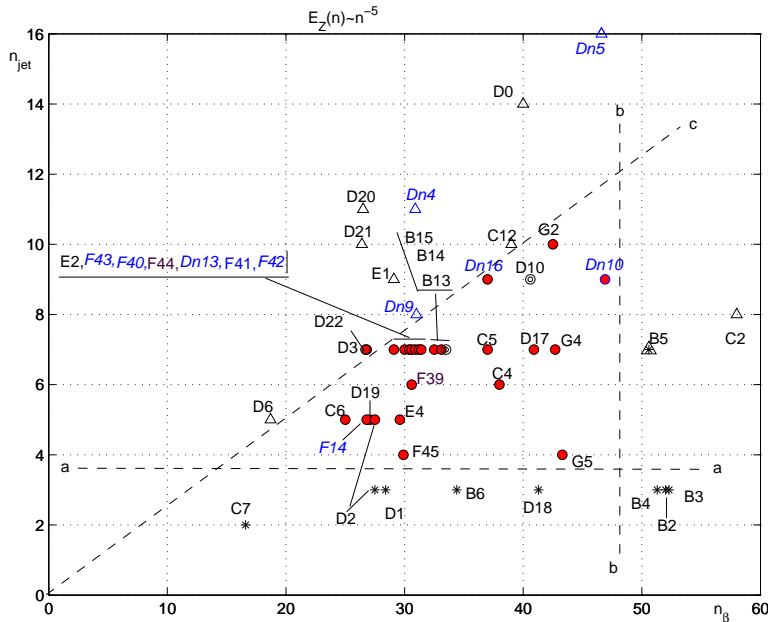


Figure 1: Parameter space of different flow regimes in β -plane turbulence.

Let us now collate information about manifestations of this universal flow regime in real world.

The Grenoble experiment

Recently, Read et al. [10] have conducted an experiment in the world's largest rotating tank (known as the Coriolis facility; its diameter is about 14 m) in Grenoble, France. The small-scale forcing was delivered by a thin layer of salt carefully sprayed over the water surface; it generated small convective plums. The experiments included cases of both straight and sloping bottom; the latter was to create a topographic β -effect. The jet-like structures (zonation) developed in sloping bottom experiments only. The energy spectrum became anisotropic; the non-zonal spectrum preserved the $-5/3$ slope while the zonal spectrum became much steeper and exhibited the tendency to attain the theoretical -5 slope given by Eq. (3) with the value of C_Z close to 0.5.

Anisotropic turbulence and large-scale circulation on giant planets

Large-scale circulation in the cloud layers of the outer planets is a good candidate for the development of the aforementioned anisotropic flow regime for the following reasons:

- large-scale planetary flows are two-dimensionalized due to the actions of stable stratification, rotation, geometrical constraints, etc.;
- the outer planets are gaseous, they don't have solid boundaries, such that their large-scale friction is relatively low;

- convective cells, solar and/or internal heating may provide the necessary small-scale forcing that would give rise to anisotropic inverse energy cascade;
- the Burger number, $Bu = (L_d/R)^2$, is small for all outer planets [11], leaving the possibility for flow barotropization and development of the anisotropic inverse cascade in the barotropic mode (here, L_d is the first baroclinic Rossby deformation radius);
- the inertial range is large since $n_\beta/n_{fr} \sim 10$ to 10^2 ;
- small n_{fr} allows considerable energy accumulation in the barotropic mode such that it may dominate the movement of the clouds and, thus, determines the shape of the cloud tracks.

Spectral analysis of zonal flows on the outer planets may help to determine the nature of their atmospheric circulations. Such analysis was performed using observational data from Voyager 1 and 2 and Hubble Space Telescope; its results are summarized on Fig. 2 borrowed from [5]. As one can see,

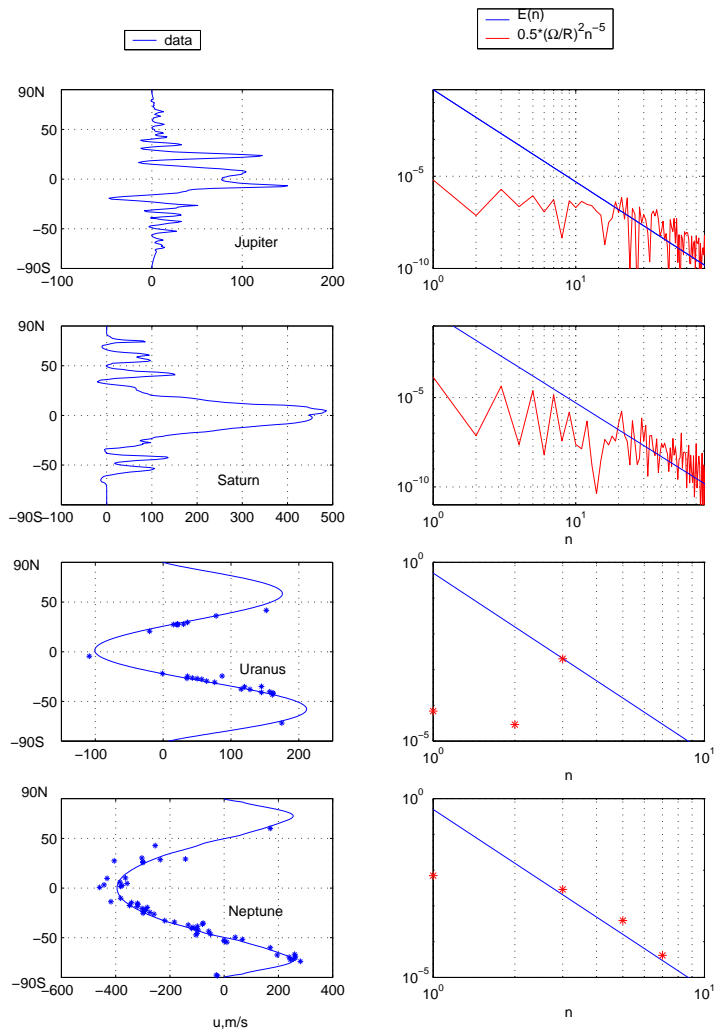


Figure 2: Top row: observed zonal profiles deduced from the motion of the cloud layers; bottom row: observed zonal spectra (solid lines and asterisks) and theoretical zonal spectra Eq. (5) (dashed lines) on the giant planets [all spectra are normalized with their respective values of $(\Omega/R)^2$]. (Note that the data for Uranus is very limited and only gives an idea of the spectral amplitude but not the slope.)

theoretical and observed spectra agree in both slope and the amplitude. A detailed discussion can be

found in [11].

Direction of the equatorial jets in simulations on rotating sphere

Numerous simulations with 2D vorticity equation on the surface of a rotating sphere produced westward equatorial jets. Although such jets agree with the circulation on Uranus and Neptune, they are at variance with the equatorial jets on Jupiter and Saturn. This indeed could be a serious limitation of the barotropic models. We have conducted a series of long-term simulations to investigate this issue in detail; the results are summarized on Fig. 3. Obviously, the idea that the equatorial jet produced

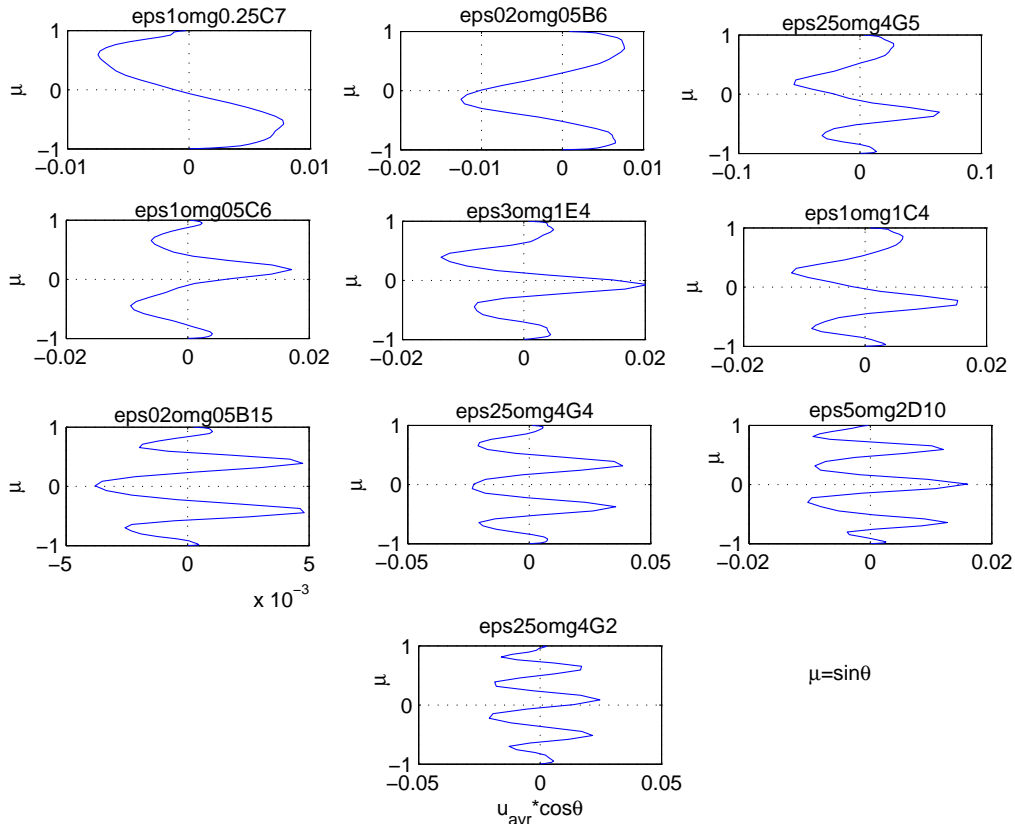


Figure 3: Zonal velocity profiles from various simulations using 2D vorticity equation on the surface of a rotating sphere.

in barotropic simulations is always directed westward is fallacious although a certain preference to the formation of westward equatorial jets was noticeable. Generally, the flow field was slowly evolving and meandering in the north-south direction as a whole such that the equatorial jets could be either eastward or westward; there were even situations when the equatorial jet did not exist at all. Slow fluctuations of the flow field and dramatic changes in the direction of the equatorial jet indicate that (a) the flow field was stochastic and (b) long-term simulations with any model are required to fully understand the nature of the equatorial circulation.

The ocean-Jupiter connection

Eddy-permitting simulations of general oceanic circulation have consistently showed systems of subsurface narrow zonal jets filling the entire ocean domain; see, e.g., [12] for the Atlantic and [13] for

the North Pacific. Recently, the narrow zonal jets signature has also been detected in the maps of the surface geostrophic currents obtained from satellite altimetry [14]. Comparing the visual appearance of the alternating zonal jets on the outer planets and in the ocean, Fig. 4 (source: [15]), one may question whether or not the resemblance between the two is more than just a coincident. To answer

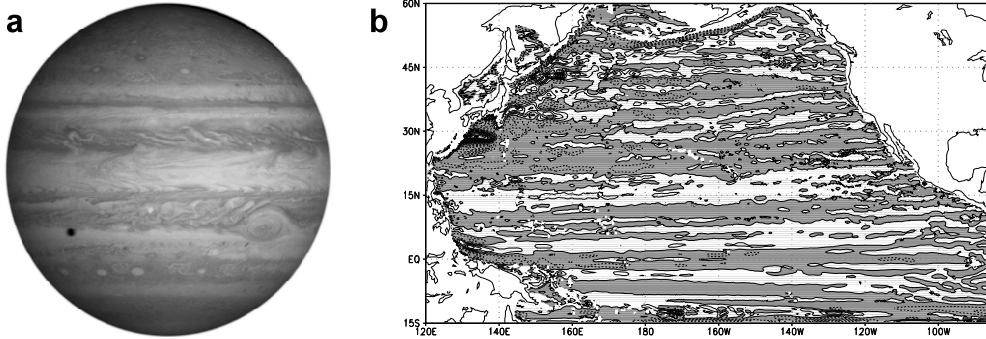


Figure 4: (a) Composite view of the banded structure of the disk of Jupiter taken by NASA's Cassini spacecraft on December 7, 2000 (image credit: NASA/JPL/University of Arizona); (b) zonal jets at 1000 m depth in the North Pacific Ocean averaged over the last five years of a 58-year long computer simulation [13]. The initial flow field was reconstructed from the Levitus climatology; the flow evolution was driven by the ECMWF climatological forcing. Shaded and white areas are westward and eastward currents, respectively; the contour interval is 2 cm/s.

this question, a spectral analysis of a 5-year long model-generated data set for the North Pacific [13] was performed. A 60° in longitude sector of the Pacific was carved out. This sector was repeated 6 fold in the northern hemisphere, mirror-reflected relative to the equator and repeated 6 more fold in the southern hemisphere to assemble a global dataset on the sphere. A spectral analysis in spherical harmonics was performed to calculate both zonal and residual spectra [15]. The calculated spectrum was averaged over the last 5 years of a 58-year long integration starting from the Levitus climatology. As the simulated jets exhibit an equivalent barotropic structure, the analysis is based on the vertical average from the surface to 500 m depth. The results of this analysis are shown on Fig. 5. The averaged zonal and non-zonal oceanic spectra are presented in Fig. 5a. A -5 slope is immediately evident for the zonal flows. Similarly to the case of giant planets (Figs. 5b and 5c), this slope extends upward to the dominant scale of the zonal jets yet for smaller n the spectrum becomes flat. The universality of $E_Z(n)$ is supported not only by the -5 slope, but also by the constancy of $C_Z \simeq 0.5$ for all cases. The energy spectrum for the nonzonal components, $E_R(n)$, exhibits a slope close to $-5/3$ over the range $n = 60 - 120$. The departure of $E_R(n)$ from the $-5/3$ slope for $n > 120$ could be attributed to various factors, such as the interaction between barotropic and baroclinic modes, the effect of direct forcing, damping by the bottom topography, etc. Currently, the resolution of the data and the surface coverage are insufficient to determine $E_R(n)$ for the flows on outer planets. Let us emphasize that both zonal and residual spectra of the horizontal currents have been obtained here from fully 3D, realistic simulations of the circulation in the north Pacific rather than from idealized barotropic 2D simulations used so far in theoretical studies.

For comparison, $E_Z(n)$ and $E_R(n)$ obtained from a model of 2D flow on a rotating sphere [5] are shown in Fig. 5e. These spectra are averaged over the equivalent of about 300 years. As could be expected, longer averaging produces smoother spectra. The observed zonal spectra for Jupiter and Saturn (Figs. 5b and 5c) are, in fact, instantaneous spectra since the characteristic time for the large-scale variability on these planets, obtained by simple energy balance arguments [16], is larger than

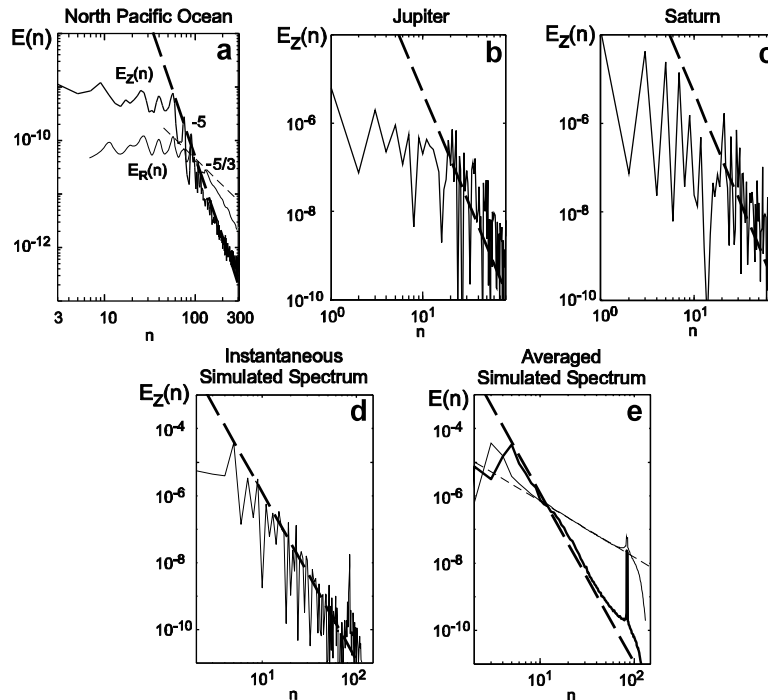


Figure 5: Averaged and instantaneous zonal (thick solid lines) and non-zonal (thin solid lines) energy spectra on rotating planets with small Bu (top row) and in barotropic 2D simulations on a rotating sphere [5] (bottom row); the high wave number spikes on the latter correspond to the small-scale forcing. All spectra are non-dimensionalized such that $E_Z(1) = C_Z$. Idealized -5 (thick dashed lines) and $-5/3$ (thin dashed lines) slopes are superimposed, based upon equations (5) and (6).

the time of observations. Recent long-term observations of the Jupiter jets confirm low variability of the off-equatorial jets main features. Note that the equatorial jets on the gas giants may be governed by different mechanisms (e.g., deep rotating convection) and their variability may be higher. Finally, Fig. 5d shows a typical instantaneous zonal spectrum from the 2D simulation. Large fluctuations are characteristic of all instantaneous spectra. Instantaneous spectra (not shown here) in the ocean also exhibit fluctuations of a similar magnitude.

The universal energy spectra of the zonal flows in terrestrial ocean, planetary atmospheres and the laboratory suggest that the jets are maintained by the momentum flux from the eddies of smaller scales. (In physical space, the convergence of eddy momentum flux balances the large-scale damping of the jets.) A rigorous confirmation of the presence of the inverse energy cascade requires consideration of the scale-by-scale budget of zonal kinetic energy which has not been performed yet.

Conclusions

- Both zonal and residual (when available) spectra found in the Grenoble experiment, on giant planets, and in the subsurface oceanic circulation follow the same anisotropic distribution as those in computer simulations;
- The coefficient C_Z appears to be the same for all flows; $C_Z \simeq 0.5$ may be a universal constant;
- Mid-depth zonal jets in the ocean and those on outer planets are governed by the same non-linear dynamics and appear to be quasi-barotropic;

- Cassini mission may provide better observational evidence for zonal jets' vertical structure for both Jupiter and Saturn;
- The Grenoble experiment links together data from the outer planets, subsurface oceanic circulation and computer simulations and seems to confirm that all these flows are governed by strongly non-linear dynamics with anisotropic inverse energy cascade;
- Mid-depth zonal jets may be important for climate dynamics as they are the fastest currents in the deep ocean.

Acknowledgments

This research has been partially supported by the US Army Research Office and by the Israel Science Foundation.

References

- [1] A. Chekhlov, S.A. Orszag, S. Sukoriansky, B. Galperin and I. Staroselsky, *Physica D*, **98** (1996) 321.
- [2] G.K Vallis and M.E. Maltrud, *J. Phys. Oceanogr.*, **23** (1993) 1346.
- [3] G. Holloway, in *Predictability of Fluid Motions*, eds. G. Holloway and B.J. West, pp. 593–599, American Institute of Physics, New York (1984).
- [4] H.-P. Huang, B. Galperin and S. Sukoriansky, *Phys. Fluids*, **13** (2001) 225.
- [5] S. Sukoriansky, B. Galperin and N. Dikovskaya, *Phys. Rev. Lett.*, **89** (2002) 124501.
- [6] S. Sukoriansky, B. Galperin and A. Chekhlov, *Phys. Fluids*, **11** (1999) 3043.
- [7] B. Galperin and S. Sukoriansky, in *Marine Turbulence - Theories, Observations and Models*, eds. H. Baumert, J. Simpson and J. Sundermann, Ch. 56, Cambridge University Press (2005).
- [8] S. Danilov and D. Gurarie, *Phys. Fluids*, **16** (2004) 2592.
- [9] S. Danilov and V.M. Gryanik, *J. Atm. Sci.*, **61** (2004) 2283.
- [10] P.L. Read, Y.H. Yamazaki, S.R. Lewis, P.D. Williams, K. Miki-Yamazaki, J. Sommeria, H. Didelle and A. Fincham, *Geophys. Res. Lett.*, **31** (2004) Art. No. L22701.
- [11] K. Menou, J. Y.-K. Cho, S. Seager, and B. M. S. Hansen, *Astrophys. J.*, **587** (2003) L113.
- [12] A. Treguier, N. Hogg, M. Maltrud, K. Speer, and V. Thierry, *J. Phys. Oceanogr.*, **33** (2003) 580.
- [13] H. Nakano and H. Hasumi, *J. Phys. Oceanogr.*, **35** (2005) 474.
- [14] N. A. Maximenko, B. Bang and H. Sasaki, *Geophys. Res. Lett.*, in press.
- [15] B. Galperin, H. Nakano, H.-P. Huang and S. Sukoriansky, *Geophys. Res. Lett.*, **31** (2004) L13303, doi:10.1029/2004GL019691.
- [16] B. Galperin, S. Sukoriansky and H.-P. Huang, *Phys. Fluids*, **13** (2001) 1545

Stratified Shear turbulence at very high Reynolds numbers

Helmut Z. Baumert

Institute for Applied Marine and Limnic Studies – IAMARIS
Hamburg, Germany; e-mail: baumert@iamaris.net

At infinitely high Reynolds numbers turbulence may be treated as a gas of elementary vortex couples (special Batchelor couples called vorticons) forming tangles of closed lines (\sim smoke rings). Similar to Brownian particles in a plane, in a (not necessarily plane) cross section through a tangle the ‘footprints’ of those lines perform chaotic movements. When colliding, due to their spin they may either be annihilated or chaotically reflected. The latter case represents diffusion of turbulence, the former its dissipation.

The statistical treatment of this simplistic mechanic image gives a system of parabolic equations (reaction-diffusion system) for turbulence kinetic energy, k , and enstrophy, Ω . It is free of empirical parameters and describes experiments very well, including stratified turbulence and its collapse into internal gravity waves. At solid walls, application of the adiabatic boundary condition for the turbulence kinetic energy leads for the non-stratified case directly to the logarithmic law of the wall without any further assumptions. The von-Karman constant is analytically derived as $1/\sqrt{2 \cdot \pi} \approx 0.399$.

In the stratified case we find the Monin-Obukhov scaling, $\Phi = 1 + 4 \cdot z/L_{MO}$, where L_{MO} is the Monin-Obukhov length and z the distance from the wall. The Prandtl-Kolmogorov relation reads in this image $K_M = c_\mu k^2/\varepsilon$ with $c_\mu = \pi^{-2} \approx 0.101$ where $\varepsilon = k\Omega/\pi$ is the dissipation rate and K_M the eddy viscosity. With the Monin-Obukhov length the Monin-Obukhov scaling reads $\Phi = 1 + 4 \cdot z/L_{MO}$ and the turbulent Prandtl number function is $\sigma = K_M/K_H = \frac{1}{2}/(1 - \tau^2/T^2)$ which for structural equilibrium gives the following simple function of the gradient Richardson number, R_g : $\sigma = \frac{1}{2}/(1 - 2 \cdot R_g)$. Here $\tau = 2\pi/\Omega$ is the time scale of turbulence and T is the period of the buoyancy oscillations.

Although the theory does not contain any spectral information (the dissipation is treated as an instantaneous point process of vorticon annihilation), the closure is compatible with a Kolmogorov spectrum and a Kolmogorov constant as follows, $C_K = \frac{2}{3} \cdot \pi^{2/3} \approx 1.43$.

This image of turbulence compares well with observations by *Businger et al.* (1971), *Dickey & Mellor* (1980), *Rohr et al.* (1988) as well as with ideas by *Van Atta* (1999) and by *D’Asaro & Lien* (2000).

One of the consequences of the new view offered here is the necessity to not longer neglect those short internal waves which are continuously generated by shear turbulence. They need to be taken into account in the momentum balance through their internal wave drag. This means that the *total* momentum flux in MO layers should almost vanish because the internal-wave drag $\langle \tilde{u} \tilde{w} \rangle$ almost compensates the Reynolds stress $\langle u' w' \rangle$.

The author thanks *Hartmut Peters* in Miami for his contributions to the present theory, *Boris Galperin* in St. Petersburg/FL, *Semion Sukoriansky* in Beer-Sheva and *Sergey Zilitinkevich* in Helsinki for important hints. Major parts of the talk may be found in [1, 2] in greater detail.

- [1] Baumert, H. Z. and H. Peters, Ch. 3 in: *Marine Turbulence – Theories, Observations and Models* (eds.: Baumert, H. Z., Simpson, J. and J. Sündermann). Cambridge Univ. Press, 2005, 630 pp. and one CD-ROM.
- [2] Baumert, H. Z., Ch. 4 and 5 in [1]: *Marine Turbulence – Theories, Observations and Models*.
- [3] D’Asaro, E. A., and R.-C. Lien, *J. Phys. Oceanography*, **30**, 1,669 – 1,678, 2000 b.

- [4] Dickey, T. D. and G. L. Mellor, *J. Fluid Mech.*, **99**, 37 – 48, 1980.
- [5] Businger, J. A., J. C. Wyngaard, Y. Izumi, and E. F. Bradley, *J. Atmos. Sci.*, **28**, 181 – 189, 1971.
- [6] Rohr, J. J. et al., *J. Fluid Mech.*, **195**, 77–111, 1988 a; **188**, 1 – 33, 1988 b.
- [7] Van Atta, C. W., A generalized Osborn-Cox model for estimating fluxes in nonequilibrium stably stratified turbulent shear flows, *J. Marine Systems*, **21**, 103 – 112, 1999.

On the validity of the Millionshchikov quasi-normality hypothesis for convective boundary layer turbulence

V. M. Gryanik^{1,2}, *J. Hartmann*¹

¹ Alfred Wegener Institute for Polar and Marine Research, Bremerhaven, Germany

² A. M. Obukhov Institute of Atmospheric Physics, Russian Academy of Sciences, Moscow, Russia

Abstract

The Millionshchikov hypothesis of quasi-normal (Gaussian) distribution of the one-point fourth-order moments fails for convective boundary layer conditions. This is because the effect of the semi-organized coherent structures (plumes) leads to skewed distributions, the third-order moments are non-zero. New closures for fourth-order moments are suggested which take into account the self organization of flow into coherent structures. These new closures depend on skewnesses. They are in very good agreement with the aircraft measurements and large-eddy simulation data.

Introduction

The Millionshchikov hypothesis [1], [2] states that in higher-order turbulence closure (HOC) models the one-point fourth-order moments (FOM) can be approximated as quasi-normal (Gaussian) even if the third-order moments (TOM) are non-zero. For a long time this hypothesis was adopted without discussion in a large number of turbulence closure models (see e.g., [3], [4]). Recent theoretical studies (e.g., [5], [6], [7]), analyses of measurements (e.g. [6], [8]), and large-eddy simulation (LES) data (e.g. [6], [7]) indicate that the Millionshchikov hypothesis fails for the FOM of vertical velocity and temperature in convective boundary layer (CBL) conditions, while the FOM of horizontal along and across wind components are close to Gaussian. In this paper we discuss (following [6], [7]) the problem of refinement of the Millionshchikov hypothesis as applied to CBL conditions. We begin with showing that the Gaussian parameterisation for FOM is a poor approximation for moments involving vertical velocity and temperature fluctuations.

Testing of the Millionshchikov hypothesis versus data and LES

In Figure 1 the FOM are plotted versus their Gaussian parameterisations

$$\overline{a'b'c'd'} = \overline{a'b'} \cdot \overline{c'd'} + \overline{a'c'} \cdot \overline{b'd'} + \overline{a'd'} \cdot \overline{b'c'}, \quad (1)$$

where a', b', c', d' are fluctuations of vertical w' , along wind u' , cross wind v' velocity components and temperature θ' . The measurements and LES data are plotted at the ordinate, and the parameterisations at the abscissae.

The aircraft measurements (dots) are obtained during the ARTIST-campaign [9] in a convectively driven boundary layer over the ocean with 8-12 m/s wind speed. The LES data (solid lines) are from a simulation of a convective boundary layer with 12 m/s geostrophic wind speed, which is described in detail in [10]. Both data sets are scaled by Deardorff scaling.

All FOM involving the vertical velocity component or the temperature are significantly larger than their Gaussian prediction. Thus the Gaussian parameterisation systematically underestimates these FOMs, and gives an estimation of a lower bound for all these moments. Both aircraft measurements and LES data show that the Millionshchikov hypothesis is applicable to horizontal velocity components.

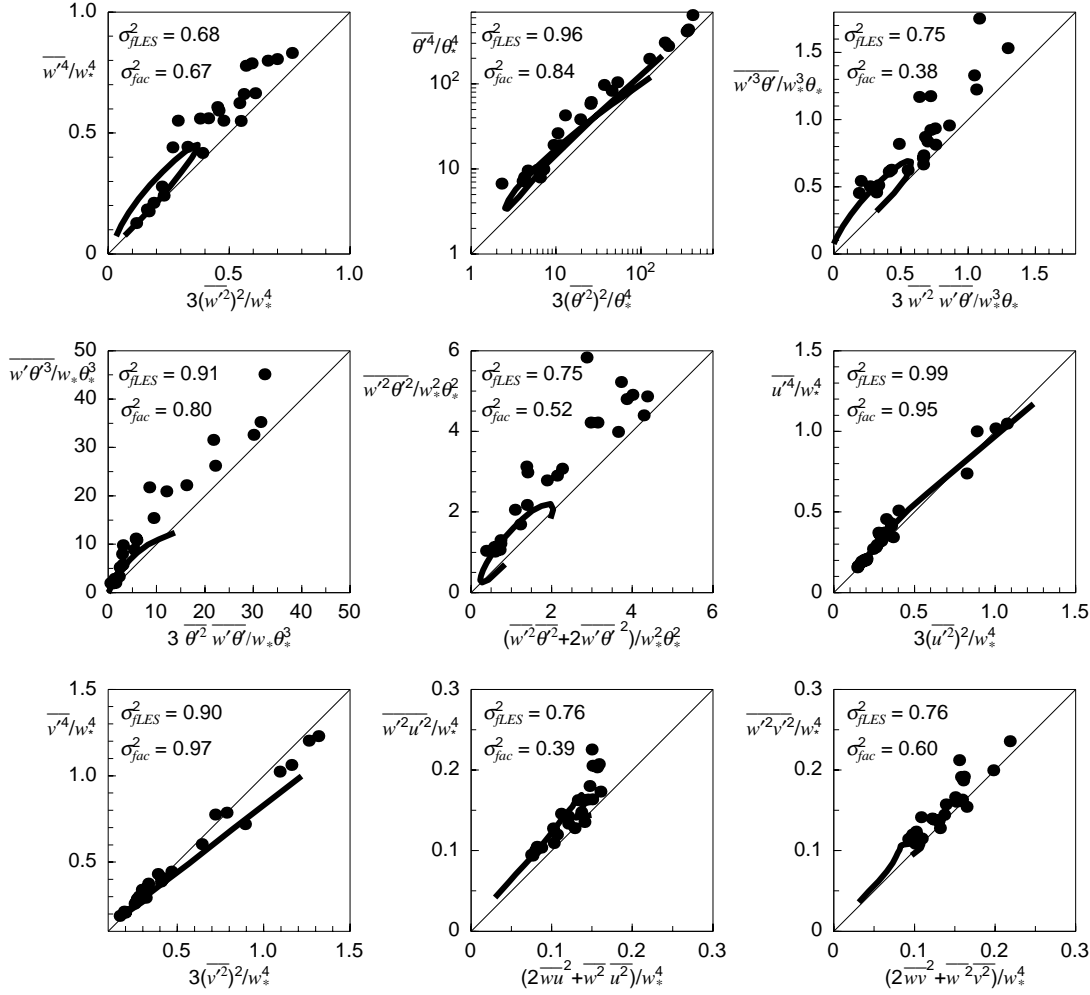


Figure 1: Aircraft measurements (dots) and LES results (solid lines) of fourth order moments (ordinates) versus their parameterisations (abscissae) based on the Gaussian assumption Eqs.(1). σ_f are the explained variances.

As an indication for the suitability of the parameterisation we calculate the explained variances $\sigma_f^2 = 1 - \overline{(y_i - f(x_i))^2}/\overline{(y_i - \overline{y})^2}$, where y_i are the aircraft measurements and LES data, respectively, and $f(x_i)$ are the corresponding parameterisations. For the vertical wind component of the LES data, the Gaussian parameterisation $3\overline{w'^2}$ only explains 68% of the variance of $\overline{w'^4}$, and for the aircraft data 67%. The agreement is worse for some cross moments for the aircraft data, since measurement accuracy contributes significantly to the unexplained variance. The LES data do not suffer such errors and lead to higher values of the explained variance.

The LES data are plotted as a continuous line in the order of increasing height. The loops in these plots, especially for the moments $\overline{w'^4}$, $\overline{w'^3\theta'}$ and $\overline{w'^2\theta'^2}$ represent an ambiguity of the relation depending on height. The ambiguity of the Gaussian parameterisation is an unphysical feature and an essential disadvantage of any parameterisation.

The refinement of the Millionshchikov hypothesis and new expressions for FOM

The drawbacks of the parameterisations (1) are linked to the fact that they do not include the effects of the coherent structures [11] that are typical of CBL turbulence. In [6], [7] we assumed that deviation of statistics from the Gaussian behaviour is caused by the most energetic CBL coherent structures - plumes. The plume flow is characterized by narrow strong updrafts of warm air surrounded by wide downdrafts of cold air. The plumes statistics is modeled with the help of 16-delta probability density function (PDF) [7]

$$\begin{aligned}
P(w', \theta', u', v') = & [p_{uwfr}\delta(w' - w_u)\delta(\theta' - \theta_w) + p_{dcfr}\delta(w' - w_d)\delta(\theta' - \theta_c) + \\
& p_{ucfr}\delta(w' - w_u)\delta(\theta' - \theta_c) + p_{dwfr}\delta(w' - w_d)\delta(\theta' - \theta_w)]\delta(u' - u_f)\delta(v' - v_r) + \\
& [p_{uwbr}\delta(w' - w_u)\delta(\theta' - \theta_w) + p_{dcbr}\delta(w' - w_d)\delta(\theta' - \theta_c) + \\
& p_{ucbr}\delta(w' - w_u)\delta(\theta' - \theta_c) + p_{dwbr}\delta(w' - w_d)\delta(\theta' - \theta_w)]\delta(u' - u_b)\delta(v' - v_r) + \\
& [p_{uwfl}\delta(w' - w_u)\delta(\theta' - \theta_w) + p_{dcfl}\delta(w' - w_d)\delta(\theta' - \theta_c) + \\
& p_{ucfl}\delta(w' - w_u)\delta(\theta' - \theta_c) + p_{dwfl}\delta(w' - w_d)\delta(\theta' - \theta_w)]\delta(u' - u_f)\delta(v' - v_l) + \\
& [p_{uwbl}\delta(w' - w_u)\delta(\theta' - \theta_w) + p_{dcbl}\delta(w' - w_d)\delta(\theta' - \theta_c) + \\
& p_{ucbl}\delta(w' - w_u)\delta(\theta' - \theta_c) + p_{dwbl}\delta(w' - w_d)\delta(\theta' - \theta_w)]\delta(u' - u_b)\delta(v' - v_l), \tag{2}
\end{aligned}$$

where $\delta(y)$ is the Dirac delta function. Here all p are the joint probabilities, and indices u, d, w, c, f, b, l, r serve to denote updraft, downdraft, warm, cold, forward, backward, left, right fluctuations, respectively. Thus p_{uwfr}, p_{dcfr} are the joint probabilities of warm updraft w_u, θ_w and cold downdraft w_d, θ_c together with the joint probability p_{ucfr}, p_{dwfr} of cold updraft w_u, θ_c and warm downdraft w_d, θ_w in along wind forward component u_f with deviation to the right v_r . The joint probabilities $p_{uwfl}, p_{dcfl}, p_{ucfl}, p_{dwfl}$ are the probabilities of warm updraft, cold downdraft, cold updraft and warm downdraft of the along wind forward component with deviation to the left v_l . The remaining joint probabilities $p_{uwbr}, p_{dcbr}, p_{ucbr}, p_{dwbr}$ and $p_{uwbl}, p_{dcbl}, p_{ucbl}, p_{dwbl}$ of along wind backward streams u_b with deviations to the right v_r and left v_r , respectively, are defined in the same way.

The PDF model (2) is the generalization of the traditional mass-flux 2-delta PDF model [12], [13] and 3-delta PDF models of [6] and [14].

Straightforward calculation of FOM using the PDF (2) leads to the FOM which are not functions of SOM only, but of TOM as well. Precisely, the FOM are quadratic functions of the skewnesses $S_y = (\overline{y'^3})/\overline{y'^2}^{3/2}$. Thus a measure of deviation of statistics from the Gaussian behaviour is provided by the skewnesses of vertical S_w , the along wind S_u , cross wind S_v horizontal velocity components and temperature S_θ .

Assuming that effects of the semi-organized coherent structures (plumes) are dominating in the limit of large skewnesses, and that in the limit of small skewnesses the FOM follow the Millionshchikov hypothesis, we suggest to generalise the Millionshchikov hypothesis to the new FOM closure:

$$\overline{w'^4} = a_3 (1 + d_3 S_w^2) \overline{w'^2}^2, \tag{3}$$

$$\overline{\theta'^4} = a_4 (1 + d_4 S_\theta^2) \overline{\theta'^2}^2, \tag{4}$$

$$\overline{w'^3 \theta'} = a_5 (1 + d_5 S_w^2) \overline{w'^2} \overline{w' \theta'}, \tag{5}$$

$$\overline{w' \theta'^3} = a_6 (1 + d_6 S_\theta^2) \overline{\theta'^2} \overline{w' \theta'}, \tag{6}$$

$$\overline{w'^2 \theta'^2} = a_7 (1 + d_7 \frac{C_{w\theta}}{1 + 2C_{w\theta}^2} S_w S_\theta) (\overline{w'^2 \theta'^2} + 2\overline{w' \theta'^2}), \tag{7}$$

for vertical velocity and temperature fluctuations, and in a similar way for vertical velocity and horizontal velocity fluctuations, e.g.

$$\overline{u'^4} = a_8 (1 + d_8 S_u^2) \overline{u'^2}^2, \quad (8)$$

$$\overline{v'^4} = a_9 (1 + d_9 S_v^2) \overline{v'^2}^2, \quad (9)$$

$$\overline{w'^2 u'^2} = a_{10} \left(1 + d_{10} \frac{C_{wu}}{1 + 2C_{wu}^2} S_w S_u\right) \left(\overline{w'^2 u'^2} + 2\overline{w' u'^2}\right), \quad (10)$$

$$\overline{w'^2 v'^2} = a_{11} \left(1 + d_{11} \frac{C_{wv}}{1 + 2C_{wv}^2} S_w S_v\right) \left(\overline{w'^2 v'^2} + 2\overline{w' v'^2}\right). \quad (11)$$

Here

$$C_{w\theta} = \frac{\overline{w'\theta'}}{w'^2^{1/2} \theta'^2^{1/2}}, \quad C_{wu} = \frac{\overline{w'u'}}{w'^2^{1/2} u'^2^{1/2}}, \quad C_{wv} = \frac{\overline{w'v'}}{w'^2^{1/2} v'^2^{1/2}} \quad (12)$$

and $a_i, (i = 3, \dots, 11)$ and $d_i, (i = 3, \dots, 11)$ are dimensionless parameters.

Assumption of Gaussian behaviour in the limit of zero skewness leads to

$$a_i = 3 (i = 3, \dots, 6, 8, 9), a_i = 1 (i = 7, 10, 11), \quad (13)$$

and requirement of 16-delta pdf in the limit of large skewness leads to

$$d_i = \frac{1}{3} (i = 3, \dots, 6, 8, 9), d_i = 1 (i = 7, 10, 11). \quad (14)$$

Such a choice is in agreement with (i) dimensional analysis, (ii) tensor invariance, (iii) symmetry conditions, and (iv) realisability requirements. Our parameterisations for FOM (eqs. (3) to (11)) are reversible in time, i.e. the moments remain the same under the transformation $t \rightarrow -t$, similar to the Gaussian parameterisations (eqs. (1)). This parameterisation was called universal model in [6], [7].

Testing of new FOM versus data and LES

In Figure 2 we compare the refined Millionshchikov parameterisations given by eqs. (3) to (11) against measurements and LES data. Judging by the explained variance, almost all moments show a better agreement for both aircraft measurements and LES data. The exception is the FOM of the across wind component $\overline{v'^4}$, which is virtually unchanged, since the skewness of v is very small.

We emphasize that the ambiguity in the relation between actual and parameterised moments has disappeared, which could be seen from the collapsed loop in the LES data. The absence of ambiguity shows that our new parameterisations are selfconsistent and physically grounded.

We also tested the parameterisations (3) to (11) with LES simulation data obtained for 4 and 0 m/s geostrophic wind speed with all other boundary layer parameters unchanged. These data confirm in the same way the unsuitability of the Millionshchikov hypothesis and show significantly better agreement with our new formulations.

Conclusions

The measurements and LES data at CBL conditions show poor performance of the Millionshchikov hypothesis. The results presented in Figures 1 and 2 show that the Millionshchikov hypothesis is not suited for parameterisation of FOM involving the vertical velocity and temperature at CBL conditions.

The new parameterisations (3) to (11) have better a skill in predicting the FOM, and can be used either to reduce the number of degrees of freedom of the traditional moment equations or to

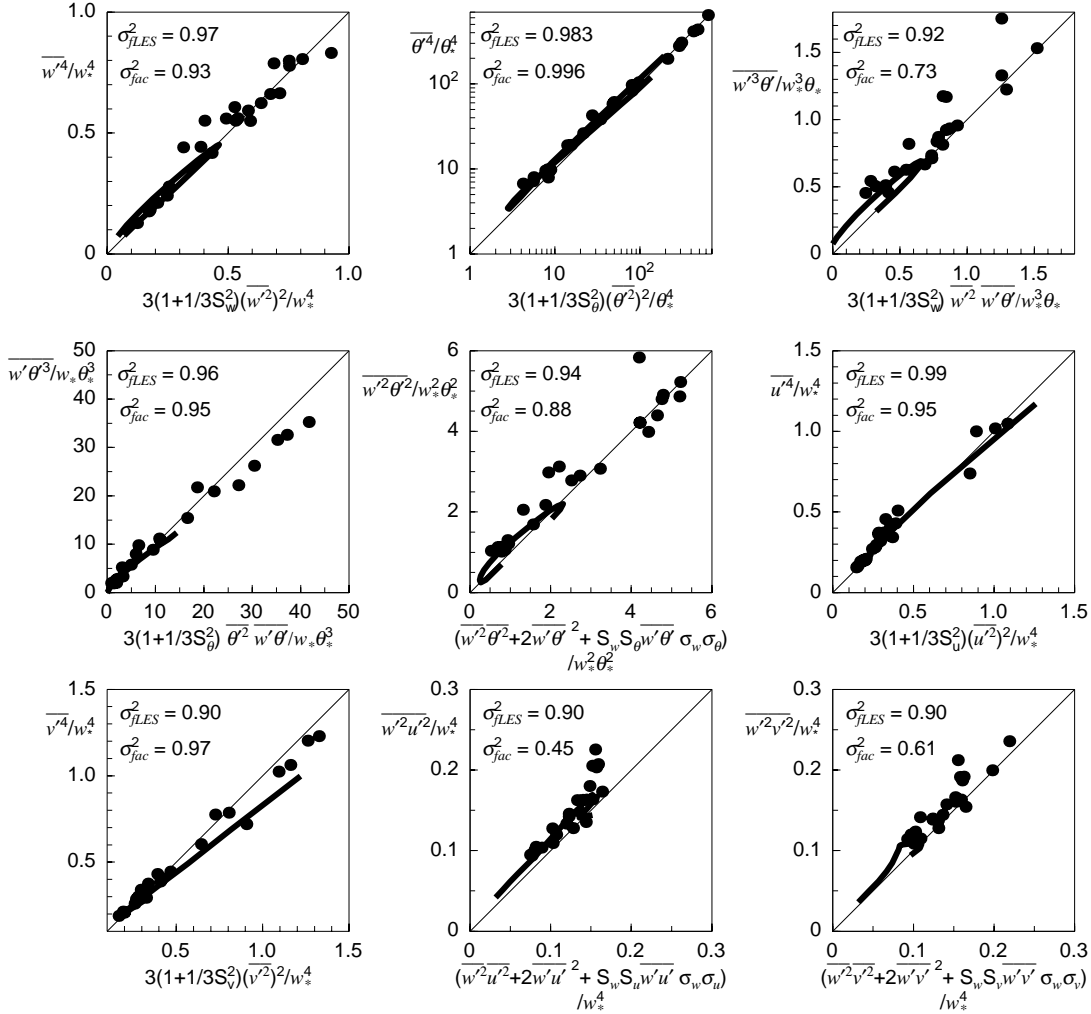


Figure 2: Aircraft measurements (dots) and LES results (solid lines) of fourth order moments (ordinates) versus the new parameterisations Eqs. (3) to (11) (abscissae). σ_f are the explained variances.

generate new closure schemes. Since the parameterisations (3) to (11) express the FOM in terms of second-order moments and TOM, the minimal closure model for convective conditions should be a TOM closure model, see e.g. [6].

The new parameterisations are quite general. A recent study [15] shows that eqs. (3) to (7) is a good approximation for FOM in deep-ocean convection with rotation conditions. Kupka has shown that eqs. (3) to (7) can be used for parameterising FOM of convection in stars (see the article of F. Kupka in this volume). Furthermore, the parameterisation is also applicable for passive scalars like the moisture in polar conditions [16].

Acknowledgements

We are glad to thank V.M. Canuto, F. Kupka, V. Lykossov and D. Mironov for fruitful discussions and very helpful comments and suggestions.

References

- [1] M.D. Millionshchikov, Doklady Acad. Nauk SSSR, **32**, (1941) 611.
- [2] A.C. Monin, A.C., A.M. Yaglom, Statistical Fluid Mechanics. Nauka, Moscow (1965). (English translation, 1971).
- [3] J.C. Andre, G. De Moor, P. Lacarrere, R. du Vachat, J. Atmos. Sci., **33**, (1976) 476.
- [4] V.M. Canuto, F. Minotti, C. Ronchi, R.M. Ypma, O. Zeman, J. Atmos. Sci., **51**, (1994) 1605.
- [5] V.M. Canuto, Y. Cheng, A. Howard, J. Atmos. Sci., **58**, (2001) 1169.
- [6] V.M. Gryanik, J. Hartmann, J. Atmos. Sci., **59**, (2002) 2729.
- [7] V.M. Gryanik, J. Hartmann, S. Raasch, M. Schröter, J. Atmos. Sci., **in press**, (2005).
- [8] S. Alberghi, A. Maurizi, E. Tampieri, J. Applied. Meteorology., **41**, (2002) 885.
- [9] J. Hartmann, F. Albers, S. Argentini, A. Bochert, U. Bonafé, W. Cohrs, W., A. Conidi, D. Freese, T. Georgiadis, A. Ippoliti, L. Kaleschke, C. Lüpkes, U. Maixner, G. Mastrantonio, F. Ravegnani, A. Reuter, G. Trivellone, A. Viola, Berichte zur Polarforschung, **305**, (1999) 81pp.
- [10] S. Raasch, M. Schröter, Meteorol. Z., **10**, (2001) 363.
- [11] R. Salmon, Lectures on Geophysical Fluid Dynamics. Oxford Univ. Press, New York (1998).
- [12] S.S. Zilitinkevich, V.M. Gryanik, V.N. Lykossov, D.V. Mironov, (1999) J. Atmos. Sci., **56**, (1999) 3463.
- [13] C.L. Lappen, D.A. Randall, J. Atmos. Sci., **58**, (2001) 2021.
- [14] D.M. Mironov, V.M. Gryanik, V.N. Lykossov, S.S. Zilitinkevich, J. Atmos. Sci., **56**, (1999) 3478.
- [15] M. Losch. Geophys. Res. Lett. **31**, (2004) L23301.
- [16] Hartmann, J., Lüpkes, C., Spiess, T., Buschmann, M.(2004). Airborne flux measurements by HELIPOD over arctic leads, Fourth Annual Meeting of the European Meteorological Society, Nice, France, 26-30 September 2004.

Turbulent convection in astrophysics and geophysics - a comparison

F. Kupka

Max-Planck-Institute for Astrophysics, Karl-Schwarzschild Str. 1,
D-85741 Garching, Germany, e-mail: fk@mpa-garching.mpg.de

Abstract

Energy transport by turbulent convection is studied in both astrophysics and geophysics. We briefly outline the physics of convection as well as the differences between astrophysical and geophysical turbulent convective flows. The case of convection in stars including our sun is described in more detail. Reynolds stress models have been suggested for quantitative predictions for both stellar and geophysical convection. One of the main problems of such models is how to account for the influence of the observed large scale coherent structures. We discuss a possible solution which has first been suggested for the convective planetary boundary layer and show how it performs when applied to convection in our sun.

Astrophysical and geophysical convection

Both astrophysics and geophysics deal with systems where a fluid with a density ρ is stratified as a function of depth by gravitational forces such that $\rho_{\text{top}} < \rho_{\text{bottom}}$. In this case a temperature stratification $T_{\text{top}} < T_{\text{bottom}}$ can become unstable, as hot fluid moving upwards expands (adiabatically) by an amount sufficiently large for its density to become smaller than the density of the surrounding, colder fluid at the new location further upwards. The result of this process is a net buoyancy force which drives the convective motions. Such a buoyancy driven instability can occur in stars as well as in the atmosphere and the oceans of the earth. The resulting flow carries heat, provides an efficient way of mixing within the fluid, and in case of hot plasmas (i.e. in stars) it may also create a magnetic dynamo and hence a (variable) magnetic field. The sun is a good example for such dynamo processes.

Astrophysical and geophysical convection involve huge length scales L and velocities U . The latter may be as large as 1/3 of the speed of sound (as in the sun, for instance). Scales of a few km (terrestrial) or even several 10000 to 100000 km (astrophysical) are to be compared with the scales of dissipation in the mm to cm range, where viscous effects dominate. The resulting Reynolds numbers $\text{Re} = UL/\nu$ (ν is the kinematic viscosity, $[\nu] = \text{cm}^2 \text{sec}^{-1}$) are of the order of 10^8 (geophysical) to 10^{14} (astrophysical). Consequently, as $\text{Re} \gg 1$, the non-linear terms in the Navier-Stokes equations such as $U\nabla U$ completely dominate over the linear ones which involve viscosity and astrophysical as well as geophysical convection are examples of turbulent flows. They are well known to feature large scale, coherent structures such as granules in the case of the sun, downdrafts in the case of the ocean and the sun, or thermals in the case of the convective planetary boundary layer of the earth.

What are the main differences between astrophysical and geophysical convection? Let us focus on stellar convection for the astrophysical case. There, a heat source such as nuclear fusion or heat stored from preceding evolutionary phases of the star, which is located in its central “core” or a spherical shell around this core, provides the energy input into the “convection zone” from below (or inside). Cooling is taking place through radiation (or conduction) at the top of such convection zones. A mean molecular weight gradient (due to a change of the ratio of H over He) may further enhance or inhibit convection. Stellar convection is hence intrinsically global (taking place within a sphere or shell). It generates a highly compressible flow and is characterised by a very low Prandtl number, the ratio of kinematic viscosity to thermometric conductivity ($10^{-10} \dots 10^{-6}$, i.e. radiative heat transfer

works much better in stars than conductive heat transfer does in air or water). The importance of rotation varies from case to case. Magnetic fields always seem to go hand in hand with this type of convection, but in more simple models they are usually neglected (the main argument being that the magnetic fields cover only a small fraction of the surface area and contain only a small fraction of the total energy of the convection zone). Cooling mostly occurs by radiation, especially close to the surface. Stellar convection is ultimately driven by one or several of the following: high opacity, which reduces the efficiency of radiative transport (thus steepening the temperature gradient); partial ionisation, which lowers the adiabatic temperature gradient (thus making the fluid more unstable to convection as well); or high luminosity, i.e. a high energy input from below (which requires a steep temperature gradient to transport that amount of flux). The latter is more important in hot, massive stars, while the former two are found in the outer layers of cooler, less massive stars. This includes our sun and thus solar convection as a special case.

In geophysical convection, the source of heating or cooling is external (cold air above the open water arctic ocean; the day time sun heating the surface underneath the planetary boundary layer). It varies on a number of time scales (contrary to the much more continuously operating heat source of stars) and is usually coupled to shear flows which are ultimately driven by rotation (winds, global currents). Mean molecular weight gradients are even more important than in the stellar case. But geophysical convection zones only occur in limited domains within a thin sphere. Compressibility is less important than in the stellar case and magnetic fields can be neglected for most problems (except for the *laminar* convection in the earth's mantle). Radiative cooling may be important in some cases (such as lakes – see the contribution by D. Mironov in this volume – or the cooling of clouds), but there are also cases where it can be neglected as well (dry convective planetary boundary layer). Finally, the Prandtl number is of order unity in most geophysical cases (between about 0.7 for air and 6 for water). Nevertheless, convection in the atmosphere and in the ocean is a highly turbulent flow with a tendency of forming large scale coherent structures with remarkable similarities to their astrophysical, stellar counterparts (cf. flow patterns in [14] and [11]).

Solar and stellar convection

The notion that stars with masses greater than about 1.1 times the solar one (M_{\odot}) have convective cores is now generally accepted in astrophysics. The central “convective sphere” is a consequence of the high energy production in these stars and the resulting high luminosity is in agreement with observations. However, these central convection zones do not reach the stellar surface. Probing has hence to be done through indirect methods which rely, for instance, on pulsational and other instabilities these stars can have. Direct observations of stellar convection are easily possible for stars with about one solar mass or less. There, the convective flow is cooled through radiation which is directly emitted into space. The convective motions leave their imprint on the observable radiation field through velocity Doppler shifts and intensity variations. This direct way of probing is restricted to layers visible from outside. For the sun this includes only the top ~ 500 km of a convection zone predicted to be 180000 km deep. The latter has been confirmed through indirect methods, particularly *helioseismology*, which aims at reconstructing the solar density and sound speed profile from observed (few ppm large) oscillations of our sun. Detection of stellar surface convection, which is not connected to the core region, is possible also for stars slightly more massive than the sun, although the higher rotational velocities found for these objects make measurements more difficult.

Our sun is the best studied example of stellar convection. The solar convection zone is characterised by the following properties. Its overall geometry is that of a convective shell within a rotating sphere. The zone features a density contrast of 625,000 and a temperature contrast of 350 between the bottom and the top. It has a depth of 30% of the solar radius. The average Mach number of the flow is about

10^{-4} and the Rossby number $Ro = U/(fL) \sim 0.1$ (f is the rotation rate). It generates solar magnetic fields and the solar activity cycle.

The visible part of the solar convection zone is dominated by large scale, upwards moving structures known as granules which are embedded into a network of rapid and narrow downdrafts. The average granule diameter is found to be around 1100 km. Near the surface the flow reaches Mach numbers of 0.3, i.e. velocities of 2 to 3 km s⁻¹. Ro is around 300 for the granules, hence rotation plays only an indirect role. The key physical process driving motions near the surface is the cooling of fluid. This results in cold and dense gas sinking as drafts which give way to gas pushing upwards from below. The best geophysical counterpart to this process is perhaps convection in the oceans. The similarities include not only high Re numbers, but also a similar topological structure due to cooling from above and a Rossby number of 10 to 25, i.e. $Ro \gg 1$. This makes a comparison between the two particularly interesting, despite the different cooling mechanism and Prandtl number.

Numerical hydrodynamical simulations have become the favourite tool to study solar granulation. From a theoretical viewpoint such calculations are large eddy simulations (LES), because they resolve the large length scales which carry most of the kinetic energy and which are subject to most of the radiative cooling. The unresolved scales are accounted for through simplified models. Detailed comparisons between such simulations and observed data have successfully been done for the calculations by [15] and subsequent numerical simulations based on their work. Observed parameters investigated include granulation sizes and life times, Doppler broadening of spectral lines, and indirect tests such as oscillation frequencies and amplitudes of the average solar radiation field. Further corroboration came from numerical simulations such as those by [14] which differ in the numerical methods used, assumptions made on the microphysics (equation of state, etc.) and on the unresolved scales, as well as in the treatment of the boundaries of the numerical simulation boxes. They predict the same average flow velocities, temperature profiles, energy fluxes, and so forth. This confirms the robustness of the numerical modelling of solar surface convection.

Why are astrophysicists interested in modelling stellar convection ? Convection has fundamental effects on stellar radii and luminosities, on the energy distribution of the emitted radiation, and as a result of all that on the actual observational parameters we find for a star with a given mass and chemical composition at a certain age of its evolution. Another reason is the superior mixing capability of turbulent convection compared to diffusion processes. Trace elements such as ⁷Li and ⁹Be can be destroyed by nuclear fusion at temperatures low enough (2.5 to 3.5 10⁶ K) to make the actual depth of convection zones a distinguishing factor in the observable chemical composition. Through mixing convective cores have access to much more hydrogen than their radiative counterparts. Thus, convection changes observational features (spectral line shapes, ...), global properties (radius, ...), as well as stellar structure and evolution (life times during different phases, ...). Unfortunately, so far the non-linear, turbulent nature of stellar convection has prevented the successful derivation of a general, fully predictive theory of this process from first principles only. Numerical simulations of stellar convection provide an expensive, case-to-case approach which cannot be hooked into a general stellar evolution code just as a global circulation simulation or a terrestrial climate simulation cannot be coupled to simulations of individual tropical storm systems. Moreover, numerical simulations of turbulent convection are not full “ab-initio” calculations either. Further progress in our theories on turbulent convection is thus one of the most wanting questions in stellar astrophysics, but arguably also in various geophysical disciplines.

Reynolds stress models

The Reynolds stress approach is a versatile formalism to model turbulent convection in global evolution calculations. The main idea behind Reynolds stress models is to derive equations from the original

Navier-Stokes equations in which the mean flow components and the mean stratification are separated from fluctuations around those mean values. The same procedure can also be applied to other fields such as concentration of helium in a star or salt in the ocean. The most urging problem encountered in the Reynolds stress approach is the fact that due to the non-linearity of the original equations any equation derived for a certain fluctuating quantity, e.g. velocity u' , depends on products of (usually) several of the involved fluctuating quantities ($u'u'$, ...). Those products are neither small nor do they normally cancel each other. Thus, approximations beyond the original Navier-Stokes equations become inevitable. To proceed only ensemble averages of the fluctuating quantities are considered. The goal of the Reynolds stress approach is to derive a closed set of equations for the mean values (of temperature, etc.) and some of the lower order moments of the fluctuations around them. The predictive capabilities of models based on this approach have to be challenged by observational data or by numerical simulations. Lack of a general theory of turbulent flows, or convective flows for that matter, puts severe limits on the range of application for such models, because their underlying approximations are often based on similarity arguments or motivated by mathematical simplicity. This is the main reason why current diffusion type algebraic models are sought to be replaced for by more complex ones which, for instance, account for non-locality and asymmetries in the turbulent flow.

The most advanced suite of turbulent convection models for both astrophysics and geophysics was proposed in a series of papers by [1], [2], [4], and [5]. The models suggest a set of differential equations for the turbulent kinetic energy $\overline{q^2}$, the squared temperature fluctuations $\overline{\theta^2}$, the (convective) temperature flux $\overline{w\theta}$, the vertical turbulent kinetic energy $\overline{w^2}$, and the kinetic energy dissipation rate ϵ , which is coupled to the equations for the mean structure of the system. Various models were also suggested for the higher order correlations (third order moments) in those papers. Successful comparisons to numerical large eddy simulations and a water tank experiment were presented in [3] and [5] and corroborated applicability to the dry convective planetary boundary layer.

For applications to stars, this approach was adapted in [9] to account for the fact that in optically thin media such as stellar atmospheres, where radiation directly escapes into space, small length scales are preferably damped (i.e. cooled) compared to large ones [9]. This is caused by large scales being less transparent to radiation. In this form, the model was used in a code for computing the structure of stellar envelopes — the outer layers of a star which are not hot enough to ignite nuclear fusion. Comparisons of convective enthalpy flux as well as vertical and horizontal root mean square velocities between this new model, a traditional one which neglects non-locality and flow topology, and numerical simulations were presented in [9] for the case of main sequence A-stars. The latter have a mass of 1.5 to 2.5 M_{\odot} and shallow surface convection zones. In [12] this comparison was extended to envelopes of various types of white dwarfs (remnants of stars with about half to one M_{\odot} which have shallow surface convection zones during parts of their long cooling phase taking place after nuclear fusion has completely stopped). While the traditional convection model strongly underestimates the extent of convective mixing when compared to numerical simulations, the new model is found to agree qualitatively very well (and also quantitatively). This is achieved without readjusting parameters when going from the case in [9] to the case discussed in [12], whereas the old model requires major adjustments of one of its parameters to match at least some results. Looking at observational constraints (surface velocities, spectral energy distribution in the visual range) the new model also performs much better ([9], [12]) than its predecessor.

As the model is successful for such stars, why not use it for the sun as well ?

Coherent structures

The cases studied in [9] and [12] are characterised by rather small values of (velocity) skewness ($S_w = \overline{w^3}/\overline{w^2}^{3/2}$) within convectively unstable regions. Although the convectively mixed parts of

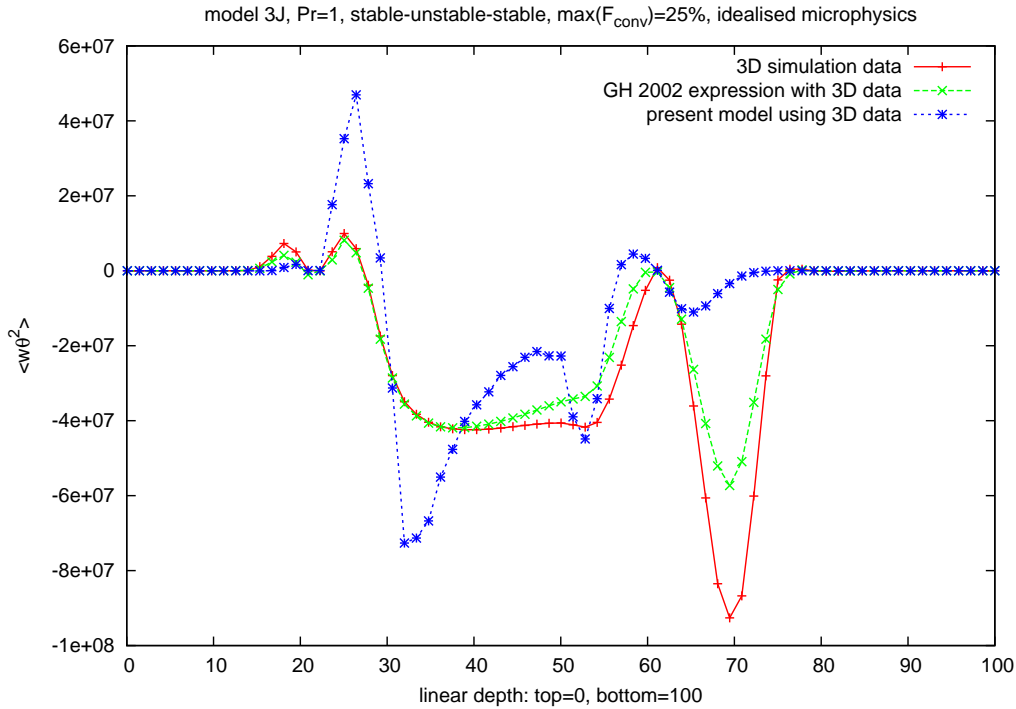


Figure 1: Models for the flux of temperature fluctuations tested with simulation data from [13] for a shallow convection zone with low skewness. The unstable zone is located between 30 and 55 on the linear depth scale. Results are not scaled but given in dimensional units.

these convection zones are rather large (9 to 10 pressure scale heights, i.e., e-folding distances of the total pressure), the actually unstable regions are small (one or two convection zones which are 1 to 1.5 pressure scale heights deep). The solar case is very different with a huge convectively unstable region of 20 pressure scale heights. Both surface observations and numerical simulations indicate large values of S_w for it. Most of the solar convection zone is very close to adiabatic, as radiative losses are very small. The convection zones studied in [9] and [12] are quite the opposite: their temperature gradients are far from adiabatic, because radiative transfer is still efficient enough to transport a large fraction of the total flux.

A look at numerical simulations of convection with idealised microphysics (perfect gas, parameterised radiative conductivity) is instructive. Fig. 1 shows that the model used in [9] and [12] to compute the correlation $\overline{w\theta^2}$ is only roughly corresponding to the directly evaluation of this quantity from a numerical simulation presented in [13]. Although the simulation was done for a much lower Re number and higher Pr number than in stars, it resembles many other aspects of the cases discussed in [9] and [12] such as size of the convectively unstable zone and the amount of convective flux in units of total flux. A similar calculation for a much deeper convection zone with less radiative contributions to energy transport (Kupka and Muthsam, to be published) shows the mismatch between model and simulation becoming unacceptable for $\overline{w\theta^2}$ (up to a factor of 10 inside the convection zone). The cases for which the model developed in [5] and used by [9] and [12] has been successful were all characterised by $|S_w| \leq 1$ which also holds for the bulk part of the original problem, the convective planetary boundary studied in [3]. But in deep convection zones, $|S_w| > 1$ is found for extended regions.

The skewness of turbulent convective flows is directly related to their flow topology. The latter is a consequence of the boundary conditions of a convection zone (heating from below, cooling from above, or both) and the non-local nature of the flow. Local excess cooling at the solar surface, for example,

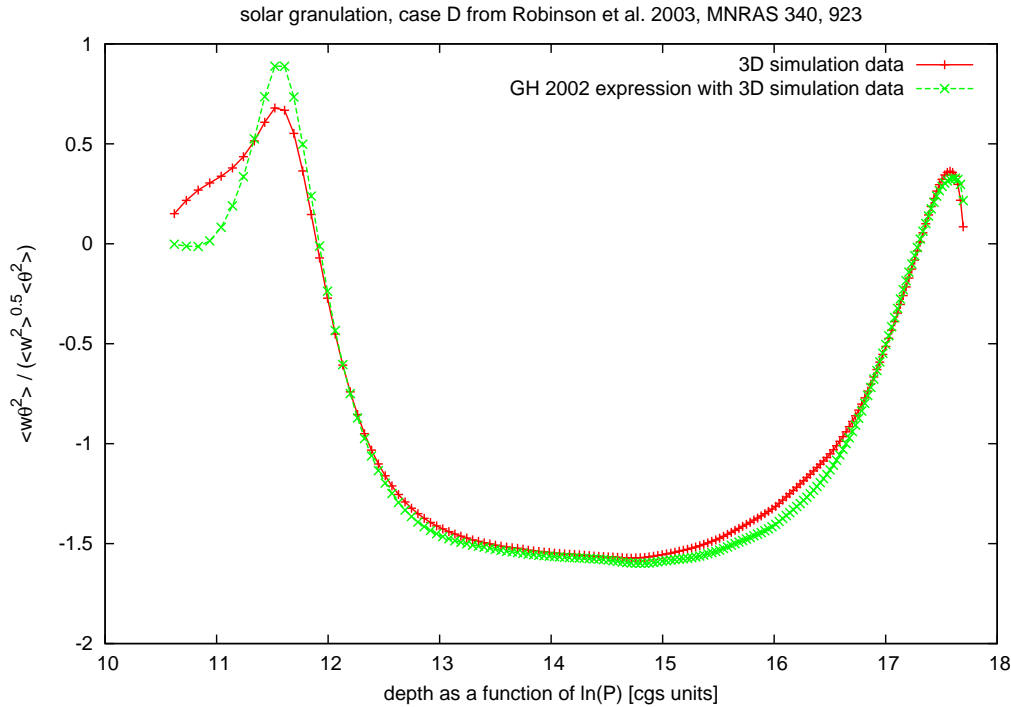


Figure 2: Normalised flux of temperature fluctuations from simulations [14] compared to a model expression suggested in [7]. Horizontally averaged pressure P measures depth.

gives rise to downdrafts while fluid is pushing upwards around them. This creates the structure we observe ([15]). It leads to the intrinsic inhomogeneity of turbulent convection and to the existence of large scale coherent structures.

As the coherent structures are responsible for the main fraction of energy transport, result from the non-local nature of turbulent convection, and are characterised by their skewness, a better model for third order moments such as $\overline{w^3}$ and $\overline{w\theta^2}$ is probably a key to improve Reynolds stress models of convection. After all, third order moments represent non-locality within these models ([1] and references therein). They can be related to skewness and the relative size of areas of up- and downflow ([4] and references in [7]). A model which accounts for the influence of coherent structures on third and fourth order moments has been proposed by [7] (see also the contribution of Gryanik and Hartmann in this volume). The model suggests an interpolation between the two limiting cases of zero skewness and very large skewness and generalises previous expressions for these correlation functions. It has been successfully tested with aircraft measurements and numerical simulations of the convective planetary boundary layer ([7], [8]). In addition, it was tested by [10] using numerical simulations of ocean convection. Fig. 2 shows another (yet unpublished) test using solar granulation simulation data from [14]. The approximative expression $\overline{w\theta^3}/\overline{\theta^2}$ matches almost exactly that one obtained from a direct evaluation of $\overline{w\theta^2}$. The match is all the more remarkable as it extends over many pressure scale heights from the observable surface (around $\ln(P) \sim 11$) well into the solar interior. Fig. 1 confirms a similar success for the shallow convection zone studied by [13] (the larger deviation below that convection zone, around a depth of 70, is in a region dominated by the much higher viscosity of that case). Fig. 3 shows a test for the fourth order moment $\overline{w\theta^3}$. A perfect model would yield a straight line at 1. Clearly, the model proposed by [7] does a much better job than the standard one (which had implicitly been assumed also in the Reynolds stress model used in [3], [5], [9], and [12]). The deviations are large

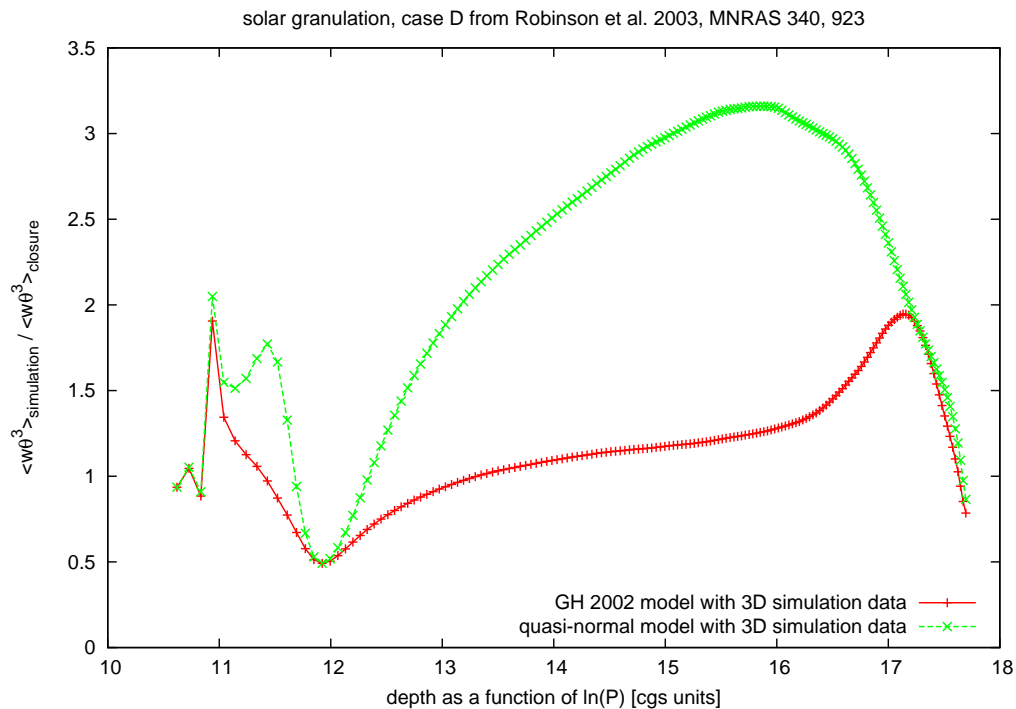


Figure 3: Similar to Fig. 2 but showing the ratio of simulation results to model expressions (with input data from simulations) for the flux of the cube of temperature fluctuations.

(factor of 2) only near the (artificial) boundaries of the simulation domain.

An alternative model was suggested by [6] (and discussed by V.M. Canuto at this workshop). The advantage of their formalism is to offer a complete Reynolds stress model which has already been tested for the planetary boundary layer using aircraft data, rather than just approximations for certain terms in the Reynolds stress equations, as proposed by [7] and [8]. However, it has not been tested yet using ocean or solar simulation data.

As this example shows the exchange of ideas on turbulent convection modelling is possible despite very different parameter ranges are encountered (Pr number) and specific physical processes (radiation, ...) are interacting with the flow. There are quite a few benefits from an such exchange of ideas. More minds working on related problems may share their knowledge and a larger or at least different parameter space can be accessed. A particular quantity may be directly measurable in one field thus providing more insight into the physics influencing it and may become more clear. Questions such as: “How universal is a particular model ?” might be sensibly posed. — And perhaps more likely be answered ?

Acknowledgements

I would like to express my gratitude to H.J. Muthsam and F.J. Robinson for permission to use their numerical simulation data.

References

- [1] V. M. Canuto, *Astrophys. Jour.* **392** (1992) 218

- [2] V. M. Canuto, *Astrophys. Jour.* **416** (1993) 331
- [3] V. M. Canuto, F. Minotti, C. Ronchi, R. M. Ypma and O. Zeman, *Jour. Atmos. Sci.* **51** (1994) 1605
- [4] V. M. Canuto and M. Dubovikov, *Astrophys. Jour.* **493** (1998) 834
- [5] V. M. Canuto, Y. Cheng and A. Howard, *Jour. Atmos. Sci.* **58** (2001) 1169
- [6] Y. Cheng, V. M. Canuto and A. M. Howard, *Jour. Atmos. Sci.* (2005) in press
- [7] V. M. Gryanik and J. Hartmann, *Jour. Atmos. Sci.* **59** (2002) 2729
- [8] V. M. Gryanik, J. Hartmann, S. Raasch and M. Schröter, *J. Atmos. Sci.*, (2005) in press
- [9] F. Kupka and M. H. Montgomery, *Mon. Not. Roy. Astr. Soc.* **330** (2002) L6
- [10] M. Losch, *Geophys. Res. Lett.* **31** (2004) L23301
- [11] D. V. Mironov, V. M. Gryanik, C.-H. Moeng, D. J. Olbers and T. H. Warncke, *Quart. Jour. Roy. Meteorol. Soc.* **126** (2000) 477
- [12] M. H. Montgomery and F. Kupka, *Mon. Not. Roy. Astr. Soc.* **350** (2004) 267
- [13] H. J. Muthsam, W. Göb, F. Kupka, W. Liebich and J. Zöchling, *Astron. & Astrophys.* **293** (1995) 127
- [14] F. J. Robinson, P. Demarque, L. H. Li, S. Sofia, Y. C. Kim, K. L. Chan and D. B. Guenther, *Mon. Not. Roy. Astr. Soc.* **340** (2003) 923
- [15] R. F. Stein and Å. Nordlund, *Astrophys. Jour.* **499** (1998) 914

Situations in stars where thermohaline convection (fingers regime) is expected to take place

S. Vauclair

Laboratoire d'astrophysique, Observatoire Midi-Pyrénées, Toulouse, France

Thermohaline convection

Thermohaline convection (fingers regime) is a wellknown process in oceanography : warm salted layers on the top of cool unsalted ones rapidly diffuse downwards even in the presence of stabilizing temperature gradients. When a blob is displaced downwards, it wants to go further down due to its overweight compared to the surroundings, but at the same time the fact that it is hotter contradicts this tendency. When the salt gradient is large compared to the thermal gradient, salted water normally mixes down until the two effects compensate. Then thermohaline convection begins. While the medium is marginally stable, salted blobs fall down like fingers while unsalted matter goes up around. This process is commonly known as “salt fingers” (Stern 1960, Kato 1966, Veronis 1965, Turner 1973, Turner and Veronis 2000, Gargett and Ruddick 2003). The reason why the medium is still unstable is due to the different diffusivities of heat and salt (for this reason it is also called “double-diffusive convection”). A warm salted blob falling down in cool fresh water sees its temperature decrease before the salt has time to diffuse out: the blob goes on falling due to its weight until it mixes with the surroundings.

The condition for the salt fingers to develop is related to the density variations induced by temperature and salinity perturbations. Two important characteristic numbers are defined:

- the density anomaly ratio

$$R_\rho = \alpha \nabla T / \beta \nabla S \quad (1)$$

where $\alpha = -(\frac{1}{\rho} \frac{\partial \rho}{\partial T})_{S,P}$ and $\beta = (\frac{1}{\rho} \frac{\partial \rho}{\partial S})_{T,P}$ while ∇T and ∇S are the average temperature and salinity gradients in the considered zone

- the so-called “Lewis number”

$$\tau = \kappa_S / \kappa_T = \tau_T / \tau_S \quad (2)$$

where κ_S and κ_T are the saline and thermal diffusivities while τ_S and τ_T are the saline and thermal diffusion time scales.

The density gradient is unstable and overturns into dynamical convection for $R_\rho < 1$ while the salt fingers grow for $R_\rho \geq 1$. On the other hand they cannot form if R_ρ is larger than the ratio of the thermal to saline diffusivities τ^{-1} as in this case the salinity difference between the blobs and the surroundings is not large enough to overcome buoyancy (Huppert and Manins 1973, Gough and Toomre 1982, Kunze 2003).

Salt fingers can grow if the following condition is satisfied:

$$1 \leq R_\rho \leq \tau^{-1} \quad (3)$$

The stellar case

Thermohaline convection may occur in stellar radiative zones when a layer with a larger mean molecular weight sits on top of layers with smaller ones (Kato 1966, Spiegel 1969, Ulrich 1972, Kippenhahn et al 1980). In this case $\nabla_\mu = d \ln \mu / d \ln P$ plays the role of the salinity gradient while the difference $\nabla_{ad} - \nabla$ (where ∇_{ad} and ∇ are the usual adiabatic and local (radiative) gradients $d \ln T / d \ln P$) plays

the role of the temperature gradient. When ∇_{ad} is smaller than ∇_{rad} , the temperature gradient is unstable against convection (Schwarzschild criterion) which corresponds to warm water below cool water in oceanography. In the opposite case the temperature gradient is stable but the medium can become convectively unstable if:

$$\nabla_{crit} = \frac{\phi}{\delta} \nabla_{\mu} + \nabla_{ad} - \nabla < 0 \quad (4)$$

where $\phi = (\partial \ln \rho / \partial \ln \mu)$ and $\delta = (\partial \ln \rho / \partial \ln T)$. When this situation occurs, convection first takes place on a dynamical time scale and the μ enriched matter mixes down with the surroundings until ∇_{crit} vanishes. Then marginal stability is achieved and thermohaline convection may begin as a “secular process”, namely on a thermal time scale (short compared to the stellar lifetime!).

Stellar situations in which fingers should occur

Such an effect has previously been studied for stars with a helium-rich accreted layer (Kippenhahn et al 1980). It was also invoked for helium-rich stars in which helium is supposed to accumulate due to diffusion in a stellar wind (as proposed by Vauclair 1975) and for roAp stars in case some helium accumulation occurs (Vauclair et al 1991).

A new interesting situation where thermohaline convection should occur is related to exoplanets hosts stars. These stars present a metallicity excess compared to stars in which no planets have been detected. This result is confirmed by all recent observations. However the reason for this excess is still a subject of debate: is it primordial, is it the result of accretion or both? If hydrogen poor matter is accreted on the top of a main-sequence type star with normal abundances, it creates an inverse μ -gradient which may lead to thermohaline convection. Comparing the stellar case with the water case, we can guess that metallic fingers will form if the following condition is verified :

$$1 \leq \left| \frac{\delta(\nabla_{ad} - \nabla)}{\phi(\nabla_{\mu})} \right| \leq \tau^{-1} \quad (5)$$

with $\tau = D_{\mu}/D_T = \tau_T/\tau_{\mu}$ where D_T and D_{μ} are the thermal and molecular diffusion coefficients while τ_T and τ_{μ} are the corresponding time scales.

The study of thermohaline mixing in stars is far from trivial. Detailed comparisons of numerical simulations and laboratory experiments in the water case have recently been published (Gargett and Ruddick 2003) but the stellar case may be different as mixing then occurs in a compressible stratified fluid.

Although approximative, the computations show that metallic matter accreted onto a star should not stay in the outer layers: it first turns over due to dynamical convection and then goes on diffusing due thermohaline convection. This type of convection should be studied in the future with numerical simulation. It may also have important effects in A-type chemically peculiar stars where the combined effect of gravity and radiative acceleration can lead to metal accumulation in internal stellar layers.

References

- [1] Gargett, A., Ruddick, B. 2003, ed., Progress in Oceanography, vol 56, issues 3-4, pages 381-570, special issues on “Double diffusion in Oceanography”,
- [2] Gough, D.O., Toomre, J., 1982, J.Fluid Mech, 125, 75
- [3] Huppert, H.E., Manins, P.C. 1973, Deep-Sea Research, 20, 315

- [4] Kato, S., 1966, PASJ, 18, 374
- [5] Kunze, E. 2003, Progress in Oceanography, 56, 399
- [6] Kippenhahn, R., Ruschenplatt, G., Thomas, H.C. 1980, A&A, 91, 175
- [7] Spiegel, E. 1969, Comments on Ap and Space Phys ; 1, 57
- [8] Stern, M.E., 1960, Tellus, 12, 2
- [9] Turner, J.S.1973, Buoyancy effects in fluids, Cambridge University Press
- [10] Turner, J.S., Veronis, G. 2000 journal fluid dynamics, 405, 269
- [11] Ulrich, R.K., 1972, Astrophys. Jour., 172, 165
- [12] Vauclair, S.1975, A&A, 45, 233
- [13] Vauclair, S., Dolez,N., Gough, D.O. 1991, A&A, 252, 618
- [14] Veronis, G.J., 1965, Marine Res.,21, 1

The need for small-scale turbulence in atmospheres of substellar objects

Christiane Helling

Scientific and Research Support Department,
ESTEC/ESA, Noordwijk, The Netherlands

Abstract

Brown dwarfs and giant gas planets are substellar objects whose spectral appearance is determined by the chemical composition of the gas and the solids/liquids in the atmosphere. Atmospheres of substellar objects possess two major scale regimes: large-scale convective motions + gravitational settling and small-scale turbulence + dust formation. Turbulence initiates dust formation spot-like on small scale, while the dust feeds back into the turbulent fluid field by its strong radiative cooling. Small, imploding dust containing areas result which eventually become isothermal. Multi-dimensional simulations show that these small-scale dust structures gather into large-scale structures, suggesting the formation of clouds made of dirty dust grains. The chemical composition of the grains, and thereby the chemical evolution of the gas phase, is a function of temperature and depends on the grain's history.

Introduction

The first brown dwarf Gliese 229B has been discovered 10 years ago by direct imaging (Kulkarni & Golimovsky 1995). These faint ($L_* = 10^{-7} \dots 10^{-1} L_\odot$), cool ($T_{\text{eff}} = 500 \dots 3200 \text{ K}$), and small ($M_* = 0.01 \dots 0.08 M_\odot$) objects bridge the physical and chemical gap between the classical understanding of stars ($M_* > 0.08 M_\odot$) and planets ($M_* < 0.01 M_\odot$). Much closer by, direct images reveal spotty, cloudy, and vortex surface pattern in the giant planet atmospheres in our own solar system (by the Cassini and Galileo spacecrafts fly-bys of Saturn and Jupiter, respectively) which guide our imagination for substellar but extra-solar atmospheres. The other major source of information is the measurement of the energy distribution of the stellar radiative flux emerging from the object's atmosphere (e.g. for Gliese 229B Oppenheimer et al. 1998). The interpretation of the resulting spectral energy distribution demands a certain completeness³ of the adopted substellar atmosphere model. Substellar atmospheres, i.e. giant gas planets and brown dwarfs, are very cool and therefore exhibit a rich molecular- and solid-/liquid-phase chemistry. Transitions between the phase regimes are to be expected. Therefore, models of substellar atmospheres – as the interface to the physical and the chemical state of the object – need to represent the *circuit of dust* (Helling 1999, Woitke & Helling 2003) which includes the formation of dust, the chemical composition of dust and gas, gravitational settling (rain), its feedback on the dust formation process, and element replenishment by upward convective motions in addition to hydrodynamics and radiative transfer. In contrast to terrestrial planets which possess their solid surface as continuous source of seed particles⁴, the actual formation of the first (solid or liquid) surface out of the gas phase has to be considered in substellar atmospheres. Convection is an efficient mechanism to continuously and intermittently dredge up fresh, uncondensed gaseous material from the very bottom of the atmosphere. The convection furthermore serves as turbulence engine inside

³e.g. in modeling the molecular regime, chemistry and hydrodynamics

⁴Seed particles on Earth are called *aerosols* which are for instance volcanic dust and tire particles, or they come from fire in the tropics and from smoke-tracks.

$\tau_{\text{sink}} = \frac{H_p}{\bar{v}_{\text{dr}}}$	15 min ... 8 month ($a = 100\mu\text{m} \dots 0.1\mu\text{m}$)	dust settling
$\tau_{\text{conv}} = \frac{l_{\text{conv}}}{v_{\text{conv}}}$	20 min ... 3.5 h	large scale convection
$\tau_{\text{gr}} = \frac{\langle a \rangle}{\chi_{\text{net}}}$	0.1 s ... 1 1/2 min ($a = 0.1\mu\text{m} \dots 100\mu\text{m}$)	dust growth
$\tau_{\text{wave}} = \frac{L}{ U + c_s}$	0.3 ... 3 s	wave propagation
$\tau_{\text{nuc}} = \frac{\rho L_0}{J_*}$	$\approx 10^{-3}$ s	seed formation
$\tau_{\text{num}} \approx \frac{Re^3 L}{10^5}$	$5 \cdot 10^5$ yr ($\approx 2 \times \text{age of mankind}$)	10^3 floating-point operations per cell and Δt with 1 gigaflop

Table 10: Time scales of the processes involved in the *circuit of dust* in a substellar atmosphere. Temperature T , density ρ , pressure scale height H_p , convective velocity v_{conv} , and velocity of sound c_s are adopted from the model results by Allard et al. (2001) and Tsuji (2002). For more details on τ_{sink} see (Woitke & Helling 2003).

the atmosphere. Consequently, modeling and understanding a substellar atmosphere means to model and to understand a reactive, dust forming, turbulent fluid field.

Catching the small scales

Classical models for substellar atmospheres represent the whole turbulent scale spectrum by only one scale, the mixing length. These models have given very reasonable fits to observed spectra in certain wavelength regimes but are challenged by the progress in observational techniques which lead to observations e.g. with higher resolutions and at longer wavelength ($\lambda > 12\mu\text{m}$). Other models like Reynolds stress and LES are in progress, all of them being challenged by the closure problem, i.e. the treatment of the smallest, unresolved scales.

In order to provide insight and understanding of the small scale regimes of a substellar atmosphere, the interaction of turbulence and dust formation has been studied by utilizing 1D and 2D simulations in the present work. The general phenomenology of a substellar atmosphere model can be demonstrated by estimating the time scale of the individual processes (Table). The gravitational settling time scale of grains τ_{sink} is the largest and is comparable to a typical convective mixing time for large grains. The smallest time is needed by the formation of seed particles out of the gas phase. The dust growth time scale is of the order of the crossing time of an acoustic wave. Hence, two time regimes appear: (i) a quasi-static regime governed by gravitational settling and large-scale convective motions, and (ii) a dynamic regime governed by the dust formation and small-scale waves (turbulence). Actually, a third regime (iii) is to be faced which concerns the computing time needed to resolve the turbulent problem (last entry Table). In order to tackle regime (iii), the small-scale regime (ii) was investigated. Here, gravitational settling can be neglected and convection acts only indirectly as turbulence driver.

The following system of dimensionless equations has been solved where Eqs. 1– 3 are the equation of continuity, of motion, and the energy equation, respectively. The source term in Eqs. 3 is due to

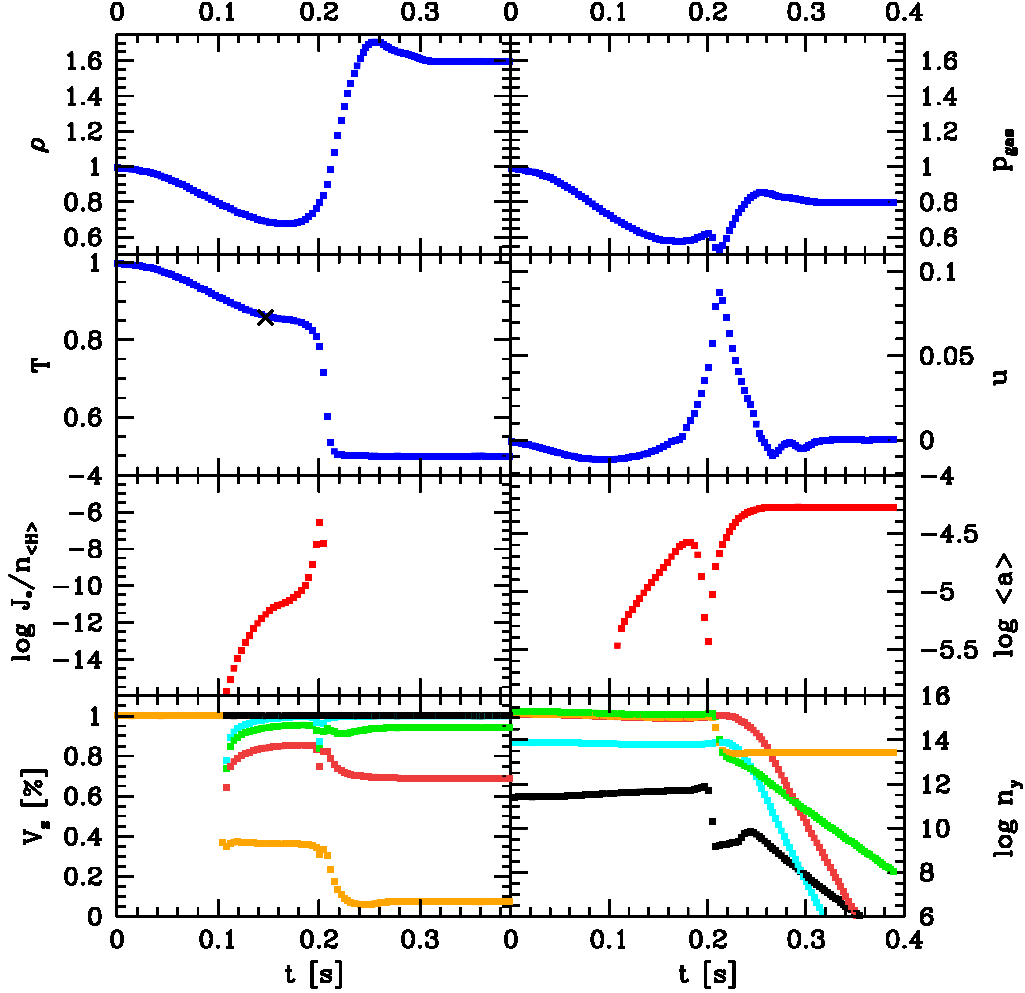


Figure 1: The feedback between turbulence and dust formation in a 1D simulation of interaction turbulence elements. The time evolution of all quantities is depicted at the site of maximum superposition of the turbulence elements.

Parameter: $T_{\text{ref}} = 1900\text{K}$, $T_{\text{RE}} = 1634\text{K}$, $\rho_{\text{ref}} = 10^{-4}\text{g/cm}^3$, $M=0.1$ ($u_{\text{ref}} = 3 \cdot 10^4\text{cm/s}$), $t_{\text{ref}} = 3\text{s}$, $l_{\text{ref}} = 10^5\text{cm}$. [numerical parameter: $N_x = 500$, $N_k = 500$, $\Delta x = 3.94 \cdot 10^2\text{cm}$, $l_{\text{max}} = l_{\text{ref}}/2$]

1st row: l.h.s. - ρ density, r.h.s. - p pressure; **2nd row:** l.h.s. - T temperature (cross - time of maximum wave superposition), r.h.s. - u fluid velocity; **3rd row:** l.h.s. - $\log J_*/n_{\langle H \rangle}$ nucleation rate [1/s], r.h.s. - $\log \langle a \rangle$ mean grain size [cm]; **4th row:** l.h.s. - $V_{\text{tot}} = \sum V_s$ cumulative volumes [%] (orange - $V_{\text{MgSiO}_3[\text{s}]}$, brown - $V_{\text{MgSiO}_3[\text{s}]} + V_{\text{SiO}_2[\text{s}]}$, green - $V_{\text{MgSiO}_3[\text{s}]} + V_{\text{SiO}_2[\text{s}]} + V_{\text{Fe}[\text{s}]}$, light blue - $V_{\text{MgSiO}_3[\text{s}]} + V_{\text{SiO}_2[\text{s}]} + V_{\text{Fe}[\text{s}]} + V_{\text{Al}_2\text{O}_3[\text{s}]}$, dark blue - $V_{\text{MgSiO}_3[\text{s}]} + V_{\text{SiO}_2[\text{s}]} + V_{\text{Fe}[\text{s}]} + V_{\text{Al}_2\text{O}_3[\text{s}]} + V_{\text{TiO}_2[\text{s}]}$), r.h.s. - $\log n_y$ number density of gaseous key species for dust formation [1/cm³] (orange - Mg, brown - SiO, green - Fe, light blue - AlOH, black - TiO₂).

radiative cooling modeled by a relaxation ansatz.

$$(\rho)_t + \nabla \cdot (\rho \mathbf{v}) = 0 \quad (1)$$

$$(\rho \mathbf{v})_t + \nabla \cdot (\rho \mathbf{v} \circ \mathbf{v}) = -\frac{1}{M^2} \nabla P - \gamma \frac{M^2}{Fr} \rho \mathbf{g} \quad (2)$$

$$(\rho e)_t + \nabla \cdot (\mathbf{v}[\rho e + P]) = Rd \kappa (T_{RE}^4 - T^4) \quad (3)$$

$$(\rho L_j)_t + \nabla \cdot (\mathbf{v} \rho L_j) = Da_d^{\text{nuc}} Se_j J_* + Da_d^{\text{gr}} \frac{j \chi^{\text{net}}}{3} \rho L_{j-1} \quad (4)$$

$$(\rho \epsilon_x)_t + \nabla \cdot (\mathbf{v} \rho \epsilon_x) = -\sum_{r=1}^R (\nu_r^{\text{nuc}} El Da_d^{\text{nuc}} \sqrt[3]{36\pi} N_1 J_* + \nu_r^{\text{gr}} El Da_d^{\text{gr}} n_{x,r} v_{\text{rel},x} \alpha_r \rho L_2) \quad (5)$$

Equations 4 ($j = 0, 1, 2, 3$; $\rho L_j(\vec{x}, t) = \int_{V_\ell}^\infty f(V, \vec{x}, t) V^{j/3} dV$ dust moments, $f(V, \vec{x}, t)$ grain size distribution function) model the dust formation as two step-process, namely, seed formation and mantle growth/evaporation being the first and the second source term, respectively. Equations 5 are element conservation equation for each chemical element ϵ_x ($x = \text{Mg, Si, O, Fe, Al, Ti}$) involved in the dust formation processes, hence each source term in Eqs. 4 is a sink for Eqs. 5 (Helling et al. 2001 for details). A strong coupling exists between Eqs. 1–3 (5 equations) and Eqs. 4, 5 (11 equations) due to the dust opacity κ since it changes by order of magnitudes if dust forms.

Turbulence ↔ Dust formation

The feedback between turbulence and dust formation can be studied in detail by 1D simulations. Interacting turbulence elements are modeled as superimposing expansion waves. Figure demonstrates the time evolution of the system at the site of constructive wave interaction.

Turbulence → Dust formation:

At about the time of superposition (black cross on T-curve, l.h.s. 2nd row), the nucleation threshold temperature (here for TiO_2 seed formation) is crossed and dust nucleation is initiated, hence the nucleation rate J_* increases. Many solid compounds are already thermally stable at such low temperatures which results in a very rapid growth of a mantle on the surface of the seed particles (here Mg_2SiO_4 _[s], SiO_2 _[s], Fe _[s], Al_2O_3 _[s], TiO_2 _[s]). As the amount of dust formed increases, the opacity κ of the dust-gas mixture increases by order of magnitudes. Therefore, the radiative cooling causes the temperature T to drop considerably (l.h.s., 2nd row). A classical instability establishes where the reason supports the cause. The cooler the gas, the more dust forms, the faster the temperature drops etc. This run-away effect stops if all condensible material was consumed or if the temperature is too low for further efficient nucleation. The time of maximum nucleation rate corresponds to a minimum in mean grain size because suddenly the available gaseous material is needed for a much larger number of grains.

Dust formation → Turbulence:

The strong temperature gradient causes a strong raise in density by a moderate pressure gradient. Without such a strong cooling, pressure equilibrium should adjust. Hence, the dust forming areas implode and cause a considerable disturbance of the velocity field (here up to 10%). A feedback-loop *turbulence* ⇒ *dust formation* ⇒ *turbulence* established as result of non-linear coupling of the model equations.

Chemistry:

Figure depicts in the lowest two panels the strong feedback of the turbulent dust formation process on the chemical composition of the dust grains and on the remaining gas phase. The cumulative dust volumes (l.h.s., 4th row) show that the dust composition changes according to the temperature

from Mg_2SiO_4 _[s]/ SiO_2 _[s]/ Fe _[s]-rich (40%/40%/10%) with Al and Ti – oxide impurities to a mean grain composition of 55% SiO_2 _[s], 25% Fe _[s], and 10% Mg_2SiO_4 _[s] with Al and Ti – oxide impurities. The chemical composition of the dust is also imprinted in the element abundances of the gas phase and the molecular abundances adjust accordingly.

Dust clouds growing from small → large

1D simulations allow a very detailed investigation of the physio-chemical interactions but fail to explain 2- or 3-dimensional phenomena like cloud or vortex formation as it was suggested by observations of Saturn’s and Jupiter’s atmospheres. The study of the formation and the possible appearance of large scale dust clouds in substellar atmospheres was performed utilizing a model for driven turbulence. Turbulence is modeled by the superposition of N_k modes each having a Kolmogoroff velocity amplitude (for details Helling et al. 2004). Convection is believed to drive the turbulence in a real substellar atmosphere. The 2D simulation (Fig.) is started from a homogeneous, dust free medium which constantly is disturbed by the turbulence driving from the left, the right and the bottom side during the simulation.

During the initial phase of the simulations small scale nucleation events occur where turbulence causes the local temperature to drop below the nucleation threshold (compare Sect.). Observe that a locally maximum J_* in Fig. a) is immediately followed by an subsequent increase in n_d (panel b). These dusty areas tend to increase as the fluid motion transports the dust into areas with a still undepleted gas phase. And indeed, as the simulation proceeds in time, larger and more compact cloud-like dust structures are formed (panel c). These large-scale structures are the result of the hydrodynamic fluid motion which gathers more and more dust also by the vortices appearing in the velocity field. Note the mushroom-like structure evolving e.g. in the right lower corner in panel c). Strong radiative cooling causes these dusty areas to become isothermal. Eventually, the cloud will leave the test volume or it will get disrupted and the small-scale fragments move out of sight. The whole dust cloud formation cycle can start again only if metal species (Mg, Si, Fe, Al, Ti, O) are replenished from outside like it has to be expected to occur by convection in a substellar atmosphere (panel d).

Conclusion

Substellar atmospheres, i.e. atmospheres of giant gas planets and brown dwarfs, possess two scale regimes: (i) the large-scale convection causing element replenishment of the upper atmosphere and the counteracting gravitational settling of dust causing an element depletion of the upper atmosphere (ii) small-scale turbulence and dust formation establishing a feedback loop.

Regime (i) can be considered as quasi-static with view on the dust formation process. The dynamic regime (ii) is determined by the turbulence initiating spot-like dust formation on small spatial scales. The strong radiative cooling by dust results in an implosion of the dust forming areas which eventually become isothermal. Velocity disturbances occur which feed back into the turbulent fluid field. The resulting mesoscopic flow gathers the dust in even larger, more compact cloud-like structures. The final chemical composition of the grain is a function of the grains history.

Acknowledgements

The ESA research fellowship program at ESTEC is acknowledged. W. Traub and M. Fridlund are thanked for discussion on aerosols. Most of the literature search has been performed with the ADS system.

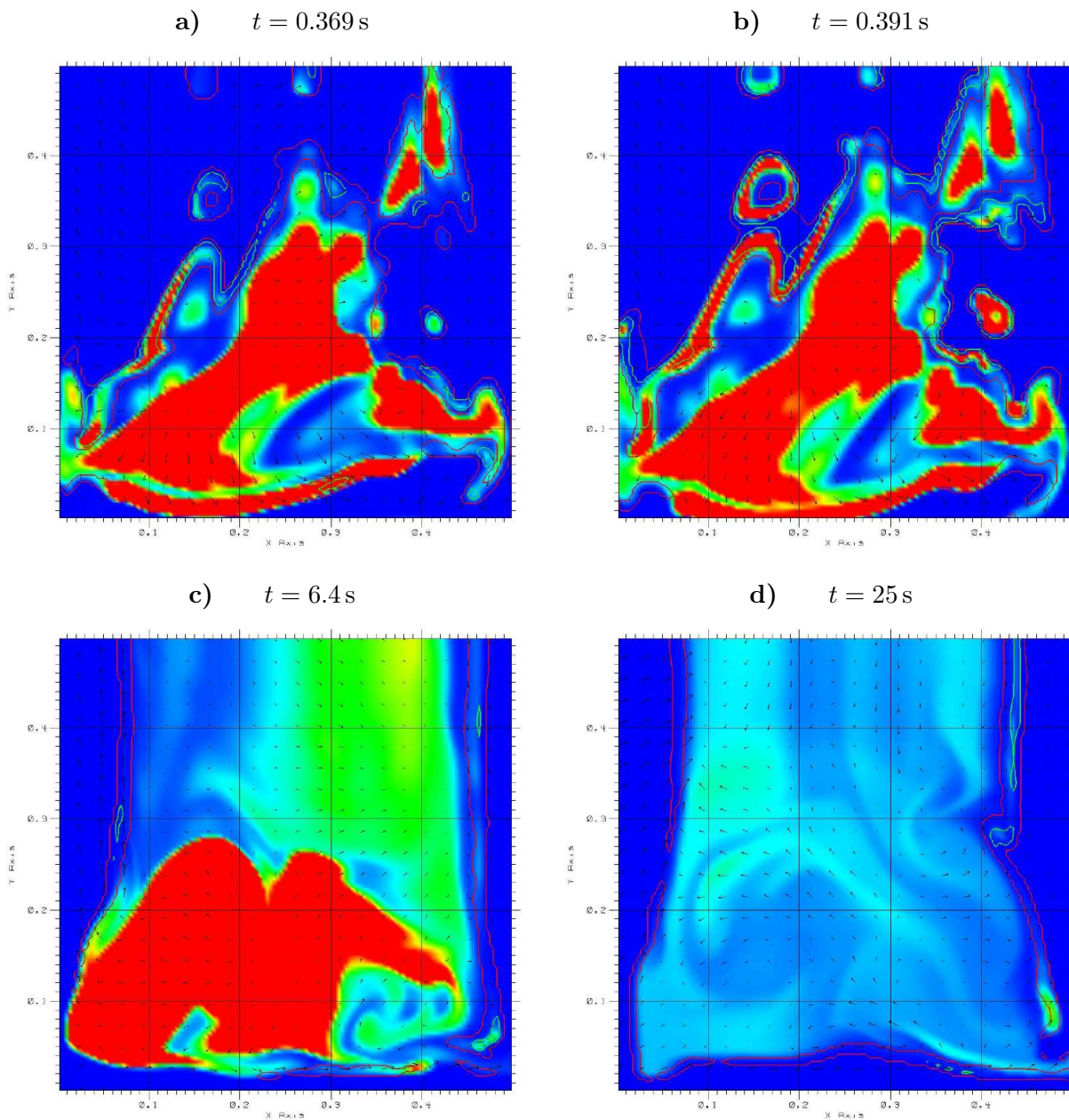


Figure 2: $T_{\text{ref}} = 2100\text{K}$, $T_{\text{RE}} = 1980\text{K}$, $g = 10^5$ g/cm², $\rho_{\text{ref}} = 3.16 \cdot 10^{-4}$ g/cm³, $M=1$ ($u_{\text{ref}} = 3 \cdot 10^5$ cm/s), $t_{\text{ref}} = 0.3$, $l_{\text{ref}} = 10^5$ cm [numerical parameter: $N_x \times N_y = 128 \times 128$, $N_k = 500$, $\Delta x = 3.94 \cdot 10^2$ cm, $l_{\text{max}} = l_{\text{ref}}/2$]

$\log n_d$ number of dust particles – false color (red = max, blue = min), $\log J_*$ nucleation rate – contour lines (green = max, red = min), $\vec{v} = v_x + v_y$ fluid velocity – vector arrows.

References

- [1] Allard, F., Hauschildt, P.H., Alexander, D.R., Tamanai, A., Schweitzer, A. 2001, ApJ **556**, 357
- [2] Helling Ch., Oevermann M., Lüttke M., Klein R., Sedlmayr E. 2001, A&A **376**, 194
- [3] Helling Ch., Klein R., Woitke, P., Nowak, U., Sedlmayr E. 2004, A&A **423**, 657
- [4] Kulkarni, S., Golimovsky, D. 1995, STScI-1995-48
- [5] Oppenheimer, B.R., Kulkarni, S.R., Matthews, K., van Kerkwijk, M.H. 1998, ApJ **502**, 932
- [6] Tsuji, T. 2002, ApJ **575**, 264
- [7] Woitke P., Helling Ch. 2003, A&A **399**, 297
- [8] Woitke P., Helling Ch. 2004, A&A **414**, 335

Flow Patterns and Transitions in Rotating Convection

K.L. Chan

The Hong Kong University of Science & Technology

Turbulent rotating convection frequently occurs in stars and planets. The process is so complex that its study often needs to resort to numerical simulations, especially since deep stratification is commonly involved. In an astrophysical context, the circulation is global, and ideally, the flows should be studied with a global model. In most instances, however, such is impractical due to the unaffordable demand on computing resources. Besides the long integration time required for thermal relaxation, the situation is worsened by the requirement of higher resolutions and shorter time steps in fast rotation situations. Therefore, some researchers adopt the convection-in-a-box approach [1, 2] which can only look at the idealized local behavior. A similar approach has long been used in geophysics; idealized atmospheric flows (predominantly two-dimensional) have been studied in localized f-planes and beta-planes. The results have been very useful in providing understanding for the basic flow processes.

Here, we report a rather special result from our numerical study of localized, deep, turbulent, rotating convection. The domain of each computation is a rectangular box termed ‘f-box’, *a la* f-plane. The angular velocity vector is held fixed in each case, but the flows are very much three-dimensional, and in particular the Coriolis force generated by the vertical velocity cannot be ignored.

Our main result can be summarized by a few sentences: Medium scale (width \sim a few scale heights) coherent structures (flow patterns) are ubiquitous in rotating convection flows. The forms of the coherent structures depend on the Coriolis number ($Co \equiv L\Omega/V$, reciprocal of the Rossby number) as well as the aspect ratio of the f-box. Pattern changes induce corresponding qualitative changes in the turbulence characteristics (e.g. moments of the fluctuating quantities). Therefore, coherent structures are crucial for the understanding of rotating convection. They are more fundamental than the concept of Reynolds stress. This conclusion is drawn from studying over one hundred cases of numerical experiments covering different input fluxes from the bottom, different latitudes (ϕ), different rotation rates (Ω), and different grid sizes. The corresponding locations of the boxes are from the equator to the North pole, and the range of Coriolis number is from 0 to 18.

The so-called coherent structures are essentially rolls tilted in different ways and thus presenting different impressions – either as convective rolls lying horizontally or slightly tilted, or as vortices with some possible tilts from the vertical.

When the rotation rate is low ($Co < 1$), there is a *negative shear* in the mean zonal flow (eastward flow decreases with height) that has a linear vertical profile and spans the full depth of the convection zone (except at the pole, see [3]). It is basically a consequence of the conservation of angular momentum [4]. In the low latitudes ($< 45^\circ$), vague features of east-west aligned rolls first appear; they can be understood as cloud streets [5] or in terms of preferential growth of linear modes [6]. The roll feature is most prominent at the equator.

When Co gets above 1, the alignment of the low-latitude rolls changes from east-west to north-south. Correspondingly the zonal-meridional component of the Reynolds stress changes from removing to feeding angular momentum towards the equator. The *negative shear* is compressed to shallower and shallower layers in the top region. The *local* value of Co remains low (V higher, L lower) there.

Remnant traces of east-west rolls can still be detected in this top region. In the lower region, the mean zonal flow tends to zero [3].

The alignment transition at the equator, however, occurs at a much higher Co (between 3 and 6). Before that the shear in the zonal flow stays negative and linear throughout the depth of the convection zone. Beyond a critical Co , it flips abruptly to a *positive linear shear*[7]. The positive shear is associated with the dominance of cyclonic rolls over anticyclonic rolls (all north-south aligned). For the same reason given in the previous paragraph, there is a shallow negative shear layer at the top of the convection zone. This process is important for explaining the occurrence of equatorial superrotation near the surface of the sun and the giant planets.

Coherent cyclonic structures in the form of vortices appear in the other latitudes around the same Co . The sizes of the vortices decrease towards the pole (as the value of the parameter $f = 2\Omega \sin \phi$ increases). These structures are accompanied by spotty horizontal distributions of thermal fields and possess very large horizontal velocities. Their presence induces a big drop in the coherence of the thermal variables with the vertical velocity. For example, the correlation coefficient between the temperature fluctuation and the vertical velocity drops from the general level of 0.75 to 0.15.

A further transition of flow pattern is found in non-equatorial regions when Co reaches about 12 - 18. Anticyclonic vortices become the dominant feature. They are stronger and larger than the cyclonic vortices which still persist. This process may be important for the generation of the Great Red Spot and White Ovals in the Jovian atmosphere.

Acknowledgements

The research is supported by the Research Grant Council of Hong Kong (HKUST6119/02P).

References

- [1] D.H. Hathaway and R.C.J. Sommerville, *J. Fluid Mech.* **126** (1983) 75.
- [2] N.H. Brummell, T.L. Clune, and J. Toomre, *ApJ* **570** (2002) 825.
- [3] K.L. Chan, *ApJ* **548** (2001) 1102.
- [4] P.A. Gilman, and P.V. Foukal, *ApJ* **229** (1979) 1179.
- [5] D.K. Lilly, *J. Atmos. Sci.* **23** (1966) 481.
- [6] D.H. Hathaway, P.A. Gilman, and J. Toomre, *Geophys. Astrophys. Fluid Dyn.* **13** (1979) 289.
- [7] K.L. Chan, in *3D Stellar Evolution*, *Astron. Soc. Pacific Conf. Series*, **293** (2003) 168.

Gravoturbulent Fragmentation: Star formation and the interplay between gravity and interstellar turbulence

S. Kitsionas, R.S. Klessen

Astrophysikalisches Institut Potsdam, An der Sternwarte 16, D-14482, Potsdam, Germany

Introduction

Star clusters form by gravoturbulent fragmentation of interstellar gas clouds. The supersonic turbulence ubiquitously observed in Galactic molecular gas generates strong density fluctuations with gravity taking over in the densest and most massive regions. Once such dense cloud regions become gravitationally unstable, collapse sets in to build up stars and star clusters.

Turbulence plays a dual role. On global scales it provides support, while at the same time it can promote local collapse. Stellar birth is thus intimately linked to the dynamical behavior of the parental gas cloud, which determines when and where protostellar cores form, and how they contract and grow in mass via accretion from the surrounding cloud material to build up stars. Slow, inefficient, isolated star formation is a hallmark of turbulent support, whereas fast, efficient, clustered star formation occurs in its absence.

In this proceedings paper we discuss the dynamical complexity arising from the interplay between supersonic turbulence and self-gravity and introduce the process of gravoturbulent fragmentation (Σ). The fact that Galactic molecular clouds are highly filamentary can be explained by a combination of compressional flows and shear (Σ). The dynamical evolution of nascent star clusters is very complex. This strongly influences the stellar mass spectrum (Σ). The equation of state (EOS) plays a pivotal role in the fragmentation process. Under typical cloud conditions, massive stars form as part of dense clusters. However, for gas with effective polytropic index greater than unity star formation becomes biased towards isolated massive stars, which may be of relevance for understanding Pop III stars (Σ).

Spatial Distribution and Timescale

Supersonic turbulence plays a dual role in star formation. While it usually is strong enough to counterbalance gravity on global scales it will usually provoke collapse locally. For further references see the reviews by Larson [15] and Mac Low & Klessen [17]. Turbulence establishes a complex network of interacting shocks, where regions of high-density build up at the stagnation points of convergent flows. These gas clumps can be dense and massive enough to become gravitationally unstable and collapse when the local Jeans length becomes smaller than the size of the fluctuation. However, the fluctuations in turbulent velocity fields are highly transient. They can disperse again once the converging flow fades away [25]. Even clumps that are strongly dominated by gravity may get disrupted by the passage of a new shock front [19].

For local collapse to result in the formation of stars, Jeans unstable, shock-generated, density fluctuations must, therefore, collapse to sufficiently high densities on time scales shorter than the typical time interval between two successive shock passages. Only then do they ‘decouple’ from the ambient flow pattern and survive subsequent shock interactions. The shorter the time between shock passages, the less likely these fluctuations are to survive. The overall efficiency of star formation depends strongly on the wavelength and strength of the driving source [5, 9], (see also Σ). Both regulate the amount of gas available for collapse on the sonic scale where turbulence turns from supersonic to subsonic [24].

The velocity field of long-wavelength turbulence is dominated by large-scale shocks which are very efficient in sweeping up molecular cloud material, thus creating massive coherent structures. These exceed the critical mass for gravitational collapse by far. The situation is similar to localised turbulent decay, and quickly a cluster of protostellar cores builds up. Prominent examples are the Trapezium Cluster in Orion with a few thousand young stars. However, this scenario also applies to the Taurus star forming region which is historically considered as a case of isolated stellar birth. Its stars have formed almost simultaneously within several coherent filaments which apparently are created by external compression [2]. This renders it a clustered star forming region in the sense of the above definition.

The efficiency of turbulent fragmentation is reduced if the driving wavelength decreases. There is less mass at the sonic scale and the network of interacting shocks is very tightly knit. Protostellar cores form independently of each other at random locations throughout the cloud and at random times. There are no coherent structures with multiple Jeans masses. Individual shock generated clumps are of low mass and the time interval between two shock passages through the same point in space is small. Hence, collapsing cores are easily destroyed again. Altogether star formation is inefficient, and stars are dispersed throughout the cloud.

Altogether, we call this intricate interaction between turbulence on the one side and gravity on the other – which eventually leads to the transformation of some fraction of molecular cloud material into stars as described above – *gravoturbulent fragmentation*. To give an example, we discuss in detail the gravitational fragmentation in shock-produced filaments that closely resembles structures observed in the Taurus star forming region.

Gravitational Fragmentation of a Filament in a Turbulent Flow

In Taurus, large-scale turbulence is thought to be responsible for the formation of a strongly filamentary structure [2]. Gravity within the filaments should then be considered as the main mechanism for forming stars. Following earlier ideas by Larson [14], Hartmann [4] has shown that the Jeans length within a filament, and the timescale for it to fragment are given by

$$\lambda_J = 1.5 T_{10} A_V^{-1} \text{ pc}, \quad (1)$$

$$\tau \sim 3.7 T_{10}^{1/2} A_V^{-1} \text{ Myr}. \quad (2)$$

where T_{10} is the temperature in units of 10 K, and A_V is the visual extinction through the center of the filament. By using a mean visual extinction for starless cores of $A_V \sim 5$, Eq. 1 gives a characteristic Jeans length of $\lambda_J \sim 0.3$ pc, and collapse should occur in about 0.74 Myr. Indeed, there are 3–4 young stellar objects per parsec which agrees well with the above numbers from linear theory of gravitational fragmentation of filaments [4].

In order to test these ideas, we resort to numerical simulations. We analyse a smoothed particle hydrodynamics (SPH; [3, 22]) calculation of a star forming region that was specifically geared to the Taurus cloud. Numerical implementation, performance and convergence properties of the method are well tested against analytic models and other numerical schemes in the context of turbulent supersonic astrophysical flows [9, 10, 11, 18].

This simulation has been performed without gravity until a particular, well defined elongated structure is formed. We then turn on self-gravity. This leads to localised collapse and a sparse cluster of protostellar cores builds up. Timescale and spatial distribution are in good agreement with findings in Taurus [4]. For illustration, we show eight column density frames of the simulation in Fig. 1. The first frame shows the structure just before self-gravity is turned on, and we note that the filament forms cores in a fraction of Myr. The time-step between frames is 0.1 Myr. The mean surface density for the filament is 0.033 g cm^{-2} , corresponding to a visual extinction of ~ 7.5 . Using Eqs. 1 and 2 this

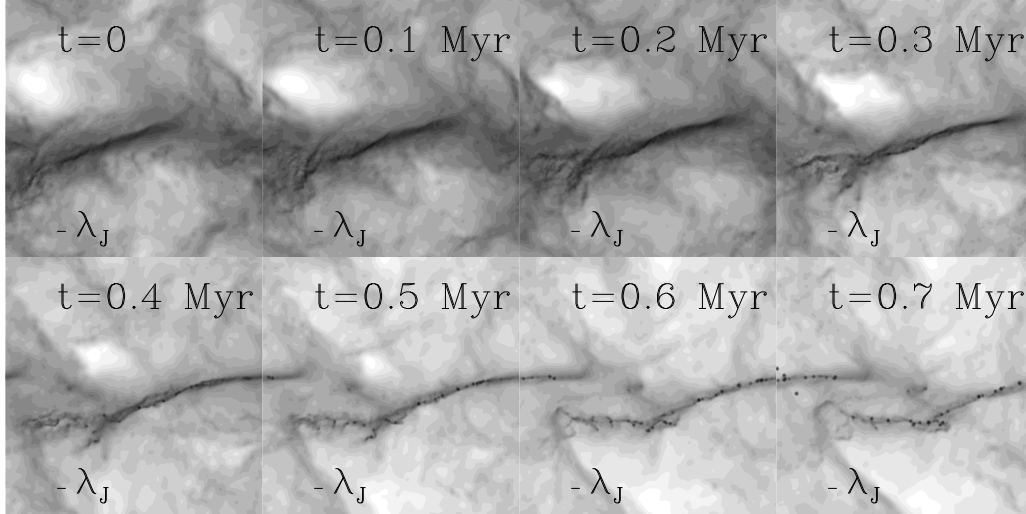


Figure 1: Evolution of the column density of an SPH simulation. The filament in the first frame (before self-gravity is turned on) shows that turbulence is responsible in forming this kind of structures. The small bar in the bottom-left of each frame denotes the Jeans length (Eq. 1) at this time. At later times, self-gravity is turned on and the filament suffers gravitational fragmentation on a free-fall timescale (Eq. 2).

value gives a Jeans length of $\lambda_J \sim 0.2$ pc, and a collapsing timescale of $\tau \sim 0.5$ Myr. Note from Fig. 1 that the first cores appear roughly at $t \sim 0.3$ Myr, although the final structure of collapsed objects is clearly defined at $t = 0.5$ Myr. The typical separation between protostellar cores (black dots in Fig. 1) is about the Jeans length λ_J .

This example demonstrates that indeed turbulence is able to produce a strongly filamentary structure and that at some point gravity takes over to form collapsing objects, the protostars. However, the situation is quite complex. Just like in Taurus, the filament in Fig. 1 is not a perfect cylinder, the collapsed objects are not perfectly equally spaced as predicted by idealised theory, and protostars do not form simultaneously but during a range of times (between $t \approx 0.3$ and 0.6 Myr). Even though the theory of gravitational fragmentation of a cylinder roughly applies, it becomes clear from looking at Fig. 1 that the properties of the star forming region not only depend on the conditions set initially but are influenced by the large-scale turbulent flow during the entire evolution. Gravoturbulent fragmentation is a continuous process that shapes the accretion history of each protostar in a stochastic manner [7].

Mass Spectra of Clumps and Protostellar Cores

The dominant parameter determining stellar evolution is the mass. We discuss now how the final stellar masses may depend on the gravoturbulent fragmentation process, and analyse four numerical models which span the full parameter range from strongly clustered to very isolated star formation [8].

Fig. 2 plots the mass distribution of all gas clumps, of the subset of Jeans critical clumps, and of collapsed cores. We show four different evolutionary phases, initially just when gravity is ‘switched on’, and after turbulent fragmentation has led to the accumulation of $M_* \approx 5\%$, $M_* \approx 30\%$ and $M_* \approx 60\%$ of the total mass in protostars. In the completely pre-stellar phase the clump mass spectrum is very steep (about the Salpeter slope, -2.33 , or less) at the high-mass end. It has a break and gets shallower below $M \approx 0.4 \langle M_J \rangle$ with slope -1.5 . The spectrum strongly declines beyond the SPH resolution limit.

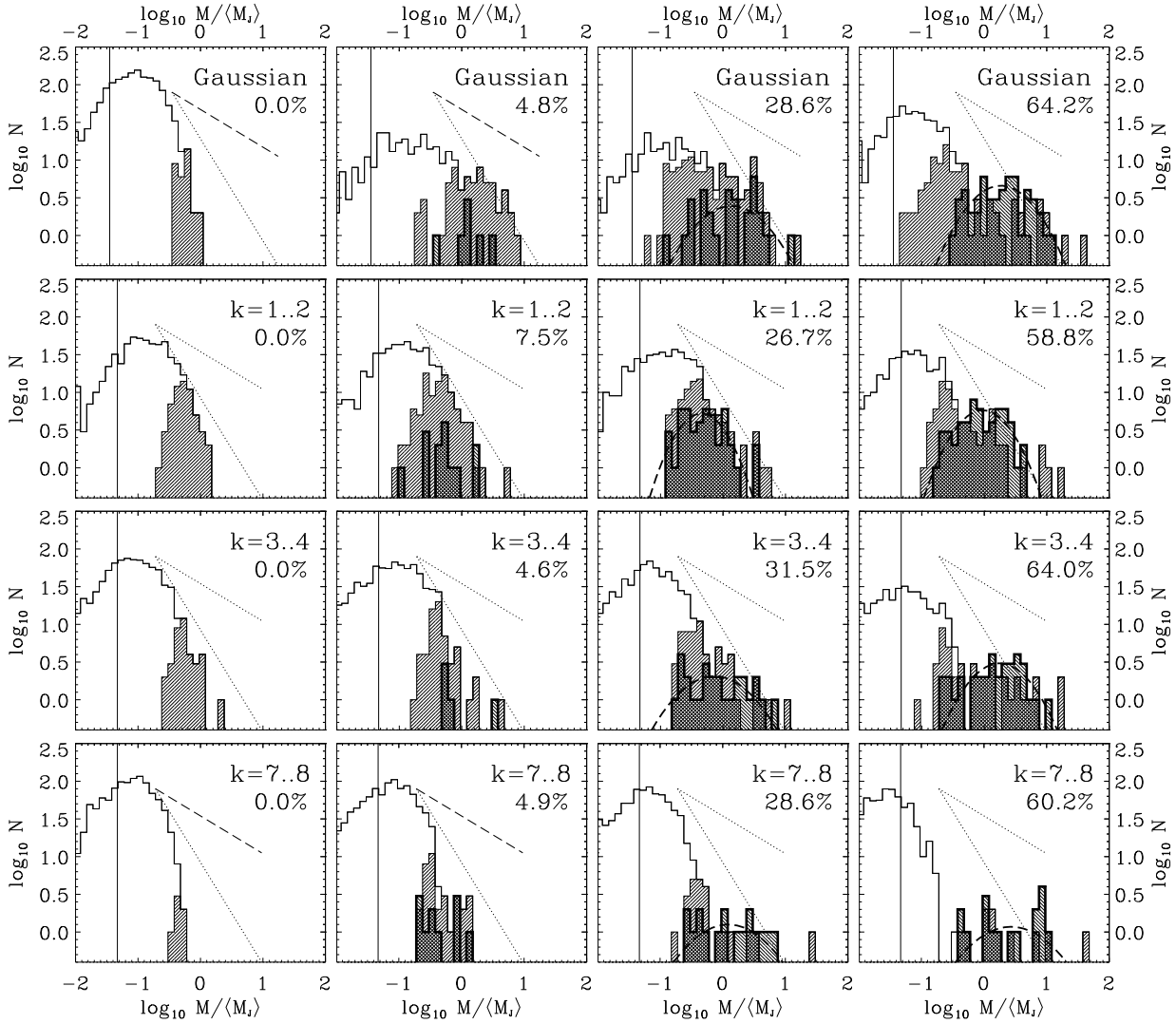


Figure 2: Mass spectra of all gas clumps (thin lines), of the subset of Jeans unstable clumps (thin lines, hatched distribution), and of collapsed cores (protostars: hatched thick-lined histograms). Different evolutionary phases are defined by the fraction of mass converted into protostars and are indicated in the upper right corner of each plot. Masses are binned logarithmically and normalised to the average Jeans mass $\langle M_J \rangle$. The vertical line shows the SPH resolution limit. Shown also are two power-law spectra with $\nu = -1.5$ and $\nu = -2.33$ [8].

Individual clumps are hardly more massive than a few $\langle M_J \rangle$. Gravitational evolution modifies the distribution of clump masses considerably. As clumps merge and grow bigger, the spectrum becomes flatter and extends towards larger masses. Consequently the number of cores that exceed the Jeans limit increases. This is most evident in the Gaussian model of decayed turbulence, where the clump mass spectrum exhibits a slope -1.5 .

The mass spectrum depends on the wavelength of the dominant velocity modes. Small-scale turbulence does not allow for massive, coherent and strongly self-gravitating structures. Together with the short interval between shock passages, this prohibits efficient merging and the build up of a large number of massive clumps. Only few clumps become Jeans unstable and collapse to form stars.

This occurs at random locations and times. The clump mass spectrum remains steep. Increasing the driving wavelength leads to more coherent and rapid core formation, resulting in a larger number of protostars.

Long-wavelength turbulence or turbulent decay produces a core mass spectrum that is well approximated by a *log-normal* distribution. It roughly peaks at the *average thermal Jeans mass* $\langle M_J \rangle$ of the system [9, 10] and is comparable in width with the observed IMF [12]. However, this is still debated [20]. The log-normal shape of the mass distribution may be explained by invoking the central limit theorem [26], as protostellar cores form and evolve through a sequence of highly stochastic events (resulting from supersonic turbulence and/or competitive accretion).

Effects of the Equation of State

So far, we focused only on isothermal models of molecular clouds. More generally, however, the balance of heating and cooling in a molecular cloud can be described by a polytropic EOS, $P = K\rho^\gamma$, where K is a constant, and P, ρ and γ are thermal pressure, gas density and polytropic index, respectively. A detailed analysis by Spaans & Silk [23] suggests that $0.2 < \gamma < 1.4$ in the interstellar medium.

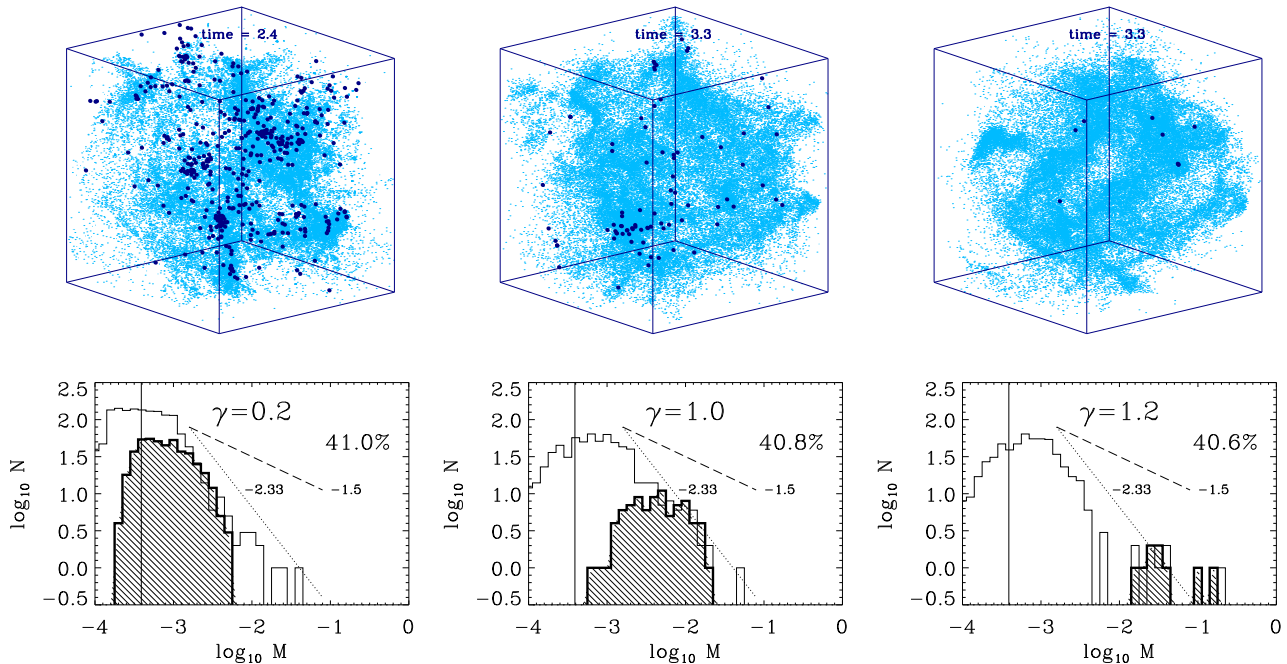


Figure 3: Top: 3-D distribution of the gas and protostars for different γ . Bottom: Mass spectra of gas clumps (*thin lines*) and of protostars (collapsed cores: *hatched thick-lined histograms*) for the corresponding cube above. The percentage shows the fraction of total mass accreted onto protostars. The vertical line shows the SPH resolution limit. Shown also are two power-law spectra with $\nu = -1.5$ (dashed-line) and $\nu = -2.33$ (dotted line). (Figure adopted from Li et al. [16].)

Li, Klessen & Mac Low [16] carried out detailed SPH simulations to determine the effects of different EOS on gravoturbulent fragmentation by varying γ in steps of 0.1 in otherwise identical simulations. Fig. 3 illustrates how low γ leads to the build-up of a dense cluster of stars, while high values of γ result in isolated star formation. It also shows that the spectra of both the gas clumps and protostars change with γ . In low- γ models, the mass distribution of the collapsed protostellar cores at the high-mass end is roughly log-normal. As γ increases, fewer but more massive cores emerge.

When $\gamma > 1.0$, the distribution is dominated by high mass protostars only, and the spectrum tends to flatten out. It is no longer described by either a log-normal or a power-law. The clump mass spectra, on the other hand, do show power-law behavior at the high mass side, even for $\gamma > 1.0$.

This suggests that in a low- γ environment stars tend to form in clusters and with small masses. On the other hand, massive stars can form in small groups or in isolation in gas with $\gamma > 1.0$.

The formation of isolated massive stars is of great interest, as usually, massive stars are found in clusters. There are indications of isolated massive stars or very small groups of massive stars in the bulge of M51 [13] as well as observations of massive, apparently isolated field stars in both the Large and Small Magellanic Clouds [21]. This is consistent with our models assuming $\gamma > 1.0$.

High resolution simulations of the formation of Population III stars [1] suggest that in very metal-deficient gas only one massive object forms per pregalactic halo. In the early Universe, inefficient cooling due to the lack of metals may result in high γ . Our models then suggest weak fragmentation, supporting the hypothesis that the very first stars build up in isolation.

This is further backed up by investigations that show that the characteristic mass for fragmentation not only depends on the average thermal Jeans mass, but also on the detailed changes of the polytropic index γ with density [6].

Acknowledgements

We thank Javier Ballesteros-Paredes, Yuexing Li, Anne-Katharina Jappsen, Stefan Schmeja, and Mordecai Mac Low for continuing discussions and collaborations. RSK acknowledges support by the Emmy Noether Programme of the Deutsche Forschungsgemeinschaft (grant no. KL1358/1).

References

- [1] Abel, T, Bryan, G., & Norman, M. L., 2002, *Science*, 295, 5552, 93
- [2] Ballesteros-Paredes, J., Hartmann, L., Vázquez-Semadeni, E., 1999, *ApJ*, 527, 285
- [3] Benz, W., 1990, in *The Numerical Modeling of Nonlinear Stellar Pulsations*, ed. J. R. Buchler (Dordrecht: Kluwer), 269
- [4] Hartmann, L. 2002, *ApJ*, 578, 914
- [5] Heitsch, F., Mac Low, M.-M., Klessen, R. S., 2001, *ApJ*, 547, 280
- [6] Jappsen, A.-K., Klessen, R. S., Larson, R. B., Li, Y., Mac Low, M.-M., 2005, *A&A*, 435, 611
- [7] Klessen, R. S., 2001a, *ApJ*, 550, L77
- [8] Klessen, R. S., 2001b, *ApJ*, 556, 837
- [9] Klessen, R. S., Burkert, A., 2000, *ApJS*, 128, 287
- [10] Klessen, R. S., Burkert, A., 2001, *ApJ*, 549, 386
- [11] Klessen, R. S., Heitsch, F., Mac Low, M.-M., 2000, *ApJ*, 535, 887
- [12] Kroupa, P., 2002, *Science*, 295, 82
- [13] Lamers, H. J. G. L. M., et al., 2002, *ApJ*, 566, 818
- [14] Larson, R. B., 1985 *MNRAS*, 214, 379

- [15] Larson, R. B., 2003, *Rep. Prog. Phys.*, 66, 1651
- [16] Li, Y., Klessen, R. S., Mac Low, M.-M., 2003, *ApJ*, 592, 975
- [17] Mac Low, M.-M., Klessen, R. S., 2004, *Rev. Mod. Phys.*, 76, 125
- [18] Mac Low, M.-M., Klessen, R. S., Burkert, A., Smith, M. D., 1998, *Phys. Rev. L.*, 80, 2754
- [19] Mac Low, M.-M., McKee, C. F., Klein, R. I., Stone, J. M., Norman, M. L., 1994, *ApJ*, 433, 757
- [20] Martel, H., Evans II, N. J., Shapiro, P. R., *ApJ*, submitted (astro-ph/0505008)
- [21] Massey, P., *ApJS*, 141, 81
- [22] Monaghan, J. J., 1992, *ARA&A*, 30, 543
- [23] Spaans, M., Silk, J., 2000, *ApJ*, 538, 115
- [24] Vázquez-Semadeni, E., Ballesteros-Paredes, J., Klessen, R. S., 2003, *ApJ*, 585, L131
- [25] Vázquez-Semadeni, E., Shadmehri, M., Ballesteros-Paredes, J., 2002, *ApJ*, submitted (astro-ph/0208245)
- [26] Zinnecker, H., 1984, *MNRAS*, 210, 43

Turbulent Combustion in Type Ia Supernova Models

F.K. Röpke, W. Hillebrandt

Max-Planck-Institut für Astrophysik, Karl-Schwarzschild-Str. 1, D-85741 Garching, Germany

Abstract

We review the astrophysical modeling of type Ia supernova explosions and describe numerical methods to implement numerical simulations of these events. Some results of such simulations are discussed.

Astrophysical and numerical models

Type Ia supernovae (SNe Ia) are among the brightest and most energetic explosions observed in the Universe. For a short time they can outshine an entire galaxy consisting of some hundred billions of stars. Assuming that SNe Ia originate from a single stellar object, only two sources of explosion energy come into consideration: the gravitational binding energy of the star and its nuclear energy. Since for the particular class of SNe Ia no compact object is found in the remnant, they are usually associated with thermonuclear explosions of white dwarf (WD) stars consisting of carbon and oxygen. The currently favored astrophysical model assumes it to be part of a binary constellation and to accrete matter from the companion until it comes close to the limiting Chandrasekhar mass. At this stage, the central density of the WD reaches values at which nuclear burning of carbon towards heavier elements ignites. After a simmering phase of several hundreds of years, a thermonuclear runaway in a tiny region close to the center leads to the formation of a thermonuclear flame.

The astrophysical interest in SNe Ia is – among other things – founded on their relevance for cosmology. On the basis of an empirical calibration relating their peak luminosities with the shapes of their lightcurves they are a suitable tool to determine cosmological distances. The geometrical survey of the Universe performed in this way led to one of the greatest surprises of modern astrophysics pointing to the fact that the Universe is predominantly made of a so far unknown “dark energy” component. SNe Ia distance measurements may in the future possibly contribute to the determination of the equation of state of this dark energy. However, the empirical calibration applied here urgently calls for a theoretical explanation and ongoing SN Ia cosmology projects crucially depend on increasing the accuracy of the measurements by getting a handle on the systematic errors. This is achievable only on the basis of a better understanding of the mechanism of SN Ia explosions.

To this end, we attempt to model SN Ia explosions from “first principles” in conjunction with detailed comparison with observations of nearby objects. The goal is to construct numerical models as parameter-free as possible.

Such a SN Ia explosion model has to describe the propagation of the thermonuclear flame from the WD’s center outwards. Hydrodynamics in principle allows for two distinct modes here. One is the so-called deflagration mode, in which the subsonic flame is mediated by the thermal conduction of the degenerate electrons, and the other is a supersonic detonation in which the flame is driven by sound waves.

A prompt detonation has been ruled out as a valid model for SNe Ia, since the entire star is incinerated with sound speed here. Therefore the material has no time to pre-expand and is burned at high densities where the nuclear reactions terminate in iron group elements. This is in disagreement with observations showing that intermediate mass elements need to be produced as well. Hence, the flame must start out subsonically in the deflagration mode. However, a laminar deflagration flame is

much too slow to release sufficient energy to explode the star. The main issue of SN Ia models is thus to identify mechanisms to accelerate the flame propagation.

This is the point where turbulence comes into play. The interaction of the flame with turbulent motions defines burning in SNe Ia as a problem of turbulent combustion. The flame propagating from the center of the star outwards produces an inverse density stratification in the gravitational field of the WD leaving light and hot nuclear ashes behind while the fuel in front of it is dense and cold. The resulting Rayleigh-Taylor instability leads to the formation of burning bubbles that buoyantly rise into the fuel. The shear flows at the interfaces of these bubbles are characterized by a Reynolds number of about 10^{14} and the Kelvin-Helmholtz instability generates turbulent eddies. These decay in a turbulent energy cascade and the flame interacts with eddies on a wide range of scales. In this way, the flame becomes corrugated and its surface area is enlarged. This enhances the net burning rate and accelerates the flame propagation. A later transition of the flame propagation mode is still hypothetical and not further discussed here.

For a numerical implementation of the deflagration SN Ia model, the scale down to which the flame interacts with turbulent motions has to be considered. This is the so-called Gibson scale, at which turbulent velocity fluctuations of the cascade reach values comparable with the laminar flame speed. At the beginning of the explosion (the WD star has a radius of about 2000 km and ignites inside the first ~ 100 km), the Gibson scale is of the order of 10^4 cm. The flame width, however, is less than a millimeter. Due to this huge scale separation, turbulent eddies interact with the flame only in a kinematic way but leave the internal flame structure unaffected. Thus, burning proceeds in the so-called flamelet regime of turbulent combustion for most parts of the explosion process. With three-dimensional simulations on scales of the WD star, it is possible to reach resolutions down to less than a kilometer. Of course, these simulations need to take into account effects of turbulence on smaller (unresolved) scales, which is implemented via a sub-grid scale model (cf. the contribution of W. Schmidt et al.). Complementary small-scale simulations are provided to test the assumptions of flame propagation around and below the Gibson scale.

One has to keep in mind, however, that the explosion process takes place on an expanding background. Due to the energy release, the WD expands. With lower fuel densities, the flame structure broadens and the laminar flame speed decreases [1]. Therefore the Gibson scale becomes smaller and eventually, in the very late phases of the explosion, turbulent eddies may be capable of penetrating the flame structure so that the distributed burning regime is entered.

The numerical implementation of the outlined SN Ia model on scales of the WD star follows [2] in a large eddy simulation (LES) approach. The resolved hydrodynamics is described by the PROMETHEUS implementation [3] of a higher-order Godunov scheme. Turbulence on unresolved scales is taken into account with a sub-grid scale model. Seen from scales of the WD, the flame appears as a sharp discontinuity separating the fuel from the ashes. Its propagation is modeled via the level set method [4], where the flame velocity is set by the physics of the flamelet regime. Here, flame propagation completely decouples from the microphysics of the burning and is determined by the turbulent velocity fluctuations on the grid scale which are known from the sub-grid scale model. The nuclear reactions are implemented in the simplified approach of [5].

Results

Numerical simulations on the basis of the outlined model have been shown to lead to explosions of the WD star. A flame ignited near the center of the star (cf. top left panel of Fig. 1) develops the typical “mushroom”-like features due to buoyancy instabilities (cf. top right panel of Fig. 1). It becomes increasingly wrinkled and the generated turbulence accelerates the flame propagation. In this way, the flame incinerates considerable fractions of the material (cf. bottom left panel of Fig. 1) and the

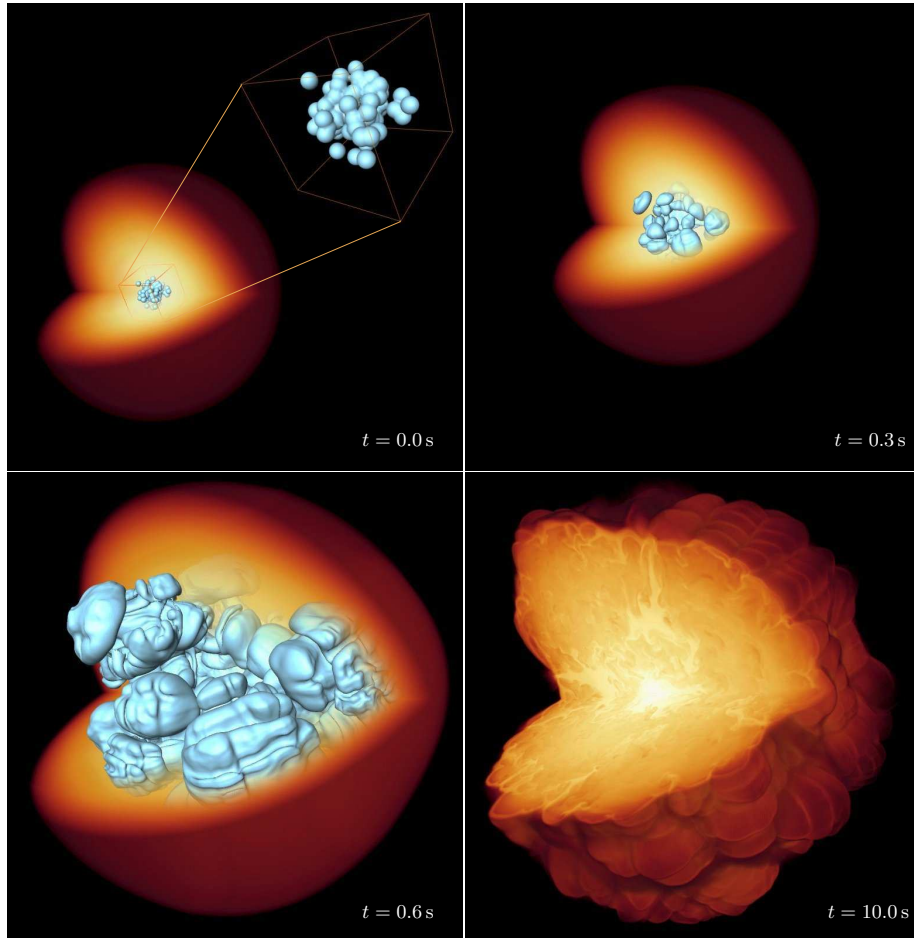


Figure 1: Snapshots from a SN Ia explosion simulation. The WD star is indicated by the volume rendering of the logarithm of the density and the isosurface corresponds to the flame front. The snapshot at $t = 10.0$ s is not on scale with the other images. (Simulation from [6])

energy release is sufficient to gravitationally unbind the WD star. A snapshot of the density structure of the remnant after the burning has ceased is shown in the bottom right panel of Fig. 1, where the imprints of turbulent burning are clearly visible. The most vigorously exploding model so far released about 7×10^{51} erg of energy [7]. Another important global quantity to assess the explosion process is the mass of produced ^{56}Ni , because its radioactive decay powers the visible event. In the mentioned simulation, $0.4 M_{\odot}$ of ^{56}Ni were obtained. Both values are within the range of expectation from observations, albeit on the low side. First synthetic light curves have been derived from explosion simulations [8] and compare well with observations.

However, current deflagration models of SNe Ia seem to have difficulties reproducing observed spectra. A spectrum of the late (“nebular”) phase at day 350 after explosion was recently derived [9] from a very simple simulation. Although reproducing the broad iron lines of observed spectra well, it showed strong indication of unburnt material at low velocities which is not seen in the observations. Both features, however, share a common origin. The rising bubbles filled with ashes distribute iron group elements over a wide range in velocity space and thus give rise to broad iron lines. At the same time, downdrafts in between these bubbles transport unburnt material towards the center producing the strong oxygen and carbon lines which are absent in the observations.

This problem may in part be attributed to the simplicity of the underlying explosion simulation. It was performed on only one octant of the star with rather low resolution and the flame was ignited in a very artificial shape. Nonetheless, it seems likely that physical ingredients are still missing in the explosion model. In particular, burning at late phases was ignored as yet. Fuel consumption was ceased when the flame reached densities of unburnt material below 10^7 g cm^{-3} , because the distributed burning regime is expected to be entered here. A recent approach [10], however, modeled the transition between the turbulent burning regimes by assuming flamelet scaling for the flame propagation velocity above this density threshold and by applying Damköhler's limit for the thin reaction zone regime [11] below. The result strongly supports the conjecture that an implementation of burning at low densities may help to cure current problems of the deflagration SN Ia model.

References

- [1] F.X. Timmes and S.E. Woosley, *ApJ* **396** (1992) 649.
- [2] M. Reinecke, W. Hillebrandt, J.C. Niemeyer, R. Klein, and A. Gröbl, *A&A* **347** (1999) 724.
- [3] B.A. Fryxell and E. Müller, MPA Green Report **449** (Max-Planck-Institut für Astrophysik, Garching, 1989).
- [4] S. Osher and J.A. Sethian, *J. Comp. Phys.* **79** (1988) 12.
- [5] M. Reinecke, W. Hillebrandt, and J.C. Niemeyer, *A&A* **386** (2002) 936.
- [6] F.K. Röpke and W. Hillebrandt, *A&A* **431** (2005) 635.
- [7] C. Travaglio, W. Hillebrandt, M. Reinecke, and F.-K. Thielemann, *A&A* **425** (2004) 1029.
- [8] E. Sorokina and S. Blinnikov, in "From Twilight to Highlight: The Physics of Supernovae" (Springer-Verlag, Berlin Heidelberg, 2003) 268.
- [9] C. Kozma, C. Fransson, W. Hillebrandt, C. Travaglio, J. Sollerman, M. Reinecke, F.K. Röpke, and J. Spyromillio, submitted to *A&A* (astro-ph/0504299).
- [10] F.K. Röpke and W. Hillebrandt, *A&A* **429** (2005) L29.
- [11] G. Damköhler, *Z. f. Electrochem.* **46** (1940) 601.

Subgrid Scale Models for Astrophysical Turbulence

W. Schmidt, J.C. Niemeyer

Lehrstuhl für Astronomie, Institut für Theoretische Physik und Astrophysik,
Universität Würzburg, Am Hubland, D-97074 Würzburg, Germany

We discuss a localised subgrid scale (SGS) model for fluid dynamical simulations which is based on the dynamical equation for the SGS turbulence energy k_{sgs} in the Germano consistent decomposition [1]. Using standard closures, this equation can be written in the following form [3, 4]:

$$\left(\frac{\partial}{\partial t} + \mathbf{v} \cdot \nabla\right) k_{\text{sgs}} - \frac{1}{\rho} \nabla \cdot \left(\rho \mathbf{C}_\kappa \Delta_{\text{eff}} \mathbf{k}_{\text{sgs}}^{1/2} \nabla \mathbf{k}_{\text{sgs}}\right) =$$

$$(C_A g_{\text{eff}} + C_\nu \Delta_{\text{eff}} |S^*|^2) k_{\text{sgs}}^{1/2} - \left(\frac{2}{3} + C_\lambda\right) k_{\text{sgs}} d - C_\epsilon \frac{k_{\text{sgs}}^{3/2}}{\Delta_{\text{eff}}}. \quad (1)$$

Here, \mathbf{v} is the velocity, $|S^*|^2$ is the norm of the trace-free rate of strain tensor, and d is the divergence of the resolved flow in a large-eddy simulation. The effective cutoff length is denoted by Δ_{eff} . The remaining parameters in the above equation are related to the different closures. For the rate of energy transfer the well known eddy-viscosity closure is applied. The strength of the localised model is the determination of the eddy-viscosity parameter C_ν from local structural properties of the resolved flow by means of a dynamical procedure [6]. The underlying similarity hypothesis was adopted from [5]. The closure parameters C_λ and C_ϵ are related to pressure and viscous dissipation, respectively. For these parameters as well as the SGS turbulent diffusivity parameter C_κ , statistical methods are applied [4]. The first term on the left hand side of equation (1) is kind of an Archimedian force which accounts for the production of turbulence due to the buoyancy of SGS density perturbations. In turbulent combustion problems, the effective gravity g_{eff} is determined by the density contrast between ash and fuel [7].

We implemented the SGS model for the three-dimensional numerical simulation of type Ia supernovae with the methodology outlined in [8]. The astronomical phenomenon called type Ia supernova is currently explained by the thermonuclear explosion of a white dwarf composed of carbon and oxygen which approaches the Chandrasekhar limit as a consequence of gas accretion from a companion star [9]. The explosion is the consequence of a runaway which is initiated when the central density and temperature exceed a certain threshold and thermonuclear flames are generated. Since the mass density of the nuclear ash is less than the density of the unburned material, Rayleigh-Taylor instabilities produce turbulent convective flow. It is known that turbulence greatly enhances the burning process by increasing the flame surface area and, consequently, the energy generation rate. This non-linear burning process incinerates and disrupts the whole star in a matter of a second [2].

Because of the enormous Reynolds numbers, it is impossible to resolve the flow and the structure of the flame surface completely. In a large-eddy simulation of the explosion, the flame fronts are therefore propagated with a turbulent flame speed, s_t , which becomes asymptotically proportional to the SGS turbulence velocity $q_{\text{sgs}} = \sqrt{\frac{1}{2} k_{\text{sgs}}}$ in the turbulent burning regime [10, 11]:

$$s_t \simeq \frac{2}{\sqrt{3}} q_{\text{sgs}} \quad (2)$$

The structure of the flame front and the dynamics of q_{sgs} for two particular instants of a simulation with 384^3 finite-volume cells is illustrated in Fig. 1 and 2. Slightly less than half a second after the ignition (Fig. 1) the flame geometry still resembles the axisymmetric initial condition, although

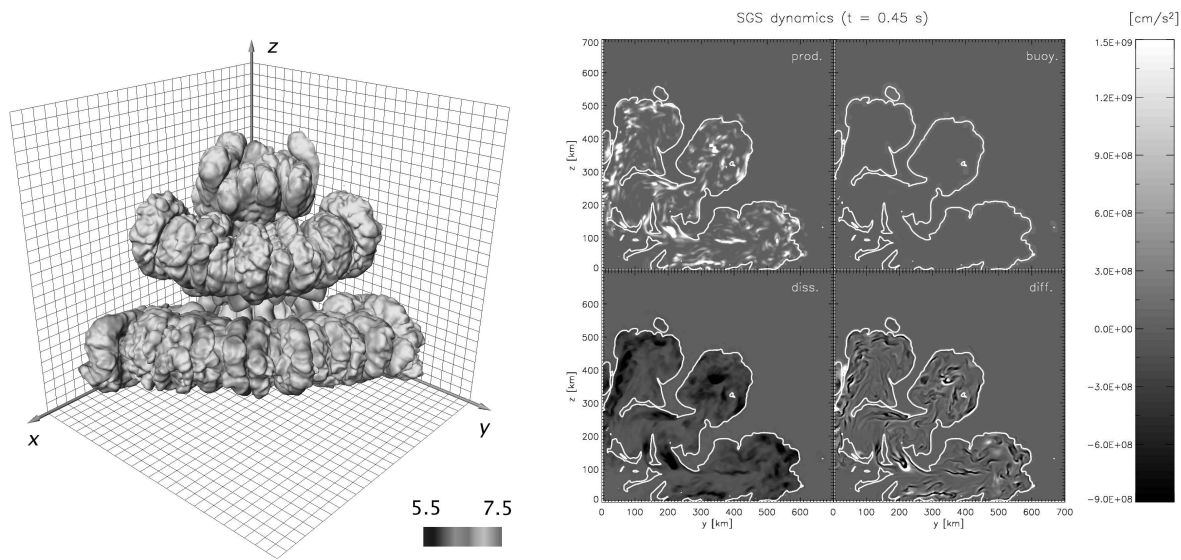


Figure 1: Three-dimensional visualisation of the flame front in thermonuclear supernova simulation at time $t = 0.45$ s after ignition (left). The colour shading indicates the SGS turbulence velocity in logarithmic scaling. Contour sections illustrating the various contributions to the SGS dynamics determined by equation (1) in a two-dimensional section perpendicular to the x -axis are shown on the right.

the sinusoidal perturbations have evolved into mushroom-like shapes which are characteristic for the Rayleigh-Taylor instability. One can also see secondary instabilities on top of the larger structures. The burned material in the interior of the flames is highly turbulent as becomes apparent from the rate of production and dissipation, respectively, shown in contour sections on the right of Fig. 1. The production includes only the contributions from turbulent energy transfer across the cutoff length. Buoyancy effects on subgrid scales, on the other hand, are typically weak compared to the energy transfer. It is a hallmark of the localised model that the transfer of energy is concentrated in small regions which appear as white spots in the contour plot. At $t = 0.75$ s (Fig. 1), the flames exhibit an intricate structure which has been formed by turbulent eddies on many different scales. Turbulence is already declining but the rate of nuclear energy generation is still high because of the very large flame surface area. However, the star is rapidly expanding at this time and, in consequence, the burning process will be quenched a few tenths of a second later.

The numerical simulation of type Ia supernovae is particularly challenging for a SGS model because the evolution of the burning process is highly sensitive to the flame speed which, in turn, is coupled to SGS turbulence. Moreover, the flow is both transient and inhomogeneous. As a result of recent investigations we conclude that the predictions of the supernova simulations are significantly altered by the localised SGS model.

Acknowledgements

We thank F. Röpke for kindly providing the co-moving grid implementation which enabled us to achieve high spatial resolution of the flames in our simulations. This work was supported by the Alfried Krupp Prize for Young University Teachers of the Alfried Krupp von Bohlen und Halbach Foundation.

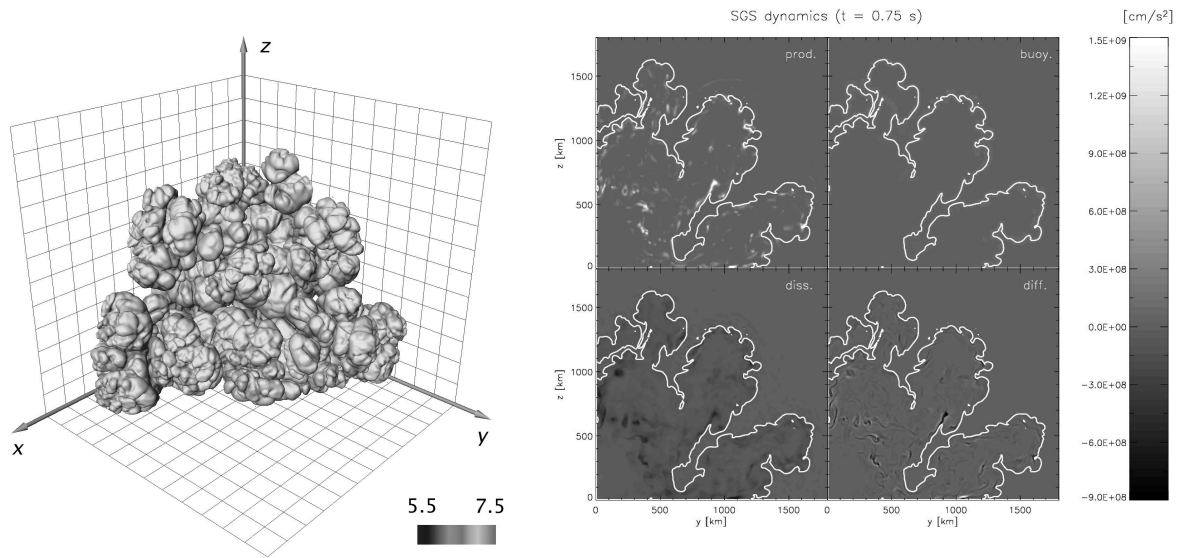


Figure 2: Same as in Fig. 1 for $t = 0.75$ s. Note the different spatial scale.

References

- [1] M. Germano, *J. Fluid Mech.* **238** (1992) 325
- [2] W. Hillebrandt and J.C. Niemeyer, *Ann. Rev. Astron. Astrophys.* **38** (2000) 191
- [3] U. Schumann, *J. Comp. Physics* **18** (1975) 376
- [4] W. Schmidt, W. Hillebrandt, and J.C. Niemeyer, accepted by *Combust. Theory Modelling*
- [5] W. Kim, S. Menon and H.C. Mongia, *Combust. Sci. and Tech.* **143** (1999) 25
- [6] M. Germano, U. Piomelli, P. Moin and W.H. Cabot, *Phys. Fluids* **3** (1991) 1760
- [7] W. Schmidt, J.C. Niemeyer and W. Hillebrandt, submitted to *Astron. Astrophys.*
- [8] F.K. Röpkke and W. Hillebrandt, *Astron. Astrophys.* **431** (2005) 635
- [9] F. Hoyle and W.A. Fowler, *Astrophys. J.* **132** (1960) 565
- [10] J.C. Niemeyer and W. Hillebrandt, *Astrophys. J.* **452** (1995) 769
- [11] N. Peters, *J. of Fluid Mech.* **384** (1999) 107

The FEARLESS Cosmic Turbulence Project

J.C. Niemeyer¹, W. Schmidt¹, C. Klingenberg²

¹ Lehrstuhl für Astronomie, Universität Würzburg, Am Hubland, D-97074 Würzburg, Germany

² Institut für Angewandte Mathematik und Statistik, Universität Würzburg, Am Hubland, D-97074 Würzburg, Germany

Abstract

We plan to develop, implement, and apply a new numerical scheme for modeling turbulent, multiphase astrophysical flows such as galaxy cluster cores and star forming regions. The method combines the capabilities of adaptive mesh refinement (AMR) and large-eddy simulations (LES) to capture localized features and to represent unresolved turbulence, respectively; it will therefore be referred to as **F**luid **m**echanics with **A**daptively **R**efined **L**arge-**E**ddy **S**imulation**S** or **FEARLESS**. Recent advances in the field of dynamical subgrid-scale (SGS) models for LES of thermonuclear supernovae enable us to formulate a self-consistent SGS model on adaptive meshes based on local similarity arguments for turbulent transport. Continuing our promising first tests, we intend to implement a full dynamical SGS model into the existing AMR hydrocode ENZO, followed by simulations of turbulent star forming clouds and galaxy cluster turbulence.

Turbulence in astrophysical phenomena

Many problems of astrophysical hydrodynamics share two important attributes: First, the ubiquitous presence of spatially localized features such as shocks, clumps, or composition discontinuities that need to be numerically resolved or at least adequately modeled; and second, large Reynolds numbers of the baryonic component indicating that fully developed, i.e. space-filling, turbulence is responsible for the mixing and dissipation properties of the gas almost everywhere. Despite great advances in computational fluid dynamics, an accurate handling of both aspects has so far proven to be very difficult as specialized numerical techniques have seemed to be mutually incompatible.

Our project aims at significantly improving this situation. The following three fields are among the most important problems of theoretical astrophysics that our approach may contribute to.

Turbulence in star formation

The efficiency, initial mass function (IMF), and feedback of star formation affects nearly every aspect of theoretical astrophysics. It is well known that turbulence plays a key role in the fragmentation of self-gravitating gas and in its support against gravity [1, 2]. The contribution of turbulence to the statistical properties of the IMF by turbulent fragmentation [3, 4] and to the transport of angular momentum during the collapse [5] are at the center of current theoretical and computational investigations. Furthermore, planned facilities such as ALMA and JWST will enable us to observe the earliest epochs of star formation in the universe.

The irregular shapes of molecular clouds and their complex emission line profiles indicate that the gas motions are supersonic and vigorously turbulent. Supersonic turbulence produces localized structures such as shocks and clumps which are amplified by gravity and cooling instabilities. Resolving these features while simultaneously accounting for the presence of low-amplitude turbulence elsewhere is one of the most challenging problems of computational astrophysics. Many simulations of turbulent star formation have used the Lagrangian method of smoothed particle hydrodynamics (SPH) (see

[2] for a review) whose capabilities for modeling turbulence are limited, however, as a result of its numerical diffusivity.

Only recently has adaptive mesh refinement (AMR) been employed for modeling supersonic turbulence in gas clouds [6, 4]. This work has demonstrated the potential of AMR to simulate turbulence in principle, opening a promising new approach that we intend to follow and improve in our project.

Primordial star formation at redshifts $z \approx 30 - 40$ plays a special role both theoretically and observationally because of its relevance for the early chemical and gravitational evolution of galaxies [7]. The pioneering AMR simulations of Abel, Bryan and Norman [8, 5] have shown the importance of angular momentum transport during the collapse and the absence of fragmentation of the central core. It will be interesting to see whether the effect of *turbulence refinement* (sec.) in FEARLESS will have a noticeable impact on these results. Together with supersonic self-gravitating turbulence, the collapse of a primordial gas cloud will provide a well-defined test bed for comparisons of the FEARLESS scheme with previous computations.

Turbulence in galaxy cluster cores

Understanding the evolution of the largest gravitationally bound structures in the universe has been one of the most active and successful fields of research in modern astrophysics. On the theoretical side, much of this progress is a result of the great advances in computational cosmological hydrodynamics, i.e. the numerical modeling of self-gravitational fluids consisting of cold dark matter and baryonic gas, coupled to a variety of relevant physical processes such as radiative cooling, supernova feedback, and chemical enrichment. The core of these models usually consists of an N-body code for the gravitational sector coupled to an Eulerian hydro solver. Great progress has been made regarding the resolution of localized structures using adaptive mesh refinement (AMR) for grid-based solvers or Lagrangian methods like smoothed particle hydrodynamics (SPH) [9, 10, 11]. Turbulence on unresolved scales, on the other hand, has in most cases been neglected in cosmological hydrodynamical simulations.

Examples for the many reasons to improve numerical models of galaxy clusters are the search for a solution of the cooling flow problem, the explanation of the rich substructure of cool cluster cores seen with X-ray instruments such as XMM and CHANDRA, and the fascinating prospect for directly detecting cluster turbulence with the ASTRO-E2 XRS high-resolution spectrometer. We will address each of these problems in the following paragraphs.

X-ray observations of cluster cores have detected less cool gas than predicted by cooling-flow models [12], suggesting that the mass deposition rate of cool gas is suppressed by an unknown mechanism. Various solutions for this problem have been proposed, including feedback from star formation and supernovae [13], turbulence induced by large-scale gas motions [14], and buoyant plasma bubbles from AGN activity [15]. We expect hydrodynamical simulations of the latter two phenomena to be greatly improved by using FEARLESS (due to the *turbulence refinement effect*, sec.) and the level set method for non-diffusive interfaces, respectively.

Observations with X-ray satellites have also shown evidence of spatially localized substructures termed “cool fronts”, “cool bullets”, and “cool filaments” in galaxy cluster cores. Their most likely origin is a combination of radiative cooling and star formation feedback resulting in a picture of hierarchical mergers of cool subclusters [16]. Simulations of such structures involving multiple fluid phases separated by a numerically unresolvable interface are usually limited by the inherent diffusivity of the hydrodynamical scheme. Again, significant improvements can be expected by using interface tracking methods such as the level set scheme proposed in our project.

Finally, the potential detection of turbulent gas motions in their X-ray spectra with the upcoming ASTRO-E2 mission further strengthens the need for highly resolved, self-consistent simulations of cluster turbulence [17, 18]. Comparisons of observations with detailed simulations will help to differentiate

between the various proposed mechanisms to ameliorate the cooling flow problem summarized above, all of which are expected to give rise to turbulence.

Modeling of type Ia supernova explosions

Owing, among other things, to their potential as cosmological distance indicators, type Ia supernovae have received widespread attention. Numerous observational campaigns are underway (e.g., the European Supernova Collaboration [19], the ESSENCE project [20], and the Nearby Supernova Factory [21]), allowing us to compare theoretical models with observed spectra and light curves in unprecedented detail.

The present consensus model for supernovae of type Ia is the thermonuclear explosion of a Chandrasekhar mass white dwarf [22]. The burning process proceeds as subsonic deflagration which is driven by turbulence [23, 24]. The production of turbulence is a consequence of Rayleigh-Taylor instabilities due to the lower mass density of nuclear ash as compared to the density of unprocessed material [25].

By means of massively parallel computation on present day supercomputers, the three-dimensional numerical simulation of type Ia supernova explosions has become feasible [26]. However, only the largest dynamical scales can be numerically resolved because the Reynolds numbers are huge and the corresponding number of degree of freedoms is beyond the capability of even the most powerful computers today. Thus, one of the major challenges is to account for the interaction between turbulent eddies and the flame propagation on unresolved length scales. This is achieved by means of a subgrid-scale model [23].

The assumption that type Ia supernovae are the result of a pure deflagration has been challenged because the corresponding numerical models fail to predict certain observational features correctly. Perhaps the most severe problem is the significant amount of unburnt carbon and oxygen at low radial velocities which occur in present deflagration models. Apart from that, the total amount of nickel and the energy output are still short of typical observational values [27, 28]. A delayed detonation scenario has been proposed which apparently resolves these difficulties [29, 30]. The transition from a subsonic deflagration phase to a supersonic detonation is hypothetical, and no plausible mechanism has been found in the particular case of thermonuclear combustion in white dwarfs [31]. On the other hand, new developments in the area of the deflagration model suggest that highly turbulent deflagrations may suffice to match observational features of type Ia supernovae. In particular, advances have been made with more realistic initial conditions, enhanced resolution with non-static grids, and improved subgrid scale models [28, 32] (see also). In any case, more powerful numerical techniques are required in order to settle the issue of the actual explosion mechanism.

Numerical Modeling Techniques

Adaptive mesh refinement

Considerable progress has been made in modeling as much flow structure as possible by direct numerical computation. The most powerful method for the treatment of non-steady flows exhibiting significant anisotropy and high degrees of intermittency is adaptive mesh refinement (AMR). AMR is based on Eulerian continuum mechanics with a hierarchy of grid patches to approximate the flow on various levels of resolution [33]. In localized regions developing structure on comparatively small length scales, a higher level of refinement is applied while smoother portions of the flow are treated with coarser grids. Astrophysical problems for which AMR is particularly well suited include strong shocks [34] and gravitational collapse [35] among many other applications [10]. All cases exhibit locally steep gradients of the state variables and/or rapid spatiotemporal changes in the velocity field.

Only recently, first steps have been taken to explore the ability of AMR to model fully developed turbulence [6]. The authors have demonstrated that AMR can exploit the fact that dissipation is concentrated in spatial regions of dimension less than three at any instant of time. This is true even for homogeneous turbulence which is commonly considered as “space filling” based on the properties of its ensemble average. Although a detailed comparison of turbulence modeled with AMR and uniform grid simulations remains to be done, it is already clear that AMR is one of the few candidates to significantly extend the range of numerically achievable Reynolds numbers.

However, in the case of astrophysically relevant Reynolds numbers unmanageable levels of refinement would be required in order to resolve the dissipative scales. Moreover, AMR suffers from an intrinsic inconsistency when applied to turbulent flows: As new levels of refinement are added, the velocity on the smallest scales is initially smooth, in contrast with the physical requirement of velocity fluctuations on all scales above the viscous (Kolmogorov) scale. As sketched in fig. 1, this inconsistency will be resolved in FEARLESS by using the subgrid-scale turbulence as an energy buffer (sec.).

Large eddy simulations

In engineering applications as well as other fields of computational fluid dynamics, large eddy simulations (LES) have been in use over several decades [36]. There is no hierarchy of dynamically changing grid patches but one static grid that may be equidistant or unstructured. The conservation laws of hydrodynamics are solved by means of spectral or finite-volume methods. Subgrid scale eddies of size smaller than the grid resolution cannot be resolved by the numerical scheme. The stress exerted by subgrid scale eddies onto resolved eddies that results in the transfer of kinetic energy from larger towards smaller scales is accounted for by a heuristic model, a so-called subgrid-scale (SGS) model [37]. An exact treatment of subgrid scale turbulence is impossible due to the non-linearity in the dynamical equations which entails the fundamental *closure problem* in turbulence theory.

The selection of an appropriate SGS model is a notorious problem because of the considerable variety of models that have been proposed. In astrophysical fluid dynamics, many researchers choose the minimal solution of letting numerical dissipation drain kinetic energy from the resolved flow. Engineers and atmospheric scientists, on the other hand, have recognized that numerical dissipation is an insufficient solution at best [38, 39]. Turbulent burning in thermonuclear supernova explosions is one of the few examples in astrophysics where a proper SGS model has been applied so far [23, 40].

LES is limited, however, in its representation of highly transient and localized phenomena. This problem can be traced back to the fact that all SGS models are in some way based on the notion of similarity. In other words, an LES must resolve the flow to an extent that turbulence becomes nearly isotropic and scale-invariant towards the smallest resolved length scales. The anisotropy of the flow stemming from large-scale features, such as boundary conditions and mechanical forces, is then mostly confined in the range of “large eddy scales”. Under the conditions mentioned above, however, this often becomes infeasible using a static grid approach. In this case, AMR would do a much better job apart from the drawback that it fails to account for small-scale turbulence.

Combining AMR and LES

Few attempts has been made so far to apply AMR in combination with a subgrid-scale (SGS) model. The outcome would be a FEARLESS scheme with locally adapting resolution (for a recent proposal along these lines, see [41]). The central idea is to track turbulent regions in the flow and to explicitly compute any transient or anisotropic features by means of AMR. For each grid patch, an SGS model with the corresponding cutoff scale must then be invoked in order to capture the effect of yet smaller, unresolved velocity fluctuations. The following conceptual and technical questions have kept the development of FEARLESS from progressing very far until now:

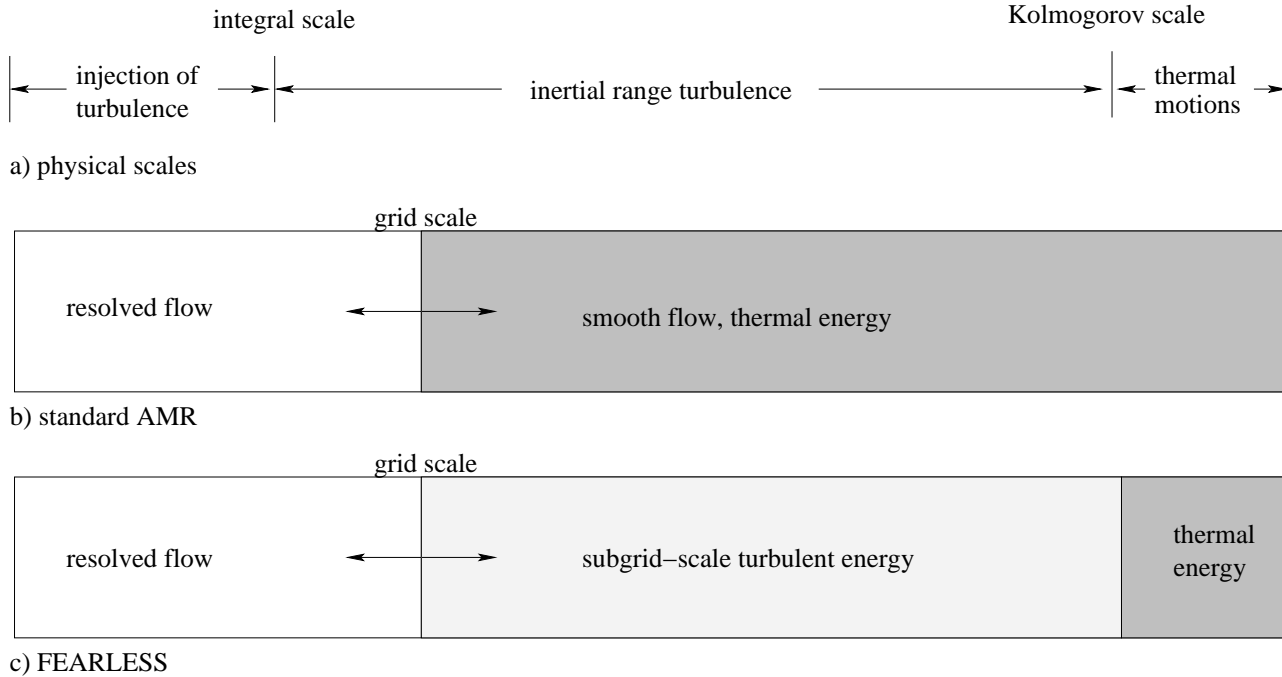


Figure 1: Comparison of the physical length scales of fully developed turbulence (a) with the partition between resolved kinetic energy, unresolved kinetic energy, and thermal energy without (standard AMR, (b)), and with (FEARLESS, (c)) an SGS model for unresolved turbulence. The arrows at the grid scale in (b) and (c) represent the variability of the grid scale in AMR and are meant to clarify the *turbulence refinement effect*.

1. How can the central similarity arguments of LES that are usually formulated in Fourier space be transferred to a grid with locally varying resolution?
2. How can filters be implemented self-consistently across AMR patches?
3. How does subgrid-scale turbulence propagate between regions of varying resolution?
4. How can grid refinement and derefinement be made consistent with the presence of turbulent velocity fluctuations that become resolved or unresolved?

Owing to our experience using localized SGS models in supernova Ia research [40, 42, 43], we are now able to answer questions 1 and 2, while 3 and 4 are currently under investigation.

We expect the most noticeable difference between FEARLESS and standard AMR simulations to be the *turbulence refinement effect* related to point 4 above. Assuming the existence of a turbulent cascade on all scales above the (unresolvable) Kolmogorov length, the addition of grid patches must account self-consistently for the kinetic energy of previously unresolved fluctuations that become a part of the resolved flow (cf. fig. 1). We intend to implement this effect by explicitly forcing fluctuations on the newly created small scales and subtracting the corresponding amount of energy from the subgrid-scale energy of the SGS model. The inverse process of derefinement will be handled accordingly by adding the appropriate kinetic energy to the SGS energy. Hence, the SGS model can be used as an energy buffer for grid resolution changes, in addition to its usual application to mimic turbulent mixing and dynamical pressure.

In situations with a large number of refinement levels, as typically encountered in the examples of sec. , the *turbulence refinement effect* can potentially become the dominant source of turbulent

fluctuations on small scales. This is one of our main motivations for revisiting these problems with a FEARLESS approach.

Acknowledgements

The research of JCN and WS is supported by the Alfried Krupp Prize for Young University Teachers of the Alfried Krupp von Bohlen und Halbach Foundation.

References

- [1] R. B. Larson, Rept. Prog. Phys. **66**, 1651 (2003), astro-ph/0306595.
- [2] M.-M. Mac Low and R. S. Klessen, Rev. Mod. Phys. **76**, 125 (2004), astro-ph/0301093.
- [3] P. Padoan and A. Nordlund, (2004), astro-ph/0411474.
- [4] P. Padoan, A. Kritsuk, M. Norman, and A. Nordlund, (2004), astro-ph/0411480.
- [5] T. Abel, G. L. Bryan, and M. L. Norman, Science **295**, 93 (2002).
- [6] A. G. Kritsuk, M. L. Norman, and P. Padoan, Astrophys. J. Lett. (2004), astro-ph/0411626, submitted.
- [7] S. C. O. Glover, (2004), astro-ph/0409737.
- [8] T. Abel, G. L. Bryan, and M. L. Norman, Astron. & Astrophys. **540**, 39 (2000), astro-ph/0002135.
- [9] B. W. O’Shea, K. Nagamine, V. Springel, L. Hernquist, and M. L. Norman, (2003), astro-ph/0312651.
- [10] M. L. Norman, (2004), astro-ph/0402230.
- [11] M. L. Norman, (2004), astro-ph/0403079.
- [12] H. Böhringer, K. Matsushita, E. Churazov, Y. Ikebe, and Y. Chen, Astron. & Astrophys. **382**, 804 (2002).
- [13] G. M. Voit and G. L. Bryan, Nature **414**, 425 (2001).
- [14] Y. Fujita, T. Matsumoto, and K. Wada, (2004), astro-ph/0407368.
- [15] M. Brüggen and C. R. Kaiser, Nature **418**, 301 (2002).
- [16] J. O. Burns, P. M. Motl, M. L. Norman, and G. L. Bryan, (2003), astro-ph/0309836.
- [17] R. A. Sunyaev, M. L. Norman, and G. L. Bryan, Astronomy Letters **29**, 783 (2003).
- [18] Y. Fujita, T. Matsumoto, K. Wada, and T. Furusho, (2004), astro-ph/0412353.
- [19] S. Benetti *et al.*, Mon. Not. Roy. Astr. Soc. **348**, 261 (2004).
- [20] T. Matheson *et al.*, (2004), astro-ph/0411357.
- [21] W. M. Wood-Vasey *et al.*, New Astronomy Review **48**, 637 (2004).
- [22] F. Hoyle and W. A. Fowler, Astrophys. J. **132**, 565 (1960).

- [23] J. C. Niemeyer and W. Hillebrandt, *Astrophys. J.* **452**, 769 (1995).
- [24] W. Hillebrandt and J. C. Niemeyer, *Annu. Rev. Astron. Astrophys.* **38**, 191 (2000).
- [25] A. M. Khokhlov, *Astrophys. J.* **449**, 695 (1995).
- [26] M. Reinecke, W. Hillebrandt, and J. C. Niemeyer, *Astron. & Astrophys.* **391**, 1167 (2002).
- [27] V. N. Gamezo, A. M. Khokhlov, E. S. Oran, A. Y. Chtchelkanova, and R. O. Rosenberg, *Science* **299**, 77 (2003).
- [28] F. K. Röpké and W. Hillebrandt, *Astron. & Astrophys.* (2004), astro-ph/0408296, submitted.
- [29] A. M. Khokhlov, *Astron. & Astrophys.* **245**, 114 (1991).
- [30] V. N. Gamezo, A. M. Khokhlov, and E. S. Oran, *Physical Review Letters* **92**, 211102 (2004).
- [31] J. C. Niemeyer, *Astrophys. J.* **523**, L57 (1999).
- [32] W. Schmidt, J. C. Niemeyer, and W. Hillebrandt, A novel flame speed model for turbulent deflagration in type Ia supernovae, in preparation, 2005.
- [33] M. J. Berger and J. Oliger, *J. Comp. Physics* **53**, 484 (1984).
- [34] M. J. Berger and P. Colella, *J. Comp. Physics* **82**, 64 (1989).
- [35] B. W. O'Shea *et al.*, Introducing Enzo, an AMR Cosmology Application, in *Adaptive Mesh Refinement - Theory and Applications*, edited by T. Plewa, T. Linde, and V. Weirs, Springer Lecture Notes in Computational Science and Engineering, 2004, astro-ph/040304.
- [36] M. Lesieur and O. Métais, *Annu. Rev. Fluid Mech.* **28**, 45 (1996).
- [37] P. Sagaut, *Large Eddy Simulation for Incompressible Flows* (Springer, 2001).
- [38] P. J. Mason, *J. Atmos. Sci.* **46**, 1492 (1988).
- [39] J. C. R. Hunt, J. C. Kaimal, and J. E. Gaynor, *Q. J. R. Meteorol. Soc.* **114**, 827 (1988).
- [40] W. Hillebrandt *et al.*, Simulations of Turbulent Thermonuclear Burning in Type Ia Supernovae, in *Analysis and Numerics of Conservation Laws*, edited by G. Warnecke, Springer-Verlag, 2004, astro-ph/0405209.
- [41] S. M. Mitran, A comparison of adaptive mesh refinement approaches for large eddy simulation, online <http://www.amath.unc.edu/Faculty/mitran/amrles.html>.
- [42] W. Schmidt, *Turbulent Thermonuclear Combustion in Degenerate Stars*, PhD thesis, Faculty of Physics, Technical University of Munich, 2004, online <http://tumb1.biblio.tu-muenchen.de/publ/diss/ph/2004/schmidt.html>.
- [43] W. Schmidt, W. Hillebrandt, and J. C. Niemeyer, Level set simulations of turbulent thermonuclear deflagration in degenerate carbon and oxygen, submitted to *Combust. Theory Modelling*, 2004.

References related to further contributions

The following references are directly related to further contributions given as oral presentations during the workshop.

1. **François Daviaud** SPEC, CEA/Saclay
F-91191 Gif sur Yvette cedex, France
e-mail: daviaud@drecam.saclay.cea.fr

M. Bourgoïn, L. Marié, F. Pétrélis, C. Gasquet, A. Guigon, J-B. Luciani, M. Moulin, F. Namer, J. Burguete, A. Chiffaudel, F. Daviaud, S. Fauve, P. Odier, J.-F. Pinton. MHD measurements in the von Kármán sodium experiment *Phys. Fluids* **14**, 3046 (2002).

F. Pétrélis, M. Bourgoïn, L. Marié, J. Burguete, A. Chiffaudel, F. Daviaud, S. Fauve, P. Odier and J.-F. Pinton Nonlinear magnetic induction by helical motion in a liquid sodium turbulent flow. *Phys. Rev. Lett.* **90**, 174501 (2003).

J. Burguete, L. Marié, F. Daviaud and J. Léorat Homogeneous dynamo: numerical analysis of experimental von Kármán type flows *Eur. Phys. J. B* **33**, 469 (2003).

2. **Bérengère Dubrulle**

Groupe Instabilité et Turbulence
CNRS, Service d'Astrophysique, CE Saclay, Lorme des Merisiers, 709
F-91191 Gif sur Yvette Cedex, France, e-mail: bdubru@drecam.saclay.cea.fr

F. Hersant, B. Dubrulle, and J.-M. Huré, Turbulence in circumstellar disks *Astron. & Astrophys.* **429**, 531-542 (2005).

Bérengère Dubrulle, Olivier Dauchot, François Daviaud, Pierre-Yves Longaretti, Denis Richard, Jean-Paul Zahn Stability and turbulent transport in Taylor-Couette flow from analysis of experimental data, to appear in *Physics of Fluids* (2005).

3. **Sergei Fedotov**

School of Mathematics, The University of Manchester, M60 1QD UK
e-mail: s.fedotov@manchester.ac.uk

Sergei Fedotov, Matthias Ihme, and Heinz Pitsch Stochastic mixing model with power law decay of variance, *Phys. Rev. E.* **71**, 016310 (2005)

4. **Dirk Olbers**

Alfred Wegener Institute for Polar and Marine Research
Postfach 120161, 27515 Bremerhaven, Germany
e-mail: dolbers@awi-bremerhaven.de

Interpreting eddy fluxes Carsten Eden, Richard J. Greatbatch, and Dirk Olbers re-submitted to *Jour. Phys. Oceanogr.* (2005).

5. Lars Umlauf

Physical Oceanography and Instrumentation, Baltic Sea Research Institute Warnemünde
address: P.O. Box 301161, D-18112 Rostock-Warnemünde, Germany
e-mail: lars.umlauf@io-warnemuende.de

Burchard, H., and K. Bolding, Comparative analysis of four second-moment turbulence closure models for the oceanic mixed layer, *J. Phys. Oceanogr.*, **31**, 1943-1968, 2001.

Umlauf, L, Modelling the effects of horizontal and vertical shear in stratified turbulent flows, *Deep-Sea Res. II*, **52**, 1181-1201, 2005.

Umlauf, L., and H. Burchard, A generic length-scale equation for geophysical turbulence models, *J. Mar. Res.*, **61**, 235-265, 2003.

Umlauf, L., and H. Burchard, Second-order turbulence closure models for geophysical boundary layers. A review of recent work, *Cont. Shelf Res.*, **25**, 795-827, 2005.

6. Hua Xia

Plasma Research Lab, Research School of Physical Sciences & Engineering
The Australian National University, Canberra, ACT 0200
e-mail: hua.xia@anu.edu.au

Shats M.G., Xia H., Punzmann H. Spectral condensation of turbulence in plasmas and fluids and its role in low-to-high phase transitions in toroidal plasma, *Physical Review E*, **71**, 046409 (2005)

Further material and references given during oral presentations at the workshop by Eberhard Bodenschatz, Vittorio M. Canuto, and Constantino Tsallis can be found in a volume of the Lecture Notes in Physics Series on the main topics of this workshop (to be published in 2006). For PDF versions of some of these presentations see: <http://www.mpa-garching.mpg.de/hydro/Turbulence/>